DGK Deutsche Geodätische Kommission
bei der Bayerischen Akademie der Wissenschaften

Reihe C | Dissertationen | Heft Nr. 695

Claudia Stephanie Stummer

Gradiometer Data Processing and Analysis for the GOCE Mission

München 2013

Verlag der Bayerischen Akademie der Wissenschaften
in Kommission beim Verlag C. H. Beck

ISSN 0065-5325 ISBN 978-3-7696-5107-2

DGK Deutsche Geodätische Kommission
bei der Bayerischen Akademie der Wissenschaften

Reihe C Dissertationen Heft Nr. 695

Gradiometer Data Processing and Analysis for the GOCE Mission

Vollständiger Abdruck
der von der Fakultät für Bauingenieur- und Vermessungswesen
der Technischen Universität München
zur Erlangung des akademischen Grades eines
Doktor-Ingenieurs (Dr.-Ing.)
genehmigten Dissertation

von

Dipl.-Ing. Claudia Stephanie Stummer

München 2013

Verlag der Bayerischen Akademie der Wissenschaften
in Kommission beim Verlag C. H. Beck

ISSN 0065-5325 ISBN 978-3-7696-5107-2

Adresse der Deutschen Geodätischen Kommission:

Deutsche Geodätische Kommission

Alfons-Goppel-Straße 11 ● D – 80 539 München

Telefon +49 – 89 – 23 031 1113 ● Telefax +49 – 89 – 23 031 - 1283 / - 1100

e-mail hornik@dgfi.badw.de ● http://www.dgk.badw.de

Prüfungskommission

Vorsitzende: Univ.-Prof. Dr.-Ing. L. Meng

Prüfer der Dissertation:
1. Univ.-Prof. Dr.techn. R. Pail
2. Univ.-Prof. Dr.techn. W.-D. Schuh, Rheinische Friedrich-Wilhelms-Universität Bonn
3. Univ.-Prof. Dr.-Ing. Dr. h.c. mult. R. Rummel (i.R.)

Die Dissertation wurde am 02.08.2012 bei der Technischen Universität München eingereicht und durch die Fakultät für Bauingenieur- und Vermessungswesen am 19.10.2012 angenommen.

Diese Dissertation ist auch auf mediaTUM – Dokumenten- und Publikationsserver der Technischen Universität München <http://mediatum.ub.tum.de/node?id=1111698> elektronisch publiziert (Erscheinungsjahr 2012)

© 2013 Deutsche Geodätische Kommission, München

Alle Rechte vorbehalten. Ohne Genehmigung der Herausgeber ist es auch nicht gestattet, die Veröffentlichung oder Teile daraus auf photomechanischem Wege (Photokopie, Mikrokopie) zu vervielfältigen.

ISSN 0065-5325 ISBN 978-3-7696-5107-2

Abstract

The Gravity field and steady-state Ocean Circulation Explorer (GOCE) satellite mission delivers data of the Earth's gravity field with unprecedented precision. With GOCE for the first time in history a gravity gradiometer is used on board of a satellite for this purpose. Consequently, new processing strategies had to be developed for the optimal exploitation of the new data type.

In this work the GOCE gradiometer data as well as the related processing strategies are analyzed, and further developed.

First, the theoretical basis for gravitational gradiometry in space in general and specifically with GOCE is discussed. The purpose of this part of the work is to introduce the reader to the subject of satellite gradiometry which goes back for several decades, and to familiarize with the most important characteristics of the GOCE mission and its sensor system, especially with the gradiometer.

In the second part the original gradiometer Level 1b processing as it has been performed during the nominal mission phase by ESA's Payload Data Segment (PDS) is analyzed in detail. A description of all important processing steps, starting with the de-packeting of the Level 0 gradiometer data up to the Level 1b gravity gradients is given. Simultaneously, related intermediate data are visualized for an example day, which allows some first quality assessment of the GOCE data.

The third part is dedicated to the gradiometer calibration. The gradiometer calibration parameters can be classified into two main types, the so-called quadratic factors and the ICMs (Inverse Calibration Matrices). The physical origin of the imperfections and the different strategies for their determination and compensation, i.e. for calibration, are discussed. The emphasis is on the determination of the ICMs. Here two main strategies exist. The first one is the original method as implemented in ESA's PDS. This method has also been implemented at IAPG. The second one was invented by ESA (Daniel Lamarre). Its results are currently used in the official Level 1b processing for calibrating the measured accelerations.

The fourth part contains data analysis in the time as well as in the frequency domain. Further quality assessment is made for the gravity gradients and their components (angular rates and differences of accelerations) as well as for the data from the three star sensors on board of GOCE. The development of the calibration parameters is investigated, and some discrepancies with respect to pre-launch expectations are identified. Also the role of the star sensors for the determination of the gradiometer calibration parameters is demonstrated.

In the fifth part alternative gradiometer processing strategies are developed and adapted for the use in PDS' Level 1b processing. In total, four upgraded methods are introduced. These are the methods for the determination of the angular rates and the attitude quaternions, the calibration of the accelerations and an additional strategy for the combination of all available star sensor measurements.

Finally, the benefit of the four upgrades is analyzed at the level of gravity gradients as well as at the level of gravity field solutions based on satellite gravity gradiometry data. The largest overall improvements are due to the new method for angular rate reconstruction, mainly at the low to medium frequencies and at the harmonics of the orbital revolution frequency. In addition, spurious artifacts in the gravity gradient V_{yy}, which are caused by non-perfect common mode rejection, can be reduced significantly by the improved calibration approach. The standard deviation of the gravity gradient tensor trace can be reduced by about 90 % for the frequencies below the gradiometer measurement band (i.e. below 5 mHz) and by about 4 % within the measurement band (from 5 to 100 mHz). The cumulative geoid error and the cumulative gravity anomaly error, between degrees 20 and 150, of satellite gravity gradiometry solutions based on 61 days of data are reduced by about 27 %. The gravity field solutions based on satellite gravity gradiometry data are combined with GOCE GPS data. In this case, the improvement due to the alternative Level 1b processing becomes much smaller, but is still observable. The cumulative geoid error and the cumulative gravity anomaly error, between degrees 20 and 150, are reduced by 10 %.

Meanwhile, these upgrades have been implemented in the PDS Level 1b processor, and the data of the whole GOCE mission are reprocessed.

Zusammenfassung

Die Satellitenmission GOCE (Gravity field and steady-state Ocean Circulation Explorer) liefert Daten des Erdschwerefelds von bisher nicht verfügbarer Qualität. Mit GOCE kommt zum ersten Mal in der Geschichte ein Schweregradiometer an Bord eines Satelliten zu diesem Zweck zum Einsatz. Folglich mussten neue Prozessierungsstrategien entwickelt werden, die den neuen Datentyp optimal ausnutzen können.

In dieser Arbeit werden sowohl die GOCE Gradiometerdaten als auch die zugehörigen Prozessierungsstrategien analysiert und weiterentwickelt.

Zunächst werden die theoretischen Grundlagen der Satellitengradiometrie im Allgemeinen und speziell für GOCE diskutiert. In diesem Teil der Arbeit soll der Leser in den Fachbereich der Satellitengradiometrie, welcher einige Dekaden zurückreicht, eingeführt werden und mit den wichtigsten Eigenschaften der GOCE-Mission, sowie dem zugehörigen Sensorsystem, insbesondere mit dem Gradiometer vertraut gemacht werden.

Im zweiten Teil findet eine detaillierte Analyse der Level 1b Gradiometerprozessierung, wie sie ursprünglich von ESA's Payload Data Segment (PDS) durchgeführt wurde, statt. Alle wichtigen Prozessierungsschritte, anfangend bei den Level 0 Gradiometerdaten bis hin zu den Level 1b Schweregradienten werden beschrieben. Gleichzeitig werden die zugehörigen Zwischenprodukte jeweils beispielhaft für einen Tag graphisch dargestellt, was erste Genauigkeitsabschätzungen der GOCE-Daten ermöglicht.

Der dritte Teil ist der Gradiometer-Kalibrierung gewidmet. Die Gradiometer-Kalibrationsparameter lassen sich in zwei Typen unterteilen, die sogenannten quadratischen Faktoren und die inversen Kalibrationsmatrizen (ICMs). Es findet eine Diskussion des physikalischen Ursprungs der Gradiometerfehler und der verschiedenen Strategien für ihre Bestimmung und Kompensation, d.h. für die Kalibrierung statt. Das Hauptaugenmerk wird dabei auf die Bestimmung der ICMs gelegt. Hierfür existierten zwei besonders wichtige Strategien. Die erste ist die ursprüngliche Methode, welche in ESAs PDS eingebaut wurde. Diese Methode wurde auch am IAPG implementiert. Die Zweite wurde von ESA (Daniel Lamarre) entwickelt. Die zugehörigen Ergebnisse werden aktuell in der offiziellen Level 1b-Prozessierung zur Kalibrierung der gemessenen Beschleunigungen verwendet.

Der vierte Teil enthält weiterführende Datenanalysen sowohl im Zeit- als auch im Frequenzbereich. Es werden weitere Genauigkeitsabschätzungen gemacht, sowohl für die Schweregradienten und ihre Bestandteile (Winkelgeschwindigkeiten und Beschleunigungsdifferenzen), als auch für die Daten der drei Sternsensoren an Bord von GOCE. Die zeitliche Entwicklung der Kalibrationsparameter wird untersucht und Abweichungen von den Erwartungen, die es vor dem Satellitenstart gab, werden identifiziert. Ebenso wird die Rolle der Sternsensoren für die Bestimmung der Gradiometer-Kalibrationsparameter aufgezeigt.

Im fünften Teil werden alternative Strategien zur Gradiometerprozessierung entwickelt und für den Gebrauch in der Level 1b-Prozessierung des PDS angepasst. Insgesamt werden vier verbesserte Methoden vorgestellt. Diese sind die Methoden zur Bestimmung der Winkelgeschwindigkeiten und der Lage-Quaternionen, die Kalibrierung der Beschleunigungen und eine zusätzliche Methode für die Kombination aller gleichzeitig verfügbarer Sternsensormessungen.

Schließlich wird der Nutzen der vier Modifikationen sowohl auf Ebene der Schweregradienten, als auch auf Ebene von Schwerefeldlösungen, basierend auf Gravitationsgradienten, analysiert. Die größte Verbesserung wird durch die neue Methode zur Bestimmung der Winkelgeschwindigkeiten, hauptsächlich für die niedrigen bis mittleren Frequenzen und für die Harmonischen der Umlauffrequenz, erzielt. Zusätzlich können durch den verbesserten Ansatz zur Kalibrierung auch Artefakte, die entlang der Bodenspuren im Schweregradient V_{yy} auftreten und welche ein restliches common mode Signal in den Messungen darstellen, signifikant reduziert werden. Die Standardabweichung der Spur des Schweregradiententensors kann für die Frequenzen unterhalb des Gradiometer-Messbands (d.h. unterhalb von 5 mHz) um ca. 90 % und innerhalb des Messbands (von 5 bis 100 mHz) um ca. 4 % reduziert werden. Der kumulative Geoidfehler und der kumulative Fehler in den Schwereanomalien von Schwerefeldlösungen, die nur auf Gravitationsgradienten von 61 Tagen basieren, werden zwischen den Graden 20 und 150 um ca. 27 % reduziert. Die auf Gravitationsgradienten basierenden Schwerefeldlösungen werden mit GOCE GPS Daten kombiniert. In diesem Fall wird die Verbesserung aufgrund der alternativen Level 1b Prozessierung deutlich kleiner, ist aber immer noch beobachtbar. Der kumulative Geoidfehler und der kumulative Fehler in den Schwereanomalien werden zwischen den Graden 20 und 150 um 10 % reduziert.

Mittlerweile wurden diese Verbesserungen auch im PDS Level 1b-Prozessor implementiert und die Daten der gesamten GOCE Mission werden entsprechend re-prozessiert.

Contents

1. Introduction

1.1. Overview of the GOCE mission

The Gravity field and steady-state Ocean Circulation Explorer (GOCE) mission was launched successfully on 17 March 2009. Since the beginning of the mission operational phase in September 2009, it is gathering data of the Earth's gravity field with unprecedented precision. GOCE is the first core explorer mission of the Living Planet programme of the European Space Agency (ESA). The GOCE mission objective is to model the Earth's static gravity field with an accuracy of 2 cm in geoid heights, and 1 mGal in gravity anomalies, at a spatial resolution of 100 km (Drinkwater et al., 2007), cf. Fig. 1.1.

Figure 1.1.: GOCE satellite. Source: ESA (2008).

The core instrument of GOCE is an electrostatic gravity gradiometer (EGG), which consists of six accelerometers mounted on three mutually orthogonal axes. It is used for satellite gravity gradiometry (SGG), cf. Fig. 1.2. Moreover, the satellite is equipped with a GPS instrument for high-low satellite-to-satellite tracking (SST-hl), and three star sensors (STR) to determine the absolute orientation in space.

The EGG measurements are used to derive common mode (CM) and differential mode (DM) accelerations. CM accelerations represent the sum of all non-conservative (non-gravitational) forces acting on the satellite, and are input signal of the drag-free control (DFC) system. It keeps the satellite in free fall at constant altitude by using ion thrusters as actuators. From the DM accelerations finally the satellite gravity gradients are derived (Cesare and Catastini, 2008b), which represent the key product to model the Earth's gravity field. One important aspect of the high performance of the GOCE mission is the fact that the EGG is not only the key driver to measure CM and DM linear accelerations, but also rotational accelerations, which are combined with the STR observations. After this angular rate reconstruction (ARR), gravity gradients at the one hand, and the attitude information of the satellite at the other hand, are derived.

The GOCE data processing at ground level is performed at several levels (SERCO/DATAMAT_Consortium, 2006; Drinkwater et al., 2007). The output of the Level 0 processing are time-ordered raw data, produced by the instruments and by the platform. These are e.g. star sensor attitude quaternions with a sampling rate of 2 Hz and the gradiometer measurements with a sampling rate of approximately 1 Hz. The Level 0 to Level 1b (L1b)

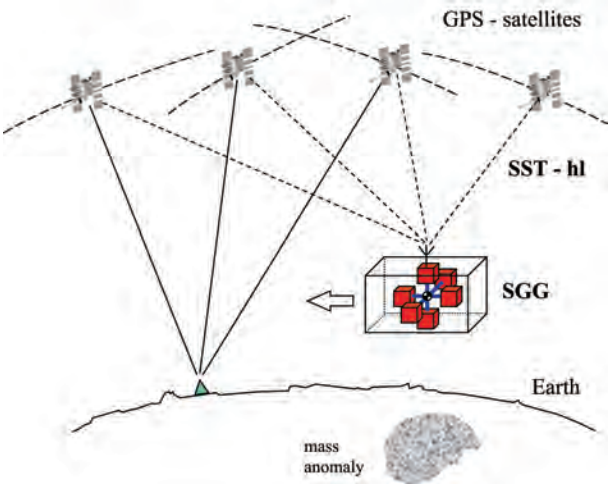

Figure 1.2.: Principle of satellite gravity gradiometry (SGG) and high-low satellite-to-satellite tracking (SST-hl).

processing is carried out by ESA's Payload Data Segment (PDS; Frommknecht et al., 2010). The ordered Level 0 time series are converted into engineering units. Furthermore, calibration, correction and geolocation of the data along the orbit takes place. The main output of the L1b processing are the gravity gradients (with a sampling rate of 1 Hz) in their instrument reference frame and the corresponding attitude and orbit data. The scientific data processing (Level 1b to Level 2), i.e. the processing of precise orbits and GOCE gravity fields, is performed by the High-level Processing Facility (HPF; Rummel et al., 2004).

1.2. Goals and topic of the work

This work is dedicated to the analysis and processing of the GOCE gradiometer data. With GOCE for the first time in history a gravity gradiometer is used on board of a satellite in order to measure the Earth's gravity field. Hence, a careful analysis of the new data type is of special importance. Some related analyses, performed by the author of this work, have already been published in Rummel et al. (2011) and Bouman et al. (2010). Also completely new processing strategies had to be developed. Before the launch of GOCE, they were enforcedly based on simulated data only (Cesare et al., 2008). Later, after the first gradiometer measurement data sets had become available, they were rechecked and refined. In this context, the author of this work has produced important contributions to the operational GOCE processing, as published in Stummer et al. (2011) and Stummer et al. (2012).

This work starts with a description of the theoretical foundations of satellite gravity gradiometry in general and specifically with GOCE (Chapter 2). The purpose is to introduce the reader to the subject of satellite gradiometry which goes back for several decades (Marussi, 1985; Rummel, 1986), and to familiarize with the most important characteristics of the GOCE mission and its sensor system, especially with the gradiometer. Related analyses can be found in Rummel et al. (2011) and Stummer (2006).

In Chapter 3 the nominal L1b gradiometer processing, as originally defined by industry (Cesare et al., 2008), is discussed. The derivation of the gravity gradients is in the focus. All important processing steps are described, starting with the de-packeting of the Level 0 gradiometer data up to the L1b gravity gradients. Special emphasis is put on the angular rate reconstruction. It is the determination of the angular rates from a combination of star sensor and gradiometer data and a key part of the L1b processing. Simultaneously, some first quality assessment of all related intermediate measurement data sets are made.

Chapter 4 describes the gradiometer calibration. The gradiometer calibration parameters can be classified into two main types, the so-called quadratic factors and the ICMs (Inverse Calibration Matrices). The physical origin of the gradiometer imperfections and different strategies for their determination and compensation, i.e. for calibration, are discussed. In this work, the emphasis is put on the determination of the ICMs. Here two main strategies exist, the original method as defined by industry (Cesare et al., 2008) and as implemented in the PDS L1b processor (Frommknecht, 2009), and the current method in use as defined by ESA (Lamarre, 2008). The two strategies are compared to each other. The original L1b method has also been implemented at IAPG, which allows some further analyses as presented in Sect. 5.2.3 of this work.

The purpose of Chapter 5 is to convey some deeper understanding of the GOCE gradiometer data, by presenting an overview of the various analyses performed by the author. The gravity gradients and their components (angular rates and differences of accelerations) as well as the data from the three star sensors on board of GOCE are analyzed in time and frequency domain. Also the temporal variations of the calibration parameters are investigated, and some discrepancies with respect to pre-launch expectations are identified. The role of the star sensors for the determination of the gradiometer calibration parameters is demonstrated, using the IAPG implementation of the nominal L1b ICM calibration method.

In Chapter 6 alternative gradiometer processing strategies are developed and adapted for the use in PDS' L1b processing. They are based on the original L1b gradiometer processing (Chapters 3 and 4) and on the findings of Chapter 5. In total, four upgraded methods are introduced. These are the methods for the determination of the angular rates and the attitude quaternions, the calibration of the accelerations, and an additional strategy for the combination of all available star sensor measurements. The development of the new method for angular rate reconstruction is explained in detail in Stummer et al. (2011). In Stummer et al. (2012) an overview of all four upgraded methods for the use in PDS' L1b processing is given.

The benefit of the four upgrades is analyzed at the level of gravity gradients as well as at the level of gravity field solutions based on satellite gravity gradiometry data (Chapter 7). The largest overall improvements are due to the new method for angular rate reconstruction, mainly at the low to medium frequencies and at the harmonics of the orbital revolution frequency. In addition, spurious artifacts in the gravity gradient V_{yy}, which are caused by non-perfect common mode rejection, can be reduced significantly by the improved calibration approach. The standard deviation of the gravity gradient tensor trace can be reduced by about 90 % for the frequencies below the gradiometer measurement band (i.e. below 5 mHz) and by about 4 % within the measurement band (from 5 to 100 mHz). The geoid error of satellite gravity gradiometry solutions based on 61 days of data is reduced from 3.0 to 2.2 cm between spherical harmonic degree 20 and 150. The corresponding gravity anomaly error is reduced from 0.7 to 0.5 mGal, which is a reduction of about 27 %. The gravity field solutions based on satellite gravity gradiometry data are combined with GOCE GPS satellite-to-satellite tracking data. In this case, the improvement due to the alternative L1b processing becomes much smaller, but is still observable. The cumulative geoid error and the cumulative gravity anomaly error, between degrees 20 and 150, are reduced by 10 %. Meanwhile, the four upgrades, discussed in this work, have been implemented in the PDS L1b processor, and the data of the whole GOCE mission are reprocessed.

Chapter 8 summarizes the most important results, and gives the conclusions of this work as well as an outlook.

2. Theoretical foundations

In this chapter the theoretical foundations of gravitational gradiometry in general and specifically with GOCE are given. We follow the explanations given in Rummel et al. (2011), Stummer (2006) and Gruber (2004). The chapter closes with a discussion of the expected gravity gradient and attitude quaternion signal.

2.1. Concepts of satellite gradiometry

We start with the theoretical foundations of gravitational gradiometry (Rummel et al., 2011). Gravitational gradiometry is the measurement of the second derivatives of the gravitational potential V, being equal to the measurement of the gradients of the components of the gravitational acceleration vector $\overline{a}$. The gravitational gradients are a second-order tensor field which is referred to as gravitational gradient tensor (GGT).

In geodesy, the GGT is often denoted as M with reference to Antonio Marussi (1908-1984), who published fundamental work on this subject (Marussi, 1985). Nevertheless, within this work the GGT is denoted as $\underline{G}$, in order to avoid any confusion with the notation in Chapter 4, where the calibration matrix is denoted as $\underline{M}$.

The GGT can be written in an arbitrarily chosen local Cartesian coordinate system at location P and in component form as

$$\underline{G}(P) = \nabla_P \otimes \overline{a}_P = \begin{bmatrix} V_{xx} & V_{xy} & V_{xz} \\ V_{yx} & V_{yy} & V_{yz} \\ V_{zx} & V_{zy} & V_{zz} \end{bmatrix} . \tag{2.1}$$

Using Newton's law of gravitation $\overline{a}$ can be written as

$$\overline{a}(P) = \nabla_P V = \nabla_P \left\{ G \iiint_{\Sigma} \frac{\rho(Q)}{|\overline{x}_P - \overline{x}_Q|} d\Sigma_Q \right\} = -G \iiint_{\Sigma} \frac{\rho(Q)}{|\overline{x_P} - \overline{x_Q}|^2} \begin{pmatrix} \frac{\Delta x}{|\overline{x}_P - \overline{x}_Q|} \\ \frac{\Delta y}{|\overline{x}_P - \overline{x}_Q|} \\ \frac{\Delta z}{|\overline{x}_P - \overline{x}_Q|} \end{pmatrix} d\Sigma_Q \, . \tag{2.2}$$

with G being the gravitational constant, ρ the density, $|\overline{x}_P - \overline{x}_Q|$ the distance between a mass particle $\rho d\Sigma$ at Q and point P, and Δx, Δy, Δz the coordinate differences between P and Q. The integral is taken over all masses contained in the volume Σ, in principle of the whole universe.

From Eqs. 2.1 and 2.2 it follows for the gravitational gradients

$$\underline{G}(P) = G \iiint_{\Sigma} \frac{\rho(Q)}{|\overline{x}_P - \overline{x}_Q|^3} \begin{pmatrix} \frac{3\Delta x^2}{|\overline{x}_P - \overline{x}_Q|^2} - 1 & \frac{3\Delta x \Delta y}{|\overline{x}_P - \overline{x}_Q|^2} & \frac{3\Delta x \Delta z}{|\overline{x}_P - \overline{x}_Q|^2} \\ \frac{3\Delta y \Delta x}{|\overline{x}_P - \overline{x}_Q|^2} & \frac{3\Delta y^2}{|\overline{x}_P - \overline{x}_Q|^2} - 1 & \frac{3\Delta y \Delta z}{|\overline{x}_P - \overline{x}_Q|^2} \\ \frac{3\Delta z \Delta x}{|\overline{x}_P - \overline{x}_Q|^2} & \frac{3\Delta z \Delta y}{|\overline{x}_P - \overline{x}_Q|^2} & \frac{3\Delta z^2}{|\overline{x}_P - \overline{x}_Q|^2} - 1 \end{pmatrix} d\Sigma_Q \quad , \tag{2.3}$$

Within the Newton's integrals for V, $\overline{a}$, and $\underline{G}$ the integral kernels change from inverse distance to inverse-squared distance to inverse-cubed distance. Hence, gravitational gradients are more sensitive to the close-by mass distributions than gravitational acceleration or potential.

There are two important basic properties from vector analysis which are related to the vector field $\overline{a}$. The first one is that for any mass distribution, $\overline{a}$ is curl-free, i.e. it holds everywhere

$$\nabla \times \overline{a} = 0 \ . \tag{2.4}$$

Therefore $\overline{a}$ is conservative and can be written as gradient of a potential V:

$$\overline{a} = \nabla V \ . \tag{2.5}$$

From this property (cf. Eqs. 2.4 and 2.5) follows symmetry of $\underline{G}$.

It has to be noted that the Earth's mass distribution is not entirely stationary due to the mass movements in atmosphere, oceans, ice shields and continental hydrology. Also the relative movement of the Sun, Moon and planets has to be considered. Since GOCE gravitational gradients have a relatively high noise level at low frequencies, they are not sensitive to temporal variations. Nevertheless, corrections from models of direct, solid Earth, ocean tides and atmosphere/ocean are available to the users, cf. Gruber et al. (2010b).

The second basic property is harmonicity. In the space outside the Earth, $\overline{a}$ is regarded as being source-free, i.e.

$$\nabla \cdot \overline{a} = 0 \ . \tag{2.6}$$

In reality, this is only an approximation. More correctly it is

$$\nabla \cdot \overline{a} = -4\pi G\rho \ . \tag{2.7}$$

However, atmospheric density is small. At GOCE's altitude it is less than $2.5 \cdot 10^{-10}$ kg/m^3, see Emiliani (1992), and for comparison, is about 1.23 kg/m^3 at the Earth's surface.

In geodesy, it is therefore common practise to correct for the contribution of the atmospheric density using a standard model (Moritz, 1980; Rummel and Rapp, 1976) and to proceed with the approximation given in Eq. 2.6.

From these two above basic properties (Eqs. 2.6 and 2.5) it follows the Laplace equation:

$$V_{xx} + V_{yy} + V_{zz} = 0 \ . \tag{2.8}$$

It is the basis of the representation of the potential V in terms of spherical harmonic series. Equation 2.8 states that $\underline{G}$ is trace-free. This property can be used as a very important internal check for the quality of the GOCE gravity gradients. From the two basic properties (symmetry and harmonicity) it follows that only five of the nine components of the GGT are independent from each other at any location.

In literature, see e.g. Marussi (1985); Ohanian and Ruffini (1994), there are two additional interpretations of $\underline{G}$. The first one is the interpretation as the tidal field induced by the Earth at the location of the gradiometer. For satellite gradiometry, as it is the case for GOCE, the gradiometer is located almost perfectly at the satellite's center of mass. Here, the tidal field is exactly zero ("zero-g"), because at this location the gravitational attraction of the Earth on the whole spacecraft is equal to that on a test mass there. With increasing distance from the satellite's center of mass, the tidal effect grows. For a distance of about 1 m the effect is roughly one part-per-million (1 ppm) of g ("micro-g"). For comparison, the distance between GOCE's center of mass and the test masses of the gravity gradiometer is about 0.25 m.

The second interpretation of $\underline{G}$ is geometrical. The elements of the GGT express, at any point, the curvature of the Earth's gravitational field, e.g. in a local {North, East, radial up}-triad:

$$\underline{G} = -g \begin{pmatrix} k_N & t & f_N \\ t & k_E & f_E \\ f_N & f_E & -H \end{pmatrix} \ . \tag{2.9}$$

In the above equation g is the gravitational acceleration, k_N and k_E are the North-South and East-West curvatures of the level surfaces of V, respectively, t is torsion, f_N and f_E are the North-South and East-West curvatures of the plumb line, respectively, and H is the mean curvature.

In the following the invariants of the GGT are discussed. Invariance implies independence from the orientation of the local triad in which the GGT components are measured. Since the GGT is symmetric and trace-free, it can be diagonalized with real-valued eigenvalues λ_1, λ_2, λ_3, according to

$$\underline{G} = \begin{bmatrix} \overline{u}_1 & \overline{u}_2 & \overline{u}_3 \end{bmatrix} \begin{bmatrix} \lambda_1 & 0 & 0 \\ 0 & \lambda_2 & 0 \\ 0 & 0 & \lambda_3 \end{bmatrix} \begin{bmatrix} \overline{u}_1^T \\ \overline{u}_2^T \\ \overline{u}_3^T \end{bmatrix} = \underline{U}\ \underline{\Lambda}\ \underline{U}^T \ , \tag{2.10}$$

with $\overline{u}_1$, $\overline{u}_2$, $\overline{u}_3$ being the corresponding eigenvectors and $\underline{\Lambda}$ the diagonal form of $\underline{G}$.

From this representation the invariants of $\underline{G}$ can be derived, cf. Baur et al. (2007)

$$\begin{aligned} I_1 &= \sum_{i=1}^{3} V_{ii} \\ &= \lambda_1 + \lambda_2 + \lambda_3 \qquad (\text{trace of } \underline{G} \text{ or } \underline{\Lambda}) \,, \end{aligned} \tag{2.11a}$$

$$\begin{aligned} I_2 &= \frac{1}{2} \sum_{i=1}^{3} \sum_{j=1}^{3} (V_{ij} V_{ji} - V_{ii} V_{jj}) \\ &= -(\lambda_1 \lambda_2 + \lambda_2 \lambda_3 + \lambda_3 \lambda_1) \,, \end{aligned} \tag{2.11b}$$

$$\begin{aligned} I_3 &= \frac{1}{6} \sum_{i=1}^{3} \sum_{j=1}^{3} \sum_{k=1}^{3} (2 V_{ij} V_{jk} V_{ki} - 3 V_{ij} V_{ji} V_{kk} + V_{ii} V_{jj} V_{kk}) \\ &= \lambda_1 \lambda_2 \lambda_3 \qquad (\text{determinant of } \underline{G} \text{ or } \underline{\Lambda}) \,. \end{aligned} \tag{2.11c}$$

The first invariant $I_1 = 0$ was already derived in Eq. 2.8. It can be used as an internal quality check of the gravity gradients. The other two invariants I_2 and I_3 can be used for global gravity field analysis as demonstrated in Baur (2007); Baur et al. (2007); Yu and Zhao (2010), see also Rummel (1986); Pedersen and Rasmussen (1990).

Laplace equation 2.8 is a second-order, homogeneous partial differential equation. Its solution in Cartesian coordinates leads to a series expansion of V and its first and second derivatives in terms of a two-dimensional Fourier-series, e.g. (Jung, 1961; Tsuboi, 1983). This representation is often applied regionally in geophysics. In geodesy, the Laplace equation is usually solved in spherical coordinates, which leads to the classical series expansion of the Earth's gravitational field in terms of spherical harmonics Y_{nm}.

In a rather compact complex notation, the gravitational potential V is written as

$$V(P) = V_0 \sum_{n=0}^{\infty} \left(\frac{a}{r}\right)^{n+1} \sum_{m=-n}^{n} t_{nm} Y_{nm}(\theta, \lambda) \ . \tag{2.12}$$

$V_0 = GM/a$ denotes a constant with GM gravitational constant times mass of the Earth and a the semi-major axis of the adopted reference ellipsoid; t_{nm} are the dimensionless coefficients of degree n and order m, and Y_{nm} the fully normalized surface spherical harmonics; the spherical coordinates of P are θ, λ, r. It is

$$t_{nm} = \begin{cases} \frac{1}{2}\left(\overline{C}_{nm} - i\overline{S}_{nm}\right) & (m \geq 0) \\ \frac{1}{2}\left(\overline{C}_{n|m|} + i\overline{S}_{n|m|}\right) & (m < 0) \,, \end{cases} \tag{2.13}$$

and

$$Y_{nm}(\theta, \lambda) = \overline{P}_{n|m|}(\theta) \exp(im\lambda) \,, \tag{2.14}$$

with $\overline{C}_{nm}$ and $\overline{S}_{nm}$ the usual fully-normalized spherical harmonic coefficients and $\overline{P}_{nm}$ the fully normalized associated Legendre functions.

In view of the high precision of the GOCE gravitational gradiometer, representation in ellipsoidal harmonics of the field may be more appropriate in order to achieve a closer fit of the base functions to the global shape of the Earth. For the connection of ellipsoidal and spherical harmonics, it is referred to Moritz (1980) and Jekeli (1988).

All nine components of $\underline{G}$ can be expanded in spherical harmonics, as discussed in Rummel and van Gelderen (1992). The so-called irreducible form of $\underline{G}$ leads to isotropic eigenvalues and integral operators, the latter are derived in Martinec (2003). See also Rummel (1997) and Schreiner (1994). Corresponding isotropic operators exist for the 2D-Fourier expansion as well. Compare again Rummel and van Gelderen (1992) or While et al. (2006).

2.2. Concepts of satellite gradiometry with GOCE

Gravitational gradients are derived from the difference of gravitational acceleration at adjacent points. The classical gradiometer instrument is the torsion balance (Eötvös, 1906; Jung, 1961). Its principle is the translation of the acceleration difference between two test masses hanging on a beam into a torsion of the fibre carrying the beam. The first proposal for a satellite gravitational gradiometer was made by Carroll and Savet (1959). Comprehensive reviews of gradiometer instrument developments and ideas of spaceborne gradiometry are performed by Forward (1974) and Wells (1984). One gradiometer system developed by Bell Aerospace, see again Wells (1984), has been used for submarines in support of inertial navigation. This instrument type was modified to the so-called gravity gradiometer system for use in gravity and exploration work, see Jekeli (1988). However, only in the eighties did sensor technology become mature enough to really build such an instrument for satellite applications. In Europe, following the GRADIO-proposal by Balmino et al. (1981, 1984) a gradiometric satellite mission, denoted ARISTOTELES, was proposed but not approved. At about the same time, professor Paik from the University of Maryland worked on the development of a super-conducting gravitational gradiometer, e.g. Chan et al. (1987). Quantum gravity gradiometry may become the measurement method of the future (McGuirk et al., 2002; Yu et al., 2006).

In the case of GOCE, the gradiometer is made of three orthogonally arranged one-axis gradiometers (OAG). They consist of two ultra-sensitive three-dimensional accelerometers mounted at the end points of a half meter baseline. Each accelerometer contains a test mass of Rhodium-Platinum, weight 320 g and $4\,\mathrm{cm} \times 4\,\mathrm{cm} \times 1\,\mathrm{cm}$ in size. It is kept levitated by an electrostatic feedback system inside a chamber with eight pairs of electrodes. The center of the three gradiometer axes coincides approximately with the satellite's center of mass. The gradiometer is shown in Fig. 2.1.

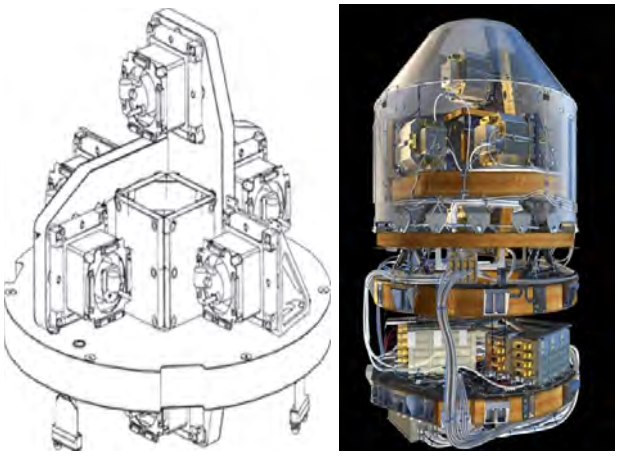

Figure 2.1.: GOCE gravitational gradiometer consisting of three orthogonal one-axis gradiometers, each 50 cm long and with two accelerometers; technical drawing (left) and actual instrument (right) (source: ESA).

Thus, the components V_{ij} of $\underline{G}$ are approximated by the finite acceleration difference over the corresponding baseline. Let us denote O as the "virtual" center of the gradiometer and A and B the locations of two accelerometers. A Taylor-series of the acceleration vector taken at point O, close to A, yields:

$$\overline{a}(O) = \overline{a}(A) - \underline{G}(O)\Delta\overline{x}_{A} + \left(o^2\right) \quad , \tag{2.15}$$

with $\Delta\overline{x}_{A} = \overline{x}_{A} - \overline{x}_{O}$. The omitted quadratic and higher order terms contain the third, forth and higher order derivative tensors of V. We assume the components of $\overline{a}$ to be measured by an accelerometer at A and a second device at a point B exactly symmetric to A relative to O. Then the acceleration difference between A and B gives

$$\overline{a}(B) - \overline{a}(A) = \underline{G}(O)\Delta\overline{x}_{AB} + \left(o^3\right) . \tag{2.16}$$

All the even terms of the neglected part drop out because of symmetry. The cubic and all higher degree terms are negligibly small, at least for gradiometers of laboratory size. Thus, the nine components of $\underline{G}$ are derived from

measured acceleration differences over baseline lengths, e.g. the component V_{xy} is derived from the difference of the x-components of the two accelerometers of the y-axis, divided by the baseline length Δy:

$$\underline{G} = \begin{pmatrix} V_{xx} & V_{xy} & V_{xz} \\ V_{yx} & V_{yy} & V_{yz} \\ V_{zx} & V_{zy} & V_{zz} \end{pmatrix} = \begin{pmatrix} \frac{\Delta a_x}{\Delta x} & \frac{\Delta a_x}{\Delta y} & \frac{\Delta a_x}{\Delta z} \\ \frac{\Delta a_y}{\Delta x} & \frac{\Delta a_y}{\Delta y} & \frac{\Delta a_y}{\Delta z} \\ \frac{\Delta a_z}{\Delta x} & \frac{\Delta a_z}{\Delta y} & \frac{\Delta a_z}{\Delta z} \end{pmatrix} + \left(o^3\right). \tag{2.17}$$

The gradiometer reference frame (GRF, Gruber et al., 2010a) is materialized by the three orthogonal one-axis gradiometers. Their axes are oriented approximately with the x-axis in flight direction, y-axis orthogonal to the orbit plane and z-axis almost radially downwards. The actual orientation is measured with arcsecond precision by a set of three star trackers and provided to the users expressed as orientation quaternions. The gradiometer rigidly mounted into the spacecraft rotates in space with the main angular velocity about the y-axis. Thus, in the GRF the accelerometers pick up any rotational motion, in addition to the gravitational signal:

$$\overline{a}'(A) = \overline{a}(A) - \underline{\Omega}\,\underline{\Omega}\Delta\overline{x}_{A} - \dot{\underline{\Omega}}\Delta\overline{x}_{A}\,, \tag{2.18}$$

with $\overline{a}'$ the accelerations measured in the rotating GRF, and with the well-known expressions for centrifugal and Euler accelerations, where

$$\underline{\Omega} = \begin{pmatrix} 0 & -\omega_z & \omega_y \\ \omega_z & 0 & -\omega_x \\ -\omega_y & \omega_x & 0 \end{pmatrix} \quad \text{and} \tag{2.19a}$$

$$\dot{\underline{\Omega}} = \begin{pmatrix} 0 & -\dot{\omega}_z & \dot{\omega}_y \\ \dot{\omega}_z & 0 & -\dot{\omega}_x \\ -\dot{\omega}_y & \dot{\omega}_x & 0 \end{pmatrix}. \tag{2.19b}$$

Thereby it is assumed that the test masses of all six accelerometers are kept "still" and levitated. The differential accelerations in the rotating frame become

$$\begin{aligned} \underline{D} = \begin{pmatrix} D_{xx} & D_{xy} & D_{xz} \\ D_{yx} & D_{yy} & D_{yz} \\ D_{zx} & D_{zy} & D_{zz} \end{pmatrix} &= \begin{pmatrix} V_{xx} & V_{xy} & V_{xz} \\ V_{yx} & V_{yy} & V_{yz} \\ V_{zx} & V_{zy} & V_{zz} \end{pmatrix} \\ &+ \begin{pmatrix} -(\omega_y^2+\omega_z^2) & \omega_x\omega_y & \omega_x\omega_z \\ \omega_y\omega_x & -(\omega_z^2+\omega_x^2) & \omega_y\omega_z \\ \omega_z\omega_x & \omega_z\omega_y & -(\omega_x^2+\omega_y^2) \end{pmatrix} \\ &+ \begin{pmatrix} 0 & -\dot{\omega}_z & \dot{\omega}_y \\ \dot{\omega}_z & 0 & -\dot{\omega}_x \\ -\dot{\omega}_y & \dot{\omega}_x & 0 \end{pmatrix} \\ &= \underline{G} + \underline{\Omega}\,\underline{\Omega} + \dot{\underline{\Omega}}\,. \end{aligned} \tag{2.20}$$

In Eq. 2.20, the left-hand side contains the measured acceleration differences per baseline length with e.g. $D_{xy} = \frac{\Delta a_x}{\Delta y}$, compare Eq. 2.17. The right-hand side is the sum of gravitational gradients and centrifugal terms with angular velocity products as well as a matrix containing angular accelerations. Symmetry of $\underline{G}$ and $\underline{\Omega}\,\underline{\Omega}$ versus skew-symmetry of $\dot{\underline{\Omega}}$ allows separation and therefore "isolation" of the angular accelerations:

$$\dot{\underline{\Omega}} = \frac{1}{2}\left(\underline{D} - \underline{D}^T\right), \tag{2.21a}$$

$$\underline{G} + \underline{\Omega}\,\underline{\Omega} = \frac{1}{2}\left(\underline{D} + \underline{D}^T\right). \tag{2.21b}$$

Integration of the angular accelerations $\dot{\underline{\Omega}}$ gives angular velocities $\underline{\Omega}$; with the elements of $\underline{\Omega}\ \underline{\Omega}$ known, the gravitational gradients in $\underline{G}$ can be determined. In fact, the angular velocities are derived from an optimized combination of these angular accelerations and angular rates derived from the star tracking.

In the case of GOCE, two additional facts need consideration. Each accelerometer is ultra-sensitive (US) along two orthogonal directions but much less sensitive (LS) along its third axis, see also Floberghagen et al. (2011). Functional testing of the accelerometers is done in the laboratory on ground. This requires levitation of the test mass under the influence of gravity. As a consequence ultimate sensitivity can only be attained along two axes, while the third one is made less sensitive. Thus it needs to be decided which direction of each accelerometer to choose for the less sensitive axis. The constellation shown in Fig. 2.2, taken from Gruber et al. (2010b), was suggested by Aguirre-Martinez and Cesare (1999) and is regarded of being advantageous.

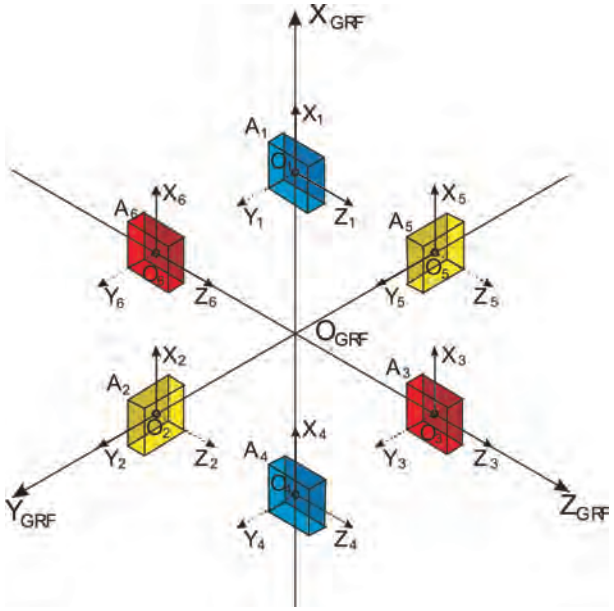

Figure 2.2.: Location of the 6 accelerometers, denoted A_i, $i = 1, 2, \cdots, 6$ in the gradiometer reference frame (GRF). The solid arrows at each of the accelerometer triads show the ultra-sensitive axes, the dashed arrows the less sensitive axes.

From this arrangement, the right hand side of Eq. 2.20 becomes:

$$\begin{pmatrix} V_{xx} & \tilde{V}_{xy} & V_{xz} \\ \tilde{V}_{yx} & V_{yy} & \tilde{V}_{yz} \\ V_{zx} & \tilde{V}_{zy} & V_{zz} \end{pmatrix} + \begin{pmatrix} -(\omega_y^2 + \tilde{\omega}_z^2) & \tilde{\omega}_x\omega_y & \tilde{\omega}_x\tilde{\omega}_z \\ \omega_y\tilde{\omega}_x & -(\tilde{\omega}_z^2 + \tilde{\omega}_x^2) & \omega_y\tilde{\omega}_z \\ \tilde{\omega}_z\tilde{\omega}_x & \tilde{\omega}_z\omega_y & -(\tilde{\omega}_x^2 + \omega_y^2) \end{pmatrix} + \begin{pmatrix} 0 & -\tilde{\dot{\omega}}_z & \dot{\omega}_y \\ \tilde{\dot{\omega}}_z & 0 & -\tilde{\dot{\omega}}_x \\ -\dot{\omega}_y & \tilde{\dot{\omega}}_x & 0 \end{pmatrix}. \tag{2.22}$$

The less sensitive elements are indicated with tilde above the variables. This choice makes sure that $\dot{\omega}_y$ can be determined with high precision, and after integration ω_y as well. This is important when determining the angular rates, because it holds $\omega_y \gg \omega_x$ or ω_z due to the rotation of the satellite about the y-axis once per orbital revolution. Essentially the four gradiometer components V_{xx}, V_{yy}, V_{zz}, and V_{xz} are resolvable with high precision.

A second property is related to the error behavior of the GOCE accelerometers. Their high precision of 10^{-12} m/s$^2/\sqrt{\text{Hz}}$ is only achieved in the measurement band (MB) between $5 \cdot 10^{-3}$ Hz and 0.1 Hz, while the noise increases with $1/f$ at lower frequencies. The $1/f$-behavior at low frequencies is typical to any accelerometer. The definition of the MB is part of the accelerometer design. Inside the MB, the accelerometers are expected to show white noise behavior. The MB represents the spectral window in which the gravity information observed by GOCE is concentrated. At its lower end and at frequencies below the MB, gravitational gradiometry has to be complemented by gravity information either from the orbits or from an available gravity field model.

Based on a detailed analysis of the error budget, performance requirements have been derived for the three axes of the accelerometers, the three one-axis gradiometers and for the sum of the three diagonal gradient components

(trace or Laplace condition). The trace requirement is included as solid black line in Fig. 5.4. For details, see Cesare (2008). The four precise gradiometer components should be measurable with a precision of 5 to 8 mE/$\sqrt{\text{Hz}}$ (1 Eötvös Unit = 1 E = 10^{-9} s^{-2}), compare again Cesare (2008).

2.3. From measured accelerations to gravity gradients

In this section the basic equations for the computation of the GOCE gravity gradients are given in detail, cf. Stummer (2006) and Gruber (2004). Note that these equations only hold if the accelerometers have their nominal position and no other gradiometric imperfections occur. In reality, there are small imperfections which are accounted for by calibration, cf. Chapter 4.

As already pointed out the accelerometers of the GOCE gradiometer are arranged in pairs along the three gradiometer arms. With the baselines L_x, L_y, L_z for the three one-axis gradiometers, the distance vectors $\bar{r}$ of the accelerometers A_1 to A_6 to the satellite's center of mass can be written as

$$\begin{aligned}
A_1 : \begin{pmatrix} r_x \\ r_y \\ r_z \end{pmatrix} &= \begin{pmatrix} \frac{L_x}{2} \\ 0 \\ 0 \end{pmatrix}; \quad A_4 : \begin{pmatrix} r_x \\ r_y \\ r_z \end{pmatrix} = \begin{pmatrix} -\frac{L_x}{2} \\ 0 \\ 0 \end{pmatrix} \\
A_2 : \begin{pmatrix} r_x \\ r_y \\ r_z \end{pmatrix} &= \begin{pmatrix} 0 \\ \frac{L_y}{2} \\ 0 \end{pmatrix}; \quad A_5 : \begin{pmatrix} r_x \\ r_y \\ r_z \end{pmatrix} = \begin{pmatrix} 0 \\ -\frac{L_y}{2} \\ 0 \end{pmatrix} \\
A_3 : \begin{pmatrix} r_x \\ r_y \\ r_z \end{pmatrix} &= \begin{pmatrix} 0 \\ 0 \\ \frac{L_z}{2} \end{pmatrix}; \quad A_6 : \begin{pmatrix} r_x \\ r_y \\ r_z \end{pmatrix} = \begin{pmatrix} 0 \\ 0 \\ -\frac{L_z}{2} \end{pmatrix}
\end{aligned} \tag{2.23}$$

By inserting these distances into Eq. 2.16, we obtain the 18 observation equations for the 6 GOCE accelerometers.

$$\begin{aligned}
a_{1,x} &= (-V_{xx} - \omega_y^2 - \omega_z^2)\frac{L_x}{2} \quad ; \quad a_{4,x} = -(-V_{xx} - \omega_y^2 - \omega_z^2)\frac{L_x}{2} \\
\tilde{a}_{1,y} &= (-V_{yx} + \dot{\omega}_z + \omega_x\omega_y)\frac{L_x}{2} \quad ; \quad \tilde{a}_{4,y} = -(-V_{yx} + \dot{\omega}_z + \omega_x\omega_y)\frac{L_x}{2} \\
a_{1,z} &= (-V_{zx} - \dot{\omega}_y + \omega_x\omega_z)\frac{L_x}{2} \quad ; \quad a_{4,z} = -(-V_{zx} - \dot{\omega}_y + \omega_x\omega_z)\frac{L_x}{2}
\end{aligned} \tag{2.24}$$

$$\begin{aligned}
a_{2,x} &= (-V_{xy} - \dot{\omega}_z + \omega_x\omega_y)\frac{L_y}{2} \quad ; \quad a_{5,x} = -(-V_{xy} - \dot{\omega}_z + \omega_x\omega_y)\frac{L_y}{2} \\
a_{2,y} &= (-V_{yy} - \omega_x^2 - \omega_z^2)\frac{L_y}{2} \quad ; \quad a_{5,y} = -(-V_{yy} - \omega_x^2 - \omega_z^2)\frac{L_y}{2} \\
\tilde{a}_{2,z} &= (-V_{zy} + \dot{\omega}_x + \omega_y\omega_z)\frac{L_y}{2} \quad ; \quad \tilde{a}_{5,z} = -(-V_{zy} + \dot{\omega}_x + \omega_y\omega_z)\frac{L_y}{2}
\end{aligned} \tag{2.25}$$

$$\begin{aligned}
a_{3,x} &= (-V_{xz} + \dot{\omega}_y + \omega_x\omega_z)\frac{L_z}{2} \quad ; \quad a_{6,x} = -(-V_{xz} + \dot{\omega}_y + \omega_x\omega_z)\frac{L_z}{2} \\
\tilde{a}_{3,y} &= (-V_{yz} - \dot{\omega}_x + \omega_y\omega_z)\frac{L_z}{2} \quad ; \quad \tilde{a}_{6,y} = -(-V_{yz} - \dot{\omega}_x + \omega_y\omega_z)\frac{L_z}{2} \\
a_{3,z} &= (-V_{zz} - \omega_x^2 - \omega_y^2)\frac{L_z}{2} \quad ; \quad a_{6,z} = -(-V_{zz} - \omega_x^2 - \omega_y^2)\frac{L_z}{2}
\end{aligned} \tag{2.26}$$

Note that again the less sensitive elements are indicated with tilde above the variable. Also in the following we will keep this notation.

For the determination of a main diagonal GGT element a measurement along the respective gradiometer arm, i.e. a so-called in-line measurement, is needed. V_{xx} e.g. appears in Eq. 2.24 in the accelerations $a_{1,x}$ and $a_{4,x}$ along the x-axis. The off-diagonal GGT elements can be determined with measurements transversal to the respective gradiometer arm, i.e. with a so-called transversal measurement.

V_{xy} occurs along the gradiometer arm 14 (x-axis) in y-direction ($a_{1,y}$ and $a_{4,y}$ in Eqs. 2.24), which is transversal to the baseline 14. V_{xy} appears also transversal to the baseline 25 (y-axis) in the accelerations $a_{2,x}$ and $a_{5,x}$, cf. Eqs. 2.25.

The so-called common mode accelerations are used for the drag control system of GOCE. They are the mean of two accelerations measured in the same direction and can be formed using Eqs. 2.24 to 2.26 according to

$$a_{c,lk,i} = \frac{1}{2}\left(a_{l,i} + a_{k,i}\right) \tag{2.27}$$

with l and k being the numbers of the two involved accelerometers and i being the direction x, y or z.

In total, 9 common mode accelerations can be built

$$\begin{aligned} a_{c,14,x} &= \frac{1}{2}\left(a_{1,x} + a_{4,x}\right) = \\ &= \frac{1}{2}\left(-V_{xx} - \omega_y^2 - \omega_z^2\right)\frac{L_x}{2} + \frac{1}{2}\left(-V_{xx} - \omega_y^2 - \omega_z^2\right)\left(-\frac{L_x}{2}\right) = \\ &= \frac{L_x}{4}\left(-V_{xx} - \omega_y^2 - \omega_z^2 + V_{xx} + \omega_y^2 + \omega_z^2\right) = 0 \end{aligned} \tag{2.28}$$

$$\begin{aligned} \tilde{a}_{c,14,y} &= \frac{1}{2}\left(\tilde{a}_{1,y} + \tilde{a}_{4,y}\right) = \\ &= \frac{1}{2}\left(-V_{yx} + \dot{\omega}_z + \omega_x\omega_y\right)\frac{L_x}{2} + \frac{1}{2}\left(-V_{yx} + \dot{\omega}_z + \omega_x\omega_y\right)\left(-\frac{L_x}{2}\right) = \\ &= \frac{L_x}{4}\left(-V_{yx} + \dot{\omega}_z + \omega_x\omega_y + V_{yx} - \dot{\omega}_z - \omega_x\omega_y\right) = 0 \end{aligned} \tag{2.29}$$

$$\begin{aligned} a_{c,14,z} &= \frac{1}{2}\left(a_{1,z} + a_{4,z}\right) = \\ &= \frac{1}{2}\left(-V_{zx} - \dot{\omega}_y + \omega_x\omega_z\right)\frac{L_x}{2} + \frac{1}{2}\left(-V_{zx} - \dot{\omega}_y + \omega_x\omega_z\right)\left(-\frac{L_x}{2}\right) = \\ &= \frac{L_x}{4}\left(-V_{zx} + \dot{\omega}_y + \omega_x\omega_z + V_{zx} - \dot{\omega}_y - \omega_x\omega_z\right) = 0 \end{aligned} \tag{2.30}$$

$$a_{c,25,x} = \frac{1}{2}\left(a_{2,x} + a_{5,x}\right) = 0 \tag{2.31}$$

$$a_{c,25,y} = \frac{1}{2}\left(a_{2,y} + a_{5,y}\right) = 0 \tag{2.32}$$

$$\tilde{a}_{c,25,z} = \frac{1}{2}\left(\tilde{a}_{2,z} + \tilde{a}_{5,z}\right) = 0 \tag{2.33}$$

$$a_{c,36,x} = \frac{1}{2}\left(a_{3,x} + a_{6,x}\right) = 0 \tag{2.34}$$

$$\tilde{a}_{c,36,y} = \frac{1}{2}\left(\tilde{a}_{3,y} + \tilde{a}_{6,y}\right) = 0 \tag{2.35}$$

$$a_{c,36,z} = \frac{1}{2}\left(a_{3,z} + a_{6,z}\right) = 0 \tag{2.36}$$

Theoretically, all 9 common mode accelerations should be zero. This also means that they should not affect the gravity gradient measurement. This is the principle of common mode rejection. In reality, disturbances, e.g. because of non-compensated air drag and solar radiation pressure acting on the satellite as a whole, are present and occur thus in the measured common mode accelerations. The principle of the drag-free control system of GOCE is to compensate for disturbances in flight (i.e. x-) direction, which are measured with the common mode accelerations in the same direction, and to compensate for these forces by firing a dedicated ion thruster assembly. This compensation is only performed in flight direction, where the satellite is exposed to the largest disturbances. All common mode accelerations in this (x-) direction are derived from US measurements

only. Hence, one can conclude the the arrangement of the accelerometers within the gradiometer is optimal for the aspect of drag compensation.

The main measurements for the determination of the gravity gradients are differential accelerations. The so-called differential mode accelerations, as used for the official GOCE processing (cf. Chapter 3) are defined in analogy to the common mode accelerations as

$$a_{d,lk,i} = \frac{1}{2}\left(a_{l,i} - a_{k,i}\right) \tag{2.37}$$

Again, l and k denote the numbers of the two involved accelerometers and i the direction x, y or z.

The 9 equations for the differential mode accelerations read

$$\begin{aligned} a_{d,14,x} &= \frac{1}{2}\left(a_{1,x} - a_{4,x}\right) = \\ &= \frac{1}{2}\left(-V_{xx} - \omega_y^2 - \omega_z^2\right)\frac{L_x}{2} - \frac{1}{2}\left(-V_{xx} - \omega_y^2 - \omega_z^2\right)\left(-\frac{L_x}{2}\right) = \\ &= \frac{L_x}{4}\left(-2V_{xx} - 2\omega_y^2 - 2\omega_z^2\right) = \frac{L_x}{2}\left(-V_{xx} - \omega_y^2 - \omega_z^2\right) \end{aligned} \tag{2.38}$$

$$\begin{aligned} \tilde{a}_{d,14,y} &= \frac{1}{2}\left(\tilde{a}_{1,y} - \tilde{a}_{4,y}\right) = \\ &= \frac{1}{2}\left(-V_{yx} + \dot{\omega}_z + \omega_x\omega_y\right)\frac{L_x}{2} - \frac{1}{2}\left(-V_{yx} + \dot{\omega}_z + \omega_x\omega_y\right)\left(-\frac{L_x}{2}\right) = \\ &= \frac{L_x}{4}\left(-2V_{yx} + 2\dot{\omega}_z + 2\omega_x\omega_y\right) = \frac{L_x}{2}\left(-V_{yx} + \dot{\omega}_z + \omega_x\omega_y\right) \end{aligned} \tag{2.39}$$

$$\begin{aligned} a_{d,14,z} &= \frac{1}{2}\left(a_{1,z} - a_{4,z}\right) = \\ &= \frac{1}{2}\left(-V_{zx} - \dot{\omega}_y + \omega_x\omega_z\right)\frac{L_x}{2} - \frac{1}{2}\left(-V_{zx} - \dot{\omega}_y + \omega_x\omega_z\right)\left(-\frac{L_x}{2}\right) = \\ &= \frac{L_x}{4}\left(-2V_{zx} - 2\dot{\omega}_y + 2\omega_x\omega_z\right) = \frac{L_x}{2}\left(-V_{zx} - \dot{\omega}_y + \omega_x\omega_z\right) \end{aligned} \tag{2.40}$$

$$a_{d,25,x} = \frac{1}{2}\left(a_{2,x} - a_{5,x}\right) = \frac{L_y}{2}\left(-V_{xy} - \dot{\omega}_z + \omega_x\omega_y\right) \tag{2.41}$$

$$a_{d,25,y} = \frac{1}{2}\left(a_{2,y} - a_{5,y}\right) = \frac{L_y}{2}\left(-V_{yy} - \omega_x^2 - \omega_z^2\right) \tag{2.42}$$

$$\tilde{a}_{d,25,z} = \frac{1}{2}\left(\tilde{a}_{2,z} - \tilde{a}_{5,z}\right) = \frac{L_y}{2}\left(-V_{zy} + \dot{\omega}_x + \omega_y\omega_z\right) \tag{2.43}$$

$$a_{d,36,x} = \frac{1}{2}\left(a_{3,x} - a_{6,x}\right) = \frac{L_z}{2}\left(-V_{xz} + \dot{\omega}_y + \omega_x\omega_z\right) \tag{2.44}$$

$$\tilde{a}_{d,36,y} = \frac{1}{2}\left(\tilde{a}_{3,y} - \tilde{a}_{6,y}\right) = \frac{L_z}{2}\left(-V_{yz} - \dot{\omega}_x + \omega_y\omega_z\right) \tag{2.45}$$

$$a_{d,36,z} = \frac{1}{2}\left(a_{3,z} - a_{6,z}\right) = \frac{L_z}{2}\left(-V_{zz} - \omega_x^2 - \omega_y^2\right) \tag{2.46}$$

In analogy to the equations for the common mode accelerations, 6 of the 9 equations contain only US measurements, and three of them are built from LS measurements (again indicated with tilde).

The in-line accelerations $a_{d,14,x}$, $a_{d,25,y}$ and $a_{d,36,z}$, which contain the main diagonal elements of the GGT and thus the largest signal contribution, are composed of US measurements only. Also in this respect, the arrangement of the accelerometers within the gradiometer is optimal.

Since the gradiometer measurements contain besides the gravity gradients also a centrifugal term and a term due to the angular acceleration of the satellite, the determination of the angular rates and angular accelerations is

necessary. The angular accelerations can be derived from the gradiometer measurements, according to Eq. 2.21a, by

$$\tilde{\dot{\omega}}_x = -\frac{\tilde{a}_{d,36,y}}{L_z} + \frac{\tilde{a}_{d,25,z}}{L_y} \tag{2.47}$$

$$\dot{\omega}_y = -\frac{a_{d,14,z}}{L_x} + \frac{a_{d,36,x}}{L_z} \tag{2.48}$$

$$\tilde{\dot{\omega}}_z = \frac{\tilde{a}_{d,14,y}}{L_x} - \frac{a_{d,25,x}}{L_y} \tag{2.49}$$

The calculation of $\dot{\omega}_x$ and $\dot{\omega}_z$ is influenced by at least one LS measurement, whereas $\dot{\omega}_y$ is determined from US measurements only. The high accuracy determination of $\dot{\omega}_y$ is most important, since the satellite rotates once per revolution about its y-axis and hence, $\dot{\omega}_y$ is the largest component. For a more detailed analysis of this aspect it is referred to Sect. 5.1. The possibility to determine $\dot{\omega}_y$ with the gradiometer (in the MB) as good as possible was one of the main drivers for the actual arrangement of the accelerometers within the gradiometer.

For the computation of the gravity gradients the angular rates have to be known. Hence, the determination of the angular rates is a key task of GOCE L1b processing, cf. Sect. 3.4. Within this processing step the attitude information of the gradiometer, which is very accurate in the gradiometer MB, is combined with star sensor data, which is most accurate at low frequencies. In Sect. 6.2 an improved method for the determination of the angular rates is described. Once the angular rates are known, the gravity gradients can be calculated. For the main diagonal GGT elements the the in-line differential mode accelerations, Eqs. 2.38, 2.42 and 2.46 are needed

$$V_{xx} = -\frac{2a_{d,14,x}}{L_x} - \omega_y^2 - \tilde{\omega}_z^2 \tag{2.50}$$

$$V_{yy} = -\frac{2a_{d,25,y}}{L_y} - \tilde{\omega}_x^2 - \tilde{\omega}_z^2 \tag{2.51}$$

$$V_{zz} = -\frac{2a_{d,36,z}}{L_z} - \tilde{\omega}_x^2 - \omega_y^2 \tag{2.52}$$

The off-diagonal elements of the GGT are derived from the transversal differential mode accelerations, using Eq. 2.21b

$$\tilde{V}_{xy} = -\frac{\tilde{a}_{d,14,y}}{L_x} - \frac{a_{d,25,x}}{L_y} + \tilde{\omega}_x\omega_y \tag{2.53}$$

$$V_{xz} = -\frac{a_{d,14,z}}{L_x} - \frac{a_{d,36,x}}{L_z} + \tilde{\omega}_x\tilde{\omega}_z \tag{2.54}$$

$$\tilde{V}_{yz} = -\frac{\tilde{a}_{d,25,z}}{L_y} - \frac{\tilde{a}_{d,36,y}}{L_z} + \omega_y\tilde{\omega}_z \tag{2.55}$$

The V_{xx}, V_{yy}, V_{zz} and V_{xz} are determined from US differential mode accelerations only, whereas V_{xy} and V_{yz} are influenced by at least one LS differential mode acceleration and are hence themselves less accurate (again indicated by tilde). In all six equations at least one less accurate angular rate component occurs. Hence, it is very important to determine all three angular rate components as good as possible using the additional attitude information from the star sensors. Further analysis on the influence of the angular rates on the accuracy of the gravity gradients is made in Sect. 5.1.

2.4. Expected signal of gravity gradients and attitude quaternions

Before we start the analysis of the data, as measured by GOCE, in the next chapter of this work, we introduce the requirement for the noise of the gravitational gradient tensor components, as well as their expected signal content. From the pre-launch analysis of industry, cf. Cesare (2008), the noise contained in the accurate gradiometer components should be white in the MB between $2 \cdot 10^{-2}$ and 0.1 Hz with a level of about 8 mE/$\sqrt{\text{Hz}}$ and a $1/f$ increase towards lower frequencies. The corresponding requirement for the noise level of the trace of the gravitational gradient tensor is 11 mE/$\sqrt{\text{Hz}}$ between $2 \cdot 10^{-2}$ Hz and 0.1 Hz and also with an increase of $1/f$ towards lower frequencies, cf. Fig. 2.4(a). At $5 \cdot 10^{-3}$ Hz, the lower end of the MB, its level should be 100 mE/$\sqrt{\text{Hz}}$. The original intention at the time of the pre-phase-A studies was to reach for the accurate gradiometer components a noise level of only 1 to 2 mE/$\sqrt{\text{Hz}}$, cf. Johannessen (1999). Several technological challenges made it impossible to reach this goal. The noise level of the less sensitive components was expected to be close to 1 E/$\sqrt{\text{Hz}}$ in the MB.

In Fig. 2.4 the root power spectral densities (PSDs) are shown for the gravity gradients in GRF, simulated from EGM2008 (Pavlis et al., 2012) up to degree/order 360, and taken along the orbits of the first measurement cycle (November and December 2009). Figure 2.4(a) contains the main diagonal elements of the GGT V_{xx}, V_{yy}, V_{zz} and the requirement for the trace. We see that the gravity signal in the MB starts from about 1 E/$\sqrt{\text{Hz}}$ at $5 \cdot 10^{-3}$ Hz and decreases to a level of 8 mE/$\sqrt{\text{Hz}}$ (the expected noise level) between $2 \cdot 10^{-2}$ and $4 \cdot 10^{-2}$ Hz with a rather steep descent at frequencies above. The signal power is highest for the V_{zz} component, and lowest for the V_{yy} component. Fig. 2.4(b) contains V_{xy}, V_{yz} and V_{yz}. The signal power is clearly lowest for the V_{xy} component. The same gravity gradients in GRF, simulated from EGM2008 up to degree/order 360, are given in Fig. 2.3 in the time domain for one day, 1 November 2009. V_{xx} and V_{yy} have a magnitude of about -1360 E, V_{zz} of about 2720 E. V_{xz} and V_{yz} are about two orders of magnitude smaller, whereas V_{xy} is about three orders of magnitude smaller. All six components of the GGT show an oscillation, which is repeating 16 times per day, as observable in Fig. 2.3 and which is hence recurring once per orbital revolution. These large oscillations are due to the Earth's flattening and additionally due to the eccentricity of the orbit.

For gravity field determination, as well as for the direct use of the gravity gradients, it is important to know their exact orientation. This aspect will be further discussed in Sect. 7.2. Within the GOCE L1b processing, cf. Sects. 3.4 and 6.3, the orientation of the satellite is generated in terms of (inertial) attitude quaternions from a combination of star sensor and gradiometer data. For comparison, Fig. 2.5 shows the attitude quaternions as derived from a pre-launch end-to-end simulation, kindly provided by industry. The individual quaternion components are oscillating between ± 1 once per two orbital revolutions, cf. Fig. 2.5(a). q_0 denotes the real part of the quaternion. The root PSD of the quaternion components, Fig. 2.5(b), has a magnitude of about 10^{-2} rad/$\sqrt{\text{Hz}}$ at 1 mHz and a rather steep decrease towards the higher frequencies, with e.g. about 10^{-6} rad/$\sqrt{\text{Hz}}$ at 10 mHz.

Note that all PSD calculations within this work are based on Welch's method (Welch, 1967). As the data sets are not strictly periodic, some windowing is applied. We chose a Kaiser window (Oppenheim and Schafer, 1989; Meyer, 1998) because it has the advantage of rapidly decreasing side maxima in the spectrum, which allows a good analysis of instrument noise (at high frequencies), cf. Appendix C. In addition, the linear trend is subtracted from the time series prior to the PSD calculation.

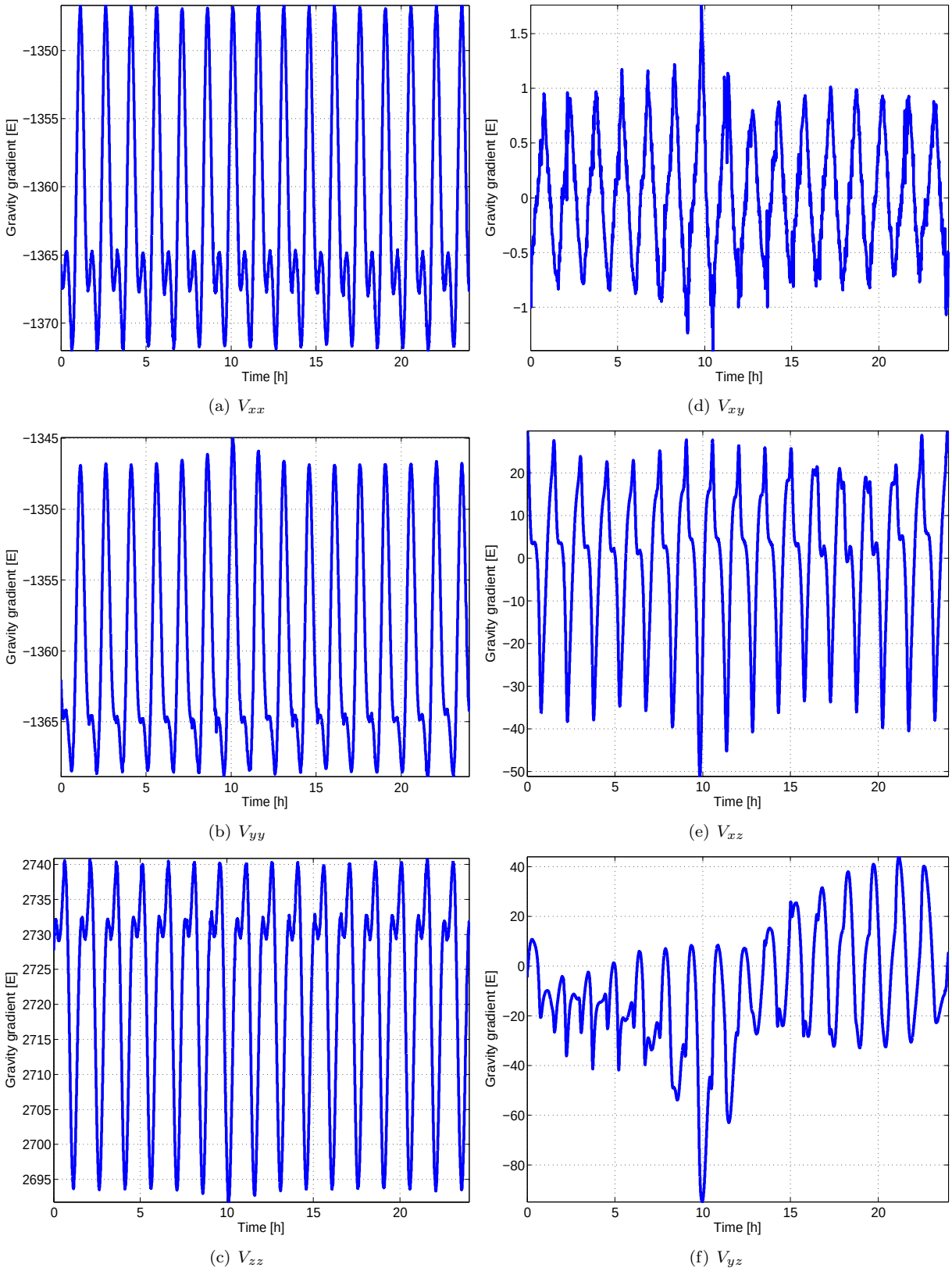

(a) V_{xx} (d) V_{xy}

(b) V_{yy} (e) V_{xz}

(c) V_{zz} (f) V_{yz}

Figure 2.3.: Main diagonal elements of gravity gradient tensor (left) and off-diagonal elements (right).

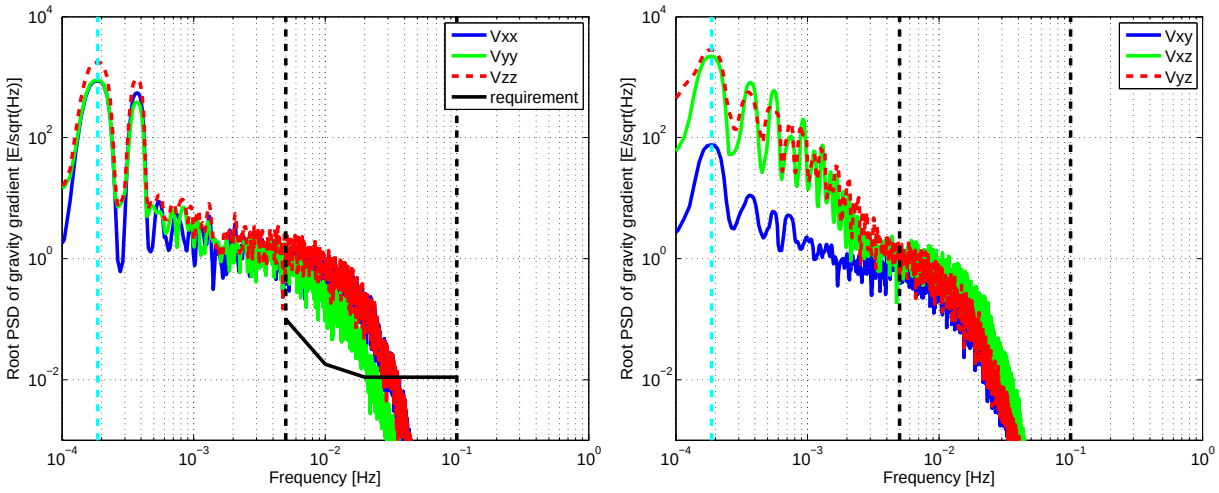

(a) (b)

Figure 2.4.: Root PSD of main diagonal elements of gravity gradient tensor (a) and off-diagonal elements (b), based on EGM2008 up to degree/order 360.

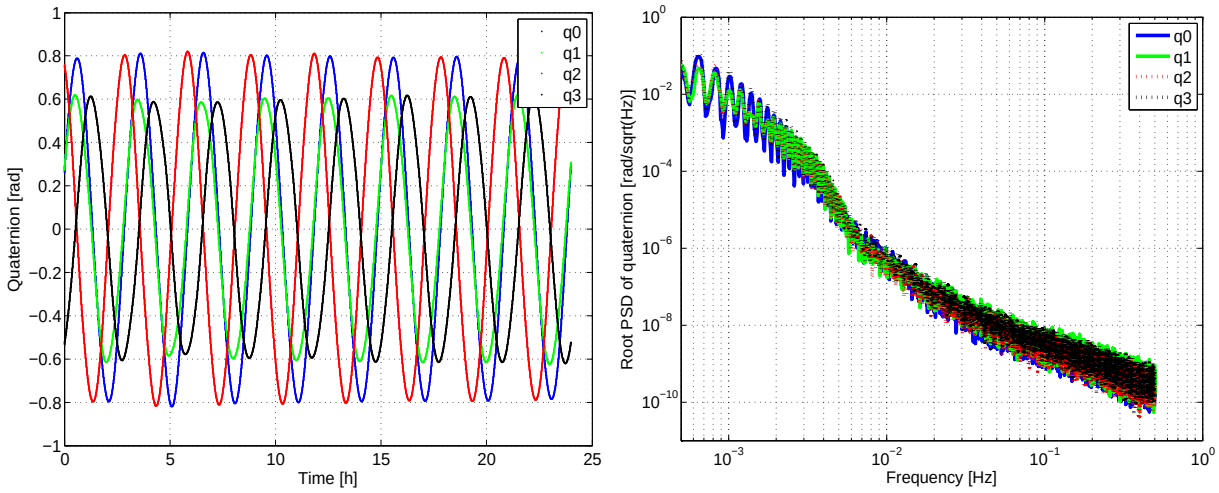

(a) (b)

Figure 2.5.: Inertial attitude quaternions (a) and corresponding root PSD (b), based on data from end-to-end simulation.

3. Nominal gradiometer data processing and analysis

In this chapter the nominal EGG processing chain is described. We follow in large parts the explanations given in Frommknecht (2009). First, an overview of the EGG processor is given, followed by a more precise analysis of the individual processing steps. Also first analysis of all important intermediate data sets for the computation of the gravity gradients are made.

Originally, the determination of the Inverse Calibration Matrices (ICMs), which are needed for the calibration of the measured accelerations, was part of the L1b gradiometer processing according to Cesare et al. (2008). Meanwhile, this important processing step was replaced by a new method (Lamarre, 2008), which is carried out by ESA. Because of its special role in the processing and its importance with respect to the quality of the gravity gradients, the determination of the ICMs is treated separately here in Chapter 4.

The EGG nominal processor transforms the EGG Level 0 products (`EGG_NOM_0`) into EGG L1b products (`EGG_NOM_1b` and `EGG_MON_1b`). For a definition of the reference frames related to the GOCE gradiometer it is referred to Appendix A. There are seven major steps within the EGG nominal processing. These steps are depicted by the flowchart in Fig. 3.1.

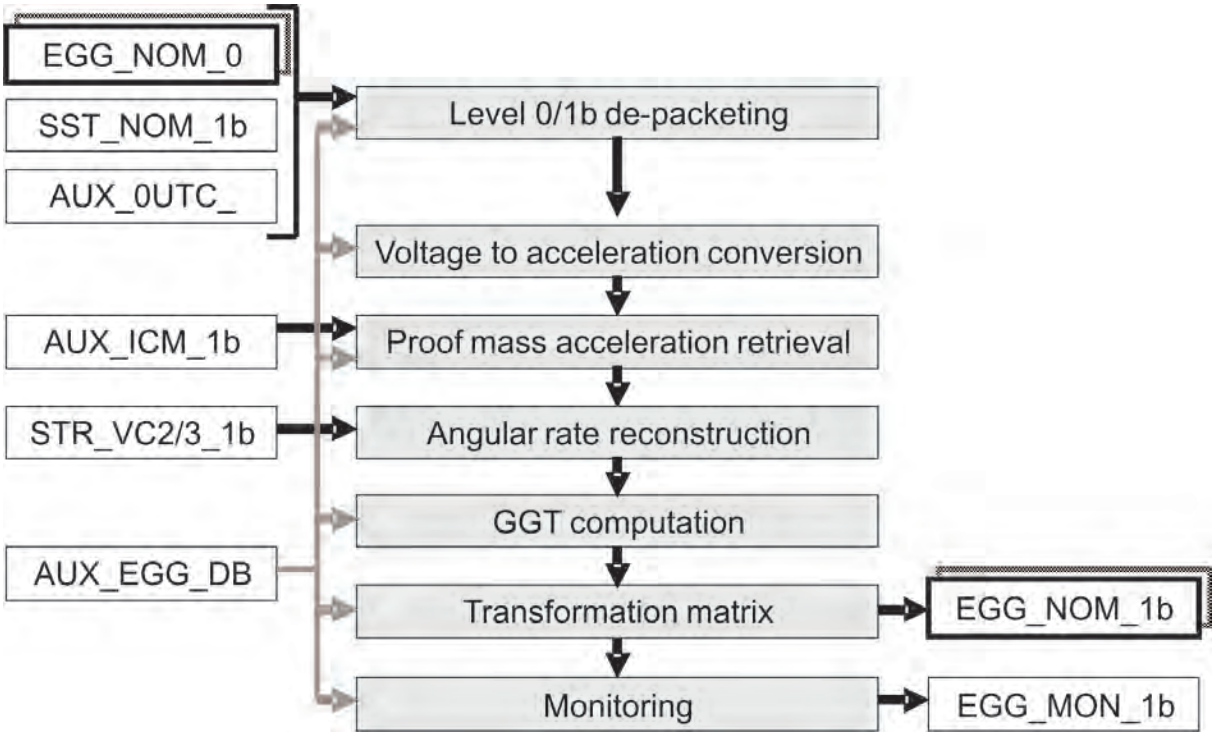

Figure 3.1.: Flowchart: Overview of the EGG nominal processor.

Accordingly, at the beginning of each section within this chapter the relevant processing steps are illustrated by a flowchart. These flowcharts indicate the input (left), the output (right), and the relevant processing steps (middle). The major input and output products are marked with a bold frame. In the following a brief summary of the seven major processing steps is given.

1. De-packeting and sorting of measurement records.
   In this step the Level 0 telemetry packets generated by the gradiometer and by the platform are extracted with their associated on-board time (OBT) stamping. The EGG control voltages are interpolated to integer

second sampling in alignment with the STR OBT. Moreover, the extracted data is converted into engineering units and the associated OBT is converted into UTC. Finally, data files containing the sorted time-series of the extracted quantities are produced.

2. Voltage to acceleration conversion.
   The control voltages of the eight electrode pairs surrounding each proof mass of the six accelerometers are corrected for errors caused by the accelerometer measurement unit (in science read-out branch and in control loop). The corrected control voltages are transformed in sets of accelerations in the accelerometer electrode system reference frame (AESRF, Gruber et al., 2010a) and in the accelerometer reference frame (ARF, Gruber et al., 2010a), e.g. in common- and differential mode accelerations. In addition, the angular accelerations about the axes of the GRF are computed.

3. Proof mass acceleration retrieval.
   The actual common and differential mode accelerations of the three accelerometer pairs along the axes of the corresponding one axis gradiometer reference frame (OAGRF, Gruber et al., 2010a) are computed from the measured common and differential mode accelerations by applying the three Inverse Calibration Matrices. From the recovered differential mode accelerations the (corrected) angular accelerations of the gradiometer about the axes of the GRF can be obtained.

4. Angular rate reconstruction.
   The inertial angular rates of the gradiometer about the axes of the GRF are calculated from the angular accelerations of the gradiometer about the axes of the GRF and from the quaternions, measured by the star sensors, which define the attitude of the star sensor reference frame (SSRF, Gruber et al., 2010a) in the inertial reference frame (IRF). Additionally, the quaternions defining the attitude of the GRF with respect to the IRF are computed.

5. GGT computation.
   In this step the six independent components of the GGT are obtained on the basis of the calibrated differential mode accelerations and on the basis of the reconstructed inertial angular rates of the gradiometer about the axes of the GRF.

6. Transformation matrix.
   The transformation matrix from GRF to the IRF is calculated. The necessary attitude information is taken from the output quaternions of the angular rate reconstruction step.

7. Monitoring.
   All relevant intermediate results undergo preliminary tests to detect anomalies. Also the trace of the GGT is computed.

3.1. De-packeting and sorting

Figure 3.2 illustrates how the EGG Level 0 product (`EGG_NOM_0`) is converted to the first intermediate product (`EGG_CTR_1i`) of the main EGG L1b product (`EGG_NOM_1b`).

After extracting the Level 0 telemetry packets generated by the gradiometer and by the platform with their associated OBT, the EGG control voltages are interpolated to an integer second sampling. The idea is to interpolate the control voltages and their associated EGG OBT exactly to the OBT of the star sensors, which is contained in `STR_VC2_1b`. Note that the STR data is given with a sampling of 2 Hz. Thus theoretically two different fractions for the 1 Hz sampling of the control voltages are possible. Therefore, the fraction of the first STR OBT closest in time to the OBT of the first EGG control voltage has to be stored for the processing of the consecutive orbital revolutions. Note that the interpolation of the control voltages has no significant impact on the error budget of the gravity gradients, when using an adequate interpolator. According to Frommknecht (2009), the natural cubic spline interpolator has been approved.

For the conversion of the EGG OBT to GPS system time and UTC, either the difference between EGG OBT and GPS system time is read out from the `SST_TCT_1i` data set, contained in the satellite-to-satellite L1b file (`SST_NOM_1b`), or, if this is not available, information from the correlation between OBT and UTC derived during the downlink process and provided in the auxiliary input file `AUX_OUTC_` is used, (Frommknecht et al., 2011). In the former case a nanosecond accuracy is reached, in contrast to the latter case where only a millisecond accuracy is reached. The results of this step are contained in the intermediate product `EGG_TCT_1i` of the file `EGG_NOM_1b`.

Also the data consecutiveness is checked. If there is a gap in the control voltages the corresponding start time, end time and the number of missing lines is recorded in the file `GAPS_DATA_SET`.

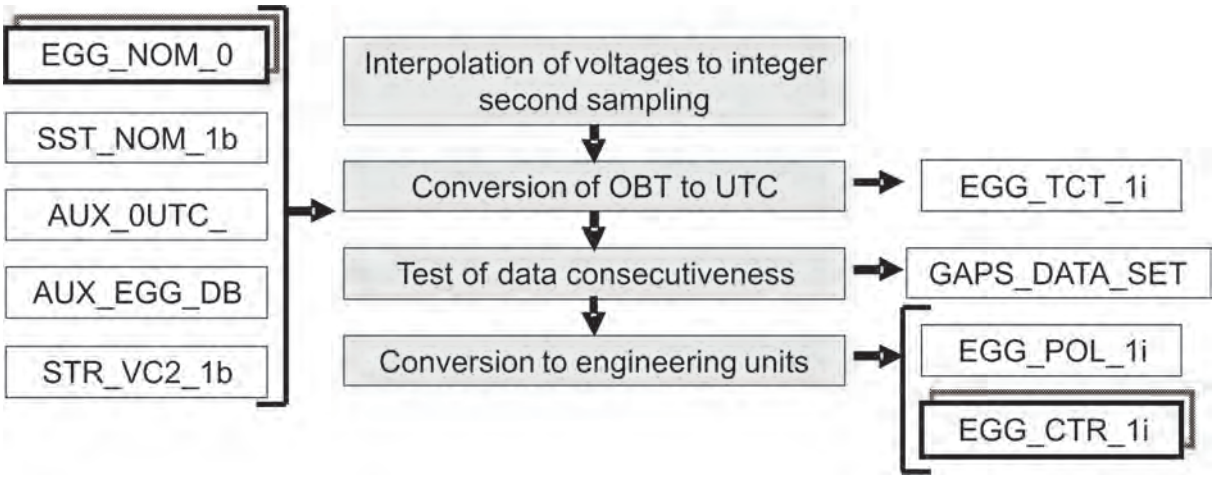

Figure 3.2.: Flowchart: De-packeting and Sorting.

Finally, the conversion to engineering units of the detection voltages, the polarization voltages and the control voltages is performed. For the control voltages a fourth order polynomial correction is foreseen in the processing, which has been used for tests with simulated data before the launch of GOCE. In the processing of the real GOCE data, this step is not necessary, and hence, not applied. The polynomial coefficients (variable `PC_CTR` in main auxiliary file `AUX_EGG_DB`) are therefore set to dummy values (only zeros and ones).

Figure 3.3 illustrates the arrangement of the 8 electrode pairs of a three-axis GOCE accelerometer. There are four electrode pairs, denoted $X1$ to $X4$, along the LS accelerometer axis of the AESRF and two electrode pairs along the two US axes, denoted $Y1/Y2$ and $Z1/Z2$, building a right-handed system. In the following the control voltages of accelerometer i, measured with the x-electrodes are denoted as $CV_{i,X1,\ldots,X4}$. The control voltages measured with the y- and z-electrodes are denoted as $CV_{i,Y1/Y2}$ and $CV_{i,Z1/Z2}$, respectively.

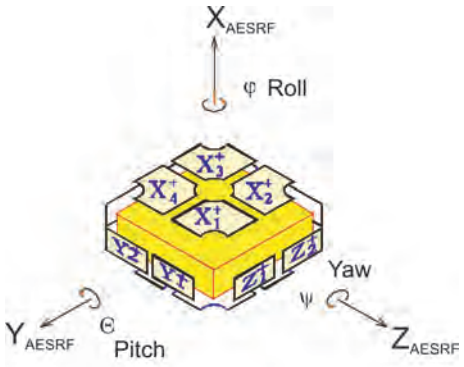

Figure 3.3.: Arrangement of the 8 electrode pairs in the accelerometer electrode system reference frame (AESRF) of a GOCE accelerometer.

In Fig. 3.4 the control voltages of one day, 11 November 2009, are shown in the time domain (left) and in the frequency domain in terms of root PSD (right), for the example of accelerometer A_1. Apart from an offset, we observe similar signals for control voltages measured in the same direction. This is true in the time domain, as well as for the root PSDs, where a potential offset is not visible anyway, because this part of the signal is reflected in the DC (direct current) at the zero frequency, which is not included in the illustration (right). In Fig. 3.4(d) the curves of the two control voltages in z-direction of the AESRF (cyan and blue) are below those of the control voltages in y-direction for frequencies below about 70 mHz. The arrangement of the accelerometers within the gradiometer is given in Fig. 3.7. For accelerometer A_1 the z-electrodes are mounted along an US axis in (negative) x-direction of its ARF and hence also in x-direction of the GRF, which is the flight direction of GOCE, cf. Table 3.1. For comparison the y-electrodes of A_1 are mounted along an US axis in z-direction of GRF. When comparing the corresponding curves in Fig. 3.4(d) we can conclude that the lower signal content of the control voltages in flight direction (Z_e) is due to the fact that in this direction the total signal has been reduced to a large extent by the drag control system. Note that these are only qualitative considerations. An

exact interpretation of the control voltages' signal content is not possible because these are (still) uncalibrated values.

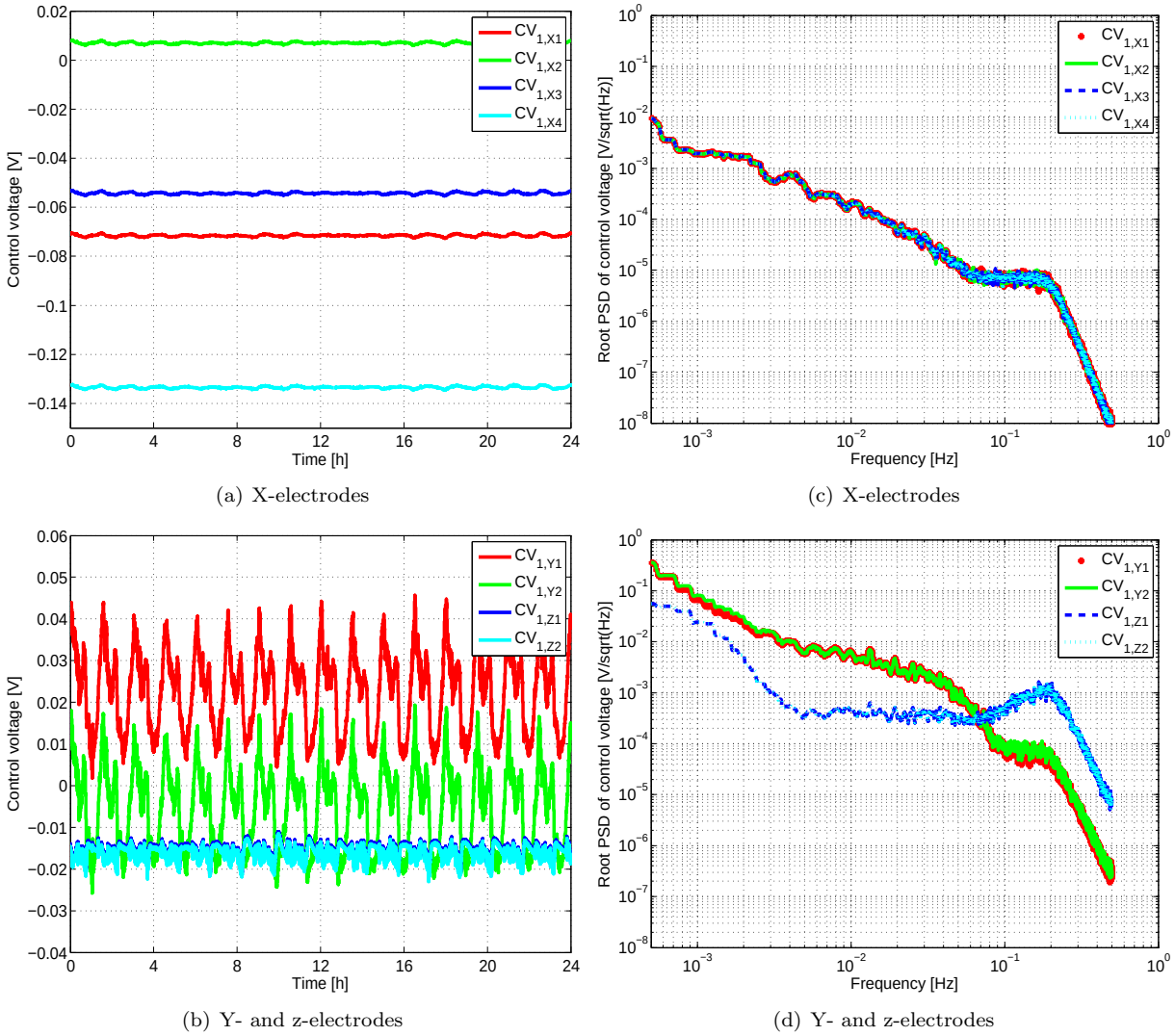

(a) X-electrodes

(c) X-electrodes

(b) Y- and z-electrodes

(d) Y- and z-electrodes

Figure 3.4.: Control voltages ($CV_{1,X1,\ldots,X4}$, $CV_{1,Y1/Y2}$ and $CV_{1,Z1/Z2}$) of accelerometer A_1 in the accelerometer electrode system reference frame (left) and corresponding root PSD (right) of 11 November 2009.

3.2. Voltage to acceleration conversion

The 48 control voltages from the previous step are converted to accelerations, as illustrated in Fig. 3.5.

Therefore, first of all, the control voltages have to be corrected for the phase delay and gain attenuation introduced by the transfer functions and electronics within the accelerometers. The necessary steps can be illustrated with the GOCE accelerometer model, see Fig. 3.6. According to Chhun and Gurard (2004) the objective is to trace the data stream backwards from the output of the accelerometer model (point D) to its input (point A). This can be divided into three steps:

- From D to C: Inversion of the science filter transfer function (filter parameters `FILT_SC` in file `AUX_EGG_DB`). The main effect is a phase correction.
- From C to B: Correction for the errors introduced by the components Read-Out and ADC2, including a non-linear correction (parameters `PC_NL` in file `AUX_EGG_DB`) and a correction for phase delay (parameters `FILT_LO` in file `AUX_EGG_DB`). With the previous steps (from D to B), corresponding to the first box in the flowchart of Fig. 3.5, the corrected control voltages (measurement data set (MDS) `EGG_CCV_1i` in files `EGG_NOM_1b`) are recovered from input control voltages (MDS `EGG_CTR_1i`).

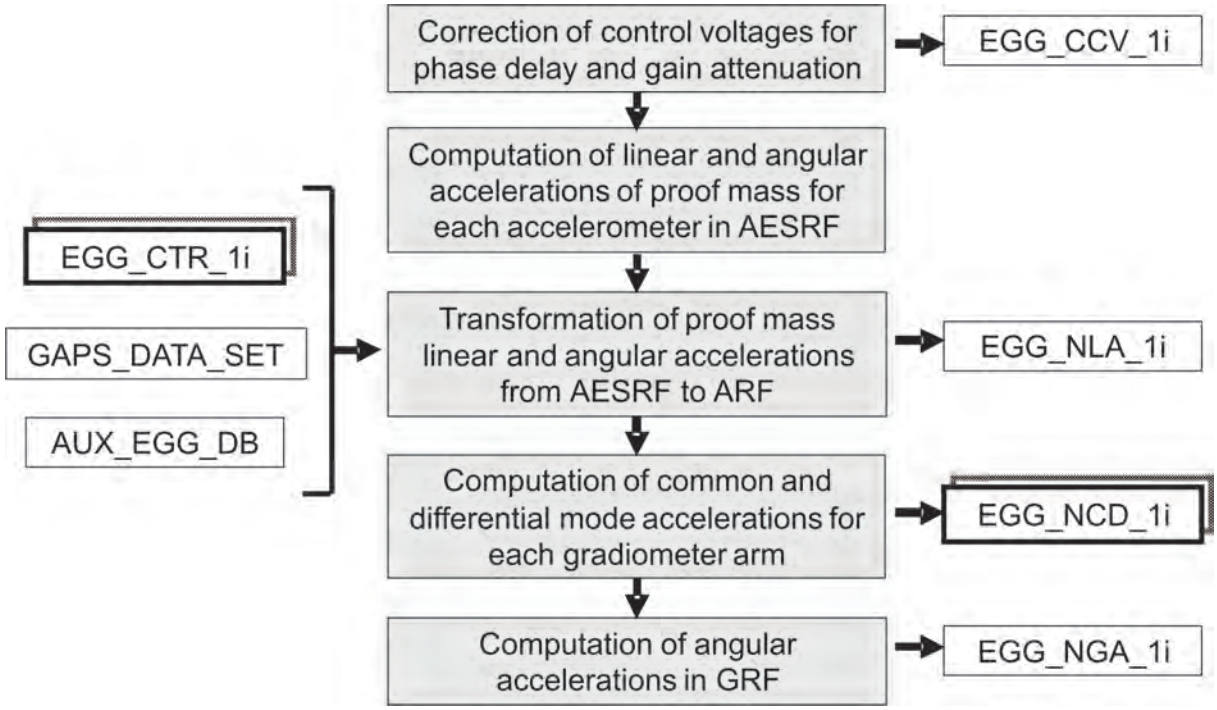

Figure 3.5.: Flowchart: Voltage to acceleration conversion.

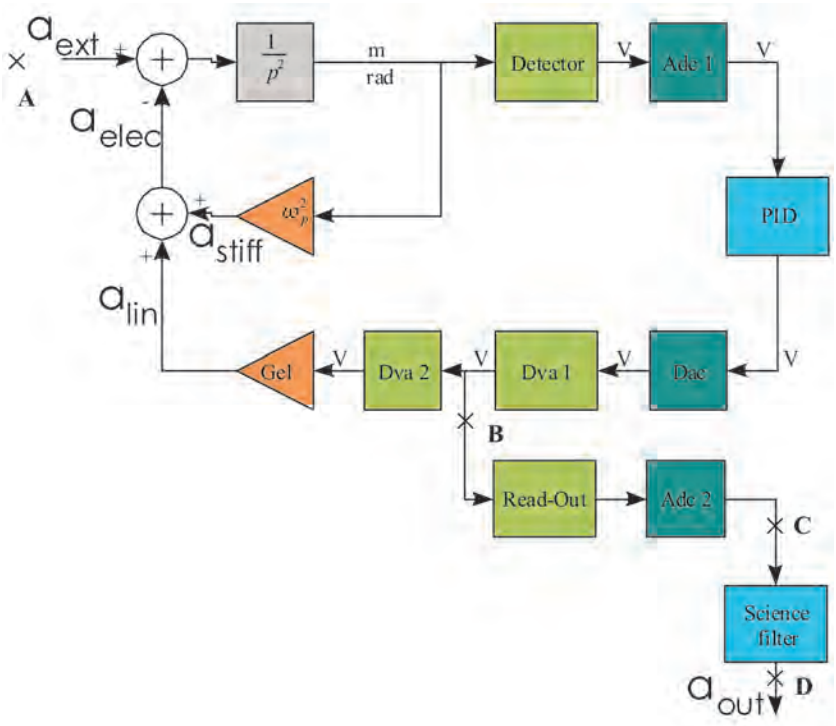

Figure 3.6.: GOCE accelerometer model. Source: Chhun and Gurard (2004).

- From B to A: Inversion of the loop transfer function. From the 48 corrected control voltages the accelerations per degree of freedom (three linear and three angular accelerations) in the AESRF are computed by recombination of the corrected control voltages and application of the electrostatic gains (parameters `ES_GAIN` in file `AUX_EGG_DB`). This corresponds to the second box in the flowchart of Fig. 3.5.

The conversion of the 8 control voltages ($CV_{i,X1}$ to $CV_{i,X4}$, $CV_{i,Y1}$, $CV_{i,Y2}$, $CV_{i,Z1}$ and $CV_{i,Z2}$) per accelerometer A_i in 6 accelerations can be written as

$$\begin{pmatrix} a_{i,1} \\ a_{i,5} \\ a_{i,6} \end{pmatrix} = \underline{A}_x \begin{pmatrix} CV_{i,X1} \\ CV_{i,X2} \\ CV_{i,X3} \\ CV_{i,X4} \end{pmatrix} \tag{3.1}$$

$$\begin{pmatrix} a_{i,2} \\ a_{i,3} \\ a_{i,4} \end{pmatrix} = \underline{A}_{yz} \begin{pmatrix} CV_{i,Y1} \\ CV_{i,Y2} \\ CV_{i,Z1} \\ CV_{i,Z2} \end{pmatrix} \tag{3.2}$$

where

$$\underline{A}_x = \frac{1}{4G_x} \begin{pmatrix} G_{es,i,1} & G_{es,i,2} & G_{es,i,3} & G_{es,i,4} \\ G_{es,i,13} & G_{es,i,14} & -G_{es,i,15} & -G_{es,i,16} \\ -G_{es,i,17} & G_{es,i,18} & G_{es,i,19} & -G_{es,i,20} \end{pmatrix} \tag{3.3}$$

and

$$\underline{A}_{yz} = \frac{1}{2G_{yz}} \begin{pmatrix} G_{es,i,5} & G_{es,i,6} & 0 & 0 \\ 0 & 0 & G_{es,i,7} & G_{es,i,8} \\ -G_{es,i,11} & G_{es,i,12} & G_{es,i,9} & -G_{es,i,10} \end{pmatrix} \tag{3.4}$$

are the so-called recombination matrices, which include the electrostatic gains $G_{es,i,k}$ with $k = 1, \ldots, 20$ of accelerometer A_i. G_x and G_{yz} (parameters `G_READ_X` and `G_READ_YZ` in file `AUX_EGG_DB`) are the read-out gains for the x-axis and respectively the y- and z-axes in AESRF.

The three linear accelerations ($a_{i,1}$, $a_{i,2}$, $a_{i,3}$) and three angular accelerations ($a_{i,4}$, $a_{i,5}$, $a_{i,6}$) per accelerometer (i.e. in total 36 accelerations) in the AESRF are transformed to the ARF, using the correspondence between the axes of the two reference frames. This correspondence is shown in Fig. 3.7, where the LS accelerometer axes are indicated by dashed lines (same as shown in Fig. 2.2), and the axes in AESRF are indicated by X_e, Y_e and Z_e for each accelerometer. The relationship is also given in Tab. 3.1. It can be seen that the x-axes in AESRF always correspond to the LS transversal axes, the y-axes in AESRF always to the US transversal axes, and the z-axes in AESRF always to the important US in-line axes. The corresponding rotation matrices from AESRF to ARF (or GRF) can be found in the parameters `R_AESRF_GRF` in file `AUX_EGG_DB`. The intermediate results of this processing step can be found in MDS `EGG_NLA_1i` of the files `EGG_NOM_1b`.

Table 3.1.: Correspondence between AESRF, ARF and GRF

accelerometer	axis of AESRF	axis of ARF	sensitivity	arrangement
A_1, A_4	X_e	$+Y_1$, $+Y_4$	LS	transversal
	Y_e	$-Z_1$, $-Z_4$	US	transversal
	Z_e	$-X_1$, $-X_4$	US	in-line
A_2, A_5	X_e	$+Z_2$, $+Z_5$	LS	transversal
	Y_e	$-X_2$, $-X_5$	US	transversal
	Z_e	$-Y_2$, $-Y_5$	US	in-line
A_3, A_6	X_e	$+Y_3$, $+Y_6$	LS	transversal
	Y_e	$-X_3$, $-X_6$	US	transversal
	Z_e	$+Z_3$, $+Z_6$	US	in-line

From the three linear accelerations per accelerometer in ARF the common and differential mode accelerations are built with Eqs. 2.27 and 2.37, cf. also (Marque et al., 2010). In the `EGG_NOM_1b` files the corresponding values are given in the data set `EGG_NCD_1i`. The common and differential mode accelerations are needed for the further gradiometer processing and are thus the main output of the voltage to acceleration conversion.

With Eqs. 2.47 to 2.49 the angular accelerations in the GRF are computed from the transversal differential mode accelerations. The related data set in the `EGG_NOM_1b` files is `EGG_NGA_1i`, where the $'N'$ indicates that these are the nominal and not yet calibrated gradiometer angular accelerations.

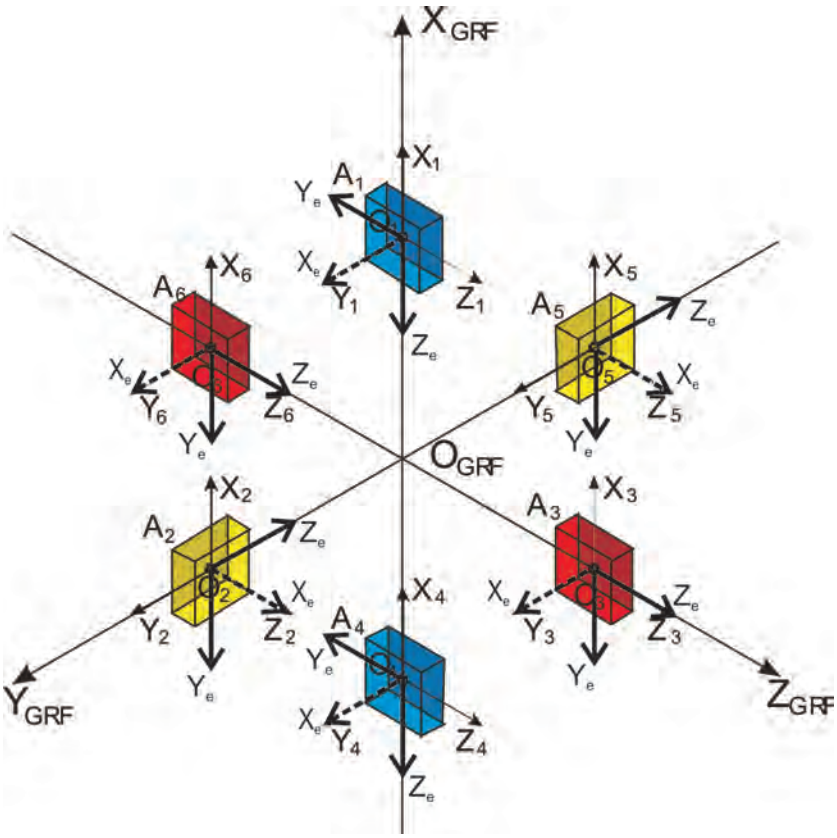

Figure 3.7.: Correspondence between AESRF (indicated by X_e, Y_e and Z_e-axes), ARF (indicated by X_i, Y_i and Z_i-axes, $i = 1, 2, ..., 6$) and GRF (indicated by X_{GRF}, Y_{GRF} and Z_{GRF}-axes). The dashed arrows indicate the less sensitive accelerometer axes.

In the following the linear accelerations in ARF, the uncalibrated common and differential mode accelerations (in the respective OAGRF) and the nominal gradiometer angular accelerations are analyzed for the day 11 November 2009. This day serves as a representative example for the data collected with GOCE during a nominal measurement phase. (The measurement phases are interrupted from time to time, e.g. for calibration, cf. Chapter 4.)

Figure 3.8 shows the linear accelerations in ARF (left) and the corresponding root PSD (right). The accelerations in time domain (left) which are measured with US axes, i.e. all accelerations in x-direction, the ones of A_2 and A_5 in y-direction, as well as the ones of A_1, A_3, A_4 and A_6 in z-direction have a magnitude of 10^{-6} m/s^2 or smaller, whereas the LS acceleration measurements are about one or two magnitudes larger. The only exception to this is the LS acceleration of A_3 in y-direction, with a magnitude of only 10^{-6} m/s^2. The corresponding root PSD (Fig. 3.8, right) in x-direction is in the gradiometer MB approximately flat and in the order 10^{-9} m/s$^2/\sqrt{\text{Hz}}$. The root PSDs in y- and z-direction, in contrast, show in the MB an increase towards lower frequencies (up to a few 10^{-8} m/s$^2/\sqrt{\text{Hz}}$). This reflects again drag compensation in x-direction.

An example for the uncalibrated common mode accelerations is given in Fig. 3.9. The CM accelerations reflect the non-conservative forces acting on the satellites' center of mass (COM). The magnitude in x-direction, Fig. 3.9(a), is smaller than in the two other directions, Fig. 3.9(b) and Fig. 3.9(c), reflecting again the drag compensation of the ion thruster assembly. Moreover, the CM acceleration in x-direction, Fig. 3.9(a), shows a significant pattern of alternating intervals of higher and smaller signal variation, which is observed once per orbital revolution. This pattern is caused by the ion thrusters, which are working at certain thrust levels. In the root PSD, Fig. 3.9(d), the functionality of the drag compensation in x-direction is again clearly visible, despite the fact that these are still uncalibrated values.

In Fig. 3.10 the uncalibrated differential mode accelerations are shown, which contain the gravity gradient and the rotational signal. For all in-line measurements ($a_{d,14,x}$, $a_{d,25,y}$, $a_{d,36,z}$) US axes have been used. The corresponding measurements have a magnitude of about 10^{-6} m/s^2 or smaller. The measurements of the LS axes have a larger magnitude, of e.g. up to 10^{-5} m/s^2 for $a_{d,36,y}$. The root PSDs (right) of the in-line measurements have a smaller magnitude in the gradiometer MB as the other differential mode accelerations. This higher magnitude of the remaining accelerations can either be rotational signal or noise due to the influence of LS measurements.

The uncalibrated gradiometer angular accelerations are shown in Fig. 3.11. All angular acceleration components should theoretically be very small. In Cesare (2008) the requirements for the angular control of the satellite are given. For the DC part of $\dot{\omega}_x$ we have $2 \cdot 10^{-6}$ rad/s^2, and for the DC part of $\dot{\omega}_y$ and $\dot{\omega}_z$ $1 \cdot 10^{-6}$ rad/s^2. We observe, Fig. 3.11(a), that the requirement for $\dot{\omega}_y$ holds. For $\dot{\omega}_x$ and $\dot{\omega}_z$ we observe a larger bias, due to the influence of the LS measurements, which does not allow the verification of the respective requirements. In the root PSD, Fig. 3.11(b), $\dot{\omega}_x$ has the largest magnitude within the MB. This is due to the geometry of the spacecraft, which has an elongated body in x-direction, making the satellite sensitive to rotational accelerations about this axis, cf. Sect. 5.1.

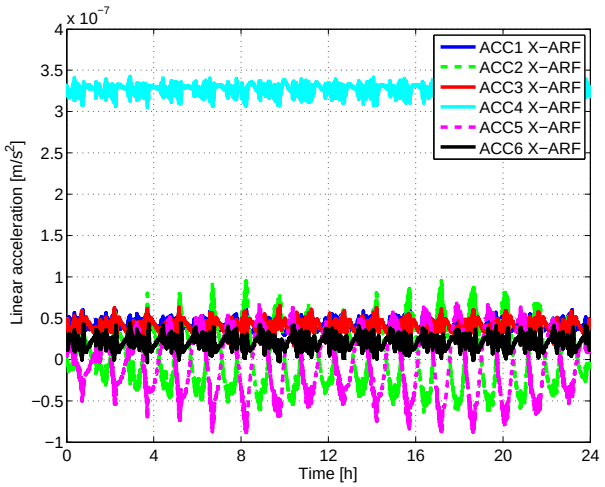

(a) X-direction of ARF

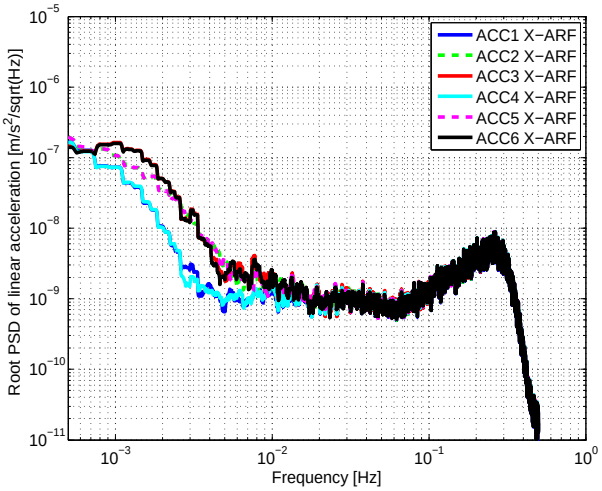

(d) X-direction of ARF

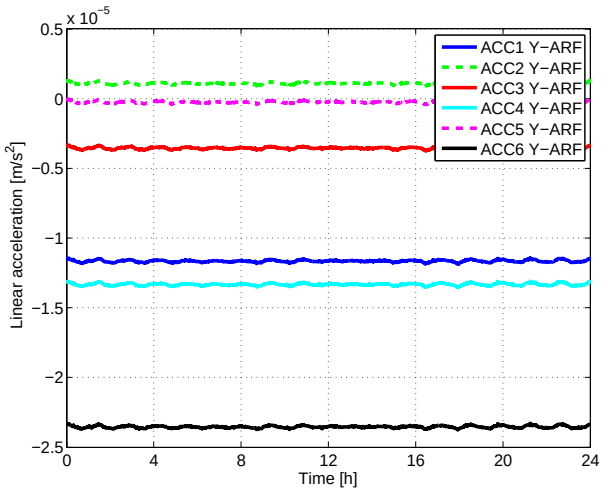

(b) Y-direction of ARF

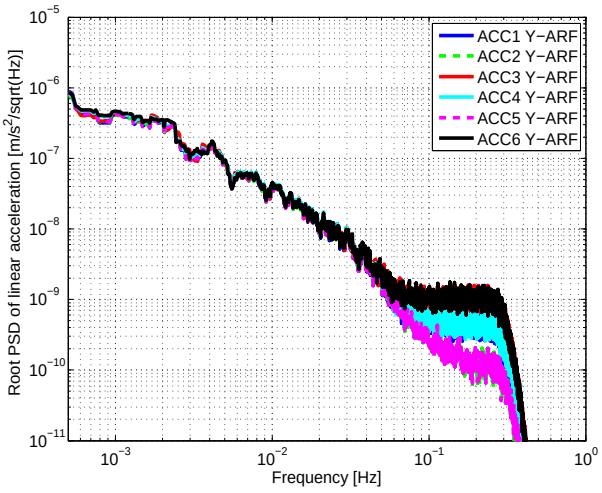

(e) Y-direction of ARF

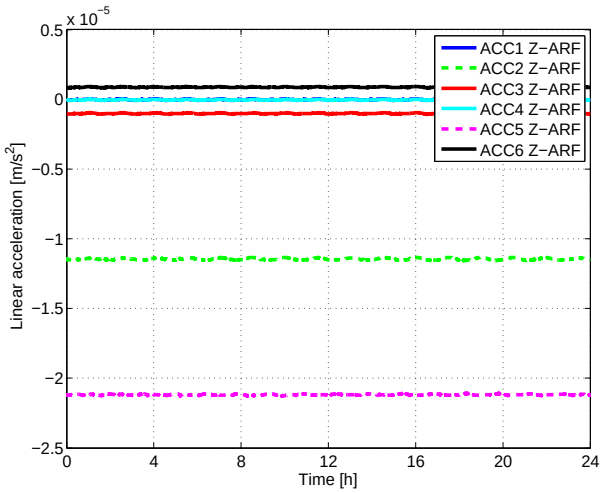

(c) Z-direction of ARF

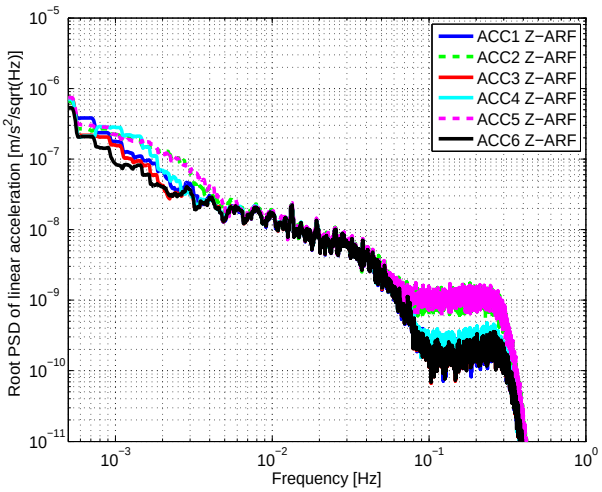

(f) Z-direction of ARF

Figure 3.8.: Linear accelerations of accelerometers A_1 to A_6 in accelerometer reference frame (ARF, left) and corresponding root PSD (right) of 11 November 2009.

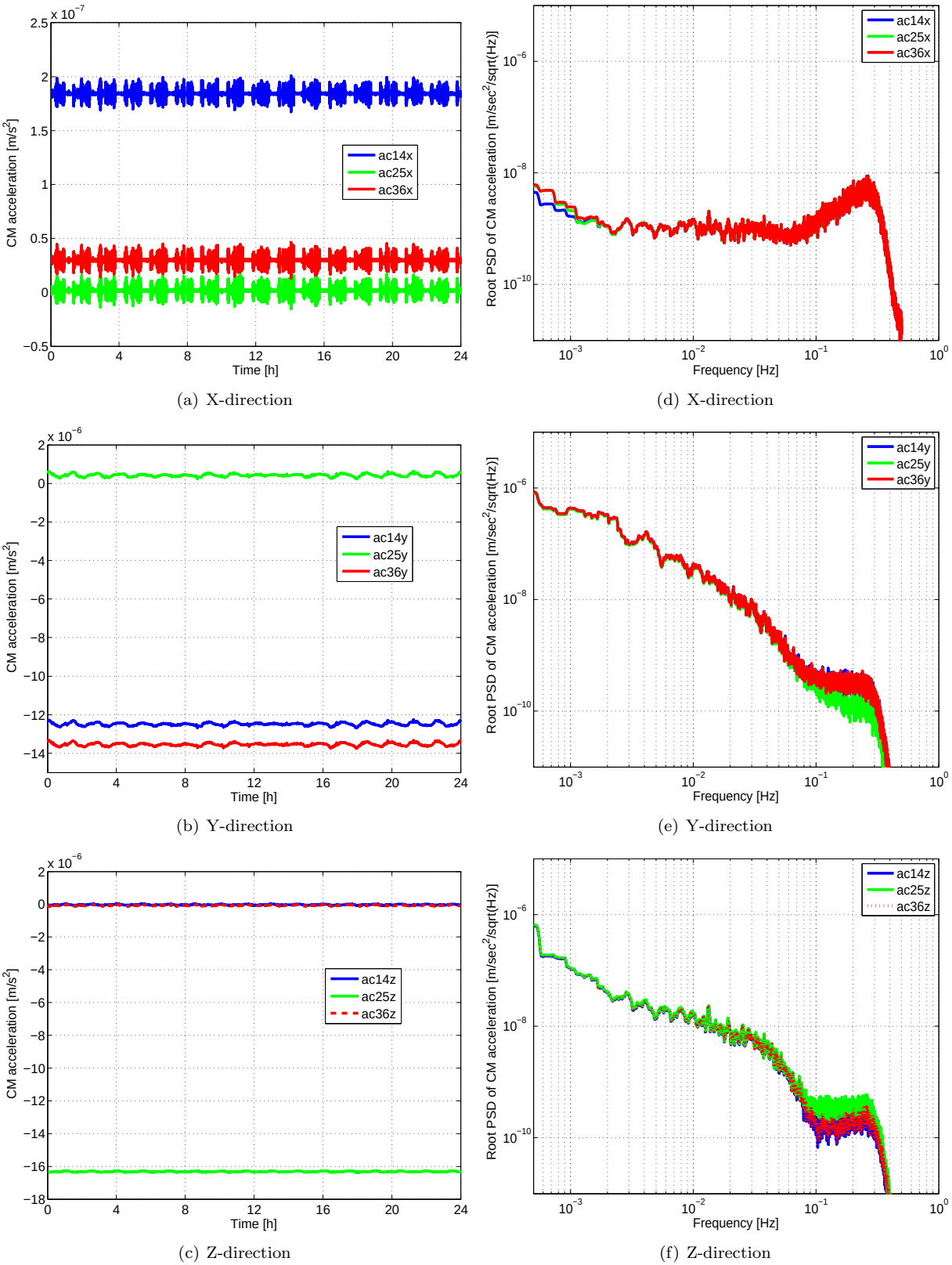

(a) X-direction (d) X-direction

(b) Y-direction (e) Y-direction

(c) Z-direction (f) Z-direction

Figure 3.9.: Uncalibrated common mode accelerations (left) and corresponding root PSD (right) of 11 November 2009.

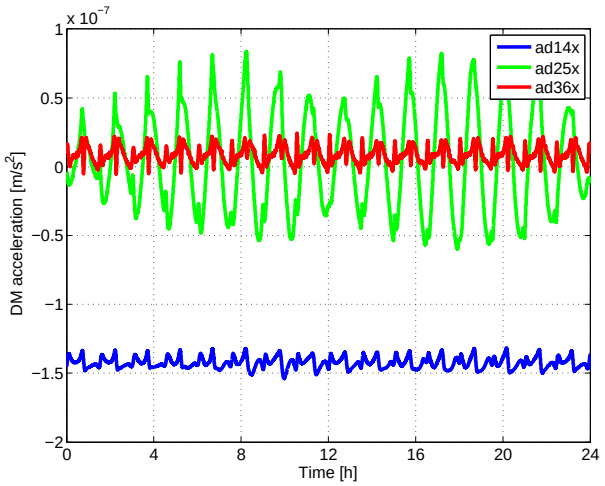

(a) X-direction

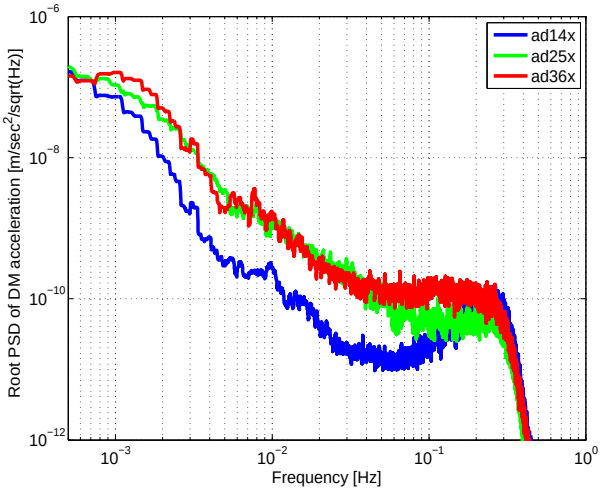

(d) X-direction

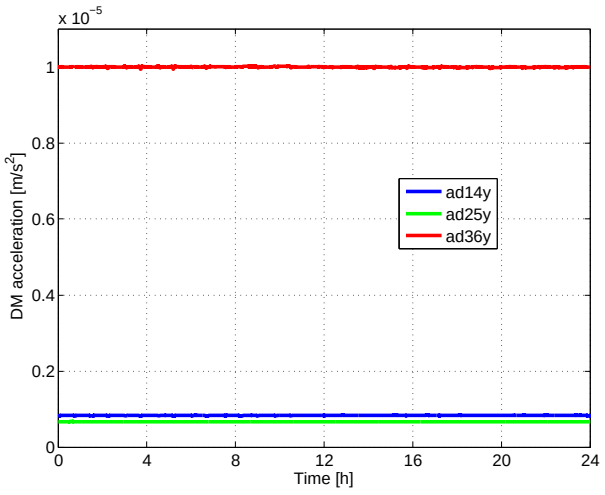

(b) Y-direction

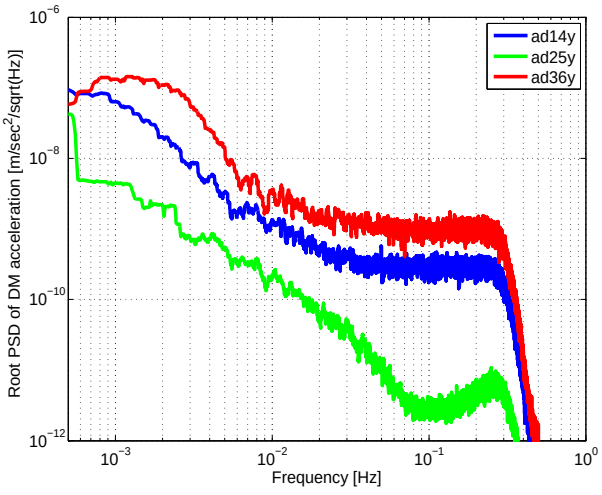

(e) Y-direction

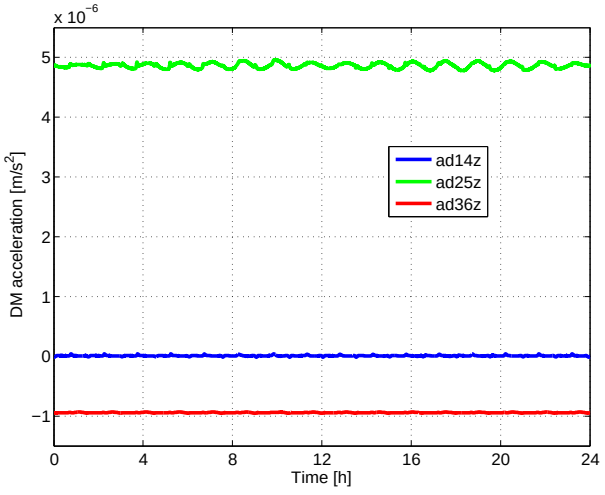

(c) Z-direction

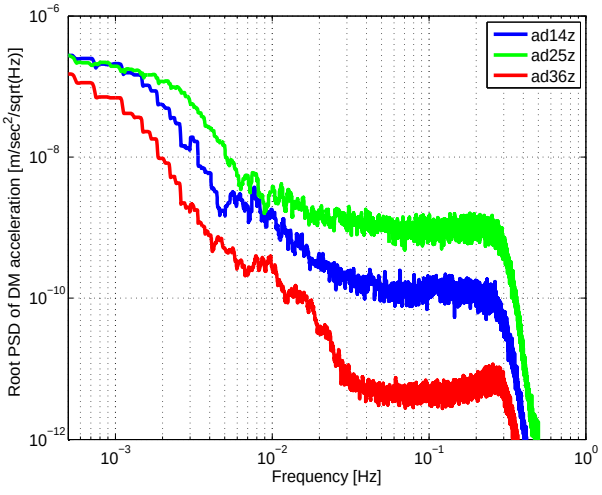

(f) Z-direction

Figure 3.10.: Uncalibrated differential mode accelerations (left) and corresponding root PSD (right) of 11 November 2009.

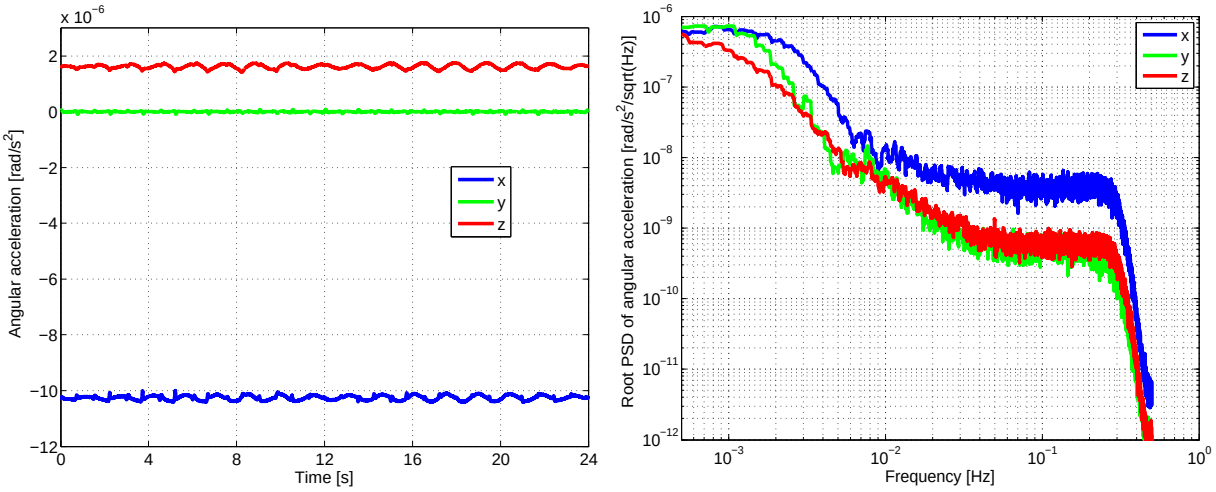

(a) (b)

Figure 3.11.: Nominal gradiometer angular accelerations (a) and corresponding root PSD (b) of 11 November 2009.

3.3. Proof mass acceleration retrieval

Fig. 3.12 illustrates the steps to recover calibrated accelerations from the nominal ones.

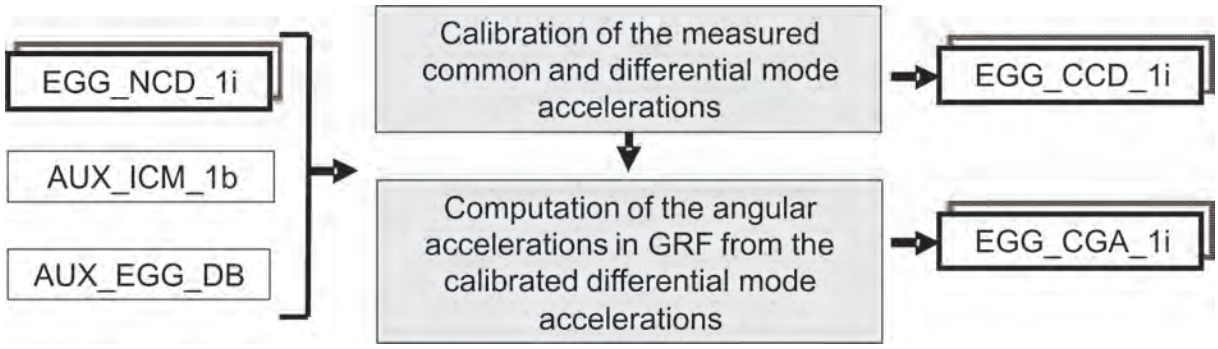

Figure 3.12.: Flowchart: Acceleration recovery.

In a first step, the nominal common and differential mode accelerations are corrected with the ICMs contained in file AUX_ICM_1b, according to Eq. 4.15. The ICMs contain the corrections for gradiometer imperfections, like scale factors of the accelerometers and non-orthogonalities of the accelerometer axes, see also Chapter 4. The calibrated common and differential mode accelerations are given in the `EGG_NOM_1b` files as `EGG_CCD_1i`.

The transversal, calibrated DM accelerations are used further on to calculate calibrated gradiometer angular accelerations, again according to Eqs. 2.47 to 2.49. In the `EGG_NOM_1b` files they are called `EGG_CGA_1i`, where the $'C'$ indicates that these are calibrated gradiometer angular accelerations.

In the following the calibrated CM, DM and angular accelerations are shown for 11 November 2009. The impact of the calibration becomes clear, when comparing these calibrated values to the uncalibrated ones, as described before.

Figure 3.13 shows the calibrated common mode accelerations. In the time domain (left), we observe only small differences with respect to the uncalibrated values as shown in Fig. 3.9, left. Still, there is a large bias present for the LS accelerations, since the calibration is not designed in order to eliminate the bias, cf. Chapter 4. Also in the root PSD of the CM accelerations no significant effect due to the calibration is visible, cf. Fig. 3.13, right and Fig. 3.9, right. The CM accelerations in one direction can be measured simultaneously with three one-axis gradiometers. We observe that these three measurements coincide within the gradiometer MB (and below) very well. Above the MB, i.e. for frequencies higher than 100 mHz, the higher noise level of the LS measurements becomes visible. This holds in y-direction for $a_{c,14,y}$ and $a_{c,26,y}$, Fig. 3.13(e), blue and red, and in z-direction for $a_{c,25,z}$, Fig. 3.13(f), green.

In Fig. 3.14 the calibrated differential mode accelerations are shown. In the time domain (left) we observe almost no impact due to calibration, cf. Fig. 3.14, left and Fig. 3.10, left. Again, the bias cannot be eliminated by calibration. Of upmost importance is the calibration within the MB. The root PSDs of the calibrated in-line DM accelerations, Fig. 3.14, right, are flat for frequencies between about 40 and 100 mHz, i.e. in the upper part of the MB. In contrast to that, the root PSDs of the respective uncalibrated differential accelerations, Fig. 3.10, right are not flat, but increase towards the lower frequencies, e.g. for $a_{d,25,y}$, Fig. 3.10(e), green. This increase is already visible for frequencies below about 80 mHz. We conclude that the calibration has successfully reduced the errors in the MB of the differential in-line measurements, which are needed for the computation of the main diagonal GGT elements. The impact of the calibration as deduced from different calibration approaches is further discussed in Sect. 5.1.3.

The calibrated gradiometer angular accelerations in Fig. 3.15 look similar to the respective uncalibrated accelerations in Fig. 3.11. We observe again the smallest bias for $\dot{\omega}_y$ (in time domain, Fig. 3.15(a)) which is composed of US measurements only, and the largest component in the MB is again $\dot{\omega}_x$ (in root PSD, Fig. 3.15(b)) due to the elongated geometry of the satellite in x-direction.

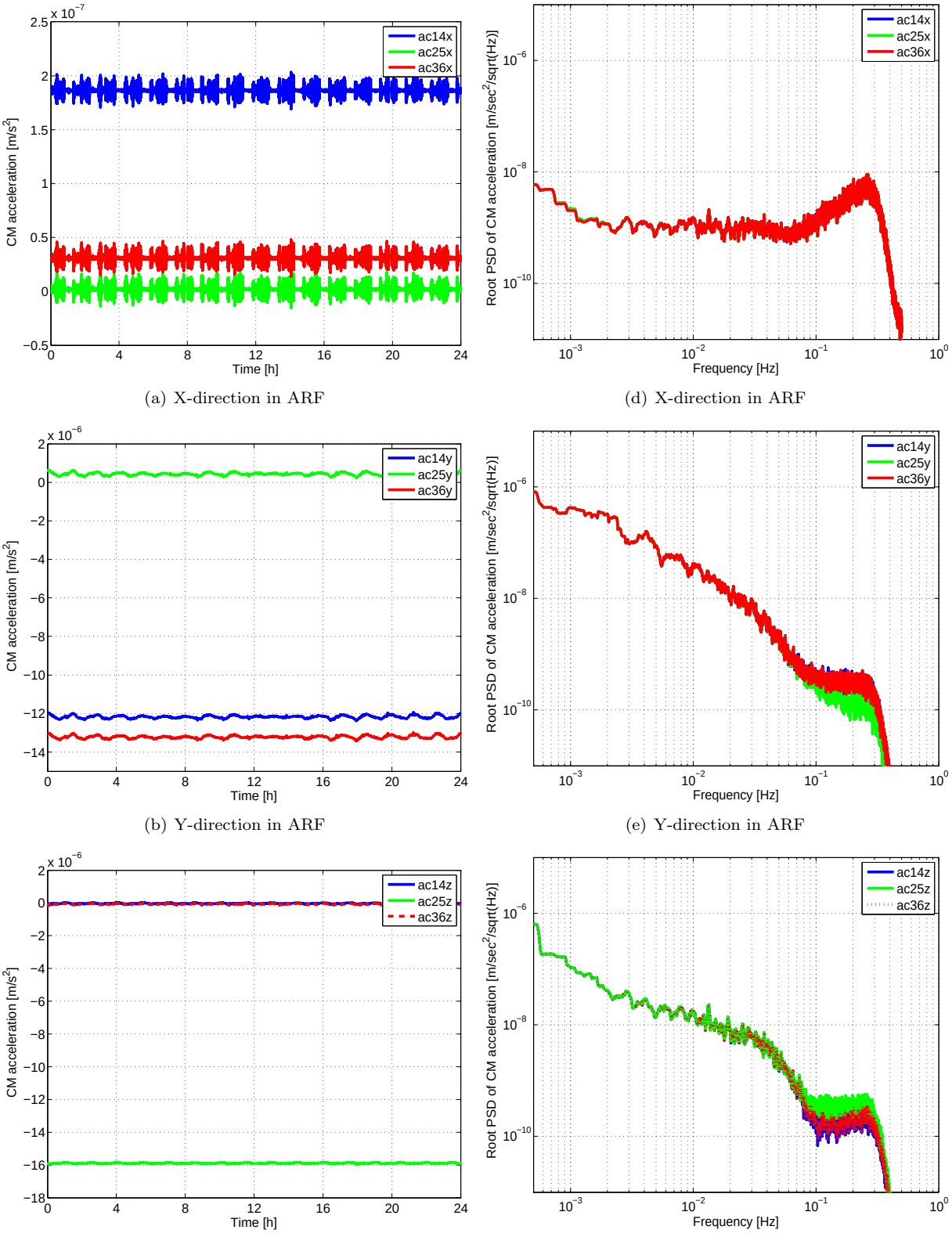

(a) X-direction in ARF

(d) X-direction in ARF

(b) Y-direction in ARF

(e) Y-direction in ARF

(c) Z-direction in ARF

(f) Z-direction in ARF

Figure 3.13.: Calibrated common mode accelerations (left) and corresponding root PSD (right) of 11 November 2009.

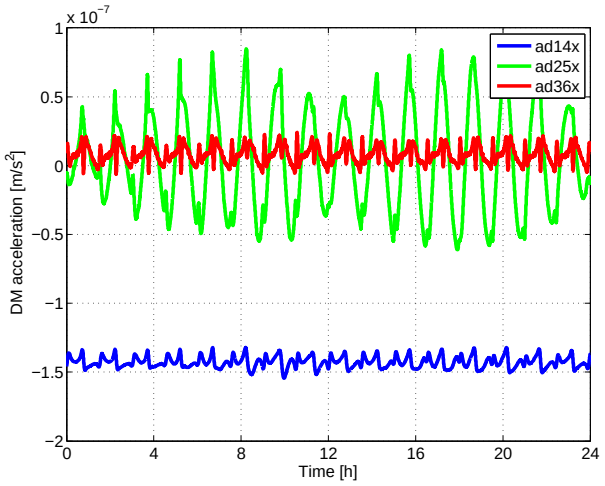

(a) X-direction in ARF

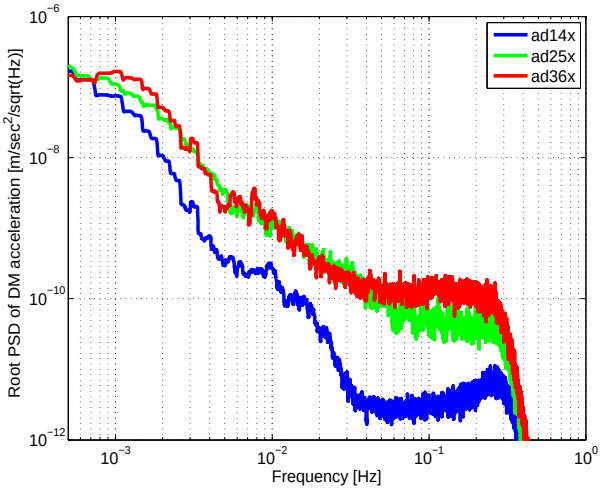

(d) X-direction in ARF

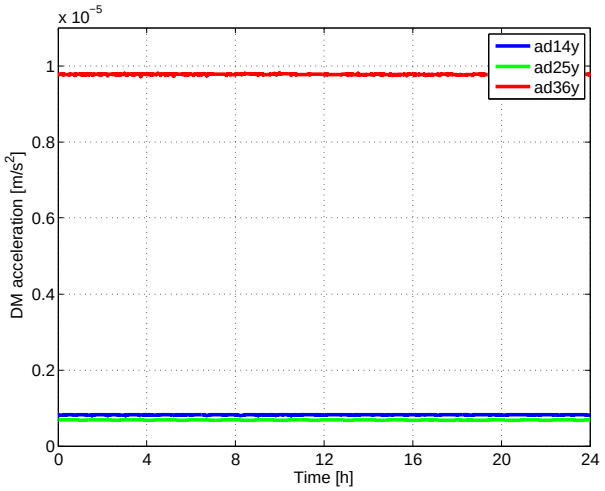

(b) Y-direction in ARF

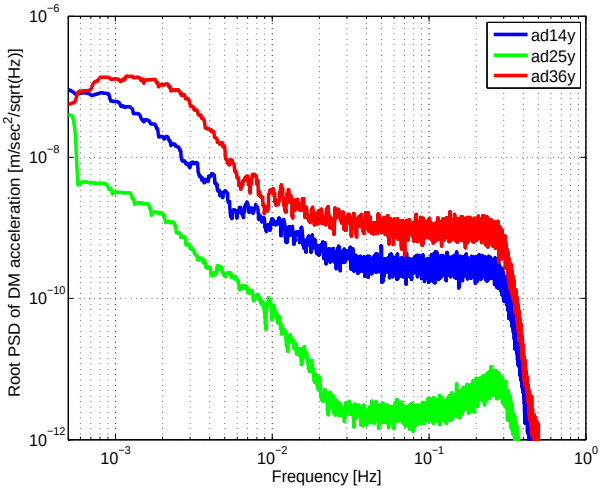

(e) Y-direction in ARF

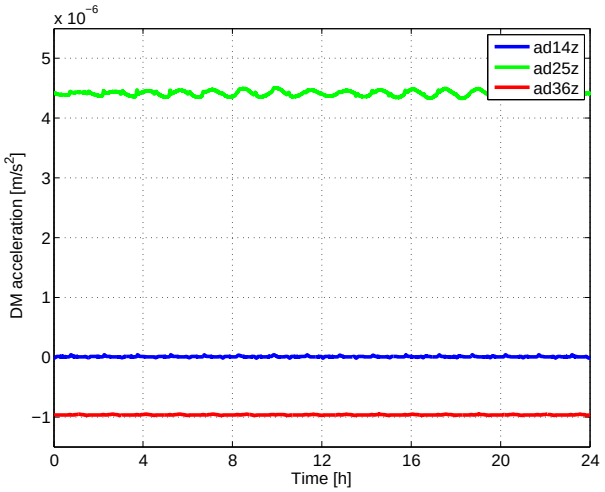

(c) Z-direction in ARF

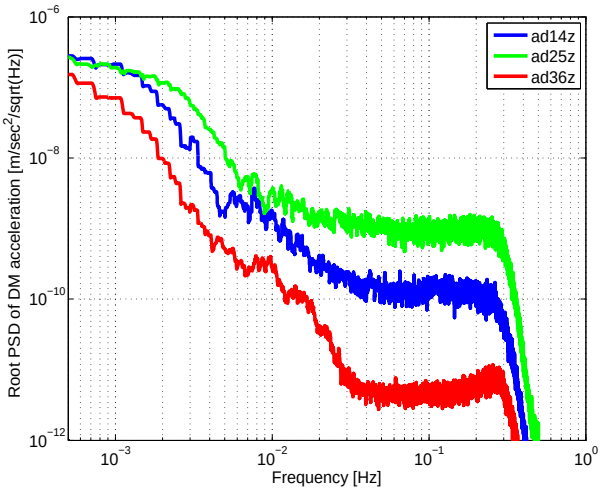

(f) Z-direction in ARF

Figure 3.14.: Calibrated differential mode accelerations (left) and corresponding root PSD (right) of 11 November 2009.

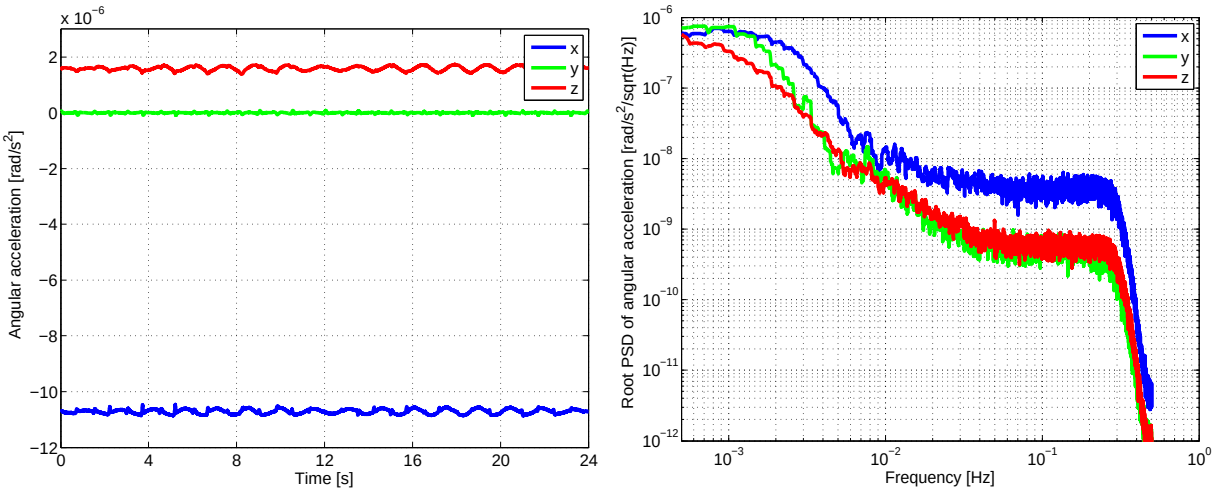

(a) (b)

Figure 3.15.: Calibrated gradiometer angular accelerations (a) and corresponding root PSD (b) of 11 November 2009.

3.4. Angular rate reconstruction

The so-called angular rate reconstruction (ARR) is the most complex part of the nominal gradiometer processing besides the determination of the ICMs (cf. Sect. 4.3). The goal is to find the best possible combination of the available attitude information to reconstruct the inertial angular rates of the gradiometer about the axes of the GRF (MDS `EGG_GAR_1i`). Attitude information is available from the gradiometer in terms of angular accelerations about the axes of the GRF (data set `EGG_CGA_1i`) and from a star sensor in terms of quaternions defining the attitude of the SSRF in the IRF (files `STR_VC2_1b`). Besides, the quaternions defining the attitude of the GRF in the IRF are determined (MDS `EGG_IAQ_1i`). In this section, the original method for the angular rate reconstruction as defined by Cesare et al. (2008) is described. In Sect. 6.2 an improved method for ARR is introduced, which has been developed by the author and which has replaced the original method within the official L1b processing, cf. Sect. 6.2.2.

Figure 3.16 shows a simplified flowchart of the necessary processing steps for the original ARR method.

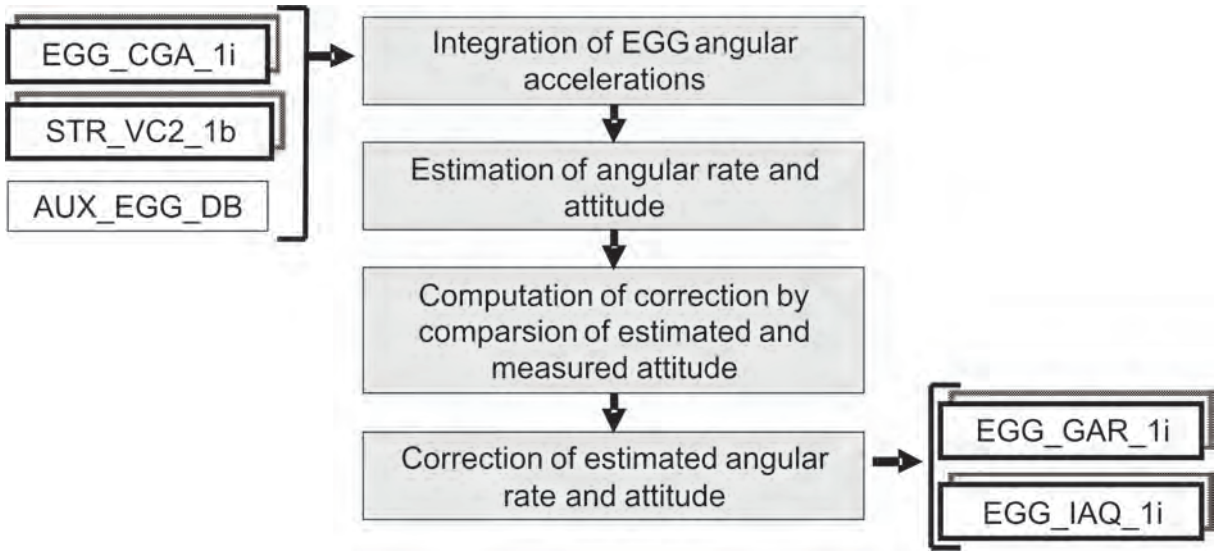

Figure 3.16.: Flowchart: Angular rate reconstruction.

To find the best possible combination of the two available sets of attitude information the error spectra of the corresponding measurement techniques are essential. The measurements of the gradiometer are highly accurate within its MB which is from 5 to 100 mHz and have increasing noise towards the lower frequencies. The star sensor measurements, in contrast, provide very accurately the absolute orientation in the respective SSRF. Hence, the combination of the attitude information is based on the following strategy, according to Cesare et al. (2008):

Inside the MB the best available measurements come from the gradiometer itself. Hence, the angular rates in the MB are obtained by integration of the gradiometer angular accelerations, Eqs. 2.47 to 2.49. For the very low frequencies the measurements from the star sensors are most accurate. To obtain angular rates from the STR quaternions, first a rotation from the SSRF into the GRF has to be carried out. This can be done using the known rotation matrices from SSRF to GRF, provided in file `AUX_EGG_DB`. Originally, the rotation matrices as determined on-ground have been used. After the first measurements of GOCE had become available, according to Strandberg (2010), a periodic difference between the differential accelerations modelled from the star sensors and from gradiometer had been found, which lead to a co-alignment between the three star sensors, using STR 1 as a reference. The results of this co-alignment have been used in the nominal L1b processing until September 2011. Since then, a new EGG processor version is utilized and, simultaneously, all EGG data from the previous measurement phases are re-processed. The improvements of the new EGG processor are described in Chapter 6 of this work. Also for the rotation matrices from SSRF to GRF new values are used. They are determined with the calibration method by Siemes et al. (2012), cf. Sect. 4.3.5, for each measurement phase. After the rotation from the SSRF into the GRF, the STR angular rates are obtained from the rotated quaternions by employing the Poisson equations (Cesare et al., 2008; Wittenburg, 1977), cf. Appendix B. The corresponding error spectrum is assumed to have a linear increase with frequency f.

In the original approach the equivalent hybridization frequency (i.e. for lower frequencies mainly STR data are used and for higher frequencies mainly EGG data) is below the MB and has different values for each axis. It was

found by Cesare et al. (2008) by comparison of the angular acceleration error spectrum, coming either from the gradiometer or from the star sensor. The error spectrum of the star sensor angular accelerations was obtained by deriving two times the error spectrum of the star sensor attitude information (cf. Appendix B).

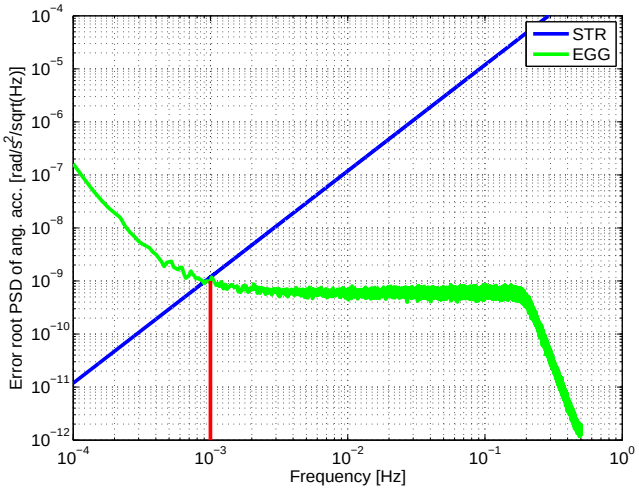

(a) X-direction

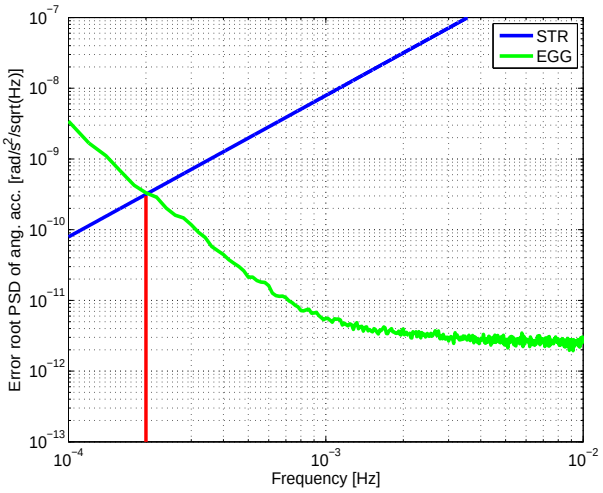

(b) Y-direction

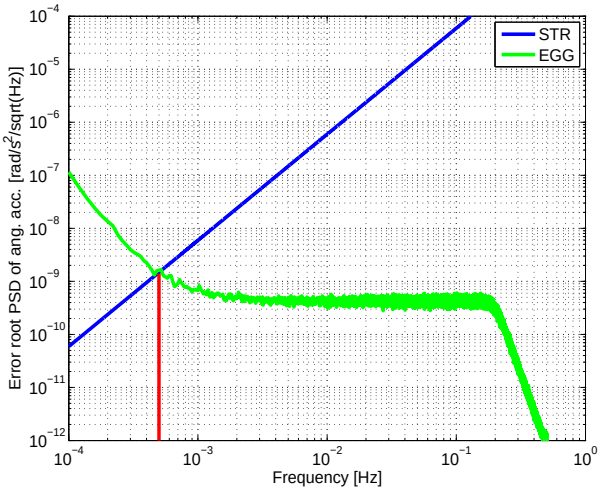

(c) Z-direction

Figure 3.17.: Concept of hybridization between STR and EGG measurements at the level of angular accelerations.

In Fig. 3.17 the concept of hybridization between STR and EGG measurements at the level of angular accelerations

is shown for all three components. The blue lines indicate the error root PSD of the STR angular accelerations from numerical simulation, whereas the green lines show the error root PSD of the EGG angular accelerations from simulation (including EGG noise only). The corresponding hybridization frequencies between the STR and the EGG error curves are highlighted in red. For the angular acceleration x-component the crossover takes place at about 1 mHz, for the y- and z-component it takes place at about 0.2 and 0.5 mHz, respectively.

Since the hybridization frequencies are well below the gradiometer MB, the angular rate within the MB can be reconstructed by numerical integration of the gradiometer angular accelerations. The star sensor measurements are used below the hybridization frequencies for the determination of the absolute angular rate (and attitude) values (i.e. for the DC part), to compensate the effects of the accelerometer drift with increasing noise towards the lower frequencies and to counteract the drift of the numerical integration of the gradiometer angular accelerations.

From a processing point of view, the angular rate reconstruction is performed by Kalman-filtering in the time domain (Cesare and Catastini, 2008b; Stummer et al., 2011). In principle, the method consists of a prediction step and a correction step, see Fig. 3.18 and cf. also the processing flowchart in Fig. 3.16.

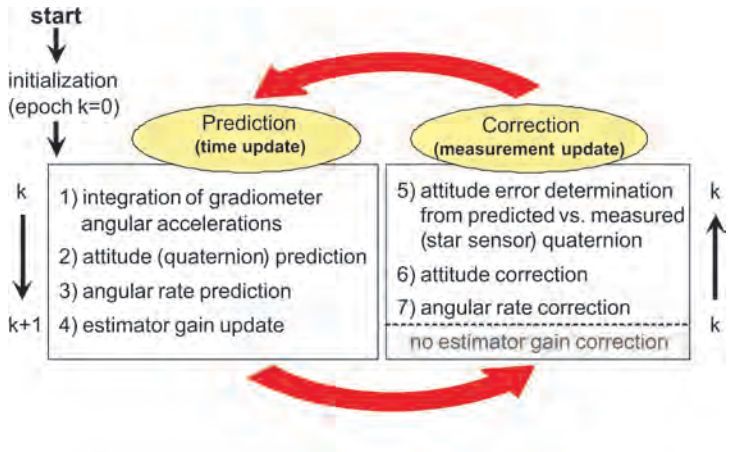

Figure 3.18.: Principle of Kalman-filtering for angular rate reconstruction.

The prediction starts with the computation of the one-step angular rate variation (between epochs k and $k+1$), which is obtained by interpolation (i.e. one-step integration) of the gradiometer angular accelerations, cf. Fig. 3.19. The integration is performed using a Lagrange interpolator with the four coefficients $c_{k=-1} = c_{k=+2} = -0.0417$ and $c_{k=0} = c_{k=1} = 0.5417$, according to Cesare et al. (2008). This means that for the computation of the angular rate variation between epochs k and $k+1$, the weighted sum of the gradiometer angular accelerations from epochs $k-1$ to $k+2$ is built.

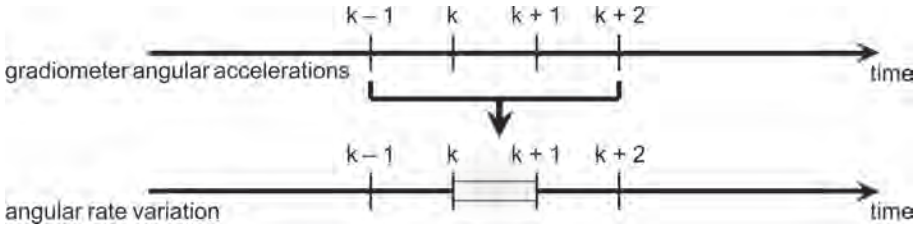

Figure 3.19.: Integration of gradiometer angular accelerations to derive the one-step angular rate variation.

The attitude quaternions of the next epoch $(k+1)$ are predicted by rotation of the attitude quaternions from the current epoch (k) to the next, using the one-step angular rate variation (between epochs k and $k+1$), according to Eq. B.21. Also the angular rates for the next epoch $(k+1)$ are predicted. Thus, for epoch $k+1$, besides the measured STR quaternion, also a predicted attitude quaternion is available. From the difference between these two sets of quaternions, the correction for the current attitude quaternion and angular rate is found. The gains of the estimator are derived from pre-launch measurement performance models of the gradiometer and the star sensor. Note that the estimator gains are not adapted to the current error behavior of the real GOCE data during the L1b processing. This is different from a classical Kalman filter approach, where also a correction of the estimator gains is foreseen. The transient of the Kalman filter is about half a day long. Hence, in the case that a re-initialization of the filters is necessary, like e.g. after a calibration phase, at least half a day of data is

lost. The new L1b implementation for the ARR, as derived in Sect. 6.2 is based on FIR (finite impulse response) filtering, where the used filters have a length of only 8401 seconds. In case of gaps, at least four times less data is lost with respect to the original implementation.

In the original processing scheme the measurements of only one star sensor, namely the one which is provided in the `STR_VC2_1b` product, are used within the ARR. In Sect. 6.4 it is shown that a combination of all simultaneously available star sensor data is possible and helps to improve the quality of several L1b products, like in particular the gravity gradients, cf. also Sect. 7.

In the following the data associated with the ARR are shown for the example day 11 November 2009. The two main input data sets are the calibrated gradiometer angular accelerations, as already discussed in the previous section with Fig. 3.15(a), and the star sensor attitude quaternions, as given in Fig. 3.20. As output the ARR provides merged inertial attitude quaternions (IAQ), cf. Fig. 3.21 and merged angular rates, cf. Fig. 3.22.

Fig. 3.20 shows the measured quaternions of star sensor 2, which are provided in the `STR_VC2_1b` files of 11 November 2009. q_0 denotes the scalar part of the quaternions. The values of the quaternions have to be within $\pm$ 1. In the time domain, Fig. 3.20(a), we observe a change in sign in all quaternion components, once per orbital revolution. Since quaternions have a sign ambiguity this change in sign has no impact on the contained attitude information. The reason for the change once per revolution is that the L1b data are provided in orbit-wise files. Hence, at every beginning of a new file the sign switch can happen. In Fig. 3.20(b) the root PSDs of the quaternions are given. Note that for the computation of the PSDs a continuous quaternion data set without sign changes has to be used. We observe an approximately continuous decay in magnitude up to a frequency of about 2 mHz, followed by an increase with its peak at about 4 mHz, and a further decay which is reached at about 50 mHz. For higher frequencies the root PSDs are approximately flat with a level of about $2 \cdot 10^{-5}$ rad/$\sqrt{\text{Hz}}$ for the components q_0 and q_2 and of about $3 \cdot 10^{-5}$ rad/$\sqrt{\text{Hz}}$ for q_1 and q_3. Further analyses of the GOCE star sensor data are made in Sect. 5.2.

In Fig. 3.21 the IAQs are shown. In the time domain, Fig. 3.21(a), we observe that these quaternions have no sign changes. They can be avoided within the original ARR implementation, because of a successive processing strategy. The corresponding root PSDs, Fig. 3.21(b), are at the low frequencies similar to the root PSDs of the star sensor quaternions in Fig. 3.20(b). For higher frequencies, where the two times integrated gradiometer angular accelerations are used, we observe a continuous decay in magnitude. The high frequencies of the star sensor only quaternions are dominated by noise, Fig. 3.20(b), whereas the root PSD of the IAQs follows (also) for high frequencies the expected behavior, cf. the root PSD of the simulated attitude quaternions in Fig. 2.5(b). In Sect. 6.3 an improved method for the determination of the IAQs is introduced, and further quality assessment is made.

The main output of the ARR are the merged angular rates, called gradiometer angular rates (GAR) in the L1b processing, as illustrated in Fig. 3.22, which should be of good quality for all frequencies. The mean angular velocity about the y-axis is about $1.2 \cdot 10^{-3}$ rad/s, Fig. 3.22(a), due to the rotation of the satellite about this axis once per revolution. ω_x and ω_z have a mean value of approximately zero and variations of up to about $1.2 \cdot 10^{-4}$ rad/s. In the corresponding root PSDs, Fig. 3.22(b), the x-component (blue) has the largest magnitude in the MB. The reason is again, as already pointed out for the calibrated gradiometer angular accelerations, which are the basis for the GAR in the high frequencies, the sensitivity of GOCE for rotations around its slight x-axis. For further analyses of the GAR see Sect. 5.1.

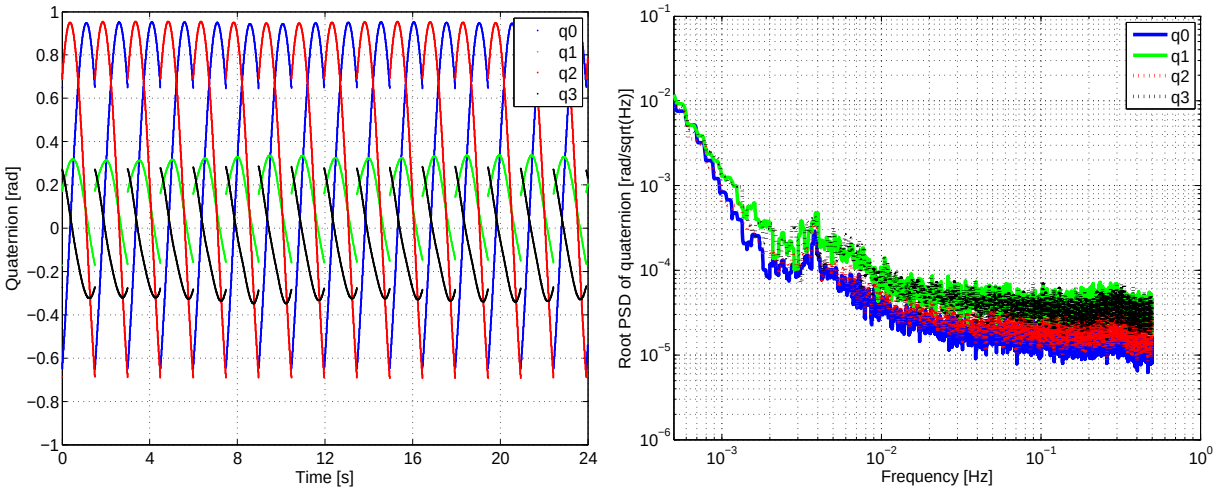

(a) (b)

Figure 3.20.: Star sensor attitude quaternions (a) and corresponding root PSD (b) of 11 November 2009.

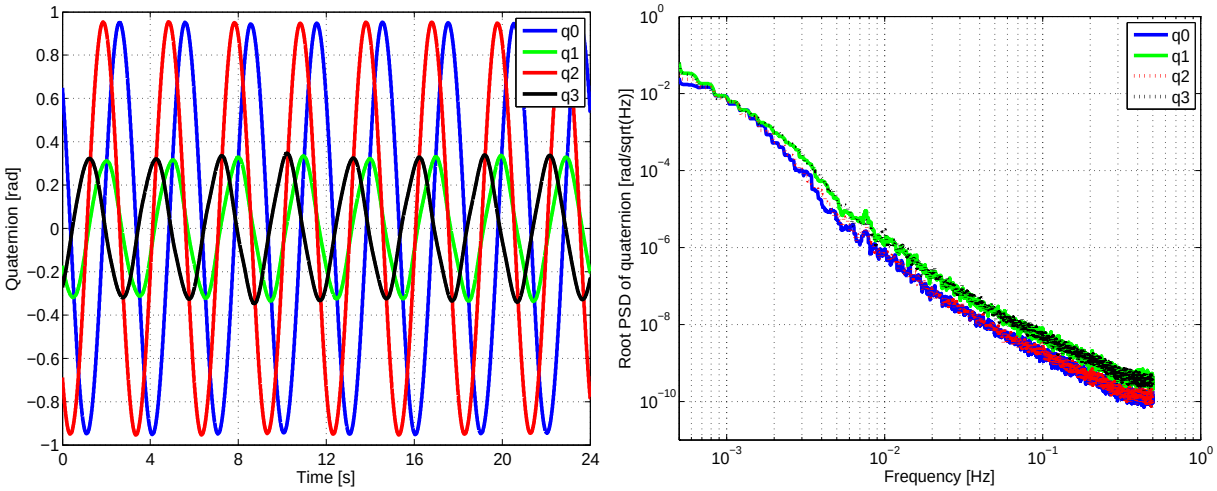

(a) (b)

Figure 3.21.: Merged inertial attitude quaternions (a) and corresponding root PSD (b) of 11 November 2009.

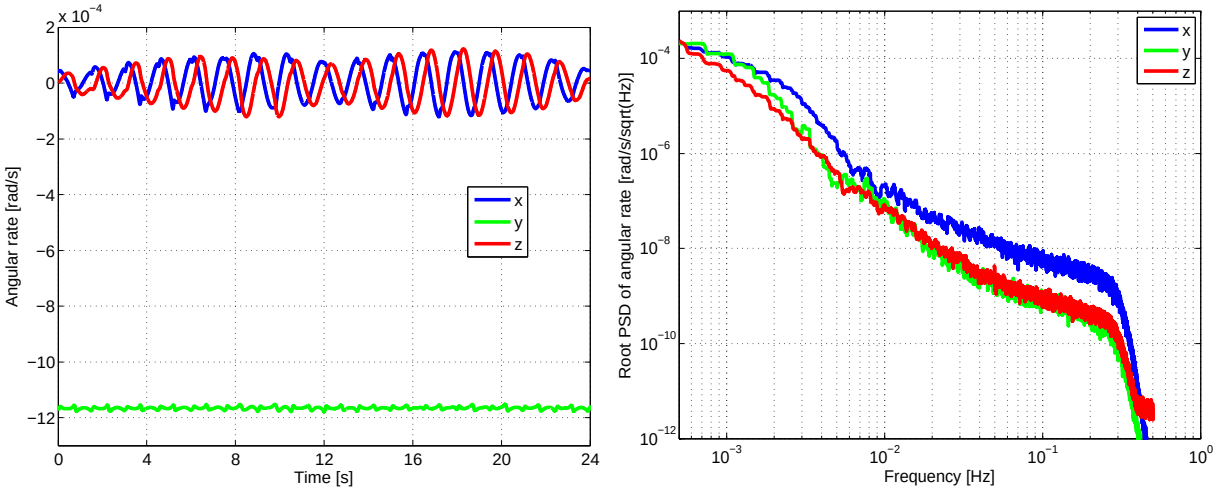

(a) (b)

Figure 3.22.: Merged angular rate (a) and corresponding root PSD (b) of 11 November 2009.

3.5. GGT computation

For the computation of the gravity gradients one further processing step is needed, cf. Fig. 3.23.

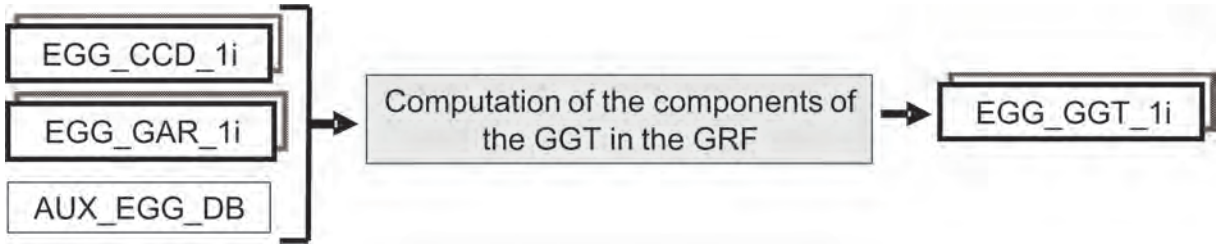

Figure 3.23.: Flowchart: GGT computation.

The gravity gradients (MDS `EGG_GGT_1i` in `EGG_NOM_1b` files) are the main product of the nominal gradiometer processing. They are obtained according to Eqs. 2.50 to 2.55 from the calibrated CM and DM accelerations (`EGG_CCD_1i`) by subtraction of the centrifugal part, which is expressed in the angular rate terms (`EGG_GAR_1i`).

For the example day 11 November 2009 the gravity gradients are given in Fig. 3.24 and their respective root PSDs in Fig. 3.25. The GGT components contain a bias with respect to the theoretical values, as shown in Sect. 2.4, Fig. 2.3. The bias is largest for the two less accurate elements V_{xy} and V_{yz}. The variation of the individual gravity gradients is about the same as for the reference data. Moreover, we observe a strong trend in V_{xy}, Fig. 3.24(d). The root PSDs of the main diagonal GGT components, Fig. 3.25(a), follow for the frequencies below about 30 mHz the expected behavior, cf. the root PSDs of the simulated gravity gradients in Fig. 2.4(a), with V_{yy} being the smallest component. For frequencies higher than about 30 mHz and lower than about 0.2 Hz the root PSDs are approximately flat, with a level of about 10 mE/$\sqrt{\text{Hz}}$ for V_{xx} and V_{yy} and about 20 mE/$\sqrt{\text{Hz}}$ for V_{zz}. The root PSDs of V_{xy}, V_{xz} and V_{yz} are given in Fig. 3.25(b). V_{xy} is the smallest component at the low frequencies, which is in accordance with expectations, cf. the simulated gravity gradients in Fig. 2.4(b). The two less sensitive components, V_{xy} and V_{yz}, have a flat noise level of about 0.6 and 0.8 E/$\sqrt{\text{Hz}}$. V_{xz}, which is a very accurate component, is similar to the (very accurate) main diagonal GGT components also flat for the frequencies higher than about 30 mHz with a magnitude of about 10 mE/$\sqrt{\text{Hz}}$. The quality of the gravity gradients, as measured with GOCE is further analyzed in Sect. 5.1.

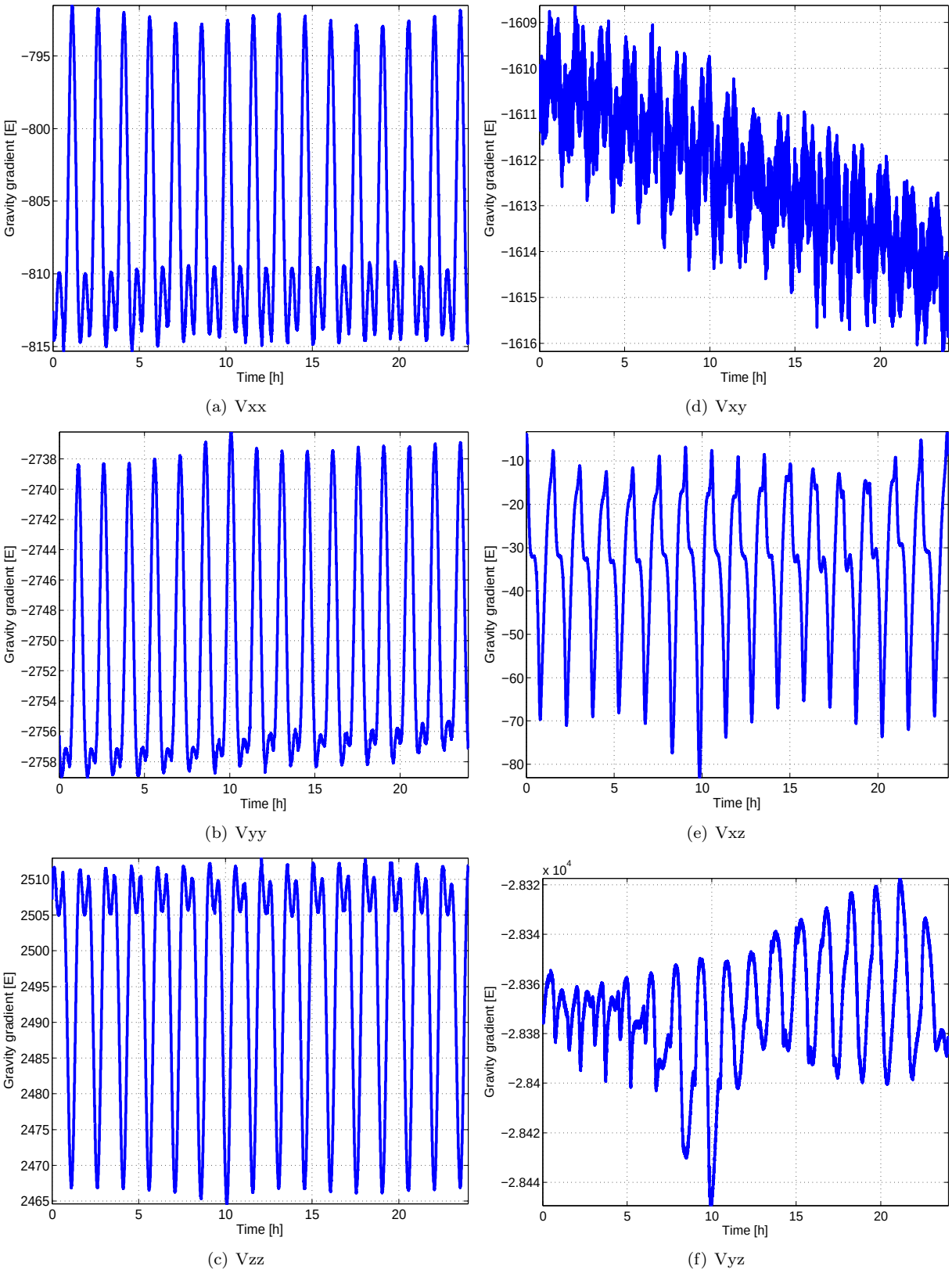

(a) Vxx (d) Vxy

(b) Vyy (e) Vxz

(c) Vzz (f) Vyz

Figure 3.24.: Main diagonal elements of gravity gradients (left) and off-diagonal elements (right) of 11 November 2009.

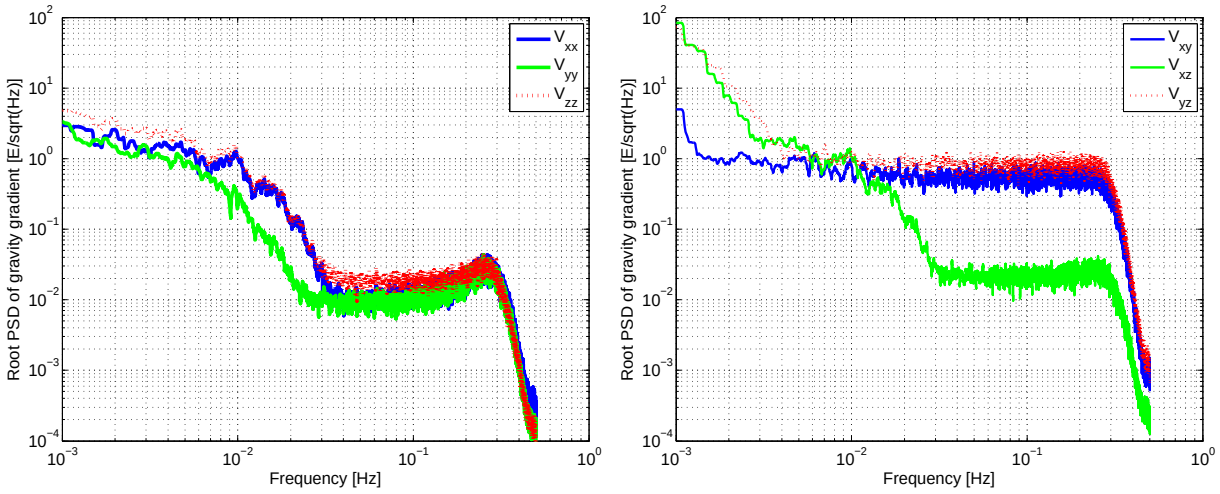

(a) (b)

Figure 3.25.: PSD of main diagonal elements of gravity gradients (a) and off-diagonal elements (b) of 11 November 2009.

3.6. Transformation matrix

After the calculation of the gravity gradients, one more data set for the `EGG_NOM_1b` files is computed, the transformation matrix from GRF to IRF, see Fig. 3.26.

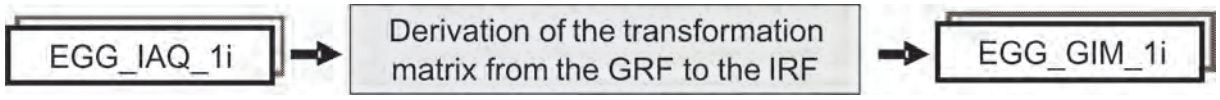

Figure 3.26.: Flowchart: Transformation matrix from GRF to IRF.

The transformation matrix from GRF to IRF (`EGG_GIM_1i`) can be obtained for every epoch from the inertial attitude quaternions (`EGG_IAQ_1i`), which are computed within the angular rate reconstruction (cf. Sect. 3.4), according to Eq. B.20, without any further auxiliary input.

3.7. Monitoring

Several tests are performed to assure the data quality, cf. Fig. 3.27.

Already at the level of voltages (control voltages in `EGG_CTR_1i`, polarization and detection voltages in `EGG_POL_1i`) the values can be compared to a corresponding threshold, which has been determined empirically and which is contained in the auxiliary data file (`AUX_EGG_DB`). Also the accelerations (the nominal linear accelerations in `EGG_NLA_1i`, the nominal CM and DM accelerations in `EGG_NCD_1i`, and the difference between the nominal and the calibrated gradiometer angular accelerations in `EGG_NGA_1i` and `EGG_CGA_1i`) can be compared to related thresholds. Moreover, the trace of the GGT is computed. It is used in a separate processor (not further discussed here) for the monitoring of the GGT trace on a daily basis by comparing it to a corresponding threshold. If during one of the described tests a threshold is breached, the corresponding epochs will be reported in the monitoring file `EGG_MON_1b`.

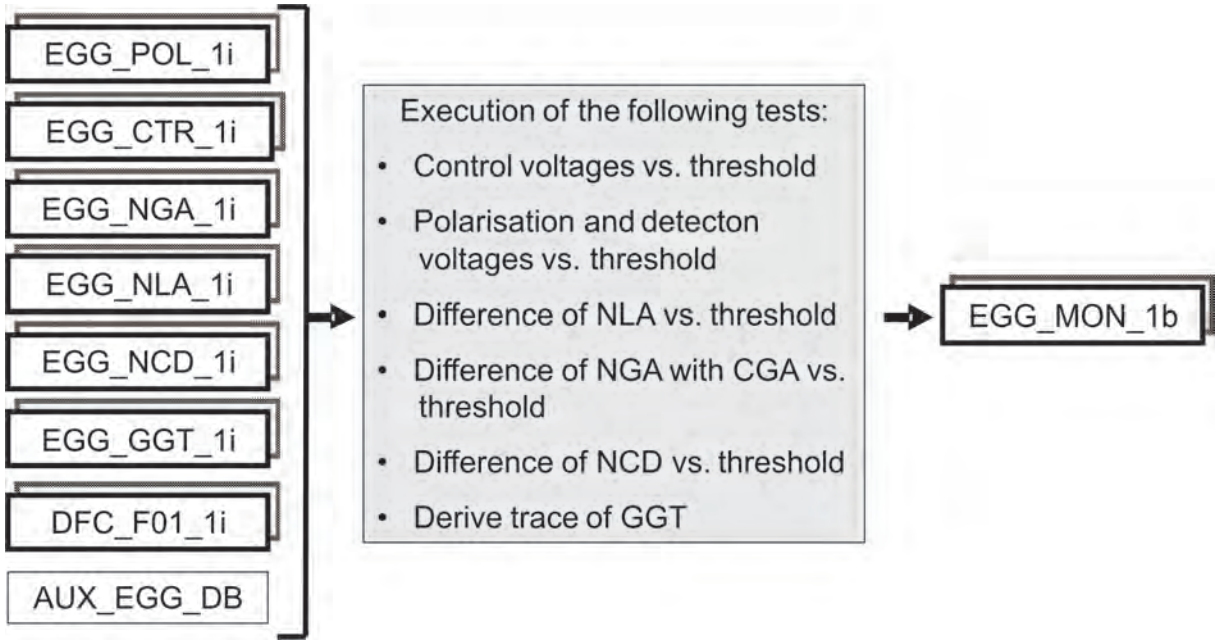

Figure 3.27.: Flowchart: Monitoring.

3.8. Level 1b gradiometer and star sensor data product overview

Table 3.2 gives an overview of the measurement data sets contained in the main gradiometer product `EGG_NOM_1b`. Since star sensor data play an important role in the gradiometer processing, an overview of the main star sensor products is given in Table 3.3. Note that the entry of a third star sensor (`STR2_VC3_1i`) in the `STR_VC3_1b` product is optional, i.e. it is possible that a `STR_VC3_1b` product contains only the data from one star sensor (`STR_VC3_1i`).

Table 3.2.: Content of main Level 1b gradiometer product.

product	MDS	description
`EGG_NOM_1b`	`EGG_TCT_1i`	time correlation table
	`EGG_CTR_1i`	gradiometer control voltages
	`EGG_NLA_1i`	uncalibrated linear/angular accelerations
	`EGG_NCD_1i`	uncalibrated common/differential accelerations
	`EGG_NGA_1i`	uncalibrated gradiometer angular accelerations
	`EGG_CCV_1i`	corrected control voltages
	`EGG_CCD_1i`	calibrated common/differential accelerations
	`EGG_CGA_1i`	calibrated gradiometer angular accelerations
	`EGG_GAR_1i`	gradiometer angular rates
	`EGG_IAQ_1i`	inertial attitude quaternions
	`EGG_GGT_1i`	gravity gradient tensor in GRF
	`EGG_GIM_1i`	rotation matrix from GRF to IRF

Table 3.3.: Content of main Level 1b star sensor products.

product	MDS	description
`STR_VC2_1b`	`STR_TCT_1i`	time correlation table
	`STR_VC2_1i`	quaternions in SSRF from first star sensor
`STR_VC3_1b`	`STR_TCT_1i`	time correlation table
	`STR_VC3_1i`	quaternions in SSRF from second star sensor
	`STR2_VC3_1i`	quaternions in SSRF from third star sensor

4. Calibration of the gradiometer

In this chapter the calibration of the gradiometer is described. The accurate calibration of the gradiometer is a pre-requisite for achieving the mission objectives (Siemes et al., 2012).

Several gradiometer imperfections have to be considered. The two main types of imperfections for the GOCE gradiometer are the so-called quadratic factors, which represent non-linearities in the accelerometer transfer functions, and the so-called inverse calibration matrices (ICMs), which account for accelerometer scale factor errors, misalignments and non-orthogonalities.

The calibration must be performed in-flight, because the gradiometer is designed to operate under micro-g conditions (Siemes et al., 2012). Nevertheless, there are also some calibration activities which already take place on-ground. They are mainly to verify the feasibility of the calibration methods and to verify that the upper limits for some of the calibration parameters have not been exceeded (Cesare and Catastini, 2008a). The on-ground calibration takes place on a special pendulum bench and cannot be performed for all of the calibration parameters due to the on-ground $(1 \cdot g)$ environment.

The calibration methods can be distinguished between internal (in-flight) and external, cf. Siemes et al. (2012). The internal methods make only use of data, which are collected by on-board sensors of GOCE. This is mainly the gradiometer and the star sensors. The external methods make use of additional data. E.g. Rispens and Bouman (2009) and Visser (2008) make use of global gravity field models to estimate calibration parameters for the accelerometer data. Bouman et al. (2004) use global gravity field models and terrestrial gravity data for estimating calibration parameters for the gravity gradients. For an overview of the existing calibration methods it is referred to Bouman (2008).

This chapter is confined to the internal calibration methods. Two approaches are discussed in detail. The first one is the original method as defined by industry, which is referred to as TAS (Thales Alenia Space) method (Cesare et al., 2008). An independent implementation of the TAS method has been developed here. Results are shown in Sects. 5.1.4 and 5.2.3. The second one is the so-called ESA-L method. The "L" in the name is referring to its inventor Daniel Lamarre. It is the baseline method for the current gradiometer processing (Lamarre, 2008). Corresponding calibration results are shown in Sect. 5.1.4. A third method is addressed in Sect. 6.5. It is based on an independent approach by Michael Kern (Kern et al., 2007) and has been refined by Christian Siemes (Siemes et al., 2012). Within this work it is referred to as ESA-S method. The method can be used for validation and correction of other calibration results, see again Sect. 6.5. For a definition of the terms calibration and validation in this context, it is referred to Drinkwater (2005).

The errors affecting the measurement of the gravity gradients can be grouped into four categories (Cesare, 2008). 1) The instrument errors, which depend only on the gradiometer elements, 2) instrument-satellite coupling errors, depending on the interaction of the gradiometer and the satellite and mission environment, 3) the satellite errors, which depend on the satellite performance only (gradiometer excluded) and 4) the processing errors, related to the transformation of the Level 0 to Level 1b products. An analysis of the main error sources related to the measurement of the GGT can also be found in Müller (2001).

The dominant part of the instrument errors is the accelerometer noise. In Sect. 5.1 the actual accelerometer noise is analyzed and compared to the pre-launch expectations. The largest portion of the instrument-satellite coupling errors is due to the coupling of non-gravitational linear accelerations acting on the satellite's COM with the in-line differential mode accelerations, which contain the main diagonal gravity gradient signal. (This refers to certain elements of the ICMs, as explained below.) In Sect. 5.1.4 performance analyses of the GOCE data are made which indicate that this coupling exceeds partially the expected limits, which leads to a degraded quality of the gravity gradients and which is taken into account in the new processing strategies (see Chapter 6). As main satellite error the satellite self-gravity is considered. It is the acceleration produced by the masses of the platform (without gradiometer). The main processing errors are due to the recovery of the angular rates (ARR), which is in the MB mainly based on the gradiometer angular accelerations and for the low frequencies mainly on the star sensor data (cf. Sect. 3.4), i.e. the accuracy of the reconstructed angular rates is in the MB limited by the accuracy of the gradiometer angular accelerations. Additionally, errors due to a not optimal combination of the two available attitude data sets (from gradiometer and star sensor) can occur. In Sect. 6.2 the quality of the angular rates is analyzed and an alternative ARR method is introduced, which reduces the processing errors.

4.1. Definition of the gradiometer calibration parameters

In this section the gradiometer calibration parameters, as introduced by Cesare (2008) for the original TAS calibration approach, are defined. The main imperfections of an accelerometer within the GOCE gradiometer, which have to be taken into account, are:

(a) scale factor error

(b) misalignment

(c) coupling (non-orthogonality)

(d) quadratic factor

(e) bias

(f) noise

In the following the calibration parameters corresponding to the above imperfections are defined.

(a) Scale factors

The scale of an accelerometer A_i in direction k is not perfectly 1, but deviates by a small value $K_{i,k}$, cf. Fig. 4.1(a). A measured acceleration $a'_{i,k}$ can thus be obtained by

$$a'_{i,k} = (1 + K_{i,k})\, a_{i,k}. \tag{4.1}$$

The corresponding scale factor matrix is defined as

$$\underline{K}_i = \begin{pmatrix} 1+K_{i,x} & 0 & 0 \\ 0 & 1+K_{i,y} & 0 \\ 0 & 0 & 1+K_{i,z} \end{pmatrix} = \underline{I} + \begin{pmatrix} K_{i,X} & 0 & 0 \\ 0 & K_{i,Y} & 0 \\ 0 & 0 & K_{i,Z} \end{pmatrix} = \underline{I}_3 + \underline{dK}_i \tag{4.2}$$

with $\underline{I}_3$ being the 3×3 identity matrix.

(b) Misalignment

A rotational deviation of an accelerometer i from its nominal orientation is called misalignment, cf. Fig. 4.1(b). It can be written, using the small angle approximation, as

$$\underline{R}_i = \begin{pmatrix} 1 & \psi_i & -\theta_i \\ -\psi_i & 1 & \varphi_i \\ \theta_i & -\varphi_i & 1 \end{pmatrix} = \underline{I}_3 + \begin{pmatrix} 0 & \psi_i & -\theta_i \\ -\psi_i & 0 & \varphi_i \\ \theta_i & -\varphi_i & 0 \end{pmatrix} = \underline{I}_3 + \underline{dR}_i. \tag{4.3}$$

(c) Coupling

If the axes of an accelerometer A_i are not perfectly perpendicular to each other, their measurements are coupled, cf. Fig. 4.1(c). The corresponding coupling matrix, for small deviations from orthogonality, is defined as

$$\underline{S}_i = \begin{pmatrix} 1 & \varepsilon_i & \eta_i \\ \varepsilon_i & 1 & \varsigma_i \\ \eta_i & \varsigma_i & 1 \end{pmatrix} = \underline{I}_3 + \begin{pmatrix} 0 & \varepsilon_i & \eta_i \\ \varepsilon_i & 0 & \varsigma_i \\ \eta_i & \varsigma_i & 0 \end{pmatrix} = \underline{I}_3 + \underline{dS}_i \tag{4.4}$$

(d) Quadratic factors

A quadratic factor represents a (second order) non-linear term in the control loop of an accelerometer. It is the non-linearity in the transfer function $\mathbf{G}$ which transforms the measured voltages back into accelerations, cf. Sect. 4.2. The measured acceleration $a'_{i,k}$ of accelerometer A_i in direction k can be expressed as

$$a'_{i,k} = K2_{i,k} \cdot a^2_{i,k} \tag{4.5}$$

with

$$\underline{K2}_i = \begin{pmatrix} K2_{i,X} & 0 & 0 \\ 0 & K2_{i,Y} & 0 \\ 0 & 0 & K2_{i,Z} \end{pmatrix} \tag{4.6}$$

being the so-called quadratic factor matrix.

(e) Accelerometer bias

Each accelerometer axis measures an unknown bias. The corresponding bias vector for accelerometer A_i is defined as

$$\overline{b}_i = \begin{pmatrix} b_{i,X} \\ b_{i,Y} \\ b_{i,Z} \end{pmatrix} \tag{4.7}$$

(f) Accelerometer noise

Along each accelerometer axis colored noise is measured. The noise vector for accelerometer A_i reads

$$\overline{n}_i = \begin{pmatrix} n_{i,X} \\ n_{i,Y} \\ n_{i,Z} \end{pmatrix} \tag{4.8}$$

Figure 4.1 illustrates the gradiometric imperfections (a) to (c) on the example of gradiometer arm 14. In this example, accelerometer A_1 is assumed to be perfect, whereas A_4 either has scale factors deviating from 1 along the x and y-axes, Fig. 4.1(a), is rotated from its nominal position about the z-axis, Fig. 4.1(b), or its x and y-axes are not perfectly perpendicular to each other, Fig. 4.1(c).

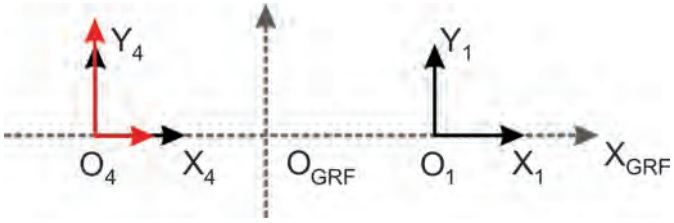

(a) Scale factor error

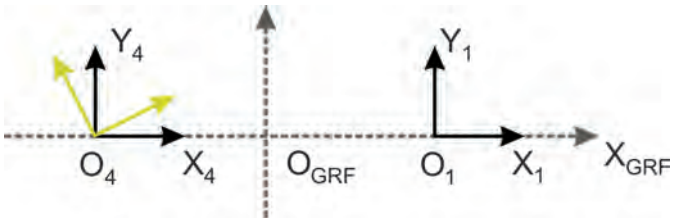

(b) Misalignment

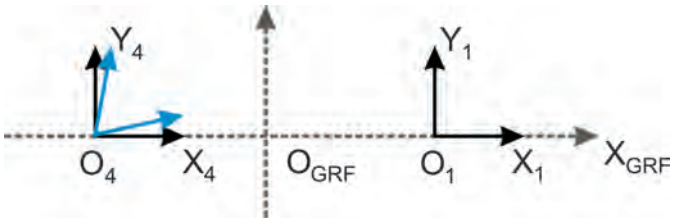

(c) Non-orthogonality

Figure 4.1.: Possible gradiometric imperfections shown for the x- and y-axes of accelerometer A_4, (a) scale factor error, i.e. deviation of the scale factor from 1, (b) misalignment, and (c) non-orthogonality.

The basic equation including all the above defined calibration parameters for the gradiometer imperfections can be written as

$$\begin{aligned} \overline{a}_i' &= (\underline{I}_3 + \underline{dK}_i) \cdot (\underline{I}_3 + \underline{dR}_i) \cdot (\underline{I}_3 + \underline{dS}_i) \cdot \overline{a}_i + \underline{K2}_i \cdot \overline{a}_i^2 + \overline{b}_i + \overline{n}_i \\ &\approx (\underline{I}_3 + \underline{dK}_i + \underline{dR}_i + \underline{dS}_i) \cdot \overline{a}_i + \underline{K2}_i \cdot \overline{a}_i^2 + \overline{b}_i + \overline{n}_i \\ \overline{a}_i' &= (\underline{K}_i + \underline{dR}_i + \underline{dS}_i) \cdot \overline{a}_i + \underline{K2}_i \cdot \overline{a}_i^2 + \overline{b}_i + \overline{n}_i \end{aligned} \tag{4.9}$$

For the nominal TAS calibration method not the absolute gradiometer calibration parameters for the individual accelerometers are used, but their so-called common and differential values between the two accelerometers on each

of the three gradiometer arms. They are defined, in analogy to the common and differential mode accelerations, e.g. for the common misalignment angle of accelerometer pair ij about the x-axis, as

$\varphi_{c,ij} = \frac{1}{2}(\varphi_i + \varphi_j)$, and respectively for the differential part as $\varphi_{d,ij} = \frac{1}{2}(\varphi_i - \varphi_j)$.

For the basic measurement equation containing all above gradiometer imperfections we get

$$\begin{pmatrix} \overline{a}'_{c,ij} \\ \overline{a}'_{d,ij} \end{pmatrix} = \underline{M}_{ij} \begin{pmatrix} \overline{a}_{c,ij} \\ \overline{a}_{d,ij} \end{pmatrix} + \frac{1}{2}\underline{K2}_{ij} \begin{pmatrix} (\overline{a}_{c,ij} + \overline{a}_{d,ij})^2 \\ (\overline{a}_{c,ij} - \overline{a}_{d,ij})^2 \end{pmatrix} + \begin{pmatrix} \overline{b}_{c,ij} \\ \overline{b}_{d,ij} \end{pmatrix} + \begin{pmatrix} \overline{n}_{c,ij} \\ \overline{n}_{d,ij} \end{pmatrix} \tag{4.10}$$

with

$$\underline{M}_{ij} = \begin{pmatrix} 1+K_{c,ij,X} & \psi_{c,ij}+\varepsilon_{c,ij} & -\theta_{c,ij}+\eta_{c,ij} & K_{d,ij,X} & \psi_{d,ij}+\varepsilon_{d,ij} & -\theta_{d,ij}+\eta_{d,ij} \\ -\psi_{c,ij}+\varepsilon_{c,ij} & 1+K_{c,ij,Y} & \varphi_{c,ij}+\varsigma_{c,ij} & -\psi_{d,ij}+\varepsilon_{d,ij} & K_{d,ij,Y} & \varphi_{d,ij}+\varsigma_{d,ij} \\ \theta_{c,ij}+\eta_{c,ij} & -\varphi_{c,ij}+\varsigma_{c,ij} & 1+K_{c,ij,Z} & \theta_{d,ij}+\eta_{d,ij} & -\varphi_{d,ij}+\varsigma_{d,ij} & K_{d,ij,Z} \\ K_{d,ij,X} & \psi_{d,ij}+\varepsilon_{d,ij} & -\theta_{d,ij}+\eta_{d,ij} & 1+K_{c,ij,X} & \psi_{c,ij}+\varepsilon_{c,ij} & -\theta_{c,ij}+\eta_{c,ij} \\ -\psi_{d,ij}+\varepsilon_{d,ij} & K_{d,ij,Y} & \varphi_{d,ij}+\varsigma_{d,ij} & -\psi_{c,ij}+\varepsilon_{c,ij} & 1+K_{c,ij,Y} & \varphi_{c,ij}+\varsigma_{c,ij} \\ \theta_{d,ij}+\eta_{d,ij} & -\varphi_{d,ij}+\varsigma_{d,ij} & K_{d,ij,Z} & \theta_{c,ij}+\eta_{c,ij} & -\varphi_{c,ij}+\varsigma_{c,ij} & 1+K_{c,ij,Z} \end{pmatrix} \tag{4.11}$$

and

$$\underline{K2}_{ij} = \begin{pmatrix} K2_{c,ij,X}+K2_{d,ij,X} & 0 & 0 \\ 0 & K2_{c,ij,Y}+K2_{d,ij,Y} & 0 \\ 0 & 0 & K2_{c,ij,Z}+K2_{d,ij,Z} \\ K2_{c,ij,X}+K2_{d,ij,X} & 0 & 0 \\ 0 & K2_{c,ij,Y}+K2_{d,ij,Y} & 0 \\ 0 & 0 & K2_{c,ij,Z}+K2_{d,ij,Z} \end{pmatrix} \quad ... \tag{4.12}$$

$$\begin{pmatrix} K2_{c,ij,X}-K2_{d,ij,X} & 0 & 0 \\ 0 & K2_{c,ij,Y}-K2_{d,ij,Y} & 0 \\ 0 & 0 & K2_{c,ij,Z}-K2_{d,ij,Z} \\ K2_{c,ij,X}-K2_{d,ij,X} & 0 & 0 \\ 0 & K2_{c,ij,Y}-K2_{d,ij,Y} & 0 \\ 0 & 0 & K2_{c,ij,Z}-K2_{d,ij,Z} \end{pmatrix},$$

$$\begin{pmatrix} (\overline{a}_{c,ij} + \overline{a}_{d,ij})^2 \\ (\overline{a}_{c,ij} - \overline{a}_{d,ij})^2 \end{pmatrix} = \begin{pmatrix} (a_{c,ij,X} + a_{d,ij,X})^2 \\ (a_{c,ij,Y} + a_{d,ij,Y})^2 \\ (a_{c,ij,Z} + a_{d,ij,Z})^2 \\ (a_{c,ij,X} - a_{d,ij,X})^2 \\ (a_{c,ij,Y} - a_{d,ij,Y})^2 \\ (a_{c,ij,Z} - a_{d,ij,Z})^2 \end{pmatrix}, \tag{4.13}$$

$$\frac{1}{2}\underline{K2}_{ij} \begin{pmatrix} (\overline{a}_{c,ij} + \overline{a}_{d,ij})^2 \\ (\overline{a}_{c,ij} - \overline{a}_{d,ij})^2 \end{pmatrix} = \begin{pmatrix} K2_{c,ij,X}\left(a_{c,ij,X}^2 + a_{d,ij,X}^2\right) + 2K2_{d,ij,X}a_{c,ij,X}a_{d,ij,X} \\ K2_{c,ij,Y}\left(a_{c,ij,Y}^2 + a_{d,ij,Y}^2\right) + 2K2_{d,ij,Y}a_{c,ij,Y}a_{d,ij,Y} \\ K2_{c,ij,Z}\left(a_{c,ij,Z}^2 + a_{d,ij,Z}^2\right) + 2K2_{d,ij,Z}a_{c,ij,Z}a_{d,ij,Z} \\ K2_{c,ij,X}\left(a_{c,ij,X}^2 + a_{d,ij,X}^2\right) + 2K2_{d,ij,X}a_{c,ij,X}a_{d,ij,X} \\ K2_{c,ij,Y}\left(a_{c,ij,Y}^2 + a_{d,ij,Y}^2\right) + 2K2_{d,ij,Y}a_{c,ij,Y}a_{d,ij,Y} \\ K2_{c,ij,Z}\left(a_{c,ij,Z}^2 + a_{d,ij,Z}^2\right) + 2K2_{d,ij,Z}a_{c,ij,Z}a_{d,ij,Z} \end{pmatrix}. \tag{4.14}$$

By inverting the relationship 4.10 and thereby neglecting bias, noise and the quadratic term, which is assumed to be already taken care of, the true differential mode accelerations, from which the gravity gradients are computed, can be derived from the measured ones by

$$\begin{pmatrix} \overline{a}_{c,ij} \\ \overline{a}_{d,ij} \end{pmatrix} = \underline{M}_{ij}^{-1} \begin{pmatrix} \overline{a}'_{c,ij} \\ \overline{a}'_{d,ij} \end{pmatrix}. \tag{4.15}$$

This equation is used within the L1b processing, cf. Sect. 3.3 for the correction of the measured common and differential accelerations with the ICMs being $\underline{M}_{ij}^{-1}$.

The quadratic factors are physically adjusted beforehand, as explained in the next section.

4.2. Quadratic factor calibration

The physical origin of the quadratic factors is explained in Lamarre (2007). Figure 4.2 is a simplified view of a control loop of one degree of freedom (along one direction k) of one accelerometer A_i.

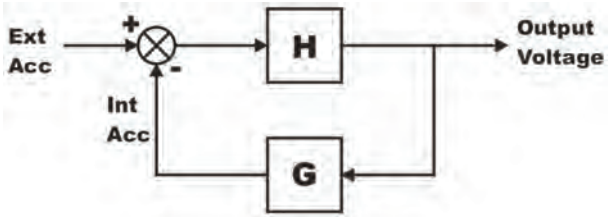

Figure 4.2.: Control loop of one accelerometer. Source: Lamarre (2007).

The feedback loop has a forward transfer function **H**, which converts accelerations acting on the proof mass to voltages, and it has a backward transfer function **G** from voltages to accelerations, which is called electrostatic gain. In a perfect control loop were all elements are linear, an external acceleration acting on the proof mass would be transformed into voltages (via **H**) and back into accelerations (via **G**) without loss of information, and the proof mass would be put back correctly to its original position. In reality there is significant non-linearity present in the electrostatic gain **G**. This non-linearity, or second order term in **G**, is the sought-after parameter, the quadratic factor $K2_{i,k}$ or shortly $K2$.

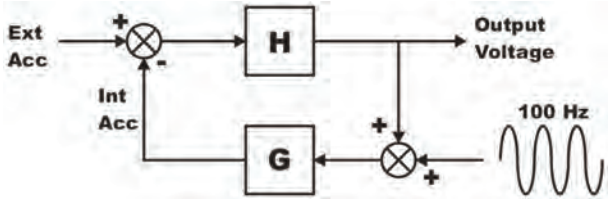

Figure 4.3.: Control loop of one accelerometer with injection of the calibration signal. Source: Lamarre (2007).

The measurement of the quadratic factors is based on the injection of a high frequency signal into the loop, compare Fig. 4.3. The bandwidth of the loop only extends up to 10 Hz, whereas the bandwidth of **G** itself is much wider and goes up to 1 kHz. In case of a linear transfer function **G** a high frequency (f_e = 100 Hz) sinusoidal calibration signal is not significantly attenuated by **G** and the calibration signal should not change the output. If **G** has a significant quadratic factor, as in reality, the calibration signal

$u_e = A_e sin(2\pi f_e t)$

is squared. With the relationship $sin(x)^2 = \frac{1}{2}(1 - cos(2x))$ the squared signal transmitted via **G** can be written as

$u_e^2 = K2 \cdot A_e^2 sin(2\pi f_e t)^2 = K2 \cdot A_e^2 \cdot \frac{1}{2}(1 - cos(2 \cdot 2\pi f_e t)) = \frac{1}{2}K2 \cdot A_e^2 - \frac{1}{2}K2 \cdot A_e^2 \cdot cos(2 \cdot 2\pi f_e t))$.

Thus the non-linear transfer function **G** not only transmits the 100 Hz calibration signal but also generates a harmonic cosine signal at $2 \cdot f_e$ = 200 Hz and an offset with half of the squared amplitude.

This shall be illustrated in the following with a simple example, cf. Fig. 4.4, where a quadratic factor of 1 is assumed. The original sine signal has an amplitude of 1 and a wavelength of 3 seconds. The corresponding squared signal consists of a cosine signal with half of the wavelength (1.5 seconds) and half of the squared amplitude (0.5), and an additional offset with half of the squared amplitude (0.5).

For the quadratic factor calibration with GOCE, the 100 Hz and the 200 Hz signals are filtered by the transfer function **H** of the loop, whereas the offset appears in the output voltages with an amplitude A_{sw} which is proportional to the quadratic factor

$A_{sw} = C\frac{A_e^2}{2}K2$.

With C being a correction factor that depends on the accelerometer output channel from which the measured acceleration is taken. C can be assumed to be known here.

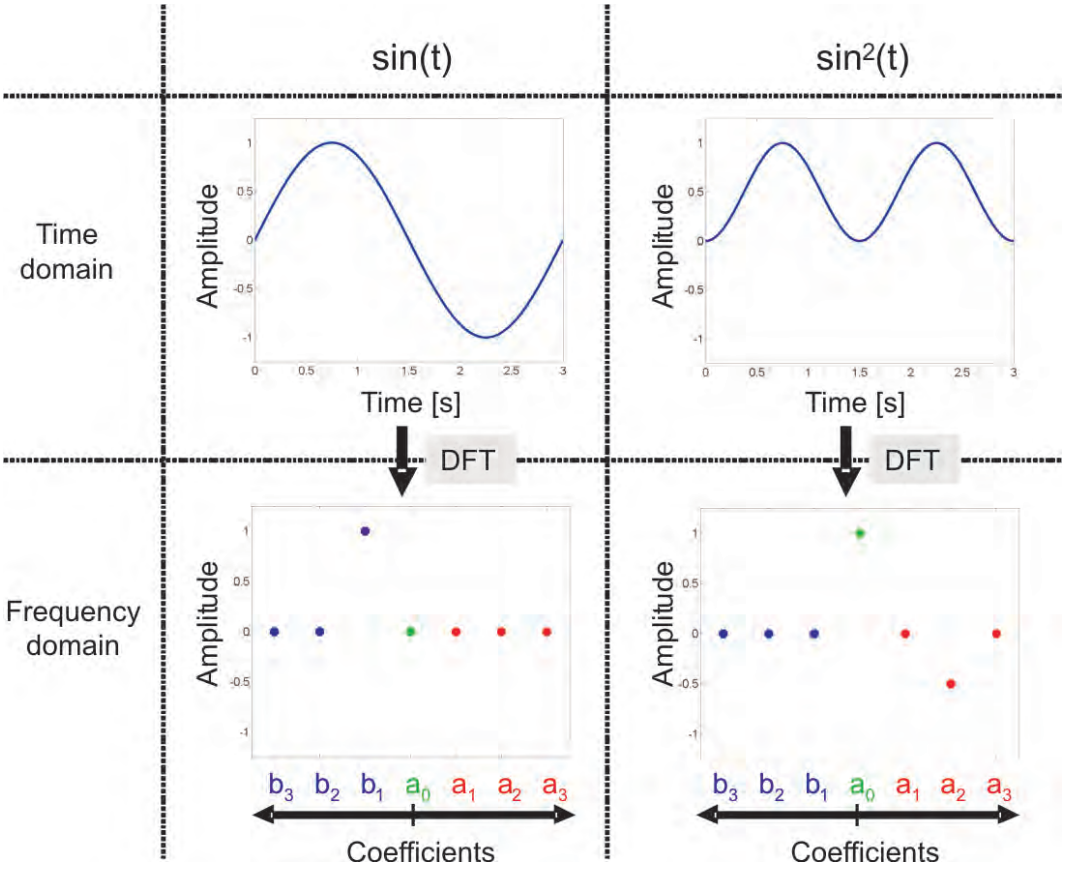

Figure 4.4.: Example for sine signal with wavelength of 3 seconds and amplitude of 1 (left) and its square (right). The upper two plots show the signals in the time domain; the lower two plots illustrate to corresponding coefficients c_k, at order k (with $a_{k=1,2,\ldots,N-1}$ being the cosine coefficients, $b_{k=1,\ldots,N-1}$ being the sine coefficients, and $a_{k=0}/2$ being the DC term) of a Digital Fourier Transformation (DFT) in the frequency domain. The squared sine signal in time domain (upper right plot) is composed of a harmonic cosine signal with wavelength of 1.5 seconds (and amplitude of 0.5) and an offset with amplitude of 0.5. In the frequency domain (lower right plot) the cosine signal with wavelength of 1.5 seconds is represented by the cosine coefficient $a_{k=2}$ with amplitude of 0.5. The offset is represented by $a_{k=0}/2$, being 1/2.

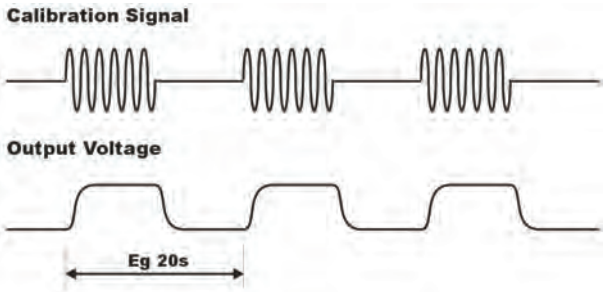

Figure 4.5.: Calibration pulse train and offset in output signal. Source: Lamarre (2007).

For the measurement of the quadratic factor a train of pulses is sent, with a pulse rate T_{sw} (e.g. 20 seconds) that lies in the MB, as shown in Fig. 4.5. The modulated offset with amplitude A_{sw} is then synchronously detected in the output voltages and has a corresponding frequency f_{sw} (e.g. 50 mHz).

The quadratic factor measurement and adjustment has to be done in-flight, i.e. during the mission. Nevertheless, there is also need for an on-ground calibration of the quadratic factors, to verify in general the feasibility of the quadratic factor adjustment by proof mass displacement and to measure the "by-construction" values of the accelerometer quadratic factors along the ultra-sensitive axes.

According to Cesare (2008) the limits under which the quadratic factors have to be reduced during the in-flight calibration process are:

- for US in-line axes: differential part 3 s^2/m; common part 6 s^2/m (or 9 s^2/m for accelerometer pair 14),

- for US transversal axes: differential and common part 9 s^2/m
- not needed for LS transversal axes: OAG14 y, OAG25 z, OAG36 y

In Frommknecht et al. (2011) it is documented that the quadratic factor calibration has been successfully performed, which means that all quadratic factors are adequately compensated.

4.3. ICM calibration

In this section the ICM calibration is illustrated. First, the calibration procedure which is performed by satellite shaking is discussed. Since the ICM calibration methods are based on several assumptions about the instrument errors which are related to the errors of the individual ICM elements, the next topic is the derivation of limit values for the ICM elements, as deduced from Cesare and Catastini (2008b). Based on these considerations, the original TAS method, cf. Sect. 4.3.3, and the ESA-L method, cf. Sect. 4.3.4, which is currently in use, are introduced.

4.3.1. Satellite shaking procedure

For the determination of the ICMs (see Sects. 4.3.3 and 4.3.4) a calibration procedure, which includes shaking of the satellite, is performed approximately every two months.

The spacecraft shaking shall fulfill the following two aims:

- The generation of a strong linear and angular acceleration signal for frequencies between 50 to 100 mHz, the so-called upper measurement band (UMB).
- The generation of a strong angular acceleration signal for the frequencies near 1.3 mHz.

The former shall guarantee that in the UMB the linear and angular accelerations induced by the spacecraft shaking are much more significant than the gravity gradient signal, which is a basic assumption for the retrieval of the (relative) ICM elements in the TAS, as well as in the ESA-L method.

The latter is conducted in order to determine the absolute accelerometer scale factors, by a comparison of star sensor and gradiometer angular rate measurements.

According to Frommknecht et al. (2011), shaking of the satellite is performed along the flight direction (x-axis) with a modulation of the ion thrust, while the 5 other degrees of freedom are excited with the Gradiometer Calibration Device (GCD). The GCD consists of 2 sets of 4 cold gas thrusters, firing in the yz-plane, the sets being at both ends of the spacecraft. It is possible to modulate the ion thrust with fine steps and to achieve a corresponding spectral density well localized between 50 and 100 mHz. The cold gas thrusters are limited to on-off operation, what makes amplitude modulation impossible. The desired spectral densities can only be approximated by a combination of frequency and duty cycle modulations.

4.3.2. Derivation of limit values for the ICMs

From Eq. 4.15 it is known that the inverse of the calibration matrices is needed to recover the true common and differential mode accelerations from the measured ones. Thus the determination of the inverse calibration matrices is crucial for the success of the GOCE mission. Upper limits for the elements of the inverse calibration matrices can be derived from known upper limits of the gradiometer imperfections by construction. Within this section it will be shown how upper limits for the elements of the ICMs can be derived. They are found from the upper limits for the elements of the calibration matrices plus the error terms of a series expansion for the inversion of the calibration matrices.

Moreover, two relationships between the elements of the inverse calibration matrices will be introduced. The first one is between the sub-matrices of the inverse calibration matrices and the second one is between the elements of the sub-matrices of the inverse calibration matrices. It will be explained how these relationships are used within the nominal GOCE ICM processing.

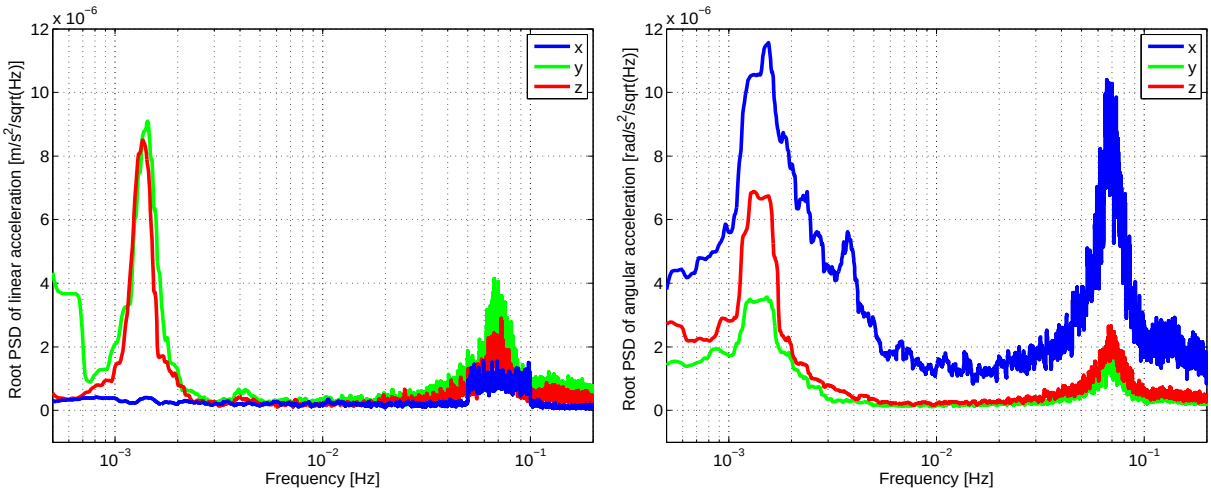

Figure 4.6.: Example for root PSD of (a) linear and (b) angular accelerations during shaking of the spacecraft. The data is taken from the third ICM calibration phase (8 October 2009). The linear accelerations are exemplarily shown for accelerometer A_1 in GRF. The angular accelerations are derived in GRF from Eqs. 2.47 to 2.49.

Limit values for the elements of the ICMs by construction

The calibration matrix of one accelerometer pair can be subdivided into a 6×6 unit matrix $\underline{I}_6$ and a 6×6 matrix $\underline{dM}_{ij}$ containing the deviations from the unit matrix.

$$
\begin{aligned}
\underline{M}_{ij} &= \underline{I}_6 + \begin{pmatrix}
K_{c,ij,X} & \psi_{c,ij} + \varepsilon_{c,ij} & -\theta_{c,ij} + \eta_{c,ij} & K_{d,ij,X} & \psi_{d,ij} + \varepsilon_{d,ij} & -\theta_{d,ij} + \eta_{d,ij} \\
-\psi_{c,ij} + \varepsilon_{c,ij} & K_{c,ij,Y} & \varphi_{c,ij} + \varsigma_{c,ij} & -\psi_{d,ij} + \varepsilon_{d,ij} & K_{d,ij,Y} & \varphi_{d,ij} + \varsigma_{d,ij} \\
\theta_{c,ij} + \eta_{c,ij} & -\varphi_{c,ij} + \varsigma_{c,ij} & K_{c,ij,Z} & \theta_{d,ij} + \eta_{d,ij} & -\varphi_{d,ij} + \varsigma_{d,ij} & K_{d,ij,Z} \\
K_{d,ij,X} & \psi_{d,ij} + \varepsilon_{d,ij} & -\theta_{d,ij} + \eta_{d,ij} & K_{c,ij,X} & \psi_{c,ij} + \varepsilon_{c,ij} & -\theta_{c,ij} + \eta_{c,ij} \\
-\psi_{d,ij} + \varepsilon_{d,ij} & K_{d,ij,Y} & \varphi_{d,ij} + \varsigma_{d,ij} & -\psi_{c,ij} + \varepsilon_{c,ij} & K_{c,ij,Y} & \varphi_{c,ij} + \varsigma_{c,ij} \\
\theta_{d,ij} + \eta_{d,ij} & -\varphi_{d,ij} + \varsigma_{d,ij} & K_{d,ij,Z} & \theta_{c,ij} + \eta_{c,ij} & -\varphi_{c,ij} + \varsigma_{c,ij} & K_{c,ij,Z}
\end{pmatrix} \\
&\equiv \underline{I}_6 + \left(\begin{array}{ccc|ccc}
dM_{c,ij,11} & dM_{c,ij,12} & dM_{c,ij,13} & dM_{d,ij,11} & dM_{d,ij,12} & dM_{d,ij,13} \\
dM_{c,ij,21} & dM_{c,ij,22} & dM_{c,ij,23} & dM_{d,ij,21} & dM_{d,ij,22} & dM_{d,ij,23} \\
dM_{c,ij,31} & dM_{c,ij,32} & dM_{c,ij,33} & dM_{d,ij,31} & dM_{d,ij,32} & dM_{d,ij,33} \\
\hline
dM_{d,ij,11} & dM_{d,ij,12} & dM_{d,ij,13} & dM_{c,ij,11} & dM_{c,ij,12} & dM_{c,ij,13} \\
dM_{d,ij,21} & dM_{d,ij,22} & dM_{d,ij,23} & dM_{c,ij,21} & dM_{c,ij,22} & dM_{c,ij,23} \\
dM_{d,ij,31} & dM_{d,ij,32} & dM_{d,ij,33} & dM_{c,ij,31} & dM_{c,ij,32} & dM_{c,ij,33}
\end{array}\right) \\
&\equiv [1]_6 + \begin{pmatrix} \underline{dM}_{c,ij} & \underline{dM}_{d,ij} \\ \underline{dM}_{d,ij} & \underline{dM}_{c,ij} \end{pmatrix} \equiv \underline{I}_6 + \underline{dM}_{ij}
\end{aligned}
\tag{4.16}
$$

The inverse of the calibration matrix can be denoted as

$$
\underline{M}_{ij}^{-1} \equiv \underline{MI}_{ij} = \begin{pmatrix}
MI_{ij,11} & MI_{ij,12} & MI_{ij,13} & MI_{ij,14} & MI_{ij,15} & MI_{ij,16} \\
MI_{ij,21} & MI_{ij,22} & MI_{ij,23} & MI_{ij,24} & MI_{ij,25} & MI_{ij,26} \\
MI_{ij,31} & MI_{ij,32} & MI_{ij,33} & MI_{ij,34} & MI_{ij,35} & MI_{ij,36} \\
MI_{ij,41} & MI_{ij,42} & MI_{ij,43} & MI_{ij,44} & MI_{ij,45} & MI_{ij,46} \\
MI_{ij,51} & MI_{ij,52} & MI_{ij,53} & MI_{ij,54} & MI_{ij,55} & MI_{ij,56} \\
MI_{ij,61} & MI_{ij,62} & MI_{ij,63} & MI_{ij,64} & MI_{ij,65} & MI_{ij,66}
\end{pmatrix} . \tag{4.17}
$$

Or in block form

$$
\underline{MI}_{ij} = \begin{pmatrix} \underline{MI}'_{c,ij} & \underline{MI}'_{d,ij} \\ \underline{MI}_{d,ij} & \underline{MI}_{c,ij} \end{pmatrix} . \tag{4.18}
$$

Thus it is possible to expand Eq. 4.15 as

$$
\begin{aligned}
\overline{a}_{c,ij} &= \underline{MI}'_{c,ij}\overline{a}'_{c,ij} + \underline{MI}'_{d,ij}\overline{a}'_{d,ij} \ , \\
\overline{a}_{d,ij} &= \underline{MI}_{d,ij}\overline{a}'_{c,ij} + \underline{MI}_{c,ij}\overline{a}'_{d,ij}
\end{aligned}
\tag{4.19}
$$

To recover the original differential mode accelerations only the sub-matrices $\underline{MI}_{d,ij}$ and $\underline{MI}_{c,ij}$, which include the elements of the last three rows of the ICM $\underline{MI}_{ij}$ are needed.

The inverse of the calibration matrix can be found by considering matrix inversion by series expansion. Analogously to the expansion of the series $\frac{1}{1+x} = 1 - x + x^2 - x^3 + ...$ (with $|x| < 1$), we have for square matrices of arbitrary order (Höpcke, 1980, p. 19):

$$\left(\underline{I}_6 + \underline{dM}_{ij}\right)^{-1} = \underline{I}_6 - \underline{dM}_{ij} + \underline{dM}_{ij}^2 - \underline{dM}_{ij}^3 + ... \tag{4.20}$$

Thus, we have as approximation for the inverse of the calibration matrix

$$\underline{MI}_{ij} \approx \underline{I}_6 - \underline{dM}_{ij} + \underline{\Delta MI}_{ij} \ , \tag{4.21}$$

with $\underline{\Delta MI}_{ij}$ including all quadratic or higher order terms.

In order to derive upper limits for the elements of the ICMs, one can use for $\underline{dM}_{ij}$ (in Eqs. 4.21 and 4.11) the upper limits for the common and differential scale factors, misalignments and coupling among the axes of the three accelerometer pairs by construction. These upper limits are given in Table D.1, according to Alenia (2002). Since $\underline{dM}_{ij}$ is symmetric (cf. Eq. 4.11), the table contains only the values of the first three rows. We have, for example, as upper limit for the common scale factor of accelerometer pair 14 in x-direction ($dM_{c,14,11}$) $4.05 \cdot 10^{-3}$.

With the given values for $\underline{dM}_{ij}$, the upper limits for the values of $\underline{\Delta MI}_{ij}$ can be computed (Table D.2). Since also this matrix is symmetric, the table shows again only the first three rows. For the example of the common scale factor of accelerometer pair 14 in x-direction we have: $\Delta MI_{14,11} < dM_{c,14,11}^2 + dM_{c,14,11}^3 = 3.31 \cdot 10^{-5}$.

Finally, one can find from Eq. 4.21 the values of the ICMs (MI_{ij}), which are expected not to be exceeded all along the on-orbit mission lifetime, by construction, Table D.3, see also Fig. 4.7. Again, it is sufficient to show the first three rows of the symmetric matrix. For example the upper limit of the element $dMI_{14,11}$ (corresponding to the common scale factor of accelerometer pair 14 in x-direction) can be found by summation of the upper limits of $dM_{c,14,11}$ and $\Delta MI_{14,11}$ and has a value of $4.08 \cdot 10^{-3}$.

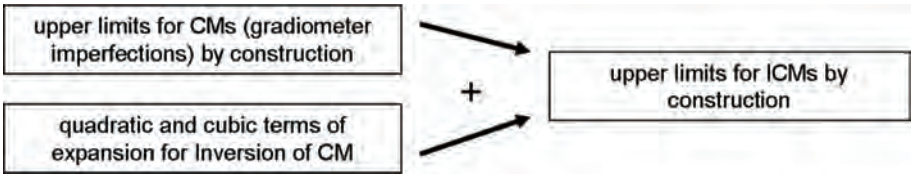

Figure 4.7.: Derivation of limit values for the ICMs by construction.

The values of $\underline{dM}_{ij}$ are based on the following numbers

- common and differential scale factors of the ultra-sensitive axes: $4.05 \cdot 10^{-3}$
- common and differential scale factors of the less sensitive axes: $5.18 \cdot 10^{-2}$
- common and differential misalignment and coupling: $1.30 \cdot 10^{-4}$, except for
- common (misalignment and) coupling of the less sensitive axes: $1.00 \cdot 10^{-5}$.

The reason for the last exception is that the direction of the less sensitive axis in the OAGRF is per definition in the middle of the projections of the less sensitive axes of the two corresponding ARFs. Hence the common part of the misalignments of the less sensitive OAGRF axis becomes zero, and there remains only the contribution of the (common) coupling. For a definition of the related reference frames it is referred to Appendix A. This principle is illustrated in Fig. 4.8 for the example of gradiometer arm 14.

The Y_{OAG1} axis is defined in the middle of the two directions Y'_{ARF1} and Y'_{ARF4}, which are the projections of Y_{ARF1} and Y_{ARF4} on the plane perpendicular to the X_{OAG1} axis. Hence the common part of the misalignments of accelerometer pair 25 about the X_{OAG1} axis becomes zero, and there remains only the contribution of the (common) coupling about the X_{OAG1} axis .

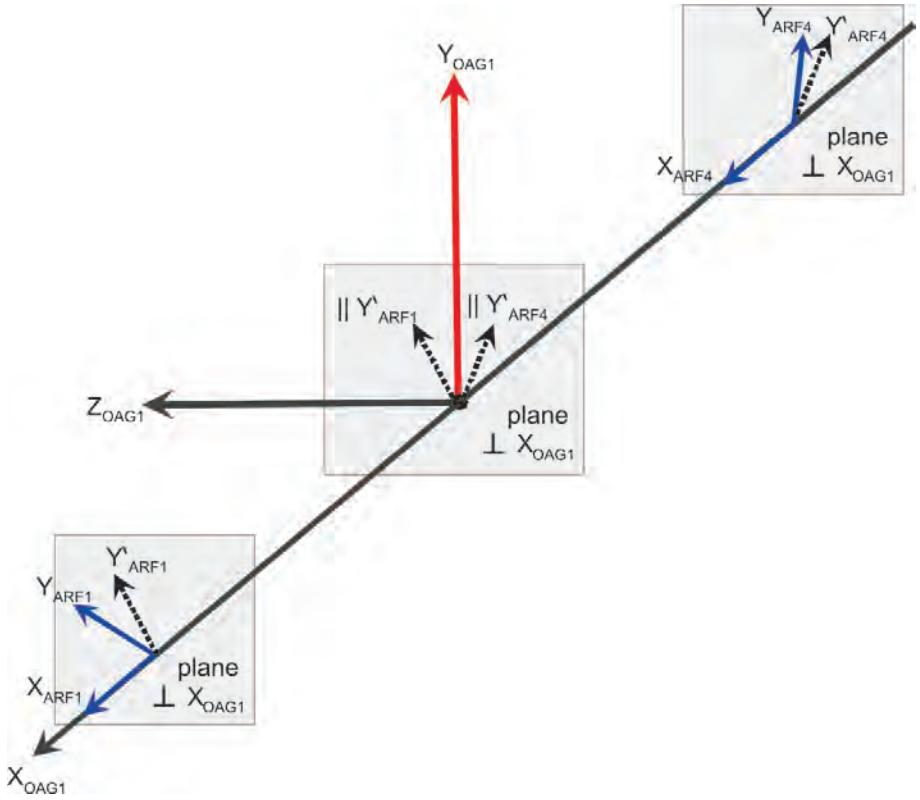

Figure 4.8.: Example for misalignment of the less sensitive axes Y_{ARF1} and Y_{ARF4} of accelerometers A_1 and A_4 about the X_{OAG1} axis. The direction of Y_{OAG1} is per definition in the middle of the two directions Y'_{ARF1} and Y'_{ARF4}, which are the projections of Y_{ARF1} and Y_{ARF4} on the plane perpendicular to the X_{OAG1} axis. Hence, the common coupling of the less sensitive Y_{OAG1} axis becomes zero.

Symmetry relationship between the sub-matrices of the ICMs

Two important relationships between the elements of the Inverse Calibration Matrices will be introduced. The first relationship can be derived from the symmetry between the sub-matrices of the Inverse Calibration Matrices:

$$\begin{aligned} \underline{MI}'_{c,ij} &= \underline{MI}_{c,ij} + \underline{\Delta MI}_{c,ij}, \\ \underline{MI}'_{d,ij} &= \underline{MI}_{d,ij} + \underline{\Delta MI}_{d,ij}. \end{aligned} \tag{4.22}$$

In detail, it reads

$$\begin{pmatrix} MI_{ij,11} & MI_{ij,12} & MI_{ij,13} \\ MI_{ij,21} & MI_{ij,22} & MI_{ij,23} \\ MI_{ij,31} & MI_{ij,32} & MI_{ij,33} \end{pmatrix} = \begin{pmatrix} MI_{ij,44} & MI_{ij,45} & MI_{ij,46} \\ MI_{ij,54} & MI_{ij,55} & MI_{ij,56} \\ MI_{ij,64} & MI_{ij,65} & MI_{ij,66} \end{pmatrix} + \begin{pmatrix} \Delta MI_{c,ij,11} & \Delta MI_{c,ij,12} & \Delta MI_{c,ij,13} \\ \Delta MI_{c,ij,21} & \Delta MI_{c,ij,22} & \Delta MI_{c,ij,23} \\ \Delta MI_{c,ij,31} & \Delta MI_{c,ij,32} & \Delta MI_{c,ij,33} \end{pmatrix},$$

$$\begin{pmatrix} MI_{ij,14} & MI_{ij,15} & MI_{ij,16} \\ MI_{ij,24} & MI_{ij,25} & MI_{ij,26} \\ MI_{ij,34} & MI_{ij,35} & MI_{ij,36} \end{pmatrix} = \begin{pmatrix} MI_{ij,41} & MI_{ij,42} & MI_{ij,43} \\ MI_{ij,51} & MI_{ij,52} & MI_{ij,53} \\ MI_{ij,61} & MI_{ij,62} & MI_{ij,63} \end{pmatrix} + \begin{pmatrix} \Delta MI_{d,ij,11} & \Delta MI_{d,ij,12} & \Delta MI_{d,ij,13} \\ \Delta MI_{d,ij,21} & \Delta MI_{d,ij,22} & \Delta MI_{d,ij,23} \\ \Delta MI_{d,ij,31} & \Delta MI_{d,ij,32} & \Delta MI_{d,ij,33} \end{pmatrix}.$$

It says that the upper limits for the elements of the first three rows of the Inverse Calibration Matrices can be derived from the upper limits of the corresponding elements of the last three rows plus the corresponding error term in $\underline{\Delta MI}_{c,ij}$ or $\underline{\Delta MI}_{d,ij}$, cf. Fig. 4.9. The upper limits for these error terms can be found by adding up the two involved errors due to matrix inversion by series expansion, cf. Table D.2. For example, $\Delta MI_{c,14,11} = \Delta MI_{d,14,11}$ has a maximum value of $\Delta MI_{14,11} + \Delta MI_{14,44} = 6.62 \cdot 10^{-5}$. All numerical values for the error terms $\underline{\Delta MI}_{c,ij}$ and $\underline{\Delta MI}_{d,ij}$ are given in Table D.4.

The main goal of the GOCE ICM processor is to determine with high accuracy the last three rows of the Inverse Calibration Matrices. They are needed for the recovery of the true differential mode accelerations and thus also for the computation of the gravity gradients. The accuracy of the first three rows is less important. Therefore, the last three rows of the ICMs are determined primarily, in a complex iterative procedure, cf. Sect. 4.3.3. Once the last three rows are computed with the required accuracy, the first three rows are obtained from the symmetry

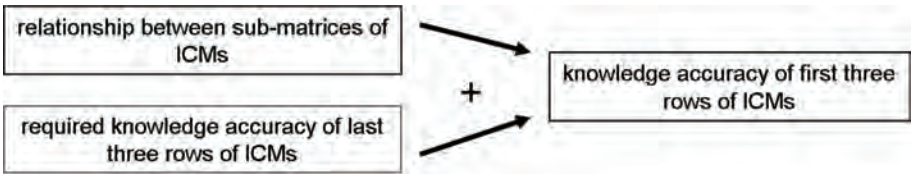

Figure 4.9.: Derivation of the accuracy of the first three rows of the ICMs.

between the sub-matrices, by using Eq. 4.22 without the error terms $\underline{\Delta MI}_{c,ij}$ and $\underline{\Delta MI}_{d,ij}$, (cf. Fig. 4.17, yellow box). Therefore, the errors in the elements of the first three rows can be larger than the errors of the elements in last three rows, by exactly the values $\underline{\Delta MI}_{c,ij}$ and $\underline{\Delta MI}_{d,ij}$.

Orthogonality relationship between the elements of the sub-matrices of the ICMs

From the instrument specification (Alenia, 2002), it is known that the coupling among the accelerometer axes ($\varepsilon_{c,ij}$, $\varepsilon_{d,ij}$, $\eta_{c,ij}$, $\eta_{d,ij}$, $\varsigma_{c,ij}$, $\varsigma_{d,ij}$) is smaller than 10^{-5}. With this additional information one can form relationships between the off-diagonal elements of the sub-matrices of $\underline{MI}_{ij}$. All these relations, in the following called *orthogonality relationships* D.1, and their upper limits are given in detail in Appendix D.5.

The relationships D.1 are obtained by building the sum of two elements (e.g. $MI_{14,12}$ and $MI_{14,21}$), which correspond to the rotation about one axis (e.g. z-axis). With the definition of the calibration matrix (Eq. 4.11) and the approximation for the inverse calibration matrix (Eq. 4.21), we have for example

$$\begin{aligned} MI_{14,12} &= -\,dM_{14,12} + \Delta MI_{14,12} = -(\psi_{c,14} + \varepsilon_{c,14}) + \Delta MI_{14,12} \\ MI_{14,21} &= -\,dM_{14,21} + \Delta MI_{14,21} = -(-\psi_{c,14} + \varepsilon_{c,14}) + \Delta MI_{14,21}\ . \\ \Rightarrow MI_{14,12} + MI_{14,21} &= -\,2 \cdot \varepsilon_{c,14} + \Delta MI_{14,12} + \Delta MI_{14,21} = \Delta MI_{14,12-21} \end{aligned}$$

Relationships D.1 give the maximum values of the sum of two corresponding elements of $\underline{MI}_{ij}$, cf. Fig. 4.10. This can be exploited in the nominal ICM calibration algorithm, compare Cesare et al. (2008) and Fig. 4.13, yellow box. Since in the iterative process of the ICM calibration algorithm only the last three rows of the inverse calibration matrices are determined, only the last six lines of relationships D.1 of each accelerometer pair, which correspond to the last three rows of the ICMs, are used. This gives in total the 18 relationships of Cesare et al. (2008), p. 58. As an example, the first one of these 18 relationships is given as:

$$\text{if } |MI_{14,51} + MI_{14,42}| > 5.2 \cdot 10^{-5} \text{ then } MI_{14,51} = -MI_{14,42} + 5.2 \cdot 10^{-5} \cdot \ \text{sign}(MI_{14,51} + MI_{14,42}) \qquad (4.23)$$

In the case that the absolute sum of the two corresponding elements $MI_{14,51}$ and $MI_{14,42}$ exceeds its maximum value defined by the relationships D.1, the element $MI_{14,51}$ is set/forced to this maximum possible value. The reason why $MI_{14,51}$ and not $MI_{14,42}$ was chosen to be changed is that the various elements of the ICMs have to be known with different accuracies. Table D.5 gives these accuracies with which the ICM elements have to be known to guarantee a substantial reduction of the gradiometric errors for the recovery of the original differential mode accelerations. Based on these numbers, in the nominal calibration algorithm there is always kept the value of the ICM element which has to be known with higher accuracy (e.g. $MI_{14,42}$, with required accuracy $< 5 \cdot 10^{-6}$) and the respective second ICM element (e.g. $MI_{14,51}$, with required accuracy $< 1.5 \cdot 10^{-4}$) is set to its maximum possible value.

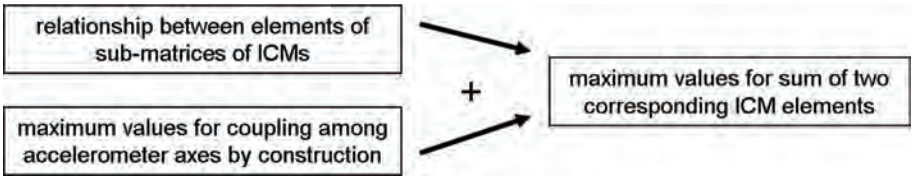

Figure 4.10.: Derivation of maximum values for the sum of two corresponding ICM elements.

ICM elements which are already accurate enough by construction

By comparing the required knowledge accuracy of the ICM elements (Table D.5) with the expected upper limits of the ICM elements which should be fulfilled all along the mission lifetime "by construction" (Table D.3), it can be found that for the following elements the knowledge accuracy requirements are already fulfilled:

- $MI_{14,51}$, $MI_{14,53}$, $MI_{14,54}$, $MI_{14,56}$, $MI_{14,64}$, $MI_{14,65}$
- $MI_{25,42}$, $MI_{25,43}$, $MI_{25,45}$, $MI_{25,46}$, $MI_{25,61}$, $MI_{25,62}$, $MI_{25,64}$, $MI_{25,65}$
- $MI_{36,45}$, $MI_{36,46}$, $MI_{36,51}$, $MI_{36,53}$, $MI_{36,54}$, $MI_{36,56}$

This means that these 20 elements do not necessarily need to be measured in flight, because their knowledge is already sufficient "by construction"'. To fulfill the required knowledge accuracy, it would also be sufficient to assume these values to be zero.

In the TAS method for the determination of the ICM elements this is exploited by applying a limit check for the ICM elements related to common coupling $MI_{14,56}$, $MI_{14,65}$, $MI_{25,46}$, $MI_{25,64}$, $MI_{36,45}$, $MI_{36,54}$ at the very end of the determination algorithm. This means, if one of these elements exceeds its threshold by construction, which is given with $1.9 \cdot 10^{-5}$, it is set to zero. E.g.

$$\text{if } |MI_{14,56}| > 1.9 \cdot 10^{-5} \text{ then } MI_{14,56} = 0 \tag{4.24}$$

In Fig. 4.17 this step is referred to as *limit check for absolute coupling* (yellow box).

Required measurement accuracy of the ICMs

The required knowledge accuracy of the ICM elements is given in Table D.5.

In the time between two calibration events, the ICM elements can show some variations, e.g. due to ageing or thermo-elastic deformations. Table D.6 gives the limits for these variations during a measurement cycle of one month as predicted before launch. The required measurement accuracy of the ICM elements (see Table D.7) during a measurement phase has been derived by subtraction of the limit values for the ICM element variations from the required knowledge accuracy, cf. Fig. 4.11.

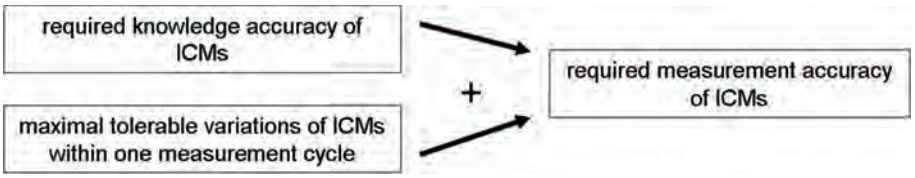

Figure 4.11.: Derivation of the required measurement accuracy of the ICMs.

4.3.3. Alenia method

In this section the nominal ICM calibration method as developed by TAS is described. Fig. 4.12 gives an overview of the logic of the calibration algorithm.

The TAS ICM calibration algorithm is composed of three major steps. Step 1 is implemented as an iterative loop (step1-loop). After the successive finalization of the first loop, it follows a loop over steps 2 and 3 (step2-3-loop). Within this loop, step 3 is again implemented as a loop (step3-loop), whereas step 2 is conducted only once in each iteration of the step2-3-loop.

Calibration step 1

Figure 4.13 gives on overview of the logic of calibration step 1. Indicated in yellow is the use of the orthogonality relationship Eq. 4.23.

Calibration step 1 works within the upper measurement band (UMB), which is from 50-100 mHz, and is based on the equations for the measured differential mode accelerations, Eqs. 2.38 to 2.46.

For calibration step 1 these 9 equations are used, assuming that the gravity gradient signal is weak in the UMB and that thus the GGT components can be omitted in the equations:

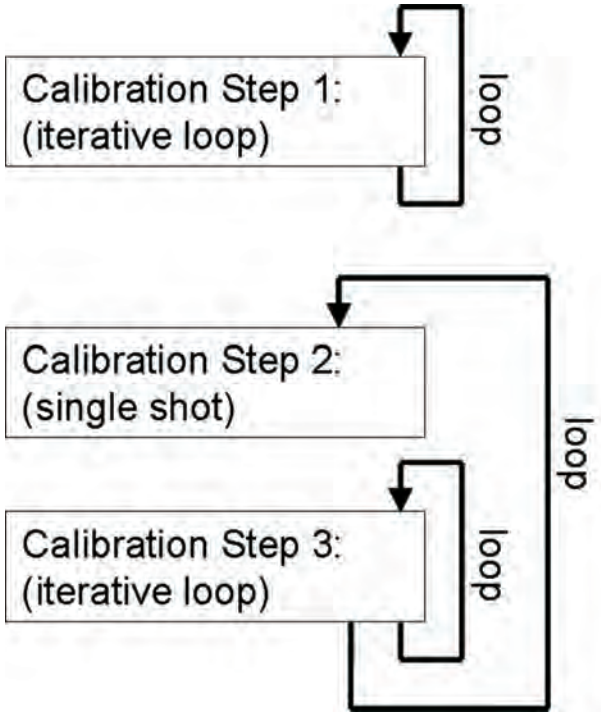

Figure 4.12.: Logic of the TAS calibration method.

$$
\begin{aligned}
a_{d,14,x} &= -\frac{L_x}{2}\left(\omega_y^2+\omega_z^2\right)\ ;\ a_{d,14,y} = L_x\omega_x\omega_y - \frac{L_x}{L_y}a_{d,25,x}\ ;\ a_{d,14,z} = L_x\omega_x\omega_z - \frac{L_x}{L_z}a_{d,36,x}\\
a_{d,25,x} &= L_y\omega_x\omega_y - \frac{L_y}{L_x}a_{d,14,y}\ ;\ a_{d,25,y} = -\frac{L_y}{2}\left(\omega_x^2+\omega_z^2\right)\ ;\ a_{d,25,z} = L_y\omega_y\omega_z - \frac{L_y}{L_z}a_{d,36,y}\\
a_{d,36,x} &= L_z\omega_x\omega_z - \frac{L_z}{L_x}a_{d,14,z}\ ;\ a_{d,36,y} = L_z\omega_y\omega_z - \frac{L_z}{L_y}a_{d,25,z}\ ;\ a_{d,36,z} = -\frac{L_z}{2}\left(\omega_x^2+\omega_y^2\right)
\end{aligned}
\tag{4.25}
$$

Next, the differential accelerations are expressed as a function of the measured common and differential accelerations and the ICM elements, e.g.:

$$
\begin{aligned}
MI_{14,41}a'_{c,14,x} + MI_{14,42}a'_{c,14,y} + MI_{14,43}a'_{c,14,z} + MI_{14,44}a'_{d,14,x} \quad &+ \quad MI_{14,45}a'_{d,14,y} + MI_{14,46}a'_{d,14,z}\\
&= \quad -\frac{L_x}{2}\left(\omega_y^2+\omega_z^2\right)
\end{aligned}
\tag{4.26}
$$

The common and differential mode accelerations and the angular rates are measured for a large number N of epochs (here $N = 86400$, calibration event lasts for one day) and 9 sets of linear equations are built, which are solved in a least squares adjustment with the elements of the last three rows of the ICMs as unknowns. The result of calibration step 1 are the last three rows of the ICMs, except of the elements related to the common scale factors (red in Fig. 4.14), which maintain their initial unitary value.

The step1-loop is exited when a certain maximum number of iterations is reached or if all elements (except the red ones in Fig. 4.14) have fulfilled their convergence criteria. This means, if one ICM element has fulfilled its convergence criterion at a certain iteration, it is kept constant in all the following iterations (step-by-step convergence).

Calibration step 2

Calibration step 1 does not provide the ICM elements related to the common scale factors. The elements related to the transversal common scale factors are determined within calibration step 2 from star sensor derived angular accelerations only, by exploiting the relationship between the differential mode and the satellite's angular accelerations. In Fig. 4.15 the logic of calibration step 2 is illustrated.

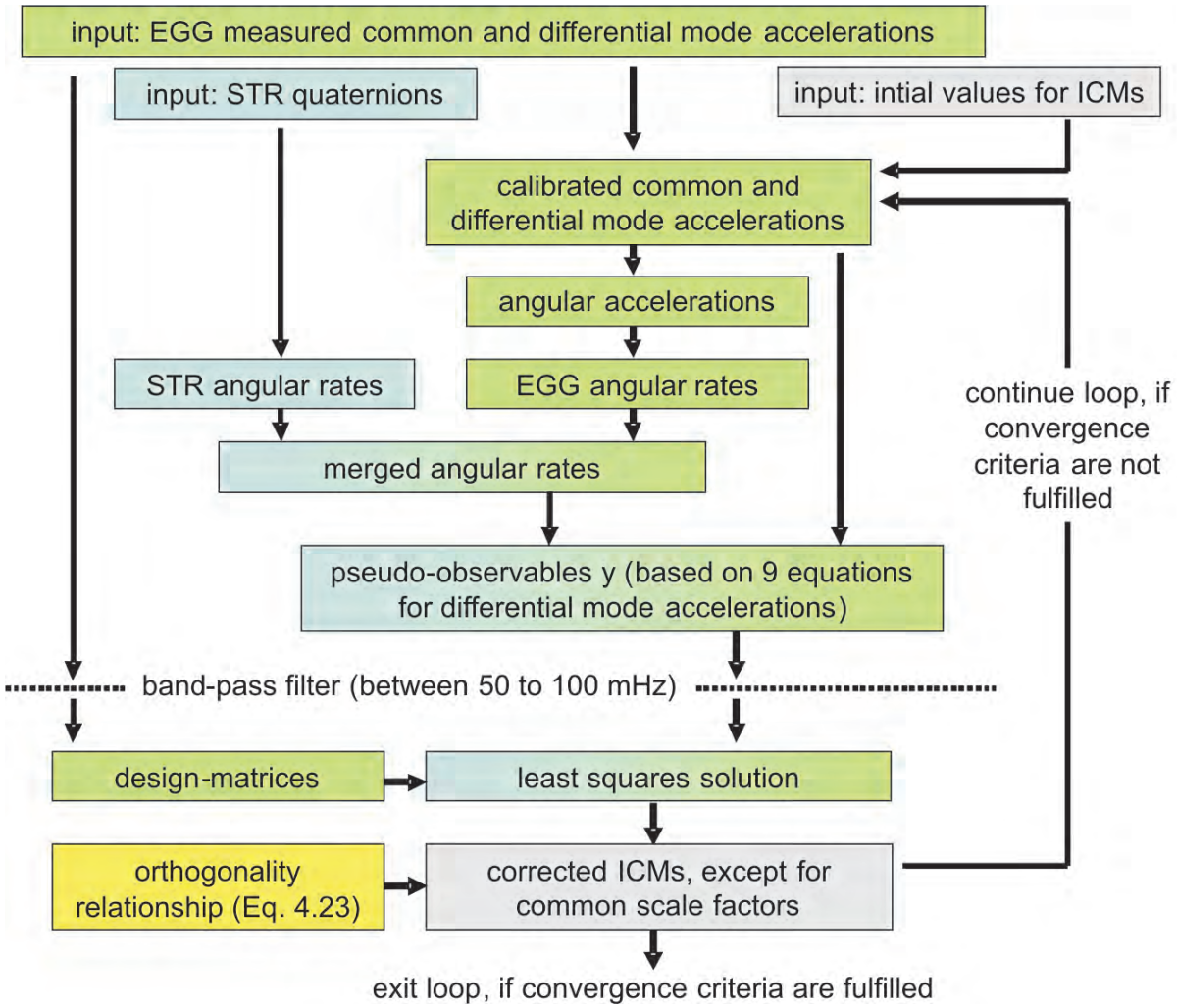

Figure 4.13.: Logic of the TAS calibration method, step 1.

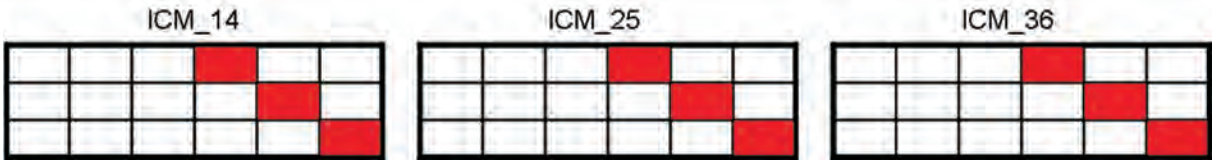

Figure 4.14.: ICM elements (of last three ICM rows) which are already determined (white) or not (red) after calibration step 1.

Calibration step 2 works below the MB of the gradiometer in a frequency band around 1.3 mHz. In this part of the spectrum the star sensor data has a good quality. Within this step the fact that the satellite angular accelerations can be determined from the gradiometer as well as from the star sensors is exploited, cf. Eqs. 2.47 to 2.49:

$$\dot{\omega}_x^{STR} = \dot{\omega}_x^{EGG} = -\frac{a_{d,3,6,y}}{L_z} + \frac{a_{d,2,5,z}}{L_y} \tag{4.27}$$

$$\dot{\omega}_y^{STR} = \dot{\omega}_y^{EGG} = -\frac{a_{d,1,4,z}}{L_x} + \frac{a_{d,3,6,x}}{L_z} \tag{4.28}$$

$$\dot{\omega}_z^{STR} = \dot{\omega}_z^{EGG} = -\frac{a_{d,2,5,x}}{L_y} + \frac{a_{d,1,4,y}}{L_x} \tag{4.29}$$

The true differential mode accelerations can be expressed as function of the measured common and differential mode accelerations and the ICM elements determined at the previous calibration step. E.g., for the differential

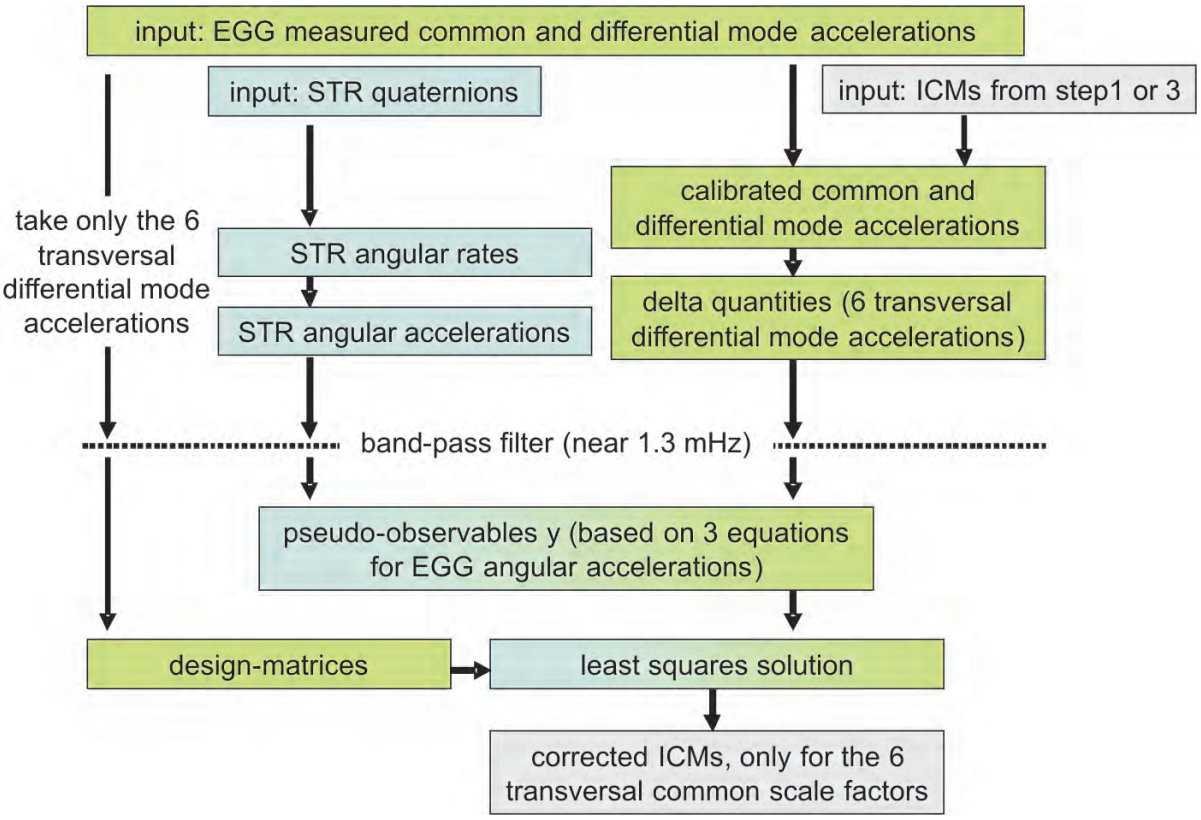

Figure 4.15.: Logic of the TAS calibration method, step 2.

mode accelerations relevant for the angular acceleration about the x-axis we get

$$\begin{aligned} a_{d,36,y} &= MI_{36,51}a'_{c,36,x} + MI_{36,52}a'_{c,36,y} + MI_{36,53}a'_{c,36,z} + MI_{36,54}a'_{d,36,x} + MI_{36,55}a'_{d,36,y} + MI_{36,56}a'_{d,36,z} \\ &= MI_{36,55}a'_{d,36,y} + \Delta a_{d,36,y} \end{aligned} \tag{4.30}$$

$$\begin{aligned} a_{d,25,z} &= MI_{25,61}a'_{c,25,x} + MI_{25,62}a'_{c,25,y} + MI_{25,63}a'_{c,25,z} + MI_{25,64}a'_{d,25,x} + MI_{25,65}a'_{d,25,y} + MI_{25,66}a'_{d,25,z} \\ &= MI_{25,66}a'_{d,25,z} + \Delta a_{d,25,z} \end{aligned} \tag{4.31}$$

When inserting the above relationships into Eq. 4.27 and proceeding analogously for Eqs. 4.28 and 4.29 we obtain

$$MI_{36,55}\left(-\frac{1}{L_z}a'_{d,36,y}\right) + MI_{25,66}\left(-\frac{1}{L_y}a'_{d,25,z}\right) = \dot{\omega}_x^{STR} + \frac{1}{L_z}\Delta a_{d,36,y} - \frac{1}{L_y}\Delta a_{d,25,z} \tag{4.32}$$

$$MI_{14,66}\left(-\frac{1}{L_x}a'_{d,14,z}\right) + MI_{36,44}\left(\frac{1}{L_z}a'_{d,36,x}\right) = \dot{\omega}_y^{STR} + \frac{1}{L_x}\Delta a_{d,14,z} - \frac{1}{L_z}\Delta a_{d,36,x} \tag{4.33}$$

$$MI_{25,44}\left(-\frac{1}{L_y}a'_{d,25,x}\right) + MI_{14,55}\left(-\frac{1}{L_x}a'_{d,14,y}\right) = \dot{\omega}_z^{STR} + \frac{1}{L_y}\Delta a_{d,25,x} - \frac{1}{L_x}\Delta a_{d,14,y} \tag{4.34}$$

The corresponding three sets of linear equations are built for a large number of epochs, and the 6 unknowns $MI_{14,55}$, $MI_{14,66}$, $MI_{25,44}$, $MI_{14,66}$, $MI_{36,44}$, $MI_{14,55}$ (the ICM elements related to the transversal common scale factors) are found by least squares adjustment.

For the first step2-3-loop the output ICMs from calibration step 1 serve as an input for calibration step 2. For the following iterations of the step2-3-loop the output ICMs from the previous calibration step 3 are used.

The result of calibration step 2 are the last three rows of the ICMs, except of those elements related to the in-line common scale factors which maintain their initial unitary value (red in Fig. 4.16).

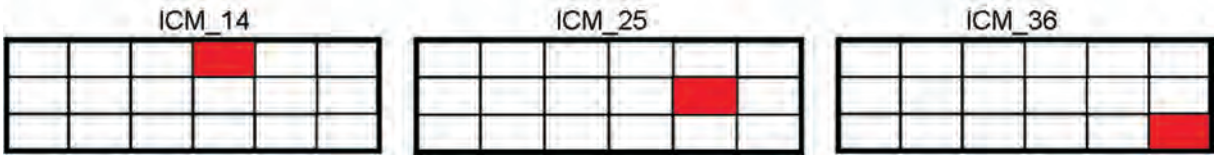

Figure 4.16.: ICM elements (of last three ICM rows) which are already determined (white) or not (red) after calibration step 2.

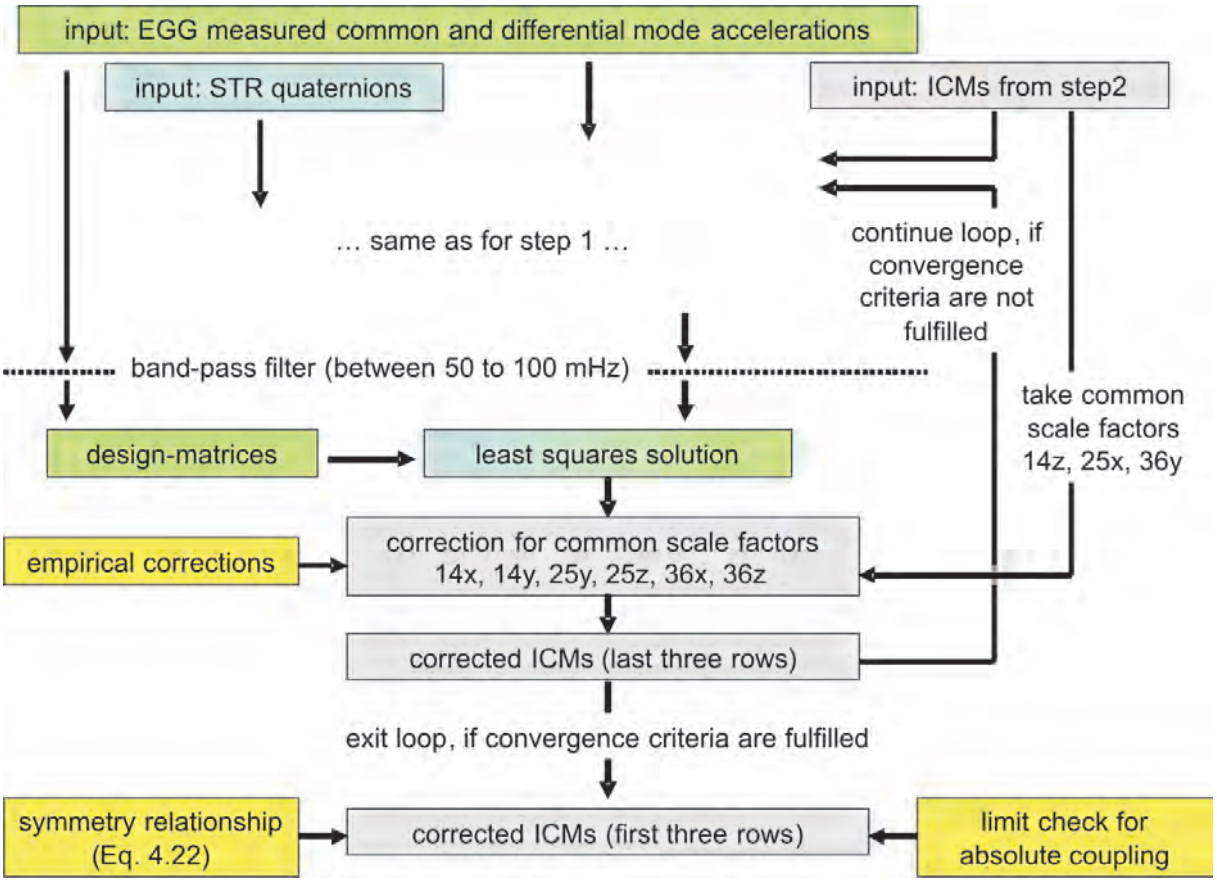

Figure 4.17.: Logic of the TAS calibration method, step 3.

Calibration step 3

Calibration step 3 is similar to calibration step 1, thus it uses the same basic equations, works within the UMB and is implemented as an iterative loop with a step-by-step convergence. The main difference of this step with respect to calibration step 1 is the application of corrections to the ICM elements which are related to common scale factors. These corrections have been derived empirically and are thus referred to as *empirical corrections*, cf. yellow box in Fig. 4.17.

These corrections are according to Cesare and Catastini (2008b) necessary, because the output ICM elements of the least squares fit, which are related to the common scale factors, are not exactly identical with the sought-after ICM elements, but are only an approximation of them.

In the following, the derivation of these empirical corrections is explained. Cesare and Catastini (2008b) have found with 9 numerical test cases the relationship between the ICM elements of the least squares fit (in the following denoted with prime), and the exact (sought-after) ICM elements (in the following denoted without prime)

$$\begin{pmatrix} \delta MI'_{14,44} \\ \delta MI'_{14,55} \\ \delta MI'_{14,66} \\ \delta MI'_{25,44} \\ \delta MI'_{25,55} \\ \delta MI'_{25,66} \\ \delta MI'_{36,44} \\ \delta MI'_{36,55} \\ \delta MI'_{36,66} \end{pmatrix} = \begin{pmatrix} 1 & 0 & -\frac{1}{2} & 0 & 0 & 0 & -\frac{1}{2} & 0 & 0 \\ 0 & 1 & 0 & -1 & 0 & 0 & 0 & 0 & 0 \\ 0 & 0 & 1 & 0 & 0 & 0 & -1 & 0 & 0 \\ 0 & -1 & 0 & 1 & 0 & 0 & 0 & 0 & 0 \\ 0 & 0 & 0 & 0 & 1 & -\frac{1}{2} & 0 & -\frac{1}{2} & 0 \\ 0 & 0 & 0 & 0 & 0 & 1 & 0 & -1 & 0 \\ 0 & 0 & -1 & 0 & 0 & 0 & 1 & 0 & 0 \\ 0 & 0 & 0 & 0 & 0 & -1 & 0 & 1 & 0 \\ 0 & 0 & -\frac{3}{7} & 0 & 0 & -\frac{1}{14} & -\frac{3}{7} & -\frac{1}{14} & 1 \end{pmatrix} \cdot \begin{pmatrix} \delta MI_{14,44} \\ \delta MI_{14,55} \\ \delta MI_{14,66} \\ \delta MI_{25,44} \\ \delta MI_{25,55} \\ \delta MI_{25,66} \\ \delta MI_{36,44} \\ \delta MI_{36,55} \\ \delta MI_{36,66} \end{pmatrix} \equiv CI \cdot \begin{pmatrix} \delta MI_{14,44} \\ \delta MI_{14,55} \\ \delta MI_{14,66} \\ \delta MI_{25,44} \\ \delta MI_{25,55} \\ \delta MI_{25,66} \\ \delta MI_{36,44} \\ \delta MI_{36,55} \\ \delta MI_{36,66} \end{pmatrix} \quad (4.35)$$

Since only 6 of the above 9 equations are independent, 3 additional properties must be known about the diagonal ICM elements to invert the CI-matrix. This additional information is taken from calibration step 2. More precisely, in calibration step 3 the corrections/differences δ to the ICM elements

- $MI_{14,66}$ (related to $\dot{\omega}_y$, US differential mode measurement)
- $MI_{25,44}$ (related to $\dot{\omega}_z$, US differential mode measurement)
- $MI_{36,55}$ (related to $\dot{\omega}_x$, LS differential mode measurement)

of calibration step 2 are used to correct the remaining 6 ICM elements, which are related to common scale factors, i.e. $MI'_{14,44}$, $MI'_{14,55}$, $MI'_{25,55}$, $MI'_{25,66}$, $MI'_{36,44}$, $MI'_{36,66}$. Note that the elements $MI_{14,66}$, $MI_{25,44}$ and $MI_{36,55}$ have been chosen in order to use as often as possible the measurements of US axes.

Hence, the empirical corrections (cf. again Fig. 4.17, yellow box) can be found by solving Eq. 4.35 for $\delta MI'_{14,44}$, $\delta MI'_{14,55}$, $\delta MI'_{25,55}$, $\delta MI'_{25,66}$, $\delta MI'_{36,44}$ and $\delta MI'_{36,66}$, using the star sensor derived values of calibration step 2 for $\delta MI'_{14,44}$, $\delta MI'_{14,55}$ and $\delta MI'_{25,55}$:

$$\begin{aligned}
\delta MI_{14,44} &= \delta MI_{14,66} - \frac{1}{4}\delta MI'_{14,66} + \frac{1}{4}\delta MI'_{36,44} + \delta MI'_{14,44} \\
\delta MI_{14,55} &= \delta MI_{25,44} - \delta MI'_{25,44} \\
\delta MI_{25,55} &= \delta MI_{36,55} + \frac{1}{4}\delta MI'_{25,66} - \frac{1}{4}\delta MI'_{36,55} + \delta MI'_{25,55} \\
\delta MI_{25,66} &= \delta MI_{36,55} + \frac{1}{2}\delta MI'_{25,66} - \frac{1}{2}\delta MI'_{36,55} \\
\delta MI_{36,44} &= \delta MI_{14,66} - \frac{1}{2}\delta MI'_{14,66} + \frac{1}{2}\delta MI'_{36,44} \\
\delta MI_{36,66} &= \frac{6}{7}\delta MI_{14,66} + \frac{1}{7}\delta MI_{36,55} + \frac{1}{28}\delta MI'_{25,66} - \frac{1}{28}\delta MI'_{36,55} - \frac{3}{14}\delta MI'_{14,66} + \frac{3}{14}\delta MI'_{36,44} + \delta MI'_{36,66}
\end{aligned} \quad (4.36)$$

After the first calibration step 3 for the first time all elements of the (last three rows of the) ICMs are determined, cf. Fig. 4.18.

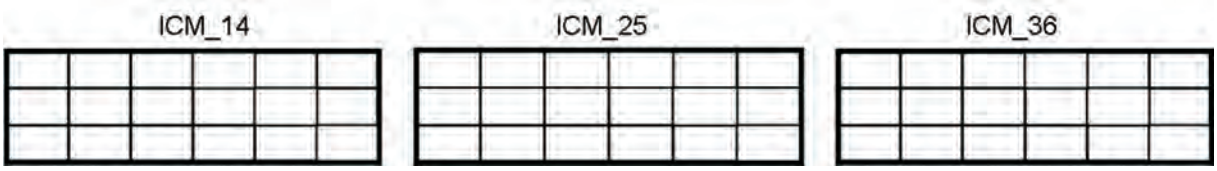

Figure 4.18.: After calibration step 3 all ICM elements are determined (white). Only the last three ICM rows are shown.

The iterative step3-loop stops if a certain maximum number of iterations is reached or if all ICM elements have fulfilled their (step-by-step) convergence criterion. This convergence check is done here between two successive output ICMs of the step3-loop.

End of Calibration

The iterative step2-3-loop stops if convergence of the elements of the last three rows of the ICMs is achieved. Again, an element-wise (step-by-step) convergence check is performed, now comparing the elements of the last step2-3-loop output with the output of the step1-loop (after the first step2-3-loop) or with the output of the previous step2-3-loop (for the following step2-3-loops).

Finally, the ICM elements related to common coupling $MI_{14,56}$, $MI_{14,65}$, $MI_{25,46}$, $MI_{25,64}$, $MI_{36,45}$, $MI_{36,54}$ have to undergo the *limit check for absolute coupling* (Eq. 4.24), and the first three rows of the ICMs are derived from the last three rows using the symmetry relationship of Eq. 4.22 and neglecting thereby the error terms $\Delta MI_{c,ij}$ and $\Delta MI_{d,ij}$

$$\begin{aligned} \underline{MI}'_{c,ij} &= \underline{MI}_{c,ij} \\ \underline{MI}'_{d,ij} &= \underline{MI}_{d,ij} \end{aligned} \tag{4.37}$$

4.3.4. ESA-L method

In this section the ESA-L method according to Lamarre (2008) is described. We follow the explanations given in Frommknecht et al. (2011).

The ESA-L calibration model takes into account the following deviations of the real accelerometers from the ideal ones:

- The response of each accelerometer axis: 3 scale factors
- The direction of each accelerometer axis: 3 x 2 angles
- The position of each accelerometer: 3 coordinates

This gives in total 12 parameters describing one accelerometer.

Since the gradiometer consists of 6 accelerometers, it is in total modelled by $6 \cdot 12 = 72$ parameters. First, the parameters between the accelerometers are determined. They are referred to as relative parameters. In a next step, the absolute scale factor of the gradiometer is determined, using the star sensor measurements as absolute external information. After the retrieval of the gradiometer parameters, they are transformed into the ICMs which are used in the L1b processing (Eq. 4.17).

Determination of relative parameters between accelerometers

The calibration is based on shaking of the spacecraft, cf. Sect. 4.3.1, in which strong linear and angular accelerations are induced. These accelerations shall be much stronger than the gravity gradient signal. The principle for the retrieval of the (relative) calibration parameters is to find those parameters which are able to remove any trace of the applied accelerations from the gravity gradient measurements. Since the gradiometer alone can not determine its own scale factor, some external information is necessary. Similarly to the principle of the TAS-method (calibration step 2) the star sensor measurements are used to deduce the absolute scale factor of the gradiometer by comparison of star sensor and gradiometer attitude data.

The shaking of the spacecraft, cf. Sect. 4.3.1, is performed in a way that the 3 angular and 3 linear accelerations are weakly correlated. Hence, each of the 6 induced accelerations has a unique signature which will allow its identification in the gradiometer measurements.

The retrieval of the relative gradiometer parameters is implemented as an iterative loop, cf. Fig. 4.19.

For the identification of the unique signatures the deviations of the real signal from the theoretical signal of an ideal gradiometer are used. Moreover, it is assumed that the gradiometer output signal during the spacecraft shaking is dominated by the induced accelerations, and hence that the centrifugal accelerations and the gravity gradients can be neglected.

In this case, for an ideal gradiometer, i.e. with all accelerometers having the same scale factors along all axes and being perfectly aligned, the 6 diagonal and off-diagonal gravity gradients should be zero. Moreover, all common mode accelerations measured in the same direction should be identical. This can be expressed by the following equations:

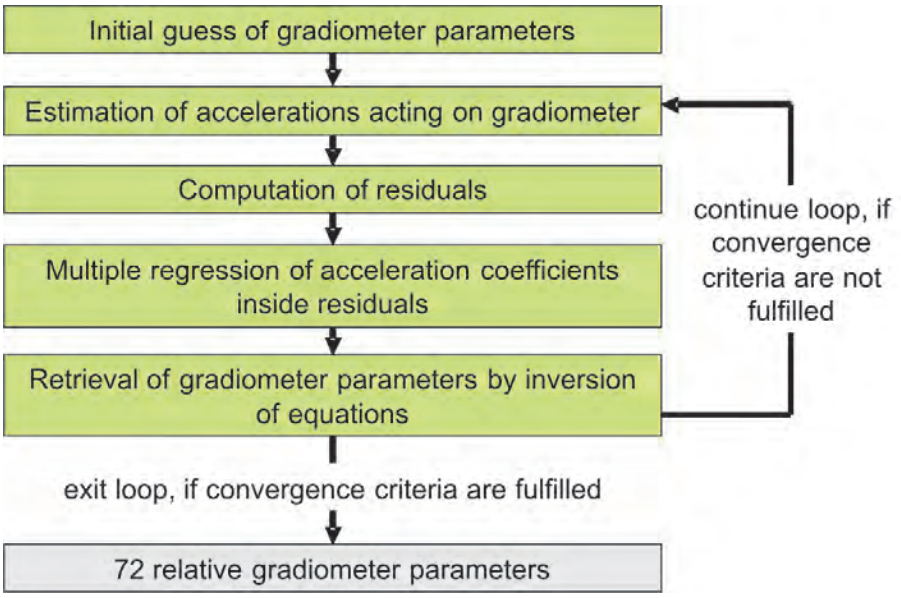

Figure 4.19.: Logic of the ESA-L calibration method, step 1. Iterative loop for the determination of the relative gradiometer parameters.

$$
\begin{aligned}
a_{d,14,x} &= 0 \text{ (related to } V_{xx}\text{)},\\
a_{d,25,y} &= 0 \text{ (related to } V_{yy}\text{)},\\
a_{d,36,z} &= 0 \text{ (related to } V_{zz}\text{)},\\
a_{d,14,y} + a_{d,25,x} &= 0 \text{ (related to } V_{xy}\text{)},\\
a_{d,14,z} + a_{d,36,x} &= 0 \text{ (related to } V_{xz}\text{)},\\
a_{d,25,z} + a_{d,36,y} &= 0 \text{ (related to } V_{yz}\text{)},\\
a_{c,14,x} + a_{c,25,x} &= 0 \text{ (related to common mode in x-direction)},\\
a_{c,14,x} + a_{c,36,x} &= 0 \text{ (related to common mode in x-direction)},\\
a_{c,25,y} + a_{c,36,y} &= 0 \text{ (related to common mode in y-direction)},\\
a_{c,25,y} + a_{c,14,y} &= 0 \text{ (related to common mode in y-direction)},\\
a_{c,36,z} + a_{c,14,z} &= 0 \text{ (related to common mode in z-direction)},\\
a_{c,36,z} + a_{c,25,z} &= 0 \text{ (related to common mode in z-direction)},
\end{aligned}
\tag{4.38}
$$

For a real gradiometer one or more of the above 12 quantities would not be zero, but a residual would appear. These residuals can be modelled as a linear combination of the 6 accelerations, which are induced by shaking of the spacecraft. The coefficients of these linear combinations can be found by a least squares solution.

This gives in total 72 ($= 6 \cdot 12$) equations, linking the residuals of the 12 above linear combinations to the 6 accelerations, induced to the spacecraft, as a function of the 72 gradiometer parameters.

According to Lamarre (2008) these equations have first been derived by numerical modelling of the gradiometer and have now also been derived analytically.

Moreover, Lamarre (2008) states that there are, in linear approximation, only 69 equations (and not 72), since an angular acceleration about a given axis cannot create a residual on the in-line gravity gradient term along the same axis.

In addition to these 69 equations further conditions are used within the ESA-L calibration method:

- The average scale factor of the gradiometer is set to 1 (1 equation). The absolute scale factor of the gradiometer will be retrieved in a second step using star sensor measurements.
- The average position and orientation of the gradiometer is nominal (6 equations). It is assumed anyhow that the position and orientation is known well enough by construction.

- The baselines between two accelerometers along a gradiometer arm are set to their nominal values (3 equations). The baselines have been measured on-ground to 100 ppm (50 μm) accuracy, which is assumed to be sufficient.
- The angles between the sensitive axes of the same accelerometer are perpendicular to within 20 μrad (18 equations). This constraint, given by manufacturing accuracy, is implemented as an orthogonality condition, with a low weight. Also the TAS calibration method makes use of this condition (cf. Eq. 4.24 *limit check for absolute coupling*).

Determination of the absolute scale factor

For the determination of the absolute scale factor external information is needed. Therefore, the star sensor measurements are used. The principle is, similar to the one of the TAS calibration method (step 2), a comparison of the gradiometer and star sensor derived attitude information. For the TAS method the comparison takes place at the level of angular accelerations, cf. Fig. 4.15, whereas for the ESA-L method it takes place at the level of angular rates, cf. Fig. 4.20. For the comparison, both, the star sensor derived, and the gradiometer derived angular rates are filtered to a 1 mHz bandwidth around 1.3 mHz. In this part of the spectrum both instrument types provide accurate measurements.

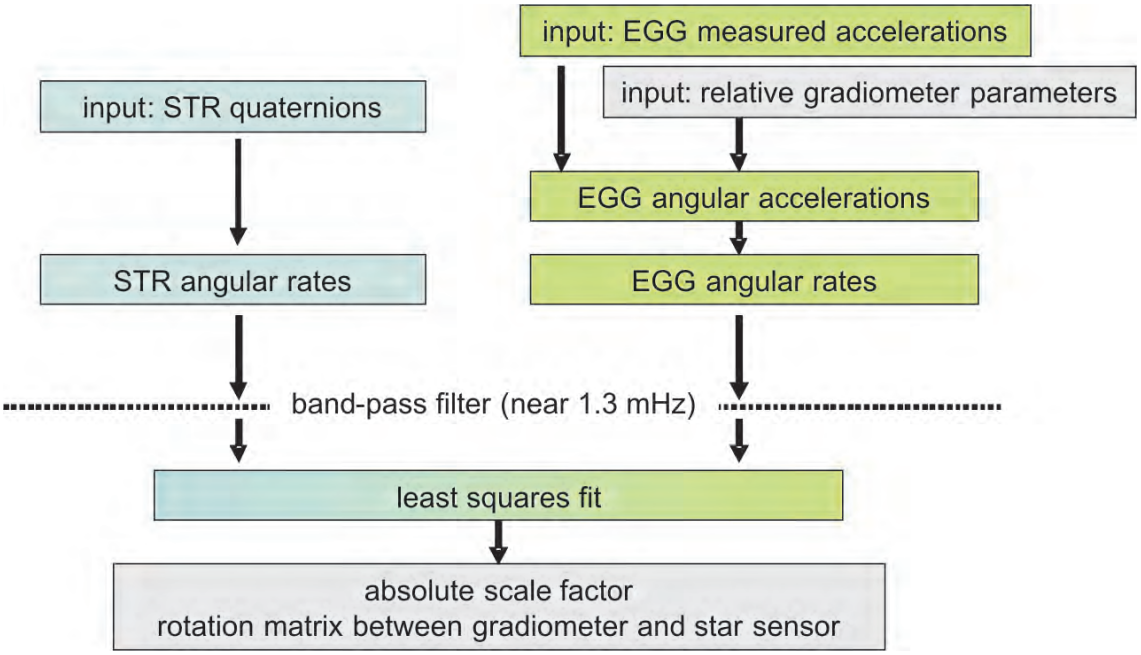

Figure 4.20.: Logic of the ESA-L calibration method, step 2. Determination of the absolute scale factor.

The least squares solution is based on the following assumptions

- The star sensor reference frames are orthogonal.
- The star sensors have a scale factor equal to 1.
- The gradiometer reference frame is orthogonal.
- The gradiometer has a scale factor different from 1.
- The gradiometer has the same scale factors along its 3 axes.
- The gradiometer reference frame is rotated with respect to the star sensor reference frame.

The corresponding model can be written as

$$\overline{W}_G = K\underline{R}\overline{W}_S \tag{4.39}$$

with $\overline{W}_G$ being the vector of gradiometer estimated angular rates, K being the absolute scale factor of the gradiometer, $\underline{R}$ being the rotation matrix between gradiometer and star sensor, and $\overline{W}_S$ being the vector of star

sensor estimated angular rates. Within the least squares fit not only the absolute scale factor K is determined, but also the rotation matrix $\underline{R}$.

For the determination of the absolute scale factor the combined data from all simultaneously available star sensors is used as far as possible. In case only one star sensor is available, according to Frommknecht et al. (2011), it is possible to improve the accuracy of the method by removing the orbital harmonics from the estimated star sensor (and for sake of consistency also gradiometer) angular rates.

Determination of the ICMs from the gradiometer parameters

The output of the ESA-L calibration method are the 72 gradiometer parameters, as described above. For the correction of the common and differential mode accelerations within the L1b processing chain (cf. Sect. 3.3), the ICMs as defined by TAS, Eq. 4.17 are needed. Hence, a transformation of the 72 gradiometer parameters into the ICMs has to be performed, cf. Fig. 4.21.

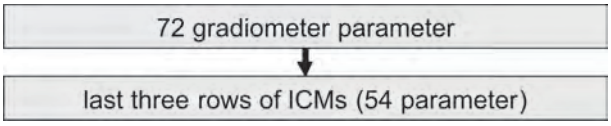

Figure 4.21.: Logic of the ESA-L calibration method. Step 3 - Determination of the ICMs from the gradiometer parameters.

Since the first three rows of the ICMs can be derived from their last three rows with Eq. 4.22, neglecting the error terms $\underline{\Delta MI}_{c,ij}$ and $\underline{\Delta MI}_{d,ij}$ the task is to transform the 72 gradiometer parameters to the 54 ($= 3 \cdot 3 \cdot 6$) elements of the last three ICM rows.

For this transformation basically the 18 position parameters have to be combined with the 54 remaining parameters of the ESA-L method. This is only possible because the average center positions, the orientations of the accelerometers and the errors of the baselines are small enough to be ignored, cf. Frommknecht et al. (2011). For the transformation the gradiometer parameters are first written as common (average) and differential (differences divided by two) values, i.e.

$$\begin{array}{cc} \text{common} & \text{differential} \\ \begin{bmatrix} \Delta k_{c,ij,x} & \Theta_{c,ij,xy} & \Theta_{c,ij,xz} \\ \Theta_{c,ij,yx} & \Delta k_{c,ij,y} & \Theta_{c,ij,yz} \\ \Theta_{c,ij,zx} & \Theta_{c,ij,zy} & \Delta k_{c,ij,z} \\ \Delta p_{c,ij,x} & \Delta p_{c,ij,y} & \Delta p_{c,ij,z} \end{bmatrix} & \begin{bmatrix} \Delta k_{d,ij,x} & \Theta_{d,ij,xy} & \Theta_{d,ij,xz} \\ \Theta_{d,ij,yx} & \Delta k_{d,ij,y} & \Theta_{d,ij,yz} \\ \Theta_{d,ij,zx} & \Theta_{d,ij,zy} & \Delta k_{d,ij,z} \\ \Delta p_{d,ij,x} & \Delta p_{d,ij,y} & \Delta p_{d,ij,z} \end{bmatrix} \end{array} \tag{4.40}$$

Next, the common positions $\Delta p_{c,ij,x}$, $\Delta p_{c,ij,y}$ and $\Delta p_{c,ij,z}$ are neglected, and the in-line (i.e. along the respective gradiometer arm) differential position is taken into account by combining it with the scale factors Δk. The transversal (i.e. perpendicular to the respective gradiometer arm) differential positions are combined with the misalignment angles Θ.

4.3.5. Comparison of methods for ICM calibration

We conclude the chapter on ICM calibration with a comparison between the TAS method by Cesare et al. (2008), and the ESA-L method by Lamarre (2008). Additionally, the ESA-S method by Siemes et al. (2012), which is meant as a validation tool (Drinkwater, 2005), is discussed.

Tables 4.1, 4.2 and 4.3 summarize the most important characteristics of the three calibration (or validation) methods. Bouman (2008) provides a similar overview for the calibration methods (status 2008). All three methods are based on EGG data, as well as on STR measurements (Table 4.1, second column). The latter are needed for the determination of the absolute scale factors.

The TAS method is designed in order to retrieve exclusively the three sets of ICMs for the three gradiometer arms (Table 4.1, third column). Primarily, only the last three rows of the ICMs, i.e. 54 parameters, are determined. They contain the common and differential parts of the gradiometer imperfections, which are needed for the retrieval of the corrected CM and DM accelerations. Hence, the TAS method uses directly the CM and DM

accelerations as input. In contrast to that, the ESA-L and the ESA-S methods start with the EGG linear and angular accelerations, in order to retrieve primarily the 72 parameters describing all six accelerometers. The 54 elements of the last three rows of the ICMs are derived from the 72 gradiometer parameters in a next step. The ESA-L and the ESA-S methods further provide corrected values for the rotation matrices from the SSRFs to the GRF. This information is used in the upgraded version of PDS' EGG processing, by introducing the new values in the respective `AUX_EGG_DB` files.

The TAS and the ESA-L method are designed for the use of calibration mode data, i.e. for the data from satellite shaking periods, which last for one day (Table 4.1, fourth column). The ESA-S method has been developed on the basis of Kern et al. (2007) with focus on estimating calibration parameters from science mode data, i.e. from the data collected during a measurement phase. For this task the ESA-S method needs a data period of (at least) two days. Moreover, the ESA-S method can also be applied to the calibration mode data. In this case, the time period of one day is sufficient, because the data from the satellite shakings has a beneficial signal to noise ratio (in the UMB).

All three methods work primarily in the UMB, i.e. the condition equations are filtered to the frequency range from 50-100 mHz, where the assumption holds that the gravity gradient signal is negligibly small an thus can be set to zero (Table 4.2). The TAS and the ESA-L methods have several similarities, e.g. that the determination of the absolute parameters is performed by comparing the data from gradiometer and from star sensors at a frequency of 1.3 mHz, and that they both make use of the orthogonality relations. For the ESA-S method we have to distinguish between science and calibration mode data, for three of the 12 condition equations. These are the equations related to the diagonal GGT elements (filtered in the UMB). In case of science mode, the centrifugal terms in these equations are assumed to be zero (in UMB), whereas in case of calibration mode, the centrifugal terms are taken from the star sensor measurements. This is according to Siemes et al. (2012) possible, because the angular accelerations generated during the satellite shaking in the UMB result in centrifugal accelerations that exceed by far the star sensor noise. The relationship between the ICMs from TAS calibration step 1 (or 3) and the exact ICM elements was found by Cesare and Catastini (2008b) with 9 numerical test cases, which leads to the application of empirical corrections. Meanwhile, most of the results from the numerical tests can be followed analytically. Nevertheless, the use of these empirical corrections might be a weakness of the TAS method. The convergence checks in the TAS iterative procedure are performed step-by-step, i.e. once the convergence of a certain ICM element is reached, it is kept constant in the following iterations. A simultaneous convergence check for all ICM elements might be more strict and thus preferable (not proven).

The TAS calibration is the only method of the three, which is fully automated in PDS (Table 4.3). This has the advantage that less human interaction is needed, as e.g. for the ESA-L method, which is carried out by ESA. On the other hand, it has the drawback that potential improvements can not be tested as easily. At IAPG, we have performed a test with our implementation of the TAS method, which indicates that the method seems to be more sensitive to errors in the STR data than the ESA-L method (cf. Sect. 5.2.3).

From theory, as well as from data analyses, as e.g. performed in Sect. 5.1.3, we conclude that the ESA-L method might be more advantageous than the TAS method. The ESA-S method delivers results of high quality, following a straightforward least squares approach, which includes also a corresponding error model. Although primarily meant for validation purposes, it seems to be competitive to the ESA-L method, when using calibration mode data. Its results obtained during the measurement phases have triggered several improvements for the calibration in PDS' L1b processing. This aspect is further discussed in Sect. 6.5.

Table 4.1.: Characteristics (input, output and calibration window) of ICM calibration methods.

Method	Input	Output	Calibration Window
TAS	CM, DM accelerations, STR data	ICMs	One day (calibration mode)
ESA-L	Linear/angular accelerations, STR data	ICMs, 72 gradiometer parameters, Rotation matrices from SSRFs to GRF	One day (calibration mode)
ESA-S	Linear/angular accelerations, STR data	ICMs, 72 gradiometer parameters, Rotation matrices from SSRFs to GRF	Two days (science mode), One day (calibration mode)

Table 4.2.: Characteristics (conditions, constraints and assumptions) of ICM calibration methods.

Method	Conditions, Constraints and Assumptions
TAS	Gravity gradient signal (in UMB) assumed to be zero, 9 equations (in UMB) based on DM for relative parameters, 3 equations (at 1.3 mHz) based on EGG + STR angular acc. for absolute scale factors, Upper limits for ICMs by construction, Relationship between sub-matrices of ICMs, Orthogonality relations, Empirical corrections
ESA-L	Gravity gradient signal (in UMB) assumed to be zero, 12 conditions (in UMB) based on gravity gradients and CM for relative parameters, 3 equations (at 1.3 mHz) based on EGG + STR angular rates for absolute parameters, Orthogonality relations
ESA-S	Gravity gradient signal (in UMB) assumed to be zero, 12 conditions based on CM, angular accelerations and diagonal elements of GGT, For science data: centrifugal terms in equations for GGT elements are zero (in UMB), For calibration data: centrifugal terms from STR used in equations for GGT elements (in UMB)

Table 4.3.: Characteristics (implementation, classification and human interaction) of ICM calibration methods.

Method	Implementation	Classification	Human Interaction
TAS	PDS	Calibration	None (automated)
ESA-L	ESA (ESTEC)	Calibration	High
ESA-S	ESA (ESTEC)	Validation	Medium

5. Analysis of real GOCE data

In this chapter we discuss various aspects of the gradiometer and star sensor measurements of GOCE. After the description of the nominal EGG processing in Chapters 3 and 4, we focus in this chapter on the real GOCE data. Further analyses of the gravity gradients can be found in Bouman et al. (2011).

In the first part of this chapter the gravity gradients and their components (angular rates and differences of accelerations) are analyzed in time and frequency domain. The impact of substituting a partial or complete accelerometer is investigated. This serves as a quality check for the individual accelerometer measurements. A spectral analysis of the CM accelerations is performed, which allows an error assessment of the individual accelerations. These errors are propagated to the level of gradiometer angular accelerations and angular rates. The temporal variations of the calibration parameters from the first 11 calibrations are discussed. It is, e.g., shown that the temporal variation of some scale factors in between two calibrations is larger than expected.

In the second part of the chapter we focus on the star sensor measurements. The arrangement of the three star sensors with respect to the gradiometer is illustrated, and its impact on the quality of the star sensor measurements in GRF is investigated. Additionally, the role of the star sensors for the determination of the calibration parameters is analyzed. We show that some scale factors are strongly depending on the star sensor measurements, especially for the TAS ICM calibration method.

5.1. Gradiometer

5.1.1. Spectral analysis of the gravity gradients

In this section we investigate various aspects of the gravitational gradients as measured by GOCE. We follow the explanations given in Rummel et al. (2011). The data used are from the first measurement cycle from 31 October to 30 December 2009. Some of the tests are based on only the day 11 November 2009. From a comparison of the data sets of the 61 days period, it can be concluded that the chosen daily segment is representative.

Angular velocities

As shown in Sect. 2.2, the components D_{ij} of Eq. 2.21b contain the centrifugal part $\underline{\Omega}\,\underline{\Omega}$. It has to be subtracted in order to arrive at the gravitational gradient tensor components V_{ij}. Thus, it has to be shown that the quality of the estimation of the angular velocities is adequate. As pointed out in Sect. 3.4, the angular velocities are derived from a combination of angular accelerations, as measured by the gradiometer, and orientation angles from star tracking, see also Stummer et al. (2011).

The root PSDs of the angular velocities (sum of signal and noise) are shown in Fig. 5.1. The components are ω_x (rotation about the x-axis or roll), ω_y (rotation about the y-axis or pitch), ω_z (rotation about the z-axis or yaw). The signal strength of ω_x is higher than that of ω_y and ω_z. This is due to the higher rotational instability of the satellite along its main body axis. The absolute value of ω_y (not shown in Fig. 5.1) is by far greater than that of ω_x and ω_z. It is caused by the high angular rate about the y-axis of one cycle per revolution (cpr) of the Earth-pointing satellite ($\omega_y \approx (2 \cdot \pi)/5400$ s $\approx 1.16 \cdot 10^{-3}$ rad/s). Figure 5.1 also displays the MB and the engineering requirements. They are given in terms of an allowed maximum signal slope in the spectral range from $5 \cdot 10^{-3}$ to $2 \cdot 10^{-2}$ Hz and a maximum signal level between $2 \cdot 10^{-2}$ to 0.1 Hz. It can be seen that the requirements are met in all three cases.

The root PSDs of the squared angular velocities, again, sum of signal and noise, show a different behavior. Squaring in the time domain corresponds to convolution of the spectrum of the time series with itself in the spectral domain. The high average value of ω_y results in a power spectral density of ω_y^2 higher than that of ω_x^2 and ω_z^2. Figure 5.2 shows the root PSDs of the diagonal terms, Fig. 5.2(a), and of the non-diagonal terms, Fig. 5.2(b), of $\underline{\Omega}\,\underline{\Omega}$. Those of the diagonal terms, containing ω_y^2, are higher than the one with $(\omega_x^2 + \omega_z^2)$, which belongs to D_{yy}. Also in the case of the non-diagonal components, the term $\omega_x\omega_z$ has a lower level than the two

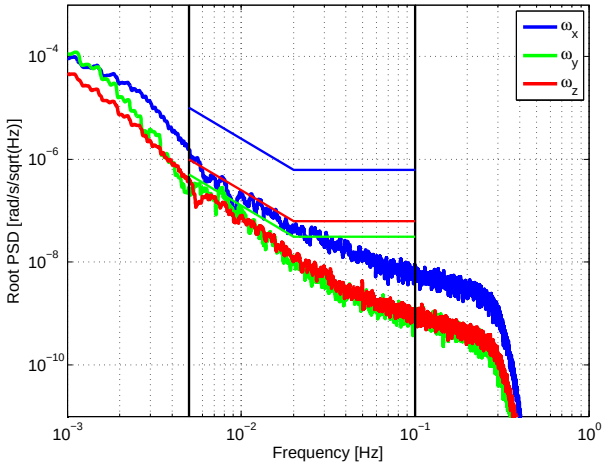

Figure 5.1.: Root PSD of angular velocities of 11 November 2009.

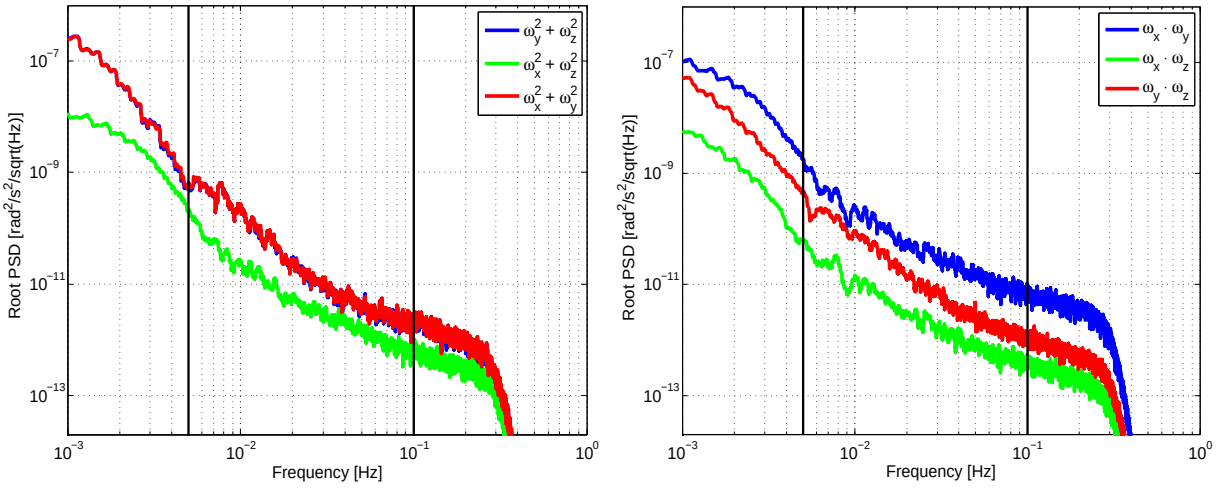

Figure 5.2.: Root PSD of combinations of angular velocities for GGT components (compare Eq. 2.20) of 11 November 2009.

others which contain ω_y. The level of $\omega_x\omega_y$ is greater than that of $\omega_y\omega_z$, because of the higher level of ω_x, as displayed in Fig. 5.1 and mentioned above.

Figure 5.3 gives the complete picture in terms of root PSDs. It shows a set of them for all six components. Each set consists of three root PSDs that of D_{ij}, V_{ij} and of the centrifugal part $\underline{\Omega}\,\underline{\Omega}$. The gravitational gradients V_{ij} are obtained by subtracting the angular velocity part from the measured D_{ij}. All quantities are derived from the actual measurements, therefore they contain signal and noise. Inside the MB, the root PSDs of D_{ij} and of V_{ij} almost coincide, which highlights the fact that the contribution of the centrifugal part is much smaller. Only for the $\{xx\}$-component the angular part comes rather close in size to the gradiometric signal at the lower end of the MB and at 3 to $4 \cdot 10^{-2}$ Hz. Below the MB, the centrifugal contribution dominates the gradiometric signal. Only for V_{xz} the contribution of the angular part is significantly lower than the gravity gradient signal over the entire range of the spectrum.

Under the assumption that the gradiometer noise is white inside the MB, it can be observed that the noise floor is reached at about $3 \cdot 10^{-2}$ Hz. The noise levels are 10 mE/$\sqrt{\text{Hz}}$ for V_{xx} and V_{yy}, and unfortunately about 20 mE/$\sqrt{\text{Hz}}$ for V_{zz} and V_{xz}. The cause of the higher noise level of V_{zz} and V_{xz} is not yet fully understood. In agreement with our expectations, the gradiometric signal is concentrated between $5 \cdot 10^{-3}$ Hz and $3 \cdot 10^{-2}$ Hz, as shown by the red curves. It decreases from about 1 E/$\sqrt{\text{Hz}}$ to the white noise floor at about $3 \cdot 10^{-2}$ Hz. As expected, the performance of V_{xy} and V_{yz} is inferior, with a noise level of between 0.6 to 0.8 E/$\sqrt{\text{Hz}}$.

Systematic behavior

In Fig. 5.4 the root PSDs of the three diagonal gravitational gradients are shown together with their trace, derived from the full two months data cycle. The MB and engineering requirements are included as well.

We will now attempt to explain the systematic behavior below the MB and the noise characteristics in the MB. The accelerometers are designed so as to have their ultra-high precision in the MB. As is the case for any accelerometer the noise increases below the MB inversely with frequency, i.e. with $1/f$. In the time domain this is comparable to the typical drift of gravimeters. Superimposed to the drift are cyclic "distortions" at one cpr and multiples of one cpr. They enter into the measurements via the orbit and attitude motion of the spacecraft. Thus, even though the gradiometer is an in-situ instrument, the orbit periods are modulated into the accelerometer measurements via orbit perturbations. In addition, periodic effects enter via the attitude motion, i.e. through periodic changes in orientation of the gradiometer. Attitude control is done by magnetic torquing. The periodicity is therefore coupled to attitude motion in the Earth's magnetic field.

In the areas of the magnetic poles, rather strong cross-winds affect the y-component of the accelerometers, cf. Lühr et al. (2007). If the gradiometer were perfect, these side winds would be measured as common-mode signal only in y-direction and would cancel out in the differential mode. For a real gradiometer and non-perfect ICMs a small effect enters the differential mode as well. It is visible in V_{yy} in the auroral regions, cf. Bouman et al. (2011).

In Fig. 5.4 as in Fig. 5.3 the white noise level is approximately 10 mE/$\sqrt{\text{Hz}}$ for V_{xx} and V_{yy} and 20 mE/$\sqrt{\text{Hz}}$ for V_{zz}. It is visible for frequencies above $3 \cdot 10^{-2}$ Hz. We see the strong gradiometric signal power in the range from $5 \cdot 10^{-3}$ Hz to $3 \cdot 10^{-2}$ Hz, towards the low frequencies more and more superimposed by the $1/f$-instrument noise, and more significantly, by the orbit and attitude induced periodic effects at one cpr and multiples of one cpr.

A very powerful test of the instrument performance is the Laplace condition, Eq. 2.8. Theoretically it gives zero, yet in practice it shows the noise level of the sum of the measured diagonal gravitational gradients. The engineering requirement of the trace, based on a pre-launch analysis of the sensor performance is 11 mE/$\sqrt{\text{Hz}}$ in the upper part of the MB. The actual trace is about 20 mE/$\sqrt{\text{Hz}}$ mainly due to the higher noise level of V_{zz}, compare Fig. 5.4. This level of 20 mE/$\sqrt{\text{Hz}}$ is almost constant between $2 \cdot 10^{-2}$ Hz and 0.1 Hz with a gradual increase towards the lower frequencies. At the lower end of the MB it is between about 40 to 100 mE/$\sqrt{\text{Hz}}$, i.e. slightly below the requirement. We also observe the $1/f$ increase and periodicities below 5 mHz. Theoretically the periodicities in the orbit and attitude control should have no effect on the closure of the Laplace condition. Possible candidates for this behavior could either be the different low frequency systematic error behavior of each of the gradiometer components or an imperfect removal of the contribution of the angular rates.

As pointed out, noise dominates signal at about $3 \cdot 10^{-2}$ Hz. This corresponds to a maximum degree and order of a spherical harmonic expansion of about $n \approx 205$. The collection of more and more gradiometer data will help us improve spherical harmonic analysis, as discussed in Pail et al. (2011). As a rule of thumb one can expect the accuracy of spherical harmonic coefficients to improve with the square-root of the number of full mission cycles (each being 61 days).

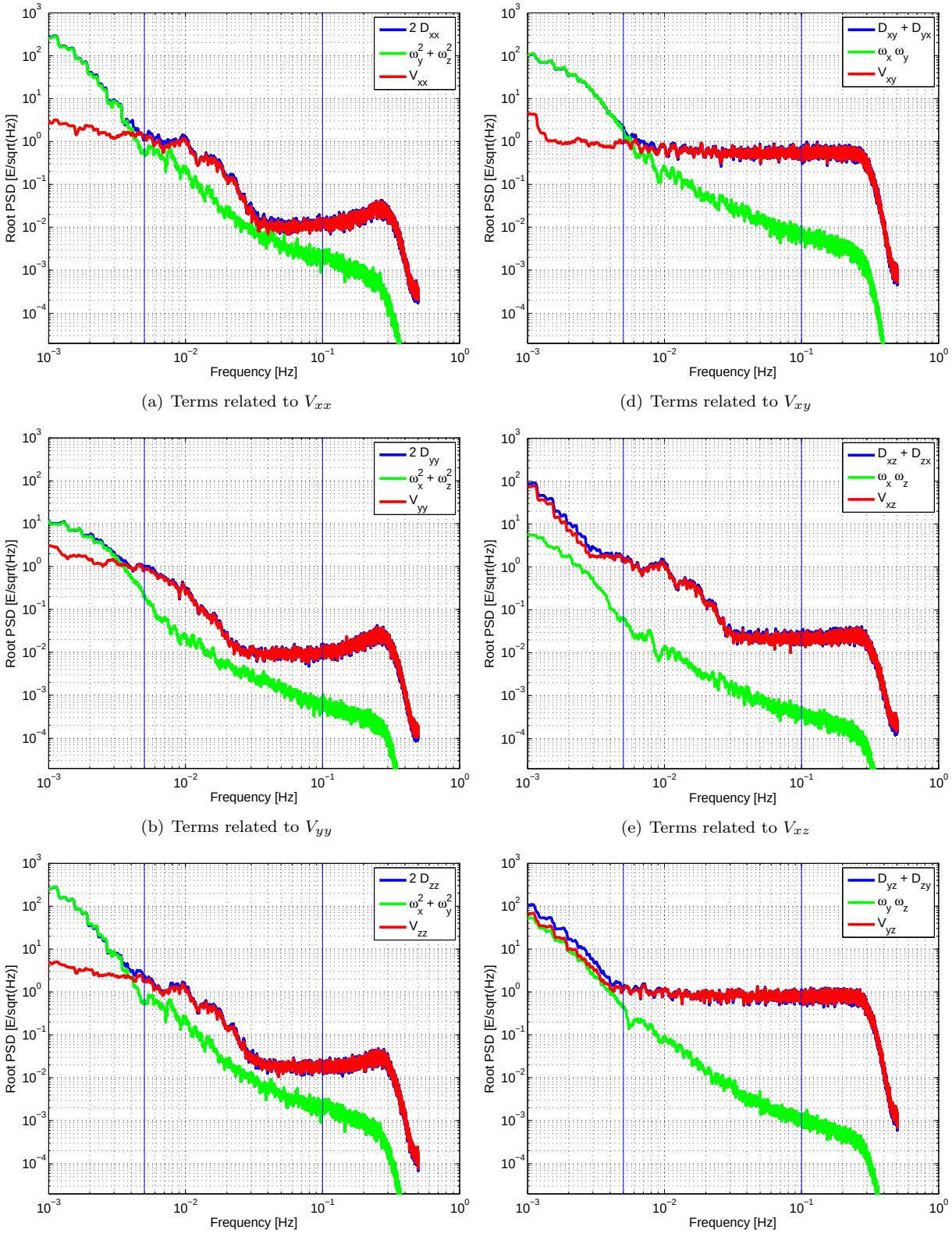

(a) Terms related to V_{xx}

(d) Terms related to V_{xy}

(b) Terms related to V_{yy}

(e) Terms related to V_{xz}

(c) Terms related to V_{zz}

(f) Terms related to V_{yz}

Figure 5.3.: Root PSD of the six measured differential accelerations (blue), the corresponding component in GGT (red) and the corresponding combination of angular velocities (green) of 11 November 2009, cf. Eq. 2.21b.

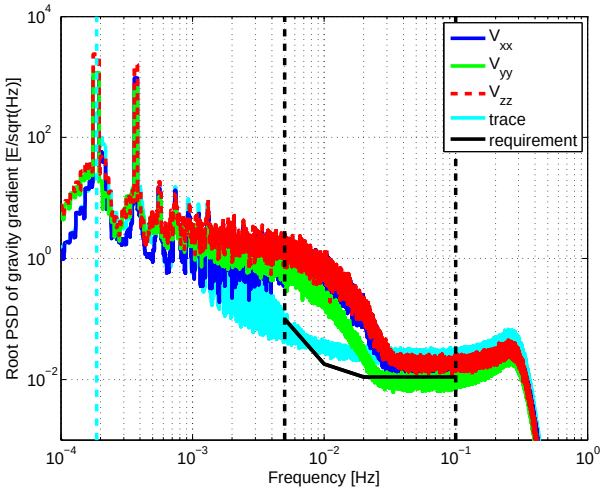

Figure 5.4.: Root PSD from two months of data of V_{xx}, V_{yy}, V_{zz} and trace; also shown is the engineering requirement for the trace (black), the measurement band (black dashed) and the once-per-revolution (cpr) frequency (cyan dashed).

From the above it can be concluded that careful filtering of the low frequency distortions is essential for an adequate use of GOCE gravitational gradients. This applies especially to the direct use of measured gradients. For spherical harmonic analysis, a correct stochastic modelling is necessary. This aspect is discussed in Pail et al. (2011), in Schuh (2002) and in Brockmann et al. (2010).

5.1.2. Substitution of a partial or complete accelerometer

Each of the six three-axis GOCE accelerometers has two ultra-sensitive and one less sensitive axes. The two US axes measure the control voltages (which are needed to keep the accelerometers proof mass stable) with two electrode pairs, whereas the LS axes have four electrode pairs, respectively. Therefore, in total there are $6 \cdot 8 = 48$ electrode pairs, cf. Fig. 3.3. To check the performance of each of these electrode pairs the original GOCE L1b processing as described in Chapter 3 has been rerun, each time replacing the measurements of one specific electrode pair with the measurements of another one along the same axis, as suggested by Cesare et al. (2008). In Eqs. 3.1 and 3.2 each time one control voltage CV_i of the six accelerometers A_i has been replaced by the corresponding one, according to Table 5.1.

Table 5.1.: Correspondence between the electrode pairs for the replacement of a control voltage.

Replaced Control Voltage	Replacing Control Voltage	Axis in AESRF
$CV_{i,X1}$	$CV_{i,X2}$	X
$CV_{i,X2}$	$CV_{i,X1}$	X
$CV_{i,X3}$	$CV_{i,X4}$	X
$CV_{i,X4}$	$CV_{i,X3}$	X
$CV_{i,X5}$	$CV_{i,X6}$	Y
$CV_{i,X6}$	$CV_{i,X5}$	Y
$CV_{i,X7}$	$CV_{i,X8}$	Z
$CV_{i,X8}$	$CV_{i,X7}$	Z

In Fig. 5.5 the impact of the replacement on the GGT trace is shown for the example day 29 January 2010. For a better visualization, always the root PSD of the difference between the specific new GGT trace (with replacement of the measurements of one electrode pair) and the original one (using all measurements) has been computed.

One can notice two things. First, the replacement of measurements along one specific axis always has a similar impact on the GGT trace. Therefore, it can be excluded that there is one electrode pair with a particularly bad performance. Second, the impact on the GGT trace depends on the axis on which the replacement is done. E.g. the replacement of a z-electrode (in AESRF, red curves) has a significant impact on the GGT trace throughout the

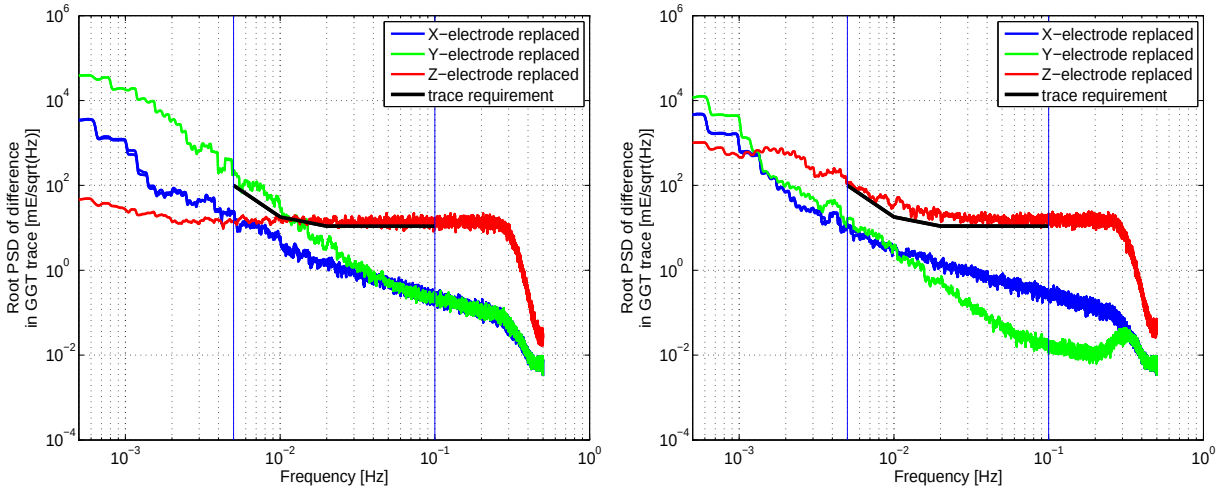

Figure 5.5.: Impact on GGT trace due to the replacement of individual control voltages of accelerometer 1 (a) and of accelerometer 2 (b). Always the root PSD of the difference between the new GGT trace (with replacement of the measurements of one electrode pair) and the original one (using the measurements of all electrode pairs) is shown. Data from 29 January 2010.

complete gradiometer MB. Table 5.2 gives a detailed overview of the impact of electrode replacements on the individual gradients.

Table 5.2.: Overview - Impact on gradients due to replacement of control voltages.

Sensitivity	Arrange-ment	A_i	Axis in AESRF	Axis in GRF	Impact on	Frequency Range
US	In-line	1/4	Z	X	V_{xx}	Within MB
		2/5	Z	Y	V_{yy}	
		3/6	Z	Z	V_{zz}	
US	Transversal	1/4	Y	Z	$\dot{\omega}_y \Rightarrow V_{xx}, V_{zz}$	Lower MB
		2/5	Y	X	$\dot{\omega}_z \Rightarrow V_{xx}, V_{yy}$	Not significant
		3/6	Y	X	$\dot{\omega}_y \Rightarrow V_{xx}, V_{zz}$	Lower MB
LS	Transversal	1/4	X	Y	$\dot{\omega}_z \Rightarrow V_{xx}, V_{yy}$	Not significant
		2/5	X	Z	$\dot{\omega}_x \Rightarrow V_{yy}, V_{zz}$	
		3/6	X	Y	$\dot{\omega}_x \Rightarrow V_{yy}, V_{zz}$	

In order to check the performance of the six accelerometers as a whole six sets of gravity gradients have been computed, according to the original GOCE L1b processing (cf. Chapter 3), each time replacing one complete accelerometer by a so-called virtual accelerometer A_{vi}, with $i = 1, ..., 6$. The virtually measured accelerations $\overline{a}_{vi}$ are formed by the CM accelerations, cf. Eq. 2.27, of the corresponding remaining accelerometers, according to Cesare et al. (2008). Table 5.3 gives an overview of the necessary modifications in the EGG processing for the replacement of a complete accelerometer.

Table 5.3.: Definition of virtually measured accelerations $\overline{a}_{vi}$ and lengths of virtual baselines L_{vx}, L_{vy}, L_{vz} for the replacement of a complete accelerometer.

Replaced Accelerometer	Virtually Measured Accelerations	Length of Virtual Baseline
A_1	$\overline{a}_{v1} = \frac{1}{2}(\overline{a}_{v3} + \overline{a}_{v6})$	$L_{vx} = \frac{1}{2} \cdot L_x$
A_2	$\overline{a}_{v2} = \frac{1}{4}(\overline{a}_{v1} + \overline{a}_{v4} + \overline{a}_{v3} + \overline{a}_{v6})$	$L_{vy} = \frac{1}{2} \cdot L_y$
A_3	$\overline{a}_{v3} = \frac{1}{2}(\overline{a}_{v1} + \overline{a}_{v4})$	$L_{vz} = \frac{1}{2} \cdot L_z$
A_4	$\overline{a}_{v4} = \frac{1}{2}(\overline{a}_{v3} + \overline{a}_{v6})$	$L_{vx} = \frac{1}{2} \cdot L_x$
A_5	$\overline{a}_{v5} = \frac{1}{4}(\overline{a}_{v1} + \overline{a}_{v4} + \overline{a}_{v3} + \overline{a}_{v6})$	$L_{vy} = \frac{1}{2} \cdot L_y$
A_6	$\overline{a}_{v6} = \frac{1}{2}(\overline{a}_{v1} + \overline{a}_{v4})$	$L_{vz} = \frac{1}{2} \cdot L_z$

The virtually measured accelerations are, as far as possible, formed by US measurements. An accelerometer along the x-axis of GRF (A_1 or A_4) is replaced by the pair A_3 and A_6, which have the same alignment of the US axes, cf. Fig. 2.2. Analogously, an accelerometer along the z-axis of GRF (A_3 or A_6) is replaced by the pair A_1 and A_4. An accelerometer along the y-axis of GRF (A_2 or A_5) is replaced by all accelerometers along the other gradiometer arms, in order to average, and thus reduce as much as possible, the measurement error along the y-direction in GRF. In this case, only LS measurements can be used, because A_1, A_4, A_3 and A_6 have their LS axis in this (y-GRF) direction. Note that also the gradiometer baselines change for the concept of a virtual accelerometer. The virtual accelerometer can be imagined at the center of the gradiometer, hence, the baseline to which the replaced accelerometer belongs, has to be divided in halves. In the EGG processing, the baseline lengths are needed for the computation of the calibrated gradiometer angular accelerations in Sect. 3.3, cf. Eqs. 2.47 to 2.49.

In Fig. 5.6 the root PSD of the GGT trace for all six cases of accelerometer replacement is shown. Again, one can notice two things. First, the impact on the GGT trace is similar for the accelerometers on the same gradiometer arm. Second, the impact is depending on the axis on which the replacement is done. The GGT trace is degraded the most, if an accelerometer on the y-axis of the GRF, i.e. accelerometer A_2 or A_5 (green curves), is replaced. The reason is that accelerometers A_2 and A_5 are the only ones with US axes in y-GRF direction, which is the main measurement direction in this case. Therefore, the y-direction of the corresponding virtual accelerometer can only be built from LS measurements.

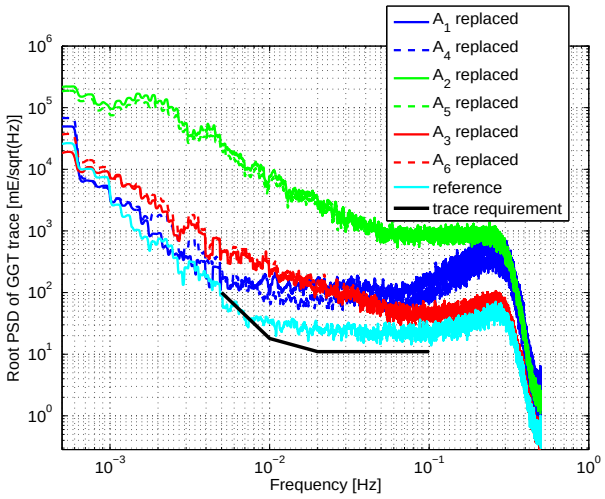

Figure 5.6.: Impact on GGT trace due to replacement of complete accelerometers. Data from 29 January 2010.

5.1.3. Spectral error analysis using common mode accelerations

With the three sets of CM accelerations the (same) linear accelerations acting on the satellite are measured. The accelerometers are mounted in such a way that the x-direction of GRF is measured by US axes only, the y-direction is measured two times by LS axes, and the z-direction is measured two times by US axes only (cf. Fig. 2.2). From simple error propagation one can derive $\sigma_{a\_comb\_US/LS} = \sqrt{2}\sigma_{a\_c/d\_US/LS}$, with $\sigma_{a\_comb\_US/LS}$ the standard deviation of the US or LS common mode combination, and $\sigma_{a\_c/d\_US/LS}$ the standard deviation of the corresponding US or LS common mode or differential acceleration. Moreover $\sigma_{a\_c/d\_US/LS} = \left(1/\sqrt{2}\right)\sigma_{a\_US/LS}$, with $\sigma_{a\_US/LS}$ the standard deviation of an individual US or LS acceleration measurement. Thus, $\sigma_{a\_comb\_US/LS} \approx \sigma_{a\_US/LS}$ holds, and the respective common mode combinations can be taken as a good indicator of the real US or LS acceleration noise.

In Fig. 5.7 the common mode combinations are shown for the day 1 November 2009. In the first row the uncalibrated values are given. In the second row, the accelerations have been calibrated with the ICMs of October 2009 as derived with the TAS method (Sect. 4.3.3). In the third row the ICMs of October 2009 as derived with the ESA-L method (Sect. 4.3.4) have been used.

The combinations of uncalibrated accelerations in x-direction (Fig. 5.7(a)) are rather flat in the MB with a level of about $10^{-11}\ m/s^2/\sqrt{Hz}$ and an increase of noise towards the lower frequencies, starting from about 10 mHz.

After calibration of the common mode accelerations with the ICMs (of October 2009) from the TAS method, the same combinations in x-direction change slightly, cf. Fig. 5.7(b). The noise level of the two combinations

including $a_{c,25,x}$ (red and blue) becomes slightly higher, whereas the noise level of the combination without $a_{c,25,x}$ (green) is slightly reduced. For the frequencies below the MB the noise level is significantly reduced for all three combinations. In this case, it is reduced the most for the combination without the measurement of gradiometer arm 36 (blue), to e.g. only $5 \cdot 10^{-11}\ m/s^2/\sqrt{Hz}$ at a frequency of 1 mHz.

When the common mode accelerations are calibrated with the ICMs (of October 2009) from the ESA-L method instead (Fig. 5.7(c)), the three combinations change slightly again. In this case the combination without the measurement of gradiometer arm 36 (blue) performs best in the MB as well as for lower frequencies. When comparing with Fig. 5.7(b), where the TAS calibration has been applied, one observes a similar noise level for frequencies below the MB and an improved behavior for the frequencies above the MB.

The combinations of the two LS common mode measurements in y-direction, Fig. 5.7(d), 5.7(e), 5.7(f), blue curves, have a flat noise level of about $4 \cdot 10^{-10}\ m/s^2/\sqrt{Hz}$ for the complete frequency range. This is true for the uncalibrated values, as well as for the calibrated values with the ICMs from TAS or ESA-L method.

For the combination of the two US common mode measurements in z-direction (Fig. 5.7, right, green curves), we observe an increase of the noise towards the lower frequencies for the uncalibrated values (Fig. 5.7(d)), and to a smaller extent also for the values, which have been calibrated with the ICMs from the TAS method (Fig. 5.7(e)). For the ESA-L calibration, in contrast, the combination in z-direction is flat in the complete MB (and also for higher frequencies) with a noise level of about $10^{-11}\ m/s^2/\sqrt{Hz}$, comparably to the noise level of the US combinations in x-direction (Fig. 5.7, left).

The common mode combinations, which are interpreted as errors of the individual US and LS accelerations, can be used for a rough estimation of the errors of derived quantities in the MB, such as the angular accelerations, angular rates, main diagonal GGT elements and the GGT trace. The corresponding equations and results of a simple error propagation are summarized in Table 5.4. Note that for these estimations a value of 0.5 meters has been used for the length of the baselines (L_x, L_y, L_z) in the equations for the angular accelerations ($\dot{\omega}_x$, $\dot{\omega}_y$, $\dot{\omega}_z$, Eqs. 2.47 to 2.49) and the diagonal components of the GGT (V_{ii}, Eqs. 2.50 to 2.52).

Table 5.4.: Error propagation within the gradiometer MB based on combinations of common mode accelerations.

Variable	Equation	Error Propagation
$a_{c/d,US/LS}$	$\frac{1}{2}(a_{US/LS} \pm a_{US/LS})$	$\sigma^2_{a_{c/d,US/LS}} = \frac{1}{2}\sigma^2_{a_{US/LS}}$
$a_{comb,US/LS}$	$a_{c,US/LS} - a_{c,US/LS}$	$\sigma^2_{a_{comb,US/LS}} = 2 \cdot \sigma^2_{a_{c/d,US/LS}}$
$\dot{\omega}_x$	$-2a_{d,LS} + 2a_{d,LS}$	$\sigma^2_{\dot{\omega}_x} = 8\sigma^2_{a_{c/d,LS}}$
$\dot{\omega}_y$	$-2a_{d,US} + 2a_{d,US}$	$\sigma^2_{\dot{\omega}_y} = 8\sigma^2_{a_{c/d,US}}$
$\dot{\omega}_z$	$+2a_{d,LS} - 2a_{d,US}$	$\sigma^2_{\dot{\omega}_y} = 4(\sigma^2_{a_{c/d,LS}} + \sigma^2_{a_{c/d,US}})$
V_{ii}	$\approx -4a_{d,US}$	$\sigma^2_{V_{ii}} = 16\sigma^2_{a_{c/d,US}}$
GGT_{trace}	$V_{xx} + V_{yy} + V_{zz}$	$\sigma^2_{GGT_{trace}} = 3\sigma^2_{V_{ii}}$

In the following the errors of these derived quantities are shown with example data. The computations are based on the error curves of common mode combination $a_{c,25,x} - a_{c,36,x}$ (calibrated with ICMs from ESA-L method, red in Fig. 5.7(c)) for the error of an US acceleration, which is representing the worst case of US combinations for this example day and on the error curve of the (only possible) common mode combination in y-direction $a_{c,14,y} - a_{c,36,y}$ (calibrated with ICMs from ESA-L method, blue in Fig. 5.7(f)) for the error of a LS acceleration.

Figure 5.8(a) shows the corresponding error root PSDs of the angular accelerations. They can be compared to the root PSDs of the calibrated gradiometer angular accelerations (including errors) of Fig. 3.15(b), which have a flat spectrum for frequencies higher than about 50 mHz, with a level of about $4 \cdot 10^{-9}\ \mathrm{rad/s^2/\sqrt{Hz}}$ for $\dot{\omega}_x$ and about $7 \cdot 10^{-10}\ \mathrm{rad/s^2/\sqrt{Hz}}$ for $\dot{\omega}_y$ and $\dot{\omega}_z$. The comparison shows that for the x- and y-component the error root PSDs are smaller than the root PSDs of the measurements (including signal and errors), whereas for the z-component the error root PSD and the root PSD of the measurement have approximately the same magnitude.

In the MB, the angular rates are obtained by integration of the gradiometer angular accelerations. Hence, the errors of the angular rates (Fig. 5.8(b)) are obtained by $\sigma_{\omega_i} = \sigma_{\dot{\omega}_i}/(2 \cdot \pi \cdot f)$, with frequency f. In Cesare (2008) requirements for the angular rate errors in the MB are given. Numerical values are provided only for the maximum errors in the MB. The development of the requirements throughout the complete MB are illustrated in a figure. We observe that these requirements are all well met for the derived angular rate errors of Fig. 5.8(b).

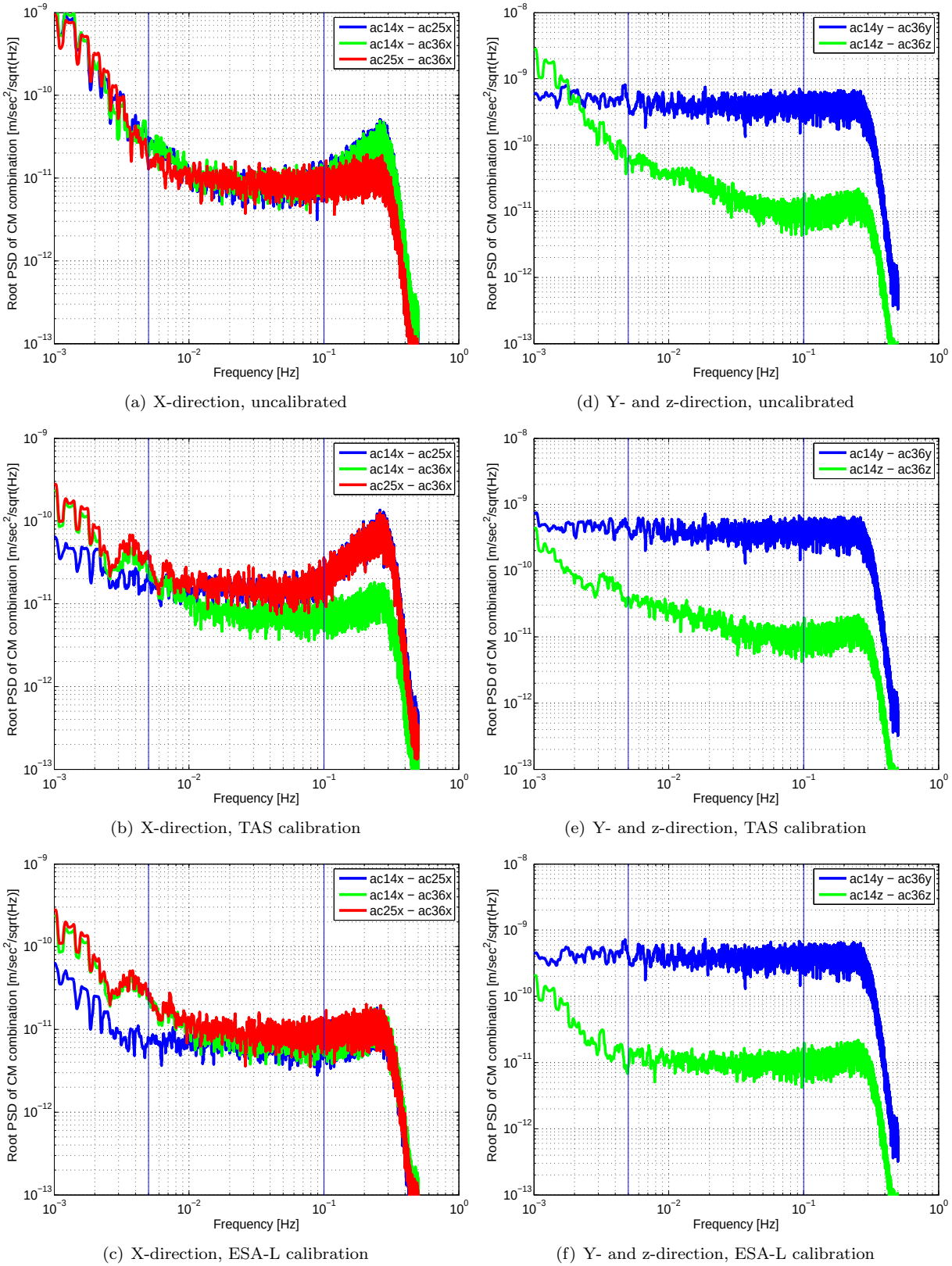

(a) X-direction, uncalibrated

(d) Y- and z-direction, uncalibrated

(b) X-direction, TAS calibration

(e) Y- and z-direction, TAS calibration

(c) X-direction, ESA-L calibration

(f) Y- and z-direction, ESA-L calibration

Figure 5.7.: Root PSD of combination of common mode accelerations in x-direction (left) and in y- and z-direction (right) of 1 November 2009. The first row shows the uncalibrated accelerations. The second and third row give the calibrated accelerations, where the ICMs from TAS method or from ESA-L method, respectively have been applied.

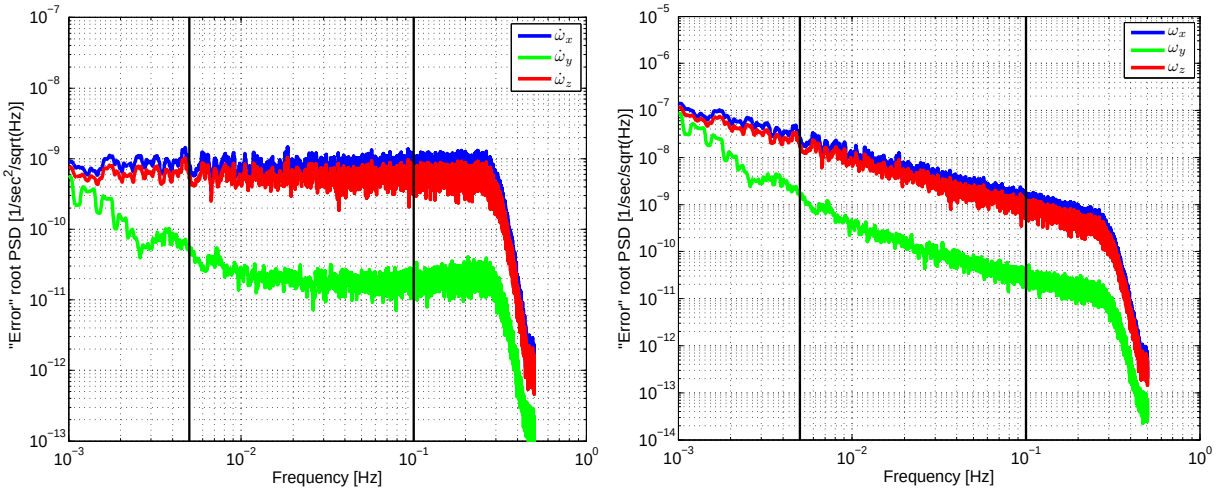

Figure 5.8.: Error root PSD of angular accelerations (a) and angular rates (b) as derived from common mode combinations.

5.1.4. Temporal variations of calibration parameters

In this section the temporal variations of the calibration parameters contained in the ICMs are discussed.

Before launch, the temporal stability of the ICMs has been predicted to be sufficient throughout a measurement cycle. Thus, in the original L1b processing, the calibration of the accelerations is based on the ICMs from the previous calibration phase.

The analysis of the ICMs from the first six calibrations has shown that the calibration parameters are in general very stable (Frommknecht et al., 2011). This holds especially for the mechanical stability of the gradiometer, corresponding to those ICM elements which account for non-orthogonal accelerometer axes and misalignments. Nevertheless, it was found that the variation of some scale factors in between two calibrations is larger than expected. This leads to a degradation of the gravity gradient performance, which is increasing with time during a measurement cycle. This fact can be explained with Eq. 4.15, which describes the calibration of the measured CM and DM accelerations using the ICMs. The last three rows of Eq. 4.15 describe how the DM accelerations, which contain the gravity gradient signal, are calibrated. In the case that ICMs are applied, which are not perfectly correct, but which have a certain error due to their temporal variation, it is possible that parts of the (measured) CM accelerations are projected onto the (corrected) DM accelerations. In the new L1b gradiometer processing, cf. Sect. 6.5, the time dependency of the calibration parameters is taken into account by linear interpolation of the ICMs of subsequent calibrations. This will prevent the quality of the gravity gradients from degradation with time.

In the following the development of the differential scale factors (dSF) of accelerometer pairs 14, 25 (Fig. 5.9) and 36 (Fig. 5.10) for the first 11 calibration events is discussed. The first two calibrations have been performed during the so-called commissioning phase of the GOCE mission (red) under different conditions as for the following calibrations (blue), which makes the corresponding results not directly comparable to the others. Between the first and second calibration phase changes in the common and differential scale factors are observed, which are attributed to the different environment of the spacecraft, i.e. passing through eclipses or not, and applying ion thruster bias or not. Between the second and third calibration also the misalignments change. This is attributed to a change in the angular control of the proof masses. The proof mass rotation about the LS axes (cf. Fig. 3.3 rotation angle ϕ) is no longer controlled by both US axes, but by the transverse US axes only, i.e. by the y-electrodes (AESRF), cf. also Table 3.1. In Figs. 5.9 and 5.10 in addition to the values of the scale factors (red and blue dots), also their required measurement accuracies as derived in Sect. 4.3.2 are indicated as (red and blue) vertical lines. Note that these lines are not the error bars of a least squares adjustment. The upper and lower limits for the bands, where the required measurement accuracies hold, are drawn from each calibration to the next as (red and blue) horizontal lines. We observe that the variation of most of the differential scale factors is (by far) smaller than their required measurement accuracy. For two of them (dSF14z, dSF36z) the variation is just about as large as the respective requirement, and for another two of them (dSF14x, dSF25y) the variation is much larger than expected. The dSF14x is coupled with the in-line CM acceleration $a_{c,14,x}$ in x-direction. In this direction the CM acceleration signal is small due to drag compensation with the ion thruster assembly, cf. Fig. 3.13(a). The dSF25y is coupled with $a_{c,25,y}$, the in-line CM acceleration in y-direction. In this direction strong CM signals occur, cf. Fig. 3.13(b). This is also confirmed by the findings of Lühr et al. (2007) for the accelerometer data of the CHAllenging MiniPayload (CHAMP) mission. In summary, the variation of the in-line differential scale factor in y-direction is much larger than expected and in addition strong CM signals occur in the same direction. From this we can presume that the calibration in y-direction might not work perfectly. In this case, artifacts of the CM signal (in y-direction) would remain in the DM accelerations (in y-direction) and thus also in the GGT component V_{yy}, cf. Eq. 2.51. In Sect. 7.1 this aspect is further discussed. The GOCE gravity gradients are compared to model gravity gradients and the assumption is confirmed that V_{yy} is affected by non-perfect common mode rejection in y-direction.

In Table 5.5 the dates of the first 11 calibration events are given.

Table 5.5.: Date of first 11 ICM calibration events.

no.	date	no.	date	no.	date
		4	11 January 2010		
1	18 June 2009	5	04 March 2010	9	27 January 2011
2	28 September 2009	6	07 May 2010	10	04 April 2011
3	08 October 2009	7	05 October 2010	11	07 June 2011
		8	07 December 2010		

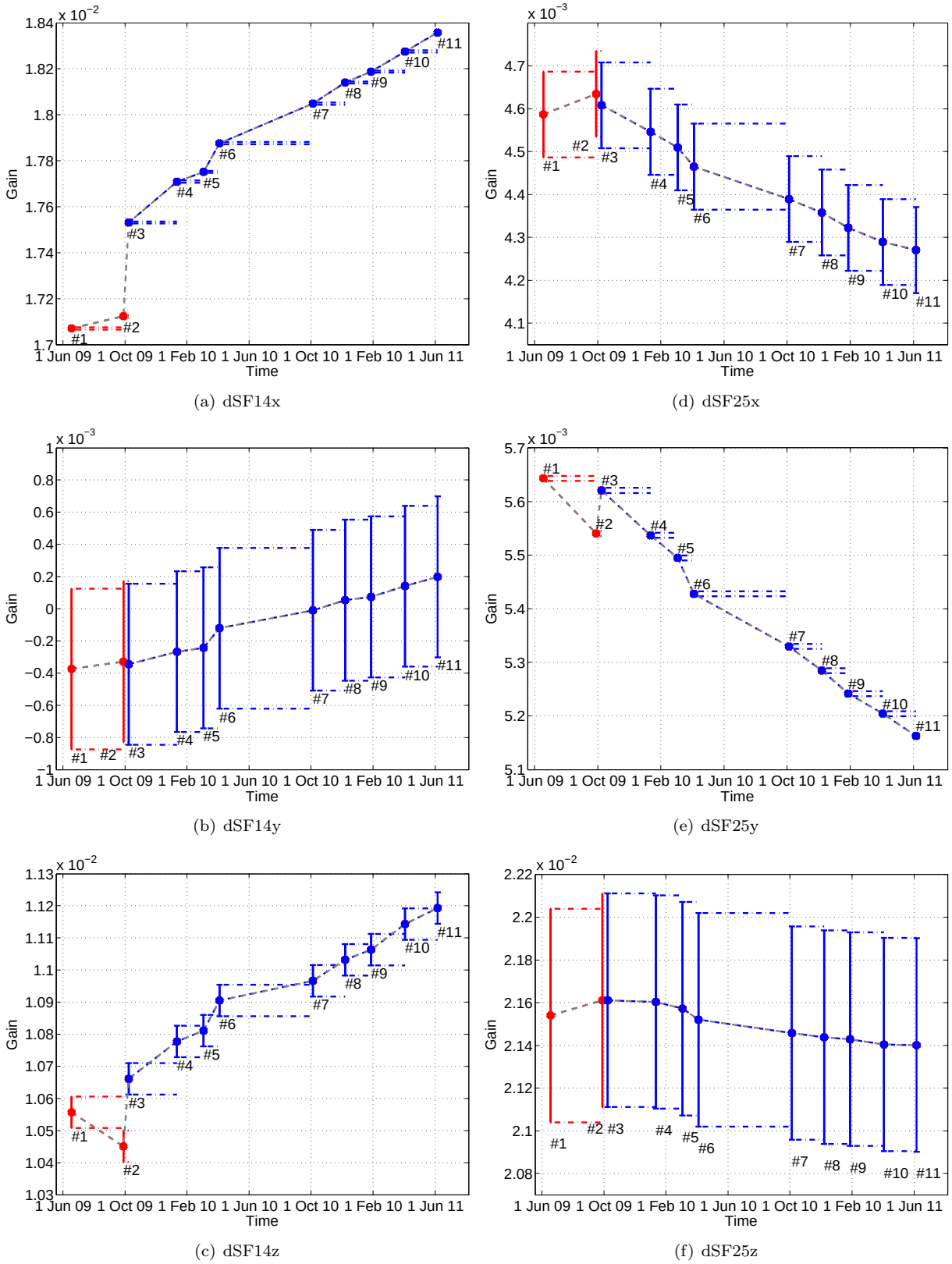

(a) dSF14x (d) dSF25x

(b) dSF14y (e) dSF25y

(c) dSF14z (f) dSF25z

Figure 5.9.: Development of differential scale factors of accelerometer pair 14 (left) and of accelerometer pair 25 (right).

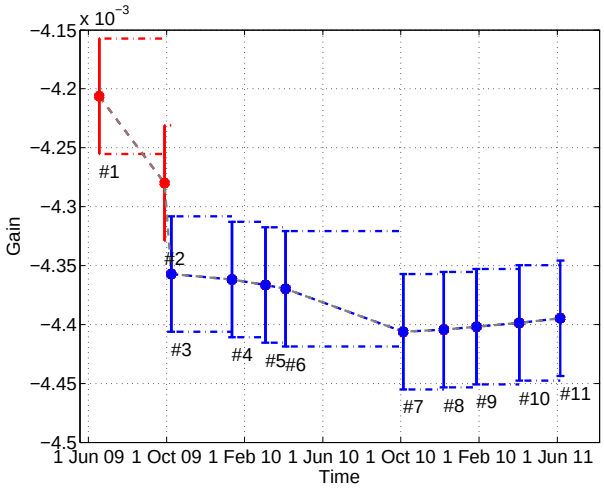

(a) dSF36x

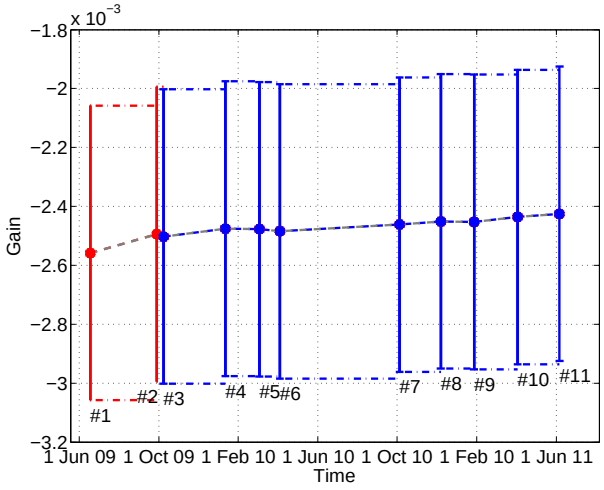

(b) dSF36y

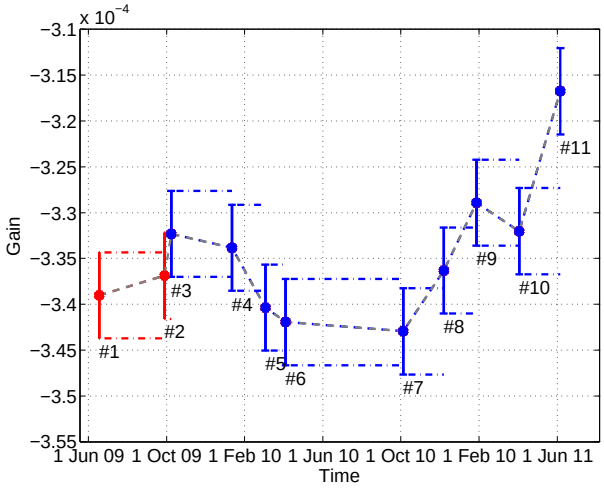

(c) dSF36z

Figure 5.10.: Development of differential scale factors of accelerometer pair 36.

5.2. Star sensors

The accuracy of each GOCE STR can be characterized by the pointing accuracy of the coordinate axes of the respective SSRF, with the z-axis being aligned with the boresight direction, and the x- and y-axes lying in the CCD plain of the STR (Wertz, 1991; Frommknecht, 2008). Due to the geometry between the direction to the observed stars and the coordinate axes of the SSRF it is possible to determine the boresight axis of the STR more accurate than the other two axes. For the GOCE STR the relative accuracy (RA) in-flight is given with 10 μrad or 2 arcseconds for the ultra sensitive boresight axis, and with 100 μrad or 20 arcseconds for the orientation of the other two less sensitive axes (Jørgensen, 2003). For the accuracy of a rotation about the SSRF axes this consequently means that the rotation about the boresight is less well determined than the rotations about the other two STR axes. The corresponding error spectrum of the orientation measurements is regarded as white noise.

5.2.1. Star sensor arrangement with respect to gradiometer

Figure 5.11 gives an overview of the arrangement of the three GOCE star sensors with respect to the gradiometer. In Fig. 5.11(a) the orientation of the boresight axes of the three star sensors within the GRF is given, cf. Gruber et al. (2010a). In Figs. 5.11(b) to 5.11(f) the orientation of all three star sensor axes within the GRF is shown in more detail, for star sensor 1 (Fig. 5.11(b)), star sensor 2 (Fig. 5.11(c)) and star sensor 3 (Figs. 5.11(d) to 5.11(f)). For another overview of the arrangement of the star sensors with respect to the gradiometer it is referred to Siemes (2011).

The SSRF is connected to the GRF by a constant rotation. In Gruber et al. (2010a) the rotation from SSRF to GRF is described with one rotation matrix plus one rotation angle for each star sensor. In order to make the connection more illustrative, in this work the rotation from SSRF to GRF is described as a series of elementary matrix rotations. Please note that both depictions are consistent and provide the same information.

$$\begin{aligned} R\_GRF\_SSRF1 &\approx \underline{R}_1(-120^\circ) \\ R\_GRF\_SSRF2 &\approx \underline{R}_1(-160^\circ) \\ R\_GRF\_SSRF3 &\approx \underline{R}_3(90^\circ) \cdot \underline{R}_2(40^\circ) \cdot \underline{R}_1(-120^\circ) \end{aligned} \tag{5.1}$$

These rotation matrices are only an approximation of the exact ones, which are provided in the L1b file containing the auxiliary data `AUX_EGG_DB`. Please note, that for the original EGG processing the rotation matrices as determined from a co-alignment between the three STRs, using STR 1 as a reference, have been used (Strandberg, 2010). For the new processing, cf. Chapter 6, the rotation matrices have been determined individually for each measurement phase with the ESA-L calibration method, cf. Chapter 4.

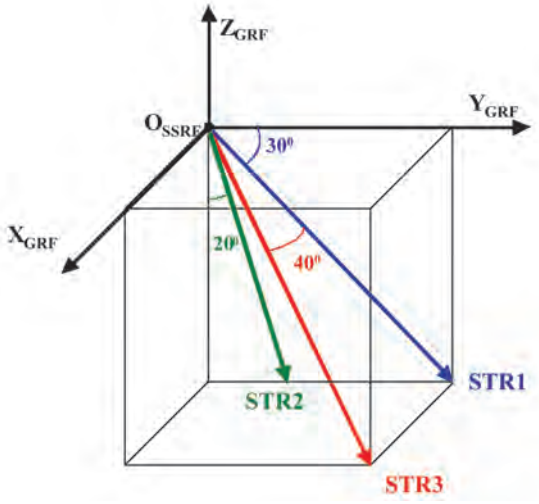

(a) Z-direction (boresight) of all three star sensors

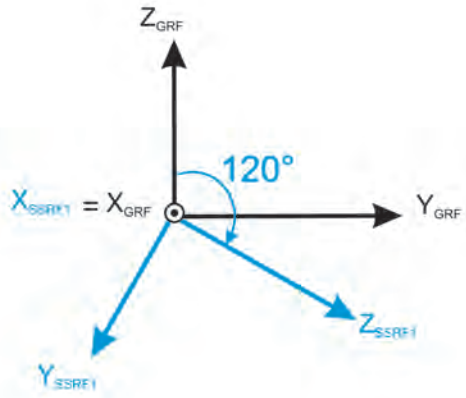

(b) Star sensor 1

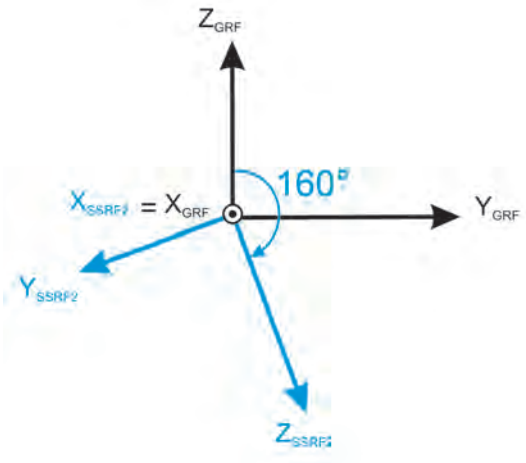

(c) Star sensor 2

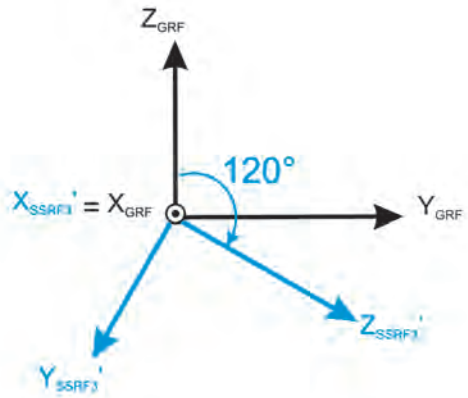

(d) Star sensor 3, first rotation

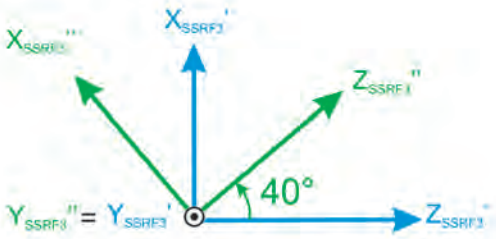

(e) Star sensor 3, second rotation

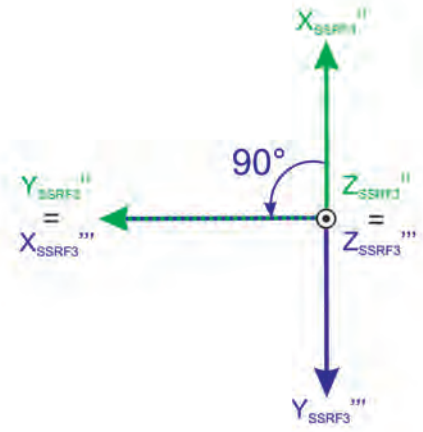

(f) Star sensor 3, third rotation

Figure 5.11.: Arrangement of the three star sensors with respect to the gradiometer. (a), overview of arrangement of boresight axes of all three star sensors; (b), arrangement of star sensor 1 (one rotation); (c), arrangement of star sensor 2 (one rotation); (d) to (f) arrangement of star sensor 3 (three rotations).

5.2.2. Analysis of the star sensor data

In this section the measurements of the GOCE star sensors are compared and analyzed at the level of angles. The star sensor data, which are measured in the respective SSRF, are rotated into the GRF with the known rotation matrices as provided in the file `AUX_EGG_DB` from the STR co-alignment (Strandberg, 2010).

As an example, Fig. 5.12(a) shows the difference between the angles roll, pitch and yaw in the GRF from star sensors 1 and 2 of day 1 November 2009. The differences in roll angle (green) are smallest, with a standard deviation of $1.7 \cdot 10^{-5}$ rad or 3.5 arcseconds. The differences for pitch (red) and roll angle (blue) are markedly larger, with a standard deviation of $1.6 \cdot 10^{-4}$ rad or 32 arcseconds (for pitch) and $1.3 \cdot 10^{-4}$ rad or 27 arcseconds (for yaw). Both star sensors, 1 and 2 have their boresight axis perpendicular to the x-axis of GRF, cf. Fig. 5.11. Hence the roll angle can be determined very accurately from both of them. The expected accuracy of the good star sensor measurements is given with 2 arcseconds. A simple error propagation gives for the differences between two good measurements $\sqrt{2}$ times the accuracy of one good measurement, which is in this case $\sqrt{2} \cdot 2$ arcseconds ≈ 3 arcseconds, and which is in very good agreement with the observed standard deviation for the differences in roll angle. Pitch and yaw are influenced by the less accurate star sensor measurements. The error of a rotation about a certain axis is increasing with the sine of the angle between the star sensor' boresight and the plane perpendicular to the axis under investigation. Hence, one could expect, cf. Fig. 5.11, that pitch could be slightly better determined than yaw. This is somewhat contradictory to our findings for the data of 1 November 2009. The mean values of the differences between the angles in GRF, as shown in Fig. 5.12(a), are 7.3 arcseconds for roll, 20 arcseconds for pitch, and -6.1 arcseconds for yaw, respectively. Note that a potential error of the STR mounting matrices fully propagates to these differences. For our analysis, we have used the STR mounting matrices from the co-alignment by (Strandberg, 2010). Meanwhile, for the new EGG L1b processing, the optimal mounting matrices of the star sensors with respect to the gradiometer are estimated for each measurement phase individually with the ESA-L calibration method. The mean differences in roll, pitch and yaw angle should become smaller when using these new STR mounting matrices (not shown here).

Figure 5.12(b) shows the root PSD of the differences in the angles of star sensor 1 and 2. It can be noted that at very high frequencies, beyond 30 mHz, the actual star sensor noise seems to behave as expected. Here, it is flat and has a magnitude of about 3 arcsec/$\sqrt{\text{Hz}}$ for roll (green) and is about one order of magnitude larger for pitch (red) and yaw (blue). For frequencies lower than about 30 mHz the star sensor noise is not flat, but increases towards the lower frequencies. We observe a significant repeat pattern at the frequency of one cycle per revolution (1 cpr $\approx 1.85 \cdot 10^{-4}$ Hz) and with a 1/f-decreasing magnitude towards higher frequencies also at the corresponding harmonics k cpr, with integer k. To highlight the repeat pattern of one cycle per revolution the differences in roll angle of 1 November 2009 (green in Fig. 5.12(a)) have been low pass filtered (with an ideal low pass filter) with cut-off frequency at 10 mHz and split up orbitwise, see Fig. 5.13. In Fig. 5.13(a) the 16 orbital revolutions of 1 November 2009 are illustrated orbit-wise. It can be noted that the differences in roll at a certain epoch are very similar to the ones of exactly one orbital revolution before. This becomes even more clear when zooming into e.g. the first five minutes of the data, as shown in Fig. 5.13(b).

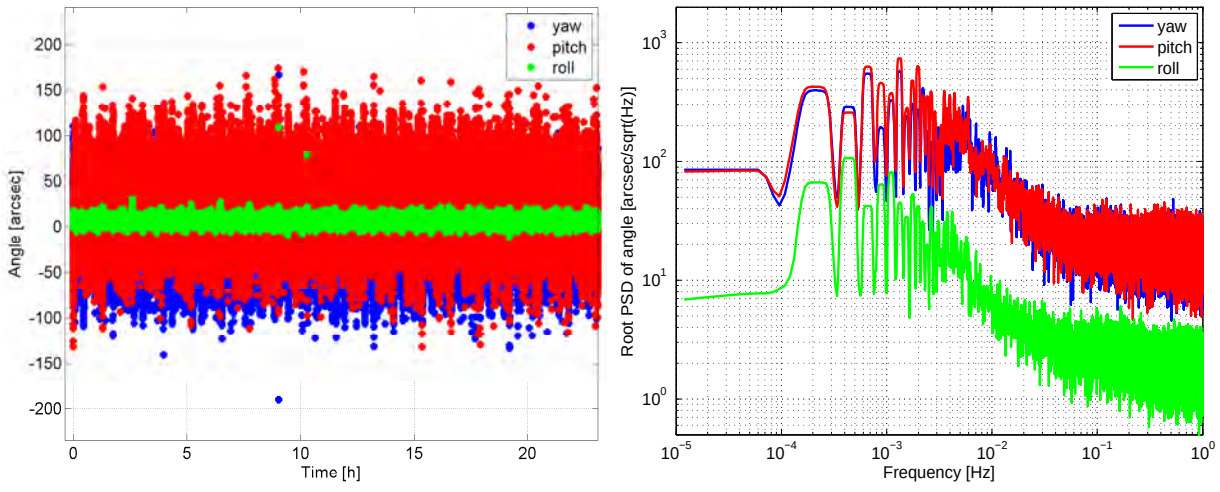

(a) (b)

Figure 5.12.: Difference between the angles (roll, pitch, yaw) in GRF of star sensors 1 and 2 (a) and corresponding root PSD (b). Data from 1 November 2009.

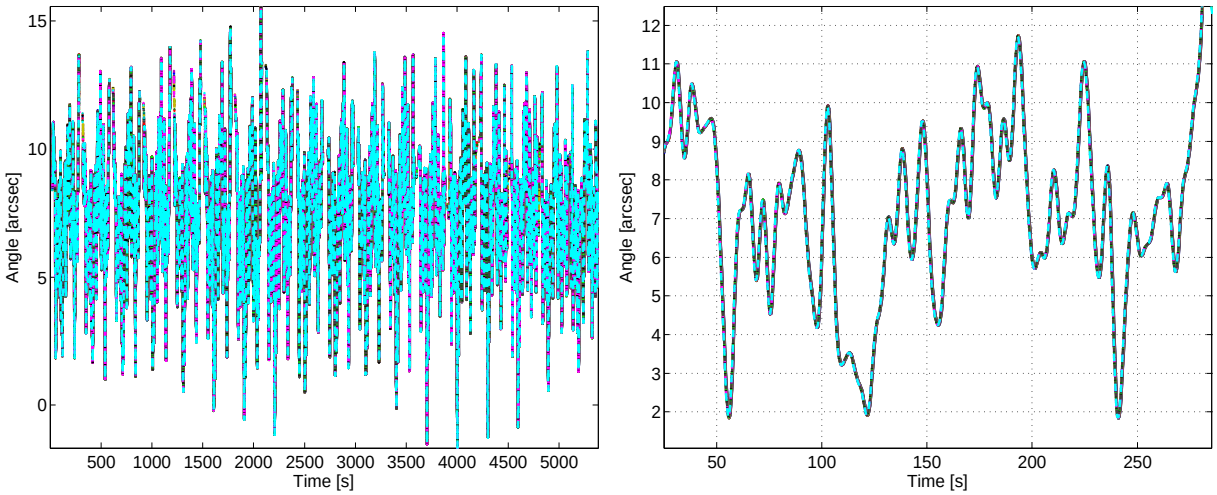

(a) (b)

Figure 5.13.: Difference between the roll angle in GRF of star sensors 1 and 2 separated into the 16 orbital revolutions of day 1 November 2009. The data have been filtered with an ideal low pass filter with cut-off frequency at 10 mHz. The right figure (b) is a zoom in the first 5 minutes of the left figure (a).

Figure 5.14 shows the root PSD of the star sensor angular rates in SSRF (left) and in GRF (right) as derived with Eqs. B.20 and B.32. For the rotation in the GRF, the star sensor mounting matrices from the co-alignment of Strandberg (2010), as used within the original L1b processing, have been applied. The first row shows as an example the root PSD of star sensor 1 for the day 25 November 2009. This is a day where star sensor 1 is in the `STR_VC2` L1b file. The second row shows the root PSD for star sensor 2 with the example day 1 November 2009, where in this case, star sensor 2 is in `STR_VC2`. The third row shows the example for star sensor 3. Here the data from 29 January 2010 is used, because at this day star sensor 3 is in `STR_VC2`. We observe for all root PSDs an increase towards higher frequencies for frequencies higher than about 20 mHz, which can be interpreted as noise. In SSRF, Figs. 5.14(a), 5.14(b) and 5.14(c), the errors for the rotation about the z-axis, i.e. about the star sensors' boresight, are as expected about one order of magnitude larger than for the errors about the other two axes. After rotation to the GRF, Figs. 5.14(d), 5.14(e) and 5.14(f), with the known rotation matrices (as given in Bigazzi and Frommknecht (2010) and in the L1b file called `AUX_EGG_DB`), which provide the mounting of the gradiometer with respect to the corresponding star sensor (cf. Sect. 5.2.1), the noise levels change. Two major aspects are noted. First, the rotation about the x-axis in GRF can be determined very accurately with star sensor 1 (Fig. 5.14(d), blue) and star sensor 2 (Fig. 5.14(e), blue). This is in accordance with expectations, similar to the result for the difference in the angle about the x-axis between star sensor 1 and star sensor 2 as already discussed with Fig. 5.12(b). Second, the rotation about the y-axis in GRF can be determined most accurately with star sensor 2, due to an advantageous arrangement with respect to GRF in comparison to the other two star sensors, cf. again Fig. 5.11.

The star sensor error characteristics play an important role in the GOCE gradiometer processing. On the one hand they are a limiting factor for the accuracy of the gravity gradients for frequencies below the gradiometer MB within the original L1b processing. This aspect is further discussed in Sect. 7.1. On the other hand they can also have a significant impact on the calibration parameters, e.g. as derived at our institute with the TAS method, see next section.

In Fig. 5.15 additionally the differences between the angular rates from star sensor 1 and star sensor 2 are given. It is the main basis for the star sensor error models as assumed in Sect. 6.2.1 for the development of an improved method for angular rate reconstruction.

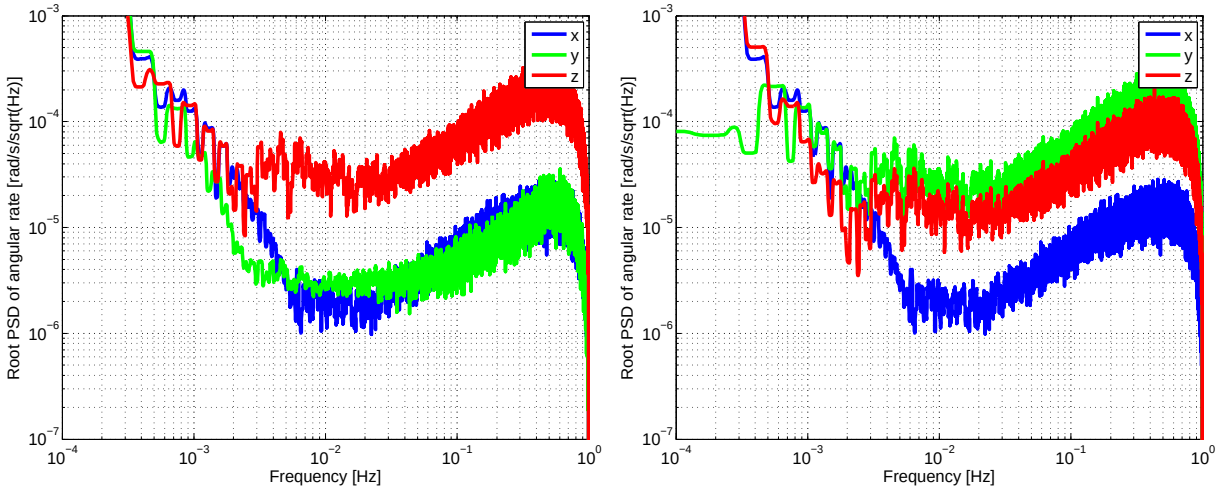

(a) Angular rate from star sensor 1 in SSRF, 25/11/2009.

(d) Angular rate from star sensor 1 in GRF, 25/11/2009.

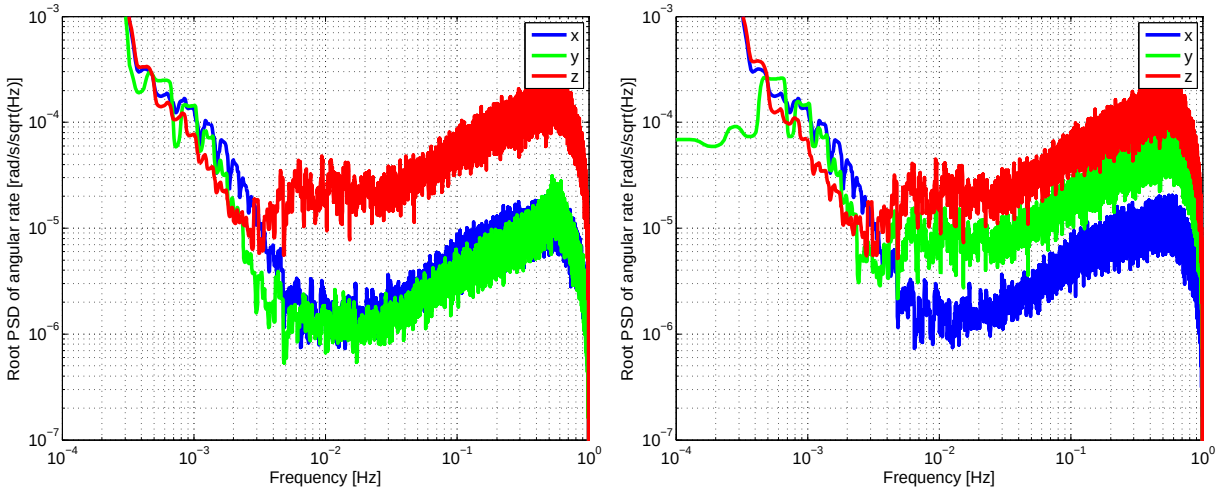

(b) Angular rate from star sensor 2 in SSRF, 01/11/2009.

(e) Angular rate from star sensor 2 in GRF, 01/11/2009.

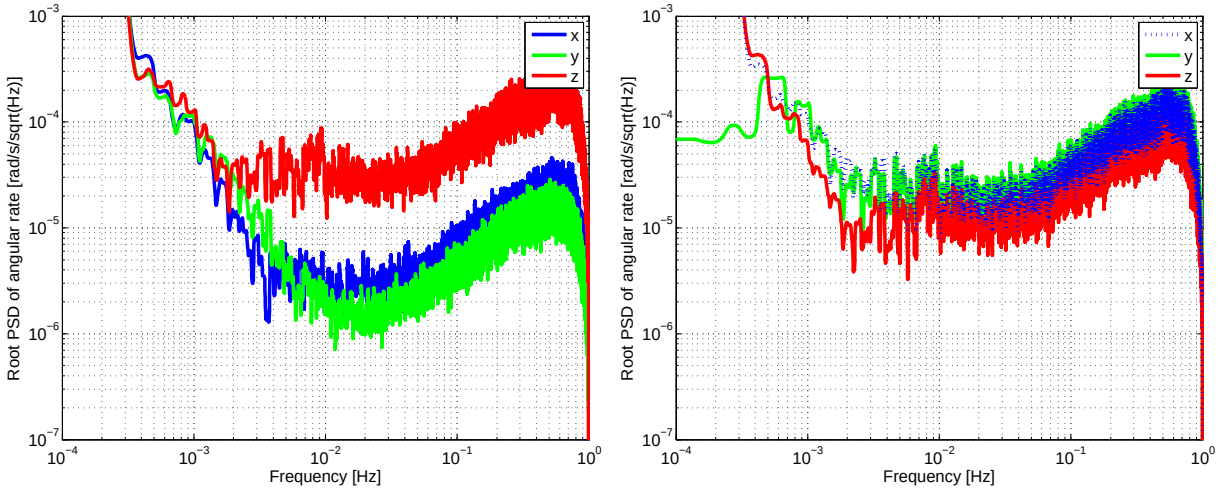

(c) Angular rate from star sensor 3 in SSRF, 29/01/2010.

(f) Angular rate from star sensor 3 in GRF, 29/01/2010.

Figure 5.14.: Root PSD of angular rate as derived from the three star sensors in the respective star sensor reference frame (left) and in the gradiometer reference frame (right).

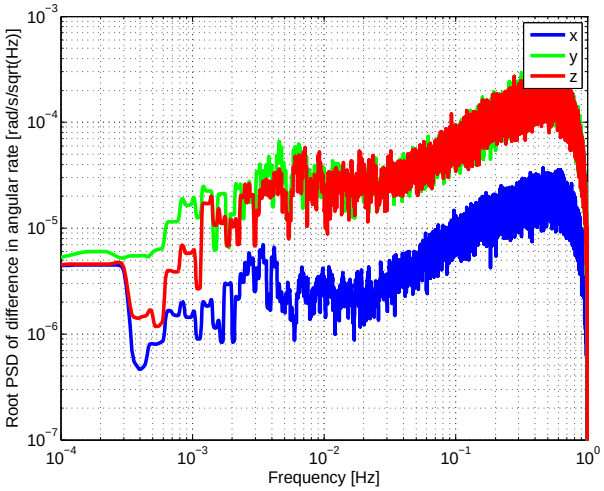

Figure 5.15.: Root PSD of difference in angular rate in GRF of star sensors 1 and 2. Data from 25 November 2009.

5.2.3. Impact of star sensors on ICM calibration

Within the TAS and also the ESA-L ICM determination method the star sensor data are used for the determination of the absolute scale factors. As pointed out in Sect. 5.2.1, the arrangement of the individual star sensors with respect to the gradiometer plays an important role for the accuracy of the star sensor data in GRF. Hence, one could assume that the results of the ICM calibration depend on the used star sensor data. Within this section the influence of the star sensors on the ICM calibration results as derived by an independent implementation of the TAS calibration method at IAPG is analyzed.

As an example, the data from the third ICM calibration phase, which took place at 8 October 2009 have been used to determine the ICMs with the TAS method either using the data of star sensor 1 only, or using the data of star sensor 2 only. The gradiometer data has been identical for the two cases.

Figure 5.16 shows the corresponding differential scale factors in blue for the use of star sensor 1 and in green for the use of star sensor 2. For comparison the results of the ESA-L method are shown in red, which makes use of both star sensors, 1 and 2. The respective required measurement accuracies as derived in Sect. 4.3.2 are indicated as (red) vertical lines. In general, we observe a strong dependency on the differential scale factors due to the use of the different star sensors with the TAS method. This is especially true for dSF14x and dSF25y where both results of the TAS method (blue and green) are farther from the ESA-L value (red) than the required measurement accuracy. Note that these two ICM elements, dSF14x and dSF25y, are also the ones which show the largest variation with time (with the ESA-L method), cf. Figs. 5.9(a) and 5.9(e) in Sect. 5.1.4. The scale factors from star sensor 2 are in general closer to the ones from the ESA-L method. For dSF14z and dSF36x the value from star sensor 2 (blue) is within the range of the required measurement accuracy from the ESA-L result, but the value from star sensor 1 (green) is not. An explanation for the better results when using star sensor 2 can be its arrangement with respect to the gradiometer, cf. Fig. 5.11. The boresight axis of star sensor 2 is closer to the plane perpendicular to the y-axis of GRF than the one of star sensor 1 (and 3). Hence, the rotation about the y-axis of GRF can be determined more accurately with star sensor 2. We assume that an accurate determination of the angular rate about this axis is most important, because GOCE rotates once per revolution about it, and therefore ω_y is the largest angular rate component, cf. also Sect. 5.1.2.

More generally, the analysis of the differential scale factors in Fig. 5.16 shows that the ICMs from the TAS calibration method are very sensitive to the star sensor measurements. The ESA-L method, which combines the measurements of all available star sensors, seems to provide more reliable results. In the case that erroneous or inaccurate differential scale factors are used for the correction of the (measured) DM accelerations (cf. the last three rows of Eq. 4.15), the common mode rejection does not fully apply and the (measured) CM accelerations are partly projected onto the (corrected) DM accelerations.

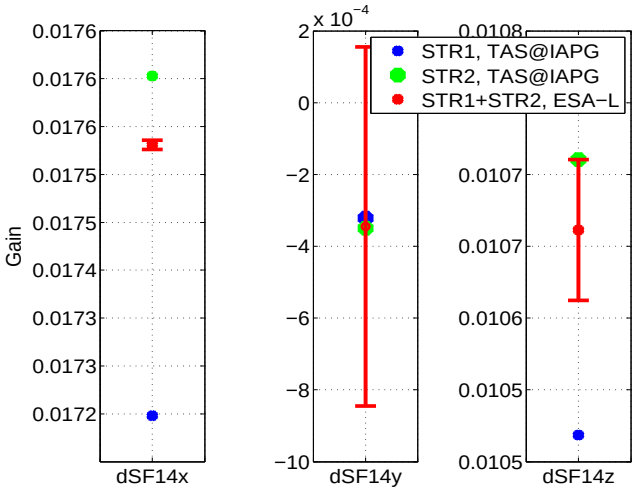

(a) dSF14.

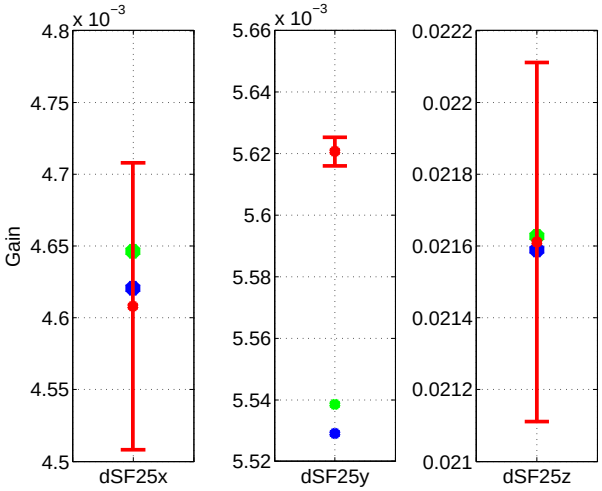

(b) dSF25.

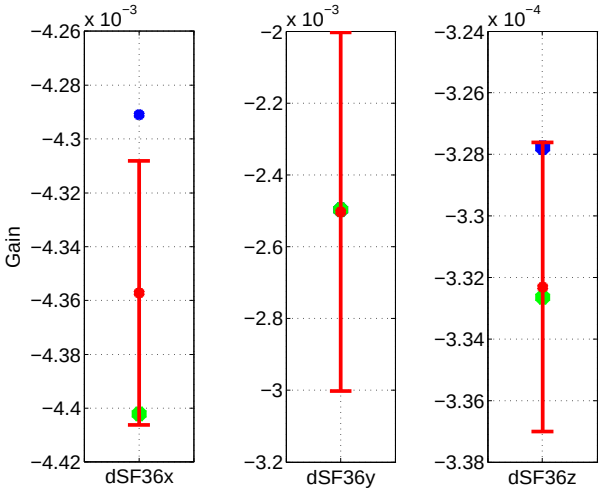

(c) dSF36.

Figure 5.16.: Impact of star sensor on calibration parameters. Comparison between the results for the differential scale factors as derived at IAPG with the TAS-method, one time using star sensor 1 only (blue) and one time using star sensor 2 only (green). In addition the results of the ESA-L method for which a combination of both star sensors has been used (red), and the required measurement accuracies (red bars) at the locations of the ESA-L results are given.

6. Alternative gradiometer processing

In this chapter methods alternative to the original gradiometer processing as described in Chapter 3 are introduced. The new methods have been adopted as the official gradiometer processing as part of ESA's PDS. All of the gradiometer data, so far originally processed, are re-processed, and also all future data will be evaluated with the new methods.

Four processing steps have been identified which can be improved, cf. Stummer et al. (2012): 1. The optimal determination of the angular rates of the satellite, based on a combination of star sensor and gradiometer data. This is the so-called angular rate reconstruction. 2. The optimal determination of the spacecraft's attitude, again based on a combination of star sensor and gradiometer data. 3. The combination of data of all simultaneously available star sensors. And, 4. the calibration of the measured accelerations is improved by taking the time dependence of selected calibration parameters into account.

6.1. Original versus alternative gradiometer processing scheme

In Chapter 3 the original gradiometer processing scheme has already been discussed in detail. Here, the original gradiometer processing scheme is compared more generally to the new one. An overview of the original GOCE L1b gradiometer processing chain is given by Fig. 6.1. The measured gradiometer accelerations are transformed to (uncalibrated) common and differential mode accelerations, cf. Sect. 3.2. In order to calibrate these accelerations, i.e. to account for small remaining gradiometer imperfections, the ICMs, which have been determined in the previous calibration phase (Chapter 4), are used, cf. Sect. 3.3. From the calibrated differential accelerations the gradiometer angular accelerations can be determined, cf. Eqs. 2.47 to 2.49. In order to be able to subtract the centrifugal part from the measurements, the angular rates have to be determined very precisely over the entire frequency range. Thus, the next processing step is the ARR, cf. Sect. 3.4, which combines the angular accelerations from the gradiometer with the attitude data from the star sensors. In the original processing, the measurements of only one star sensor, namely the one which is provided in the `STR_VC2_1b` product, are used within the ARR. Each star sensor measures the attitude of its instrument reference frame, the SSRF, with respect to the IRF. The provided attitude quaternions of the used star sensor are transformed to the GRF, with the known rotation matrices, which provide the mounting of the gradiometer with respect to the corresponding star sensor. The rotated attitude quaternions of the used star sensor serve as input for the ARR. The ARR itself is based on Kalman filtering in the time domain. The coefficients for the filtering are based on pre-launch stochastic models of the gradiometer and the star sensors. Besides the determination of combined angular rates, combined inertial attitude quaternions (IAQ, based on star sensor and gradiometer data) are reconstructed simultaneously (Cesare et al., 2008). After the ARR, the gravity gradients can be derived by subtraction of the angular rates from the calibrated differential mode accelerations, using Eqs. 2.50 to 2.55, cf. Sect. 3.5.

Figure 6.2 gives an overview over the new gradiometer processing. The workflow remains in general the same as for the original processing (cf. Fig. 6.1), except for those steps, where improvements have been identified (highlighted in light blue in Fig. 6.2). The modified steps are the calibration of the common and differential mode accelerations, the reconstruction of the angular rates and the attitude quaternions, as well as the treatment of the star sensor data. In the original processing, the calibration of the accelerations is only based on the ICMs from the previous calibration, whereas in the new processing the ICMs from the previous and the following calibration phase are used to compute interpolated and improved calibration parameters. The new ARR method is based on FIR (finite impulse response) filtering in the time domain and replaces the original Kalman filter implementation. The reconstruction of the IAQs in the new processing is decoupled from the determination of the angular rates. It is again performed by FIR filtering in the time domain, using the reconstructed angular rates from the new ARR method and the star sensor data from a new combination method, to obtain improved IAQs. The new star sensor processing foresees not only the use of one star sensor, but performs a combination of all simultaneously available star sensor measurements. Until May 2011 the data of two star sensors are available. Afterwards the data of all three star sensors are downloaded from the satellite. Due to the star sensor combination, an enhanced accuracy of the reconstructed angular rates and the reconstructed inertial attitude quaternions can be achieved.

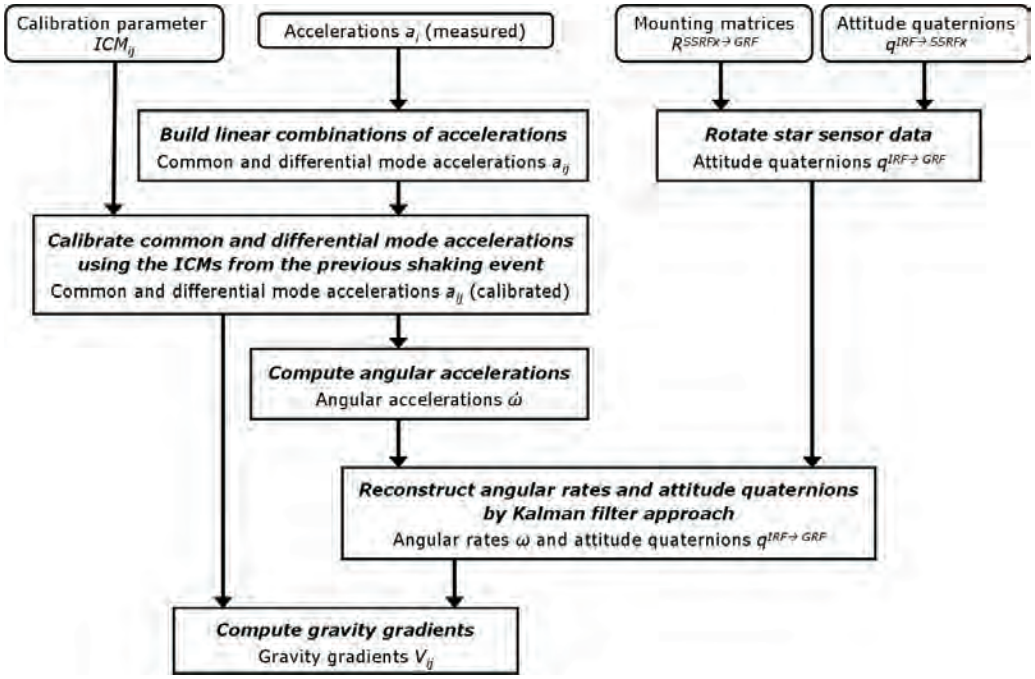

Figure 6.1.: Overview of original gradiometer processing.

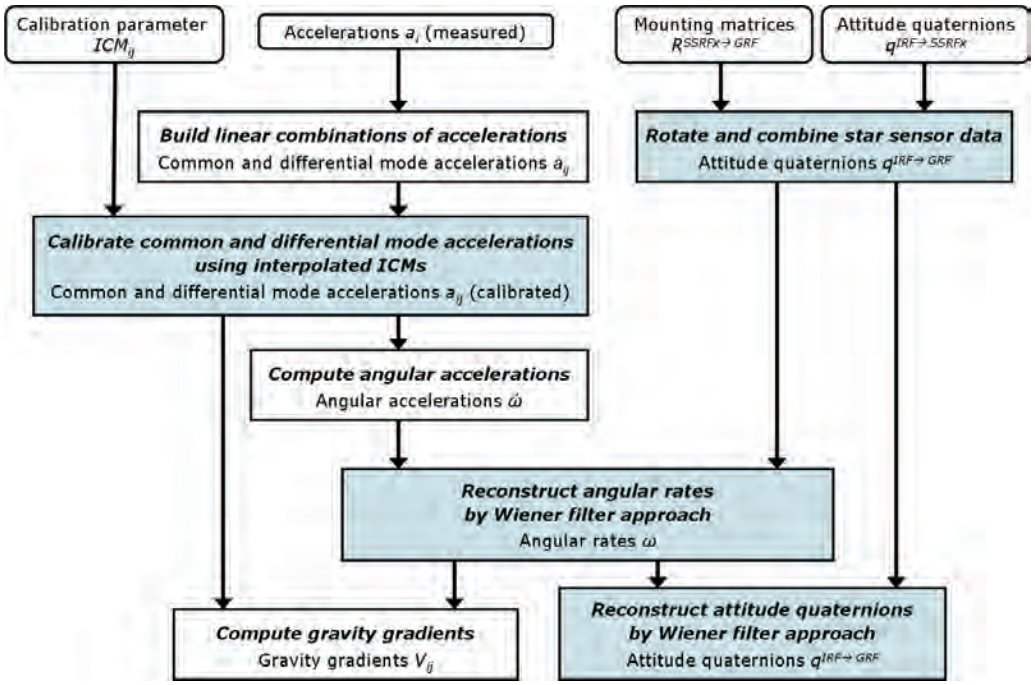

Figure 6.2.: Overview of the new gradiometer processing. The upgraded steps are indicated in light blue.

6.2. Angular rate reconstruction

First, an improved method for the angular rate reconstruction has been developed in frequency domain as documented in Stummer et al. (2011). In a next step, this approach has been adapted according to the constraints within ESA's PDS. Adequate FIR filters in time domain have been found, which preserve the improved quality of the angular rates and which are in addition as short as possible in order to reduce the warm-up time and thus to avoid unnecessary data loss.

6.2.1. Wiener method for angular rate reconstruction in the frequency domain

The newly developed method for angular rate determination performs a spectral combination of the three angular rate components (of STR and EGG) about the axes of the GRF in the IRF. To obtain angular rates from the STR quaternions, first a rotation from the SSRF into the GRF has to be carried out. This can be done using the known rotation matrices from SSRF to GRF (in file *AUX_EGG_DB*, cf. Sect. 5.2.1). The STR angular rates are obtained from the rotated quaternions by applying the Poisson's equations, see also Appendix B. To obtain angular rates from the gradiometer, the EGG angular accelerations from Eqs. 2.47 to 2.49 are numerically integrated in the frequency domain (Best, 1991). The EGG angular rates are already in the desired reference frame, the GRF. The optimal combination between STR and EGG angular rate is performed by weighting the angular rate components according to their noise PSD. The weights H_k for the Wiener filter (Papoulis, 1984) are obtained according to

$$H\left(STR\right)_k = \frac{\sigma_k^2\left(EGG\right)}{\sigma_k^2\left(EGG\right) + \sigma_k^2\left(STR\right)} \tag{6.1}$$

$$H\left(EGG\right)_k = \frac{\sigma_k^2\left(STR\right)}{\sigma_k^2\left(EGG\right) + \sigma_k^2\left(STR\right)} \tag{6.2}$$

with σ_k^2 being the variances of the gradiometer (EGG) and star sensor (STR) noise at frequency k, respectively. Therefore, the sum of the weights for all frequencies equals one:

$$H\left(STR\right)_k + H\left(EGG\right)_k = 1\ . \tag{6.3}$$

The merging of the angular rates is performed componentwise according to

$$F\left(merge\right)_k = F\left(STR\right)_k \cdot H\left(STR\right)_k + F\left(EGG\right)_k \cdot H\left(EGG\right)_k \tag{6.4}$$

with F being the frequency domain representation of the EGG, STR or merged (merge) angular rate components at frequency k. The merged angular rates in the frequency domain are transformed back into the time domain to obtain the combined angular rates.

Since the weights of the Wiener filter are based on the noise characteristics of the star sensor and gradiometer measurements, representative noise power spectral densities, for both, STR and EGG angular rates have to be derived. Based on the findings of Sect. 5.2, four different sets of STR and EGG noise models have been empirically designed. The four versions of assumed noise have been used within the Wiener method for angular rate determination, each time using the combined STR data. (The combination of star sensor data is discussed in Sect. 6.4.) For version 1 (V1), different noise spectral densities for the three angular rate components from STR and from EGG are assumed, according to Tab. 6.1 and as illustrated in Fig. 6.3.

Table 6.1.: Version 1 of assumed gradiometer and star sensor angular rate noise

EGG	Below MBW	Within MBW	Above MBW
x/z	$1/f^2$-behavior	10^{-8}	f^2-behavior
y	$1/f^2$-behavior	10^{-9}	f^2-behavior

STR	Below 3 mHz	From 3 to 30 mHz	Above 30 mHz
x	f-behavior	$4 \cdot 10^{-6}$	f-behavior
y/z	f-behavior	$4 \cdot 10^{-5}$	f-behavior

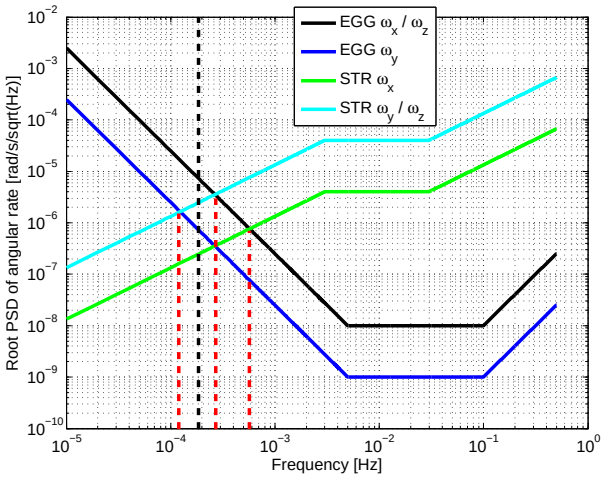

Figure 6.3.: Root PSD of assumed STR and EGG angular rate noise - version 1.

The corresponding cross-over frequencies between STR and EGG are at about $1.2 \cdot 10^{-4}$ Hz for the y-component and at about $2.7 \cdot 10^{-4}$ Hz and $5.7 \cdot 10^{-4}$ Hz for the z- and x-components, respectively (red lines in Fig. 6.3). For comparison, the 1 cpr frequency is about $1.85 \cdot 10^{-4}$ Hz (black line). For versions 2 to 4 (V2, V3, V4) always the same noise for all three angular rate components has been assumed (for V2 the noise of V1 in y-direction, for V3 the noise of V1 in z-direction, and for V4 the noise of V1 in x-direction), see Fig. 6.4.

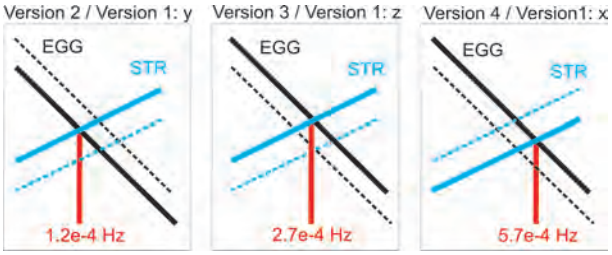

Figure 6.4.: Root PSD of assumed STR and EGG angular rate noise - versions 2 to 4.

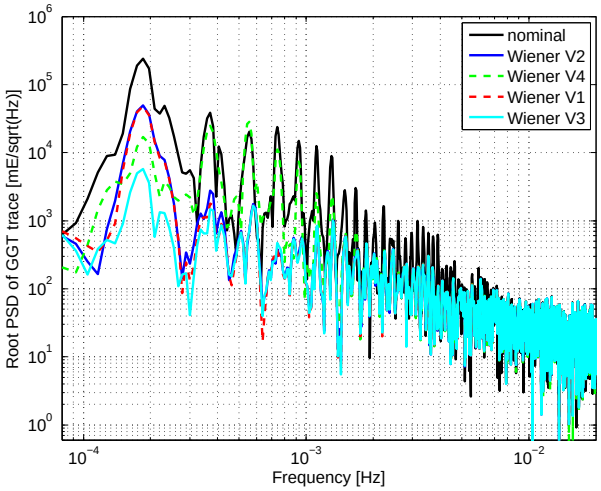

Figure 6.5.: Root PSD of GGT trace - impact of different cross-over frequencies between STR and EGG.

With these four versions of assumed noise the angular rate determination, applying the Wiener method, and using combined STRs, has been carried out. The new angular rates have been used to compute four sets of gravity gradients (cf. Eqs. 2.50 to 2.55). The quality of the new gradients can be evaluated by comparing the

gravity gradient tensor trace. From theory we know that the Laplace condition holds, i.e., the sum of the three main diagonal GGT components should be zero. In reality the remaining content in the GGT trace reflects the instrument noise. In our case this is the noise after the spectral combination of STR and EGG. Since in the spectral combination the STR is mainly used for the low frequencies and the EGG for the medium to high frequencies, we can conclude that also the noise, reflected in the GGT trace, can either be mainly attributed to the STR or to the EGG for the respective frequency bands. Figure 6.5 shows the GGT trace for all four versions of noise assumptions. Additionally, the trace from the original L1b gradients (black curve) is given for comparison.

It can be noticed:

- The trace from the original gradients (black) has the highest noise content in the frequency range from about $1 \cdot 10^{-4}$ to $7 \cdot 10^{-4}$ Hz. So, the Wiener method generally gives improved gradients for all four tested versions at the lower end of the MB and below.
- For the higher frequencies (from about $7 \cdot 10^{-3}$ Hz and higher) no improvement with respect to the original method can be achieved.
- V3 (cyan curve) performs best. The cross-over frequency is in this case at $2.7 \cdot 10^{-4}$ Hz, which corresponds to the first minimum (in between the 1 cpr peak and its first harmonic of 2 cpr) in the instrument noise root PSD.
- V1 has three different cross-over frequencies for the three angular rate components, and therefore fits best to the expected noise from simulations. However, in this case the GGT trace (red curve) increases significantly at the 1 cpr peak and slightly also at 2 cpr ($\approx 3.7 \cdot 10^{-4}$ Hz) compared to V3 (cyan).
- In V2 the cross-over frequency for all three components is at $1.2 \cdot 10^{-4}$ Hz, i.e. below the 1 cpr frequency. In this case the GGT trace (blue) is similar to V1 (red). So we see again a degradation with respect to the best case mainly at the 1 cpr peak.
- It can be concluded that in V1 and V2 the cross-over frequencies (or at least one cross-over frequency for V1) are assumed too low. This indicates that the noise of the EGG is larger than the noise of the STR at the 1 cpr peak.
- For V4 the cross-over frequency for all components is at $5.7 \cdot 10^{-4}$ Hz, which corresponds approximately to 3 cpr. In this case the GGT trace (green curve) is clearly larger than the one for the best case (V3, cyan curve), mainly for frequencies from $3 \cdot 10^{-4}$ Hz to about $1.5 \cdot 10^{-3}$ Hz. In this frequency range the GGT trace noise (green) is comparable with the trace from the original gradients (black). To a lesser extent also the frequencies around the first peak are degraded in this case. Thus one can conclude that in V4 the cross-over frequencies have been chosen too high.

In summary, the test with different versions of stochastic models has shown that the GGT trace performance is best, when the cross-over frequency for all angular rate components is in the low between the first and second peak of the noise root PSD. This corresponds to V3 of the assumed noise and weights for the Wiener filter. Therefore, the adaption of the Wiener method for the use within the official gradiometer processing of the PDS is based on V3. More generally, one can conclude from these tests that the EGG noise is smaller than the STR noise down to very low frequencies. Only for the frequencies corresponding to the 1 cpr peak and below the star sensors are performing better than the gradiometer, at the level of angular rates.

6.2.2. Wiener method for angular rate reconstruction in the time domain

In order to make the new ARR method appropriate for the use within the PDS, the Wiener filters in frequency domain have to be realized in time domain. Thereby, the goal is to maintain (at least) the improved performance (as achieved with V3 of the assumed star sensor and gradiometer noise) of the new method in frequency domain and to reduce data loss whenever a re-initialization of the filters is necessary (e.g. after an in-flight calibration) with respect to the original processing as much as possible.

In the original processing the approach for the ARR (Cesare et al., 2008) is based on Kalman filtering in the time domain. An advantage of Kalman filtering is that it allows theoretically sequential processing. One drawback of the original implementation is that the Kalman filter transient has a length of about half a day (i.e. about 8 orbital revolutions). This means that whenever a re-initialization of the filters is necessary at least half a day of data is lost.

The new ARR method is based on FIR filtering of the angular rates in time domain. The FIR filters are symmetric moving average filters. They are the inverse Fourier transform of the Wiener filters V3 in frequency domain, with

a length of 8401 seconds, cf. Fig. 6.6. Several tests have been performed to analyze the impact of the filter length. The optimal filter length has been found empirically, considering the following aspects. On the one side, long FIR filters are able to map the (long) Wiener filters in frequency domain more precisely in the time domain. On the other side, long FIR filters have the drawback of a long warm-up time, which results in more data loss, in case of a filter re-initialization. A tradeoff between these two aspects had to be found. From our tests we have concluded that the FIR filters with a length of 8401 seconds are the shortest possible realization in time domain of the Wiener filters V3 in frequency domain without loosing accuracy. The root PSD of these Wiener filters is shown in Fig. 6.7(b). Figure 6.7(a) shows the root PSD of the underlying assumed STR (blue) and EGG (green) noise. One advantage of the new ARR implementation in PDS with respect to the original one is, that in case of large gaps, now at least four times less data is lost. The cross-over frequency, (i.e. for lower frequencies STR data have a higher weight in the combination and for higher frequencies EGG data) of these filters is at about 0.27 mHz. It was found that for higher frequencies (i.e. above 0.27 mHz) the gradiometer angular rates are more accurate than the star sensor ones. This reflects the excellent quality of the gradiometer measurements for frequencies below the MB.

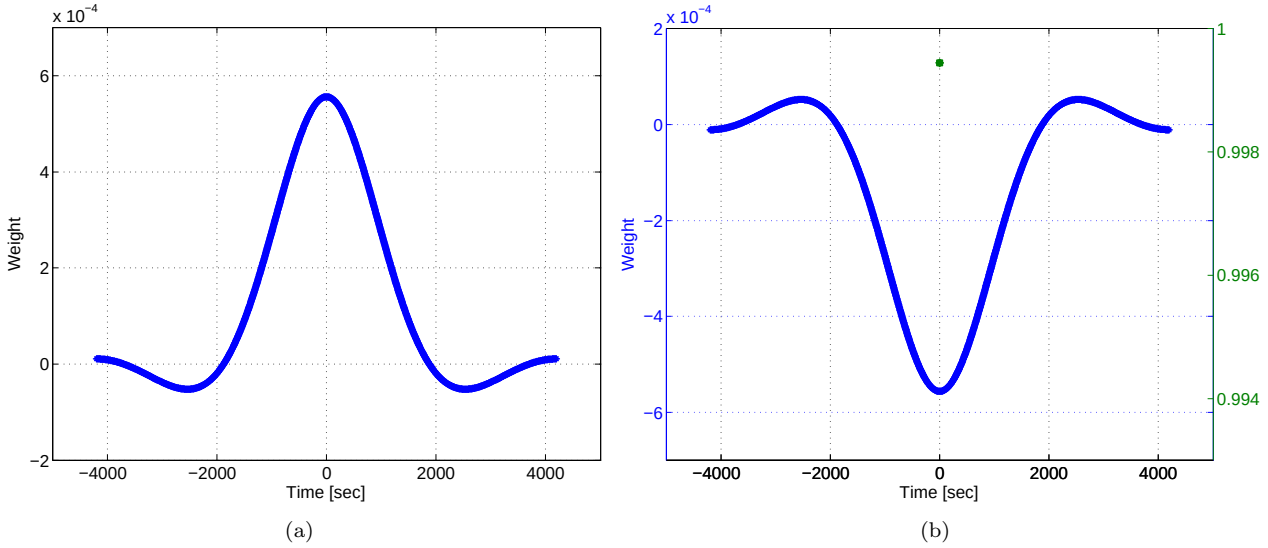

Figure 6.6.: Wiener filter for low pass filtering of star sensor angular rates (a) and for high pass filtering the gradiometer angular rates (b) in time domain.

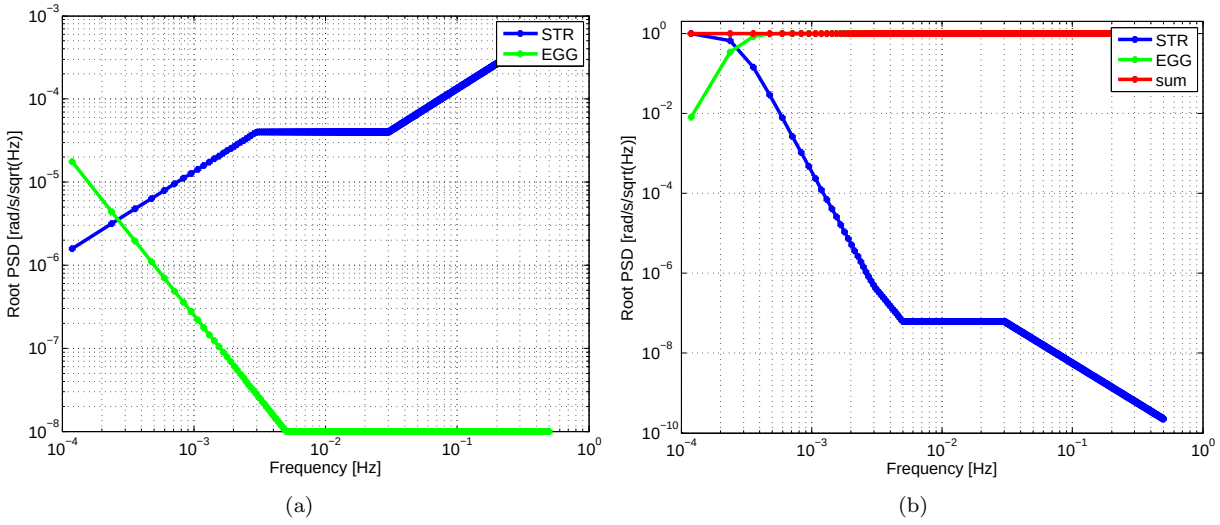

Figure 6.7.: Root PSD of assumed STR and EGG angular rate noise (a) and corresponding weights of Wiener filters in frequency domain (b).

Figure 6.8 illustrates the logic of the new ARR method. The combination of the STR and EGG data is performed at the level of angular rates. To obtain the STR angular rates, the STR quaternions have to undergo a differentiation process, which makes use of the Poisson's equations, cf. Appendix B. In the new processing, the STR

quaternions in GRF from the new STR combination method (cf. Sect. 6.4) are used. To obtain EGG angular rates, the EGG angular accelerations are numerically integrated in the time domain, using the same (Lagrange) interpolator as used within the original ARR approach (Cesare et al., 2008), cf. Sect. 3.4. In a next step, the above described FIR filters are used to extract the low frequency content mainly from the STR angular rates and the high frequency content mainly from the EGG ones by convolution. The sum of the two filtered time series gives the optimally combined angular rates (GAR). The combination can be written as

$$\omega\left(merge\right)_n = \omega\left(STR\right)_n * h\left(STR\right)_n + \omega\left(EGG\right)_n * h\left(EGG\right)_n \tag{6.5}$$

with $h\left(STR\right)$ and $h\left(EGG\right)$ being the Wiener filter coefficients and ω being the EGG, STR or merged (merge) angular rate component at epoch n.

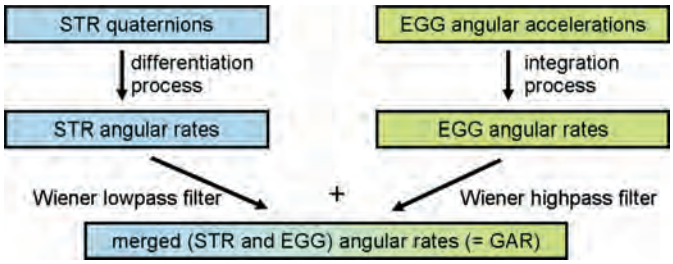

Figure 6.8.: New method for the reconstruction of the inertial angular rates.

To highlight this principle with an example, Fig. 6.9 shows for the data from 18 to 20 November 2009 the root PSDs of the EGG (green), STR (blue) and merged (red) angular rate z-component.

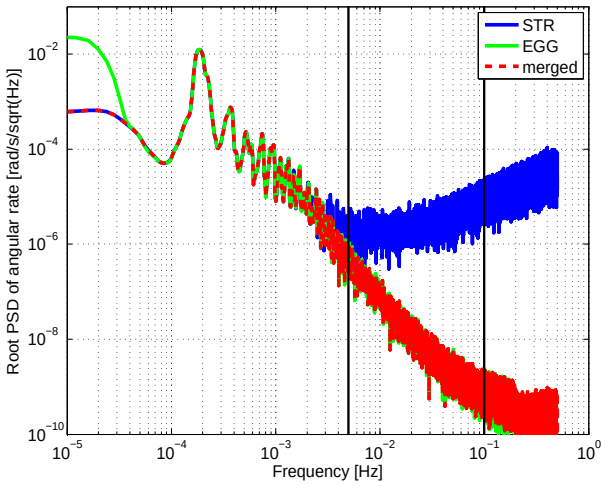

Figure 6.9.: Example, root PSD of angular rate about z-axis of GRF. Data from 18 to 20 November 2009.

In Fig. 6.10 the logic of the new ARR method is illustrated in more detail for the handling of the gradiometer data, with emphasis on the time keeping during the sequential L1b processing. In a first step the EGG angular accelerations are lowpass filtered in order to avoid aliasing in the following processing steps (from blue to green in Fig. 6.10). A Lanczos filter (Lanczos, 1956; Duchon, 1979) with a length of 1401 seconds and a cut-off frequency of 200 mHz is used. The filtered angular accelerations are interpolated with a Lagrange interpolator with a length of 4 seconds, which is the same as used in the original processing, cf. Sect. 3.4. By numerical integration, i.e. summation over the interpolated EGG angular accelerations, EGG angular rates are obtained. From these EGG angular rates the very accurate high frequency content is extracted by using the Wiener highpass filter which has a length of 8401 seconds. These filtered EGG angular rates are combined with the Wiener lowpass filtered STR angular rates as described above to obtain the merged angular rates (GAR). In total, for the computation of one epoch of the GAR there are needed $N_{lp} + N_{La} + N_W = 700 + 2 + 4200 = 4902$ epochs from the past and $N_{lp} + N_{La} - 1 + N_W = 700 + 1 + 4200 = 4901$ epochs from the future with respect to the current epoch. Note that for the computation of each epoch of merged angular rates the integration of the gradiometer angular accelerations has to be re-initialized and performed for the length of the Wiener filters. By doing so, the processing of different time periods is independent from each other. In principle one could also perform the integration of the angular

accelerations for longer time periods without new initialization. This would have the advantage of less processing effort, but the drawback of (very slowly) decreasing accuracy of the results and of inducing a time dependency in the processing. This means in this case the complete time period under investigation would have to be processed sequentially as it was the case for the original EGG processing.

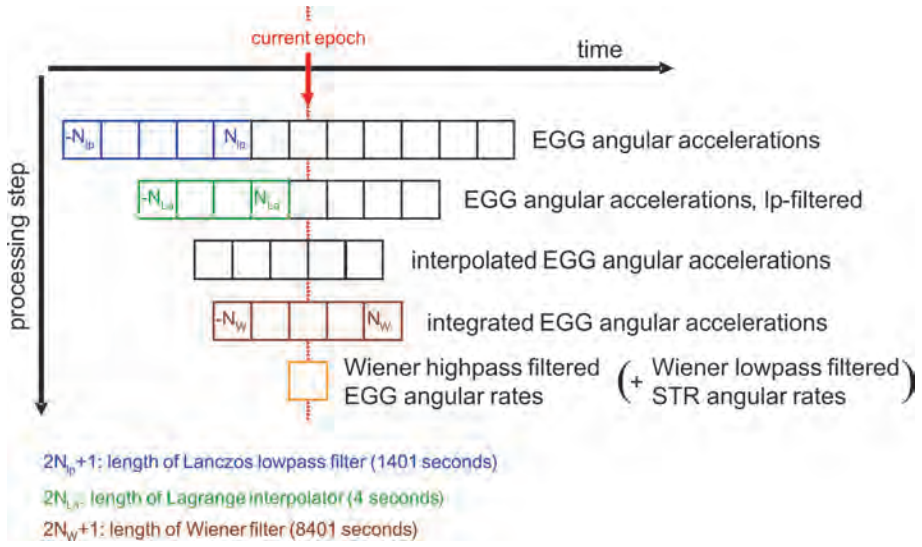

Figure 6.10.: New reconstruction of inertial angular rates from a processing point of view.

6.3. Attitude reconstruction

The aim of the attitude reconstruction (ATR) is to find the best possible estimation of the inertial attitude, using the available star sensor and gradiometer data.

In the original processing, the inertial attitude is determined simultaneously with the angular rates by Kalman filtering, in the ARR step (cf. Fig. 6.1). In the updated processing, the ATR is decoupled from the angular rate reconstruction (cf. Fig. 6.2).

The new method for ATR is based on FIR filtering in the time domain, analogously to the new ARR approach. The combination of STR and EGG data takes place at the level of attitude quaternions, cf. Fig. 6.11. From the new STR combination method (Sect. 6.4) attitude quaternions are available, which are very accurate at the low frequencies. For higher frequencies, the STR attitude can be improved by using EGG data. Thus, in the new ATR approach the optimally estimated angular rates from the new ARR method are integrated to obtain attitude quaternions, which are very accurate at the high frequencies. The principle of this integration step is rotating the quaternions from the previous epoch $n-1$ to the current epoch n using a mean (interpolated) angular rate, according to the Poisson's equations (Eq. B.22). Initial values for the integration are taken from the combined STR quaternions of Sect. 6.4. The integration has the property of increasing the noise of the low frequencies, cf. Siemes (2011). For this reason, the integrated quaternions have to be merged with the quaternions from star sensor combination (Sect. 6.4) in order to obtain very accurate quaternions for all frequencies. The combination is performed by convolution in the time domain, according to

$$q\,(merge)_n = q\,(STR)_n * h\,(STR)_n + q\,(INT)_n * h\,(EGG)_n \tag{6.6}$$

using the same FIR filters with coefficients $h\,(STR)$ and $h\,(EGG)$ as for the new ARR method. Note that the convolution is performed independently for each of the four quaternion components. Hence, a normalization of the quaternions after filtering is necessary. In order to avoid the accumulation of small errors due to integration with time, the integration is re-initialized for each step of the convolution.

To highlight this principle with an example, Fig. 6.12 shows the root PSD of the integrated GAR (green), STR (blue) and merged (red) real quaternion component for the data from 18 to 20 November 2009.

In Fig. 6.13 the logic of the new ARR method is illustrated in more detail for the EGG data, with emphasis on the time keeping during the sequential processing. The merged angular rates (GAR) are interpolated using a Lagrange interpolator (same as used before) which has a length of 4 seconds. In an integration step, GAR based

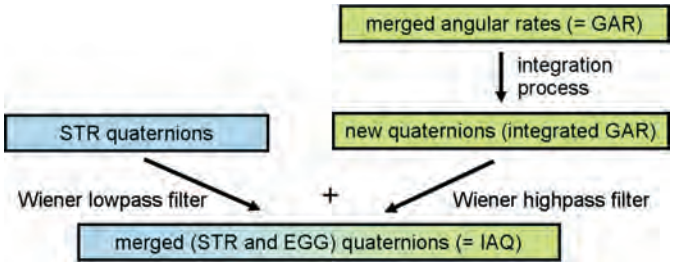

Figure 6.11.: New method for the reconstruction of the inertial attitude quaternions.

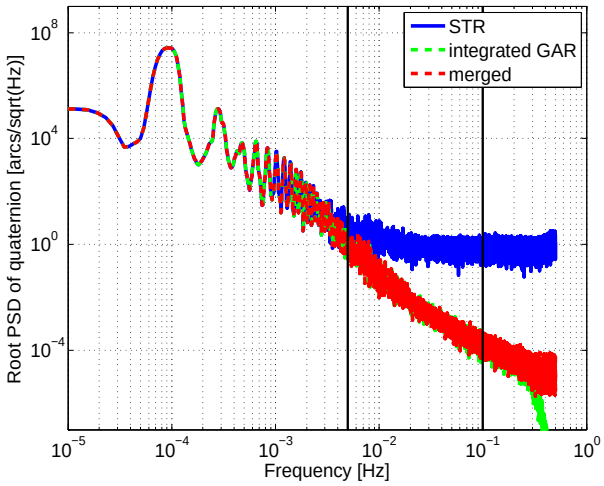

Figure 6.12.: Merging of real component of the inertial attitude quaternions. Data from 18 to 20 November 2009.

quaternions are derived from the interpolated angular rates. The new quaternions, which are based on EGG data in the high frequencies, are highpass filtered with the corresponding Wiener filter (same as used before) which has a length of 8401 seconds. In total, for the computation of one epoch of merged quaternions (IAQ) $N_{La} - 1 + N_W = 1 + 4200 = 4201$ epochs of merged angular rates (GAR) before and after the current epoch are needed.

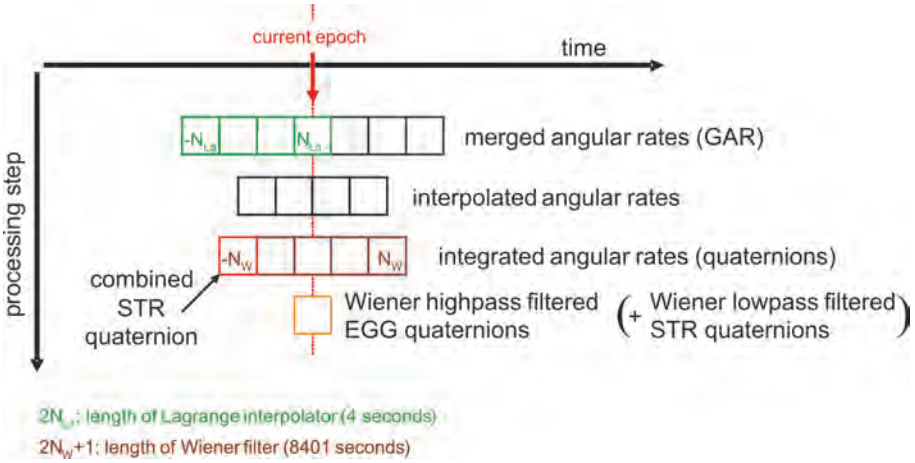

Figure 6.13.: New reconstruction of inertial attitude quaternions from a processing point of view.

One novelty of the new gradiometer processing with respect to the original one is that the ARR and the ATR are no longer performed simultaneously in the new approach. Nevertheless the consistency between the corresponding angular rates (GAR) and quaternions (IAQ) has to be maintained. The consistency can be shown with the following example. Angular rates have been derived from the IAQ to compare them with the GAR. The

differences between these sets of angular rates serve as a measure for the consistency between the GAR and IAQ. Figure 6.14(a) shows these differences for the original Kalman filter approach in blue and for the new Wiener filter approach in red for about two weeks at the beginning of November 2009. Figure 6.14(b) is a zoom in the red curves (new approach) of Fig. 6.14(a). The differences become smaller by a factor of about 10 to 100 with the new ARR and ATR. We conclude that the consistency between the GAR and IAQ is improving significantly due to the new ARR and ATR.

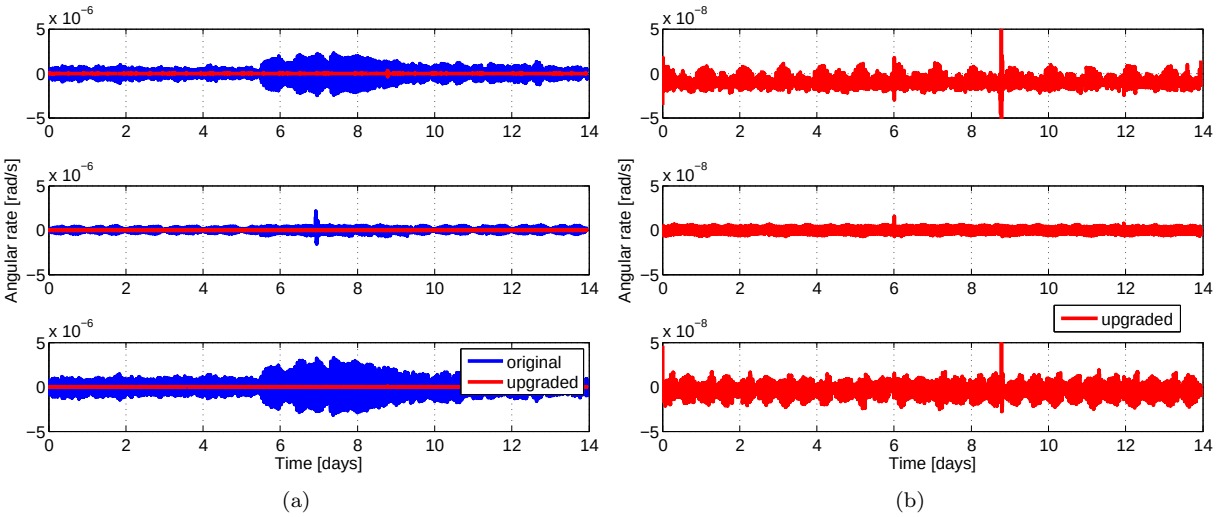

Figure 6.14.: Difference between angular rates from ARR (=GAR) and angular rates computed from the quaternions of ATR (=IAQ) (upper: x-GRF, middle: y-GRF, lower: z-GRF). (a), the results of the original ARR and ATR method (blue) as well as the results of the upgraded ARR and ATR (red) are shown. (b), only the results of the upgraded ARR and ATR (red) are shown.

6.4. Star sensor combination

The star sensor combination is performed in order to have the best possible (star sensor only) inertial attitude quaternions as input for the ARR and the ATR.

In the original processing, the data of only one star sensor is used, i.e. no combination of star sensor data is implemented. In the new processing the data of all available star sensors is optimally combined in a least squares sense, cf. Fig. 6.15.

Each GOCE star sensor measures the angular velocity about its boresight less accurately than the angular velocities about the two axes which are perpendicular to the boresight, by a factor of about 10. This is in accordance with pre-launch expectations. The angle with which the star sensors are mounted on board GOCE is at minimum 40° (Bigazzi and Frommknecht, 2010), cf. also Sect. 5.2.1. Thus, the less accurate measurements of an individual star sensor are measured more accurately by another, and it is therefore possible to compensate the influence of the less sensitive measurements by building a combination of the star sensors.

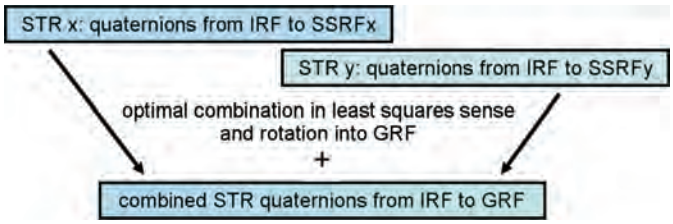

Figure 6.15.: Method for the combination of the measurements from two star sensors.

The combination method is the same as implemented within the ground processing of the GRACE (Gravity Recovery and Climate Experiment) mission. In the following the mathematical background is briefly explained. For sake of simplicity, the rotation of the star sensor quaternions from the SSRF to GRF has been omitted. Note that in the new processing, the related rotation matrices have been determined individually for each measurement

phase with the ESA-L calibration method (Chapter 4), whereas in the original processing the rotation matrices have been used as determined from a co-alignment between the three STRs, using STR 1 as a reference (Strandberg, 2010). For a complete description of the algorithm, see the corresponding GRACE literature (Romans, 2003; Wu et al., 2006), or also Siemes (2011).

The measured quaternion $\overline{q}^{measIRF \to SSRFx}$ is modelled as the true quaternion $\overline{q}^{trueIRF \to SSRFx}$ plus a small measurement error $\overline{q}^{noiseSTRx}$

$$\overline{q}^{measIRF \to SSRFx} = \overline{q}^{trueIRF \to SSRFx} \star \overline{q}^{noiseSTRx} \ , \tag{6.7}$$

with

$$\overline{q}^{noiseSTRx} = \begin{bmatrix} 1 \\ 0.5 \cdot e_1^{STRx} \\ 0.5 \cdot e_2^{STRx} \\ 0.5 \cdot e_3^{STRx} \end{bmatrix}$$

and e_1^{STRx}, e_2^{STRx}, e_3^{STRx} representing small angles. The $\star$ operator indicates quaternion multiplication, as defined in Appendix B. The optimal quaternion is found by minimizing the weighted square-sum

$$\Omega = \sum_x \left(\overline{e}^{STRx}\right)^T \cdot \underline{P}^{STRx} \cdot \overline{e}^{STRx}, \tag{6.8}$$

where

$$\overline{e}^{STRx} = \begin{bmatrix} e_1^{STRx} \\ e_2^{STRx} \\ e_3^{STRx} \end{bmatrix}$$

contains the star sensor noise and

$$\underline{P}^{STRx} = \begin{bmatrix} 1 & 0 & 0 \\ 0 & 1 & 0 \\ 0 & 0 & 0.01 \end{bmatrix}$$

is the weighting matrix. The element being equal to 0.01 reflects that the attitude about the boresight is 10 times less accurate than the attitude about the axes in the focal plane of the star sensor.

The solution for the optimal quaternion is

$$\overline{q}^{optIRF \to SSRFx} = \overline{q}^{measIRF \to SSRFx} \star \begin{bmatrix} 1 \\ -0.5 \cdot \overline{e}^{STRx} \end{bmatrix} \ .$$

$\overline{e}^{STRx}$ can be derived from the small relative errors between the measurements of two star sensors.

Due to the fact that the three GOCE star sensors are mounted on board GOCE with a minimum angle of 40°, the leaking of less sensitive measurements into the very accurate ones, when performing the rotation from the SSRF to GRF, can be avoided by the combination of the different star sensors. The accuracy of the combined star sensor quaternions in GRF is almost identical for the rotations about all three axes, cf. Fig. 6.16, i.e. the accuracy of the combined star sensor data in GRF is improved by up to a factor of about 10 with respect to the accuracy of the data from only one single star sensor, cf. Fig. 5.14.

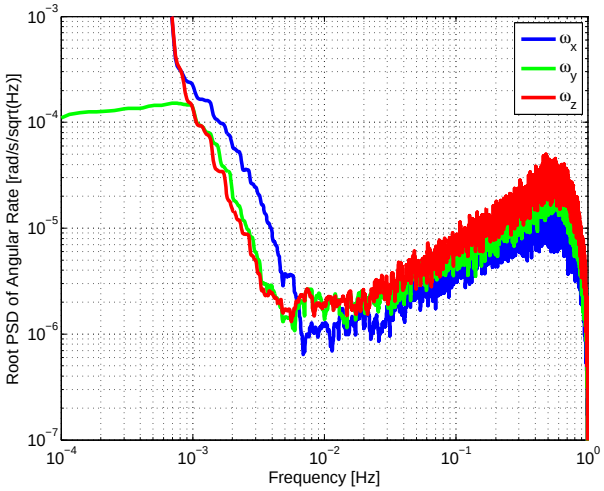

Figure 6.16.: Root PSD of angular rate (in GRF) from combination of STR 1 and STR 2.

6.5. Calibration

One pre-requisite for achieving highly accurate gravity gradients is a successful calibration of the gradiometer. The calibration, which takes place in-flight, consists of two parts. The first part is the determination and elimination of the so-called quadratic factors, cf. Sect. 4.2. They represent a non-linearity in the accelerometer transfer function, which relates the control voltages to the accelerations (Lamarre, 2007). The quadratic factors are zeroed by physically adjusting the accelerometer proof mass position.

The second part of the gradiometer calibration is the determination of the ICMs, cf. Chapter 4. There exist three ICMs, one for each gradiometer arm. The ICMs account for the remaining gradiometer imperfections. These are the accelerometer scale factors, (slightly) non-orthogonal accelerometer axes and accelerometer misalignments, meaning small deviations of the accelerometers from their nominal positions (Cesare and Catastini, 2008b), cf. Sect. 4.1. The ICMs are determined from the data of dedicated satellite shaking phases, which last for one day and take place approximately every two months, cf. Sect. 4.3.1.

In the original L1b processing, the calibration of the accelerations is based on the ICMs from the previous calibration phase, assuming that the temporal stability of the ICMs is sufficient throughout a measurement cycle. Frommknecht et al. (2011) show for the first six calibrations that the calibration parameters are in general very stable. Especially the ICM elements corresponding to non-orthogonal accelerometer axes and misalignments are very stable. These elements describe the mechanical stability of the gradiometer. For some of the accelerometer scale factors the situation is different. The variation of some scale factors in between two calibrations was found to be larger than expected, cf. Figs. 5.9 and 5.10. This leads to a degradation of the gravity gradient performance, which is increasing with time during a measurement cycle. In the new L1b gradiometer processing the time dependency of the calibration parameters is taken into account by linear interpolation of the ICMs from the previous and following calibrations. This will prevent the quality of the gravity gradients from degradation with time.

Figure 6.17 shows the evolution of the differential scale factor along the gradiometer arm 25 (dSF25y) for the time from November 2009 to May 2010. For this time period, e.g. Frommknecht et al. (2011) have shown that only the variation of dSF25y has a significant impact on the accuracy of the gravity gradients. In the original L1b processing, the calibration of the accelerations is based on the ICMs from the previous calibration event, cf. Fig. 6.17 (option 1, red lines). In the updated L1b processing, the variation of the ICM elements is taken into account by a linear interpolation of the ICMs in between two successive calibrations, (Fig. 6.17, option 2, blue lines). Moreover, the ICMs can be determined with an independent validation method, here called ESA-S method, which uses science mode data and can thus deliver the ICMs on a two-daily basis, (Siemes et al. (2010, 2012), black dots in Fig. 6.17). From the validation values for the dSF25y a small bias with respect to the linearly interpolated dSF25y of the calibration events (Fig. 6.17, blue curve) can be determined. This results in the green curve of Fig. 6.17 (option 3). For the first measurement cycle, from November 2009 to January 2010, this offset has a value of -36 ppm.

All the analysis of the updated calibration in Sects. 7.1 and 7.2 is based on option 3, Fig. 6.17.

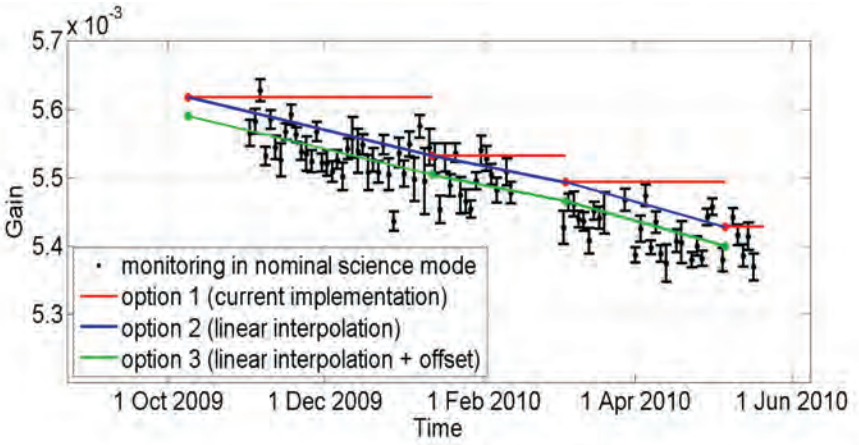

Figure 6.17.: Evolution of differential scale factor in y-direction for gradiometer arm 25. Red: estimate from in-flight calibration; black dots: validation in science mode with error bars; blue: linear interpolation between successive in-flight calibrations; green: linear interpolation and offset applied.

7. Results from the alternative gradiometer processing

In this chapter the impact of the four L1b processor updates (new ARR method, STR combination, interpolation of calibration parameters and new ATR method) is discussed, starting with a brief description of the used data sets. First, the individual impact of the four updated processing steps is in the focus. For these analyses, five different sets of gravity gradients and attitude quaternions, cf. Table 7.1, have been derived. They are analyzed at the level of gravity gradients (Sect. 7.1) and also at the level of gravity field solutions (Sect. 7.2), which have been derived with the gravity field processor Quick-Look Gravity Field Analysis (Pail et al., 2007), and wich are based only on satellite gravity gradiometry. Note that large part of Sects. 7.1 and 7.2 has already been published in Stummer et al. (2011) and Stummer et al. (2012). Second, the overall impact of the L1b reprocessing is discussed for full scale gravity field solutions in Sect. 7.3. In Sect. 7.3.1 the benefit of the L1b reprocessing is shown for full scale SGG-only gravity field solutions. In Sect. 7.3.2 the remaining benefit for combined gravity field models, which include the SST component is discussed.

All numerical studies presented in the following are based on 61 days of GOCE data (1 November 2009 to 31 December 2009). For the generation of the gravity gradients the following L1b products have been used:

- `EGG_NOM_1b`: gradiometer control voltages
- `STR_VC2_1b`, `STR_VC3_1b`: star sensor inertial attitude quaternions
- `AUX_EGG_DB`: gradiometer arm lengths and SSRFs to GRF rotation matrices
- `AUX_ICM_1b`: calibration parameters (ICMs)

To assure the universality of the results, we have tested the L1b processor updates at the level of gravity gradients also for several shorter time periods of one or a few days and for a time period of 20 days (12 March 2011 to 31 March 2011). Our findings as shown in this work for November and December 2009 have been confirmed (not shown here).

7.1. Gravity gradients

To highlight the impact of the individual processing steps, i.e. the new ARR and ATR methods, the STR combination and the interpolation of the calibration parameters, five different sets of gravity gradients and attitude quaternions have been computed. They are summarized in Table 7.1.

Table 7.1.: Five sets of gravity gradients and attitude quaternions.

case	ARR method	STR combination	ICM calibration	ATR method
A	old	old	old	old
B	new	old	old	old
C	new	new	old	old
D	new	new	new	old
E	new	new	new	new

Note that the absolute orientation with respect to the inertial frame, which is given by the IAQs, is not needed for the determination of the gravity gradients in the GRF. Hence, the gravity gradients of case D are the same as the ones of case E. The difference between these two cases is, that one time the IAQs are obtained from the original ATR method (case D) and one time from the new ATR approach (case E).

Case A, which reflects the original L1b processing, serves as a reference in the analysis of cases B to E. From cases B to E, the upgraded processing steps, i.e. the new ARR method, STR combination, interpolation of calibration parameters, and the new ATR approach have been activated step-by-step.

The performance of the gravity gradients can be evaluated using the trace condition for the GGT. Figure 7.1 shows the root PSD of the GGT trace of the four sets A to D of gravity gradients. Since the GGT trace is invariant against rotations, it does not reflect the impact of the upgraded attitude reconstruction, case E. It can be noted:

- In a large part of the MB (except for frequencies below about 8 mHz) all four GG sets have a similar noise root PSD. For frequencies lower than about 8 mHz, the trace of gravity gradient set A (blue), which reflects the original L1b processing, has the largest noise root PSD.
- Gravity gradient set B (green), reflecting the use of the new ARR method, shows a significant improvement with respect to the set A. The largest noise reduction is observed for lower frequencies, in particular at the frequency of one cycle per revolution (1 cpr $\approx 1.85 \cdot 10^{-4}$ Hz) and multiples of it. Here the improvement is about one order of magnitude. A smaller improvement can still be observed for frequencies up to about 8 mHz.
- Due to the additional use of the STR combination (gravity gradient set C, grey), the GGT trace performance can be further improved. However, the improvement is much smaller than the improvement due to the new ARR method. In this case, the improvement is mainly visible in the frequency range from 0.2 to 5 mHz.
- The trace of gravity gradient set D, which reflects the interpolation of the calibration parameters, and thus the performance of the completely upgraded L1b processing, shows a further improvement in the frequency range from 1 to 8 mHz. Here, the impact coming from the variation of the calibration parameters (mainly of dSF25y, cf. Sect. 6.5) on the gravity gradients (mainly on V_{yy}) can be reduced. This improvement seems rather small, when compared to the impact of the other processor updates. In Sect. 7.2, however, it is shown that the corresponding improvement at gravity field level can be very large at regional scale.

Overall, i.e. from case A to case D, the standard deviation of the gravity gradient tensor trace can be reduced by about 90 % for the frequencies below the MB and by about 4 % within the MB.

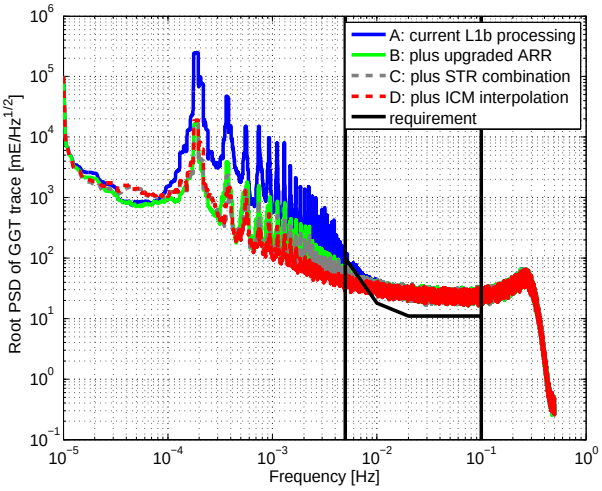

Figure 7.1.: Improvement of GGT trace due to the new method for angular rate reconstruction, star sensor combination and the interpolation of the calibration parameters. Since the GGT trace is invariant against rotations, it does not reflect the impact of the upgraded attitude reconstruction.

The quality of the gravity gradients and attitude quaternions can be analyzed by comparison to reference gravity gradients along the GOCE orbit in GRF. The reference gravity gradients have been derived from the ITG-Grace2010s gravity field model (Mayer-Gürr et al., 2010) up to degree/order 180, which is only based on satellite data from the GRACE mission, and which is thus independent from the GOCE measurements. We did not compare to a combined gravity field model like EGM2008 (Pavlis et al., 2012), which includes also terrestrial data, because we have found that this model seems to be inaccurate for several regions (Amazon region, Africa, Antarctica, Himalaya), where probably terrestrial gravity data of lower quality has been used, cf. Fig. 7.6. In order to avoid a related manipulation of our analysis, which includes also filtering of the gravity gradients, we preferred to use the ITG-Grace2010s model. For the rotation in GRF the IAQs either from the original ATR method

(cases A to D) or from the new ATR method (case E) have been used. Figures 7.2 to 7.5 show geographical maps of the differences between the GOCE gravity gradients (V_{xx}, V_{yy}, V_{zz}, V_{xz}) and the reference gravity gradients in GRF, filtered to the frequencies between 1 and 50 mHz.

For V_{xx} (Fig. 7.2) and V_{zz} (Fig. 7.4) the differences to the reference gravity gradients can be reduced the most from case A to B, i.e. due to the new ARR method. For V_{yy} (Fig. 7.3) we observe in addition to the strong reduction due to the new ARR method also a very strong reduction due to the new calibration strategy (from case C to D). The component V_{xz} is extremely sensitive with respect to rotational errors (Pail, 2005), cf. Fig. 5.3(e). Hence, we can expect that this component benefits most from an improved attitude information. The analysis of V_{xz} (Fig. 7.5) shows that this is indeed the case. Only for case E, where the new IAQs are used for the rotation of the reference gradients in GRF, a strong reduction can be achieved. This confirms that the quality of the IAQs is improving significantly with the new ATR method.

In the following we want to explain the error structures in Figs. 7.2 to 7.5. For the gradients from the original processing (cases A) we observe a rather scattered pattern, in which the ground-tracks of GOCE can be roughly identified. Due to the processor updates the dominating patterns change. For the main diagonal GGT elements this change takes already place for the cases B, i.e. when using the new method for ARR. For V_{xz} (Fig. 5.3(e)) the change can not be observed until all processor updates are enabled, i.e. only after also the new method for ATR (case E) is used.

In the remaining error patterns (cases E) a strong signal can be seen following the magnetic equator. According to Peterseim et al. (2011) this signal is most likely caused by ionospheric turbulences acting upon the satellite. For V_{yy} (Fig. 7.3) cases A, B, and C we observe a strong signal at the auroral oval region south of Australia, especially in the ascending tracks. In the following, we try to explain possible reasons for this pattern. From the accelerometer data of the CHAMP mission Lühr et al. (2007) found out that strong cross track winds occur in these regions. Moreover, Liu et al. (2005) discovered at CHAMP altitudes a thermospheric mass density over the polar regions, especially concerning the auroral ovals, which is 20-30 % higher during night hours local time than the estimation of commonly used models, cf. Peterseim et al. (2011). This could be the reason, why the signal is stronger in the ascending tracks of V_{yy} (Fig. 7.3, left). These are always related to dusk in local time.

These strong atmospheric signals are reflected in the CM accelerations as measured by GOCE. The goal of the calibration is to better separate the DM and CM signal using the ICMs, cf. Eq. 4.15. If there are remaining CM signals in the DM and thus also in the gravity gradients (here in V_{yy}), this means that the principle of common mode rejection did not work perfectly, because the variation of the CM signal was too strong, and the ICMs have not been capable to reject the CM signal completely.

Mainly V_{yy} is affected, because the cross winds are measured primarily by the (in-line) cross-track component $a_{c,25,y}$, which is coupled with the DM $a_{d,25,y}$ via the scale factor dSF25y (Eq. 4.15). Also in Sect. 5.1.4 we have shown that the dSF25y is changing significantly with time. Furthermore, the DM acceleration $a_{d,25,y}$ contains the GGT component V_{yy}, cf. Eq. 2.51. With the new calibration approach (case D), which takes into account the temporal variations of the ICM elements, the strong pattern at the auroral region south of Australia vanishes almost completely.

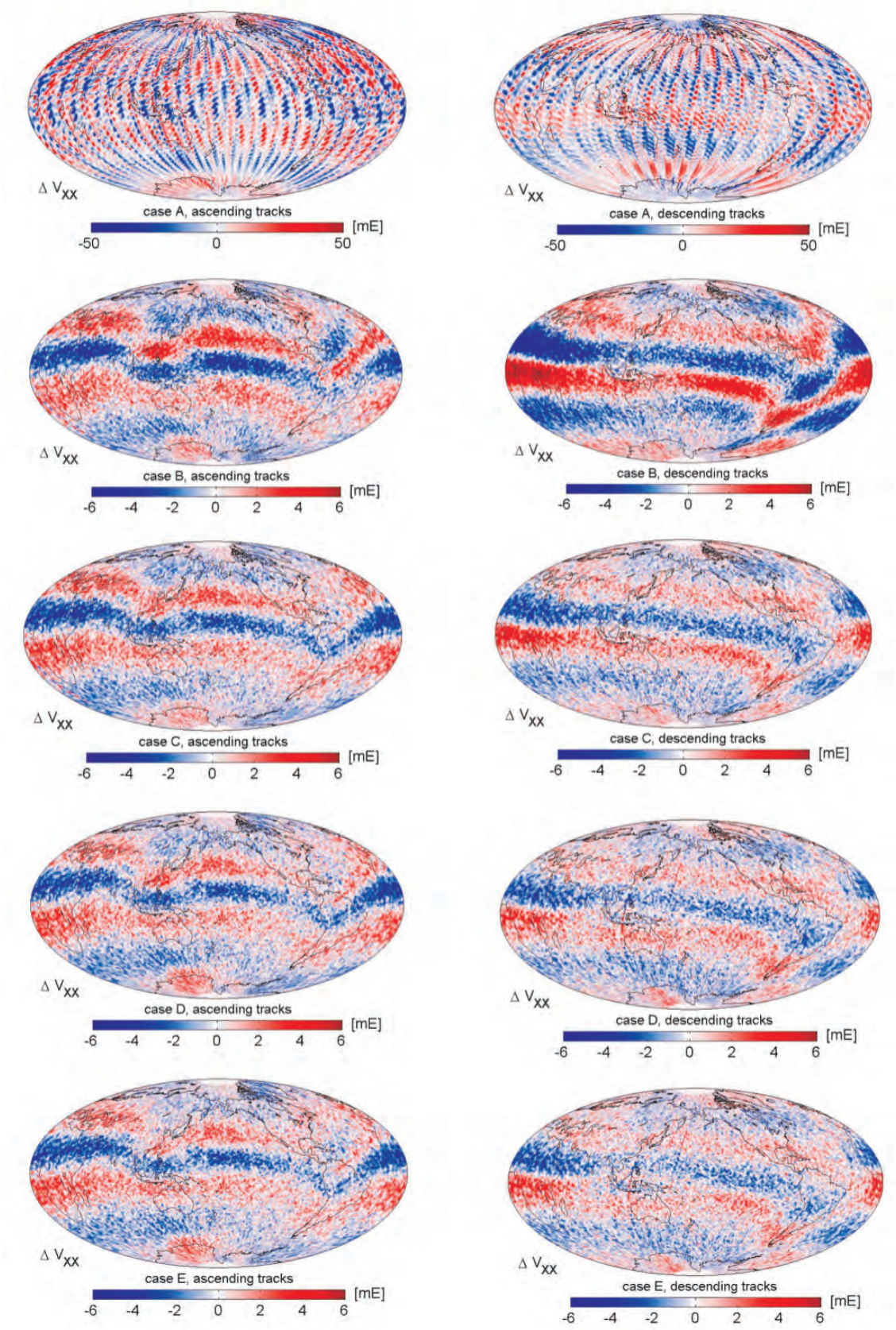

Figure 7.2.: Differences of gravity gradient V_{xx} to the ITG-Grace2010s model in GRF for case A to E, filtered to 1 to 50 mHz.

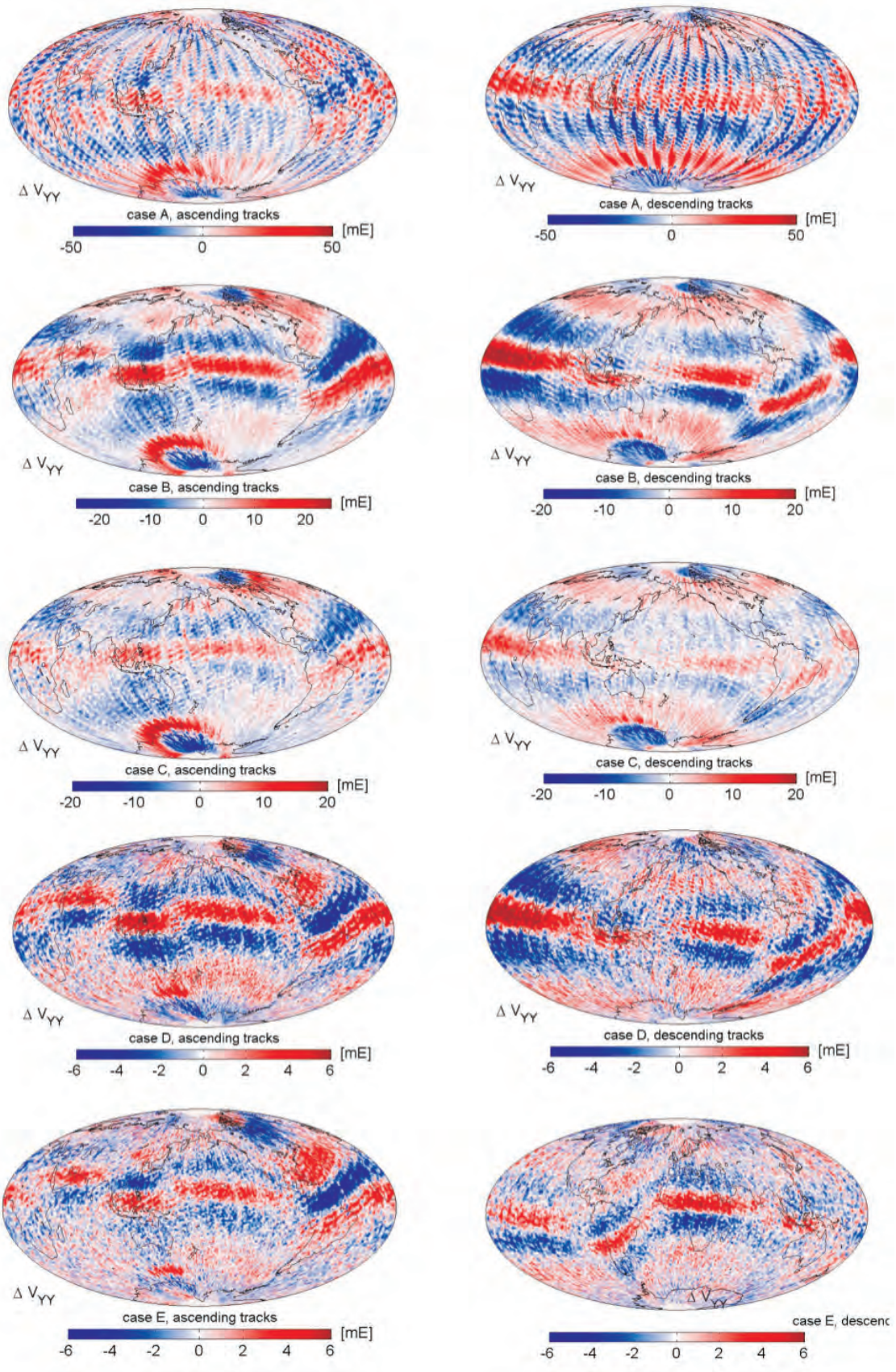

Figure 7.3.: Differences of gravity gradient V_{yy} to the ITG-Grace2010s model in GRF for case A to E, filtered to 1 to 50 mHz.

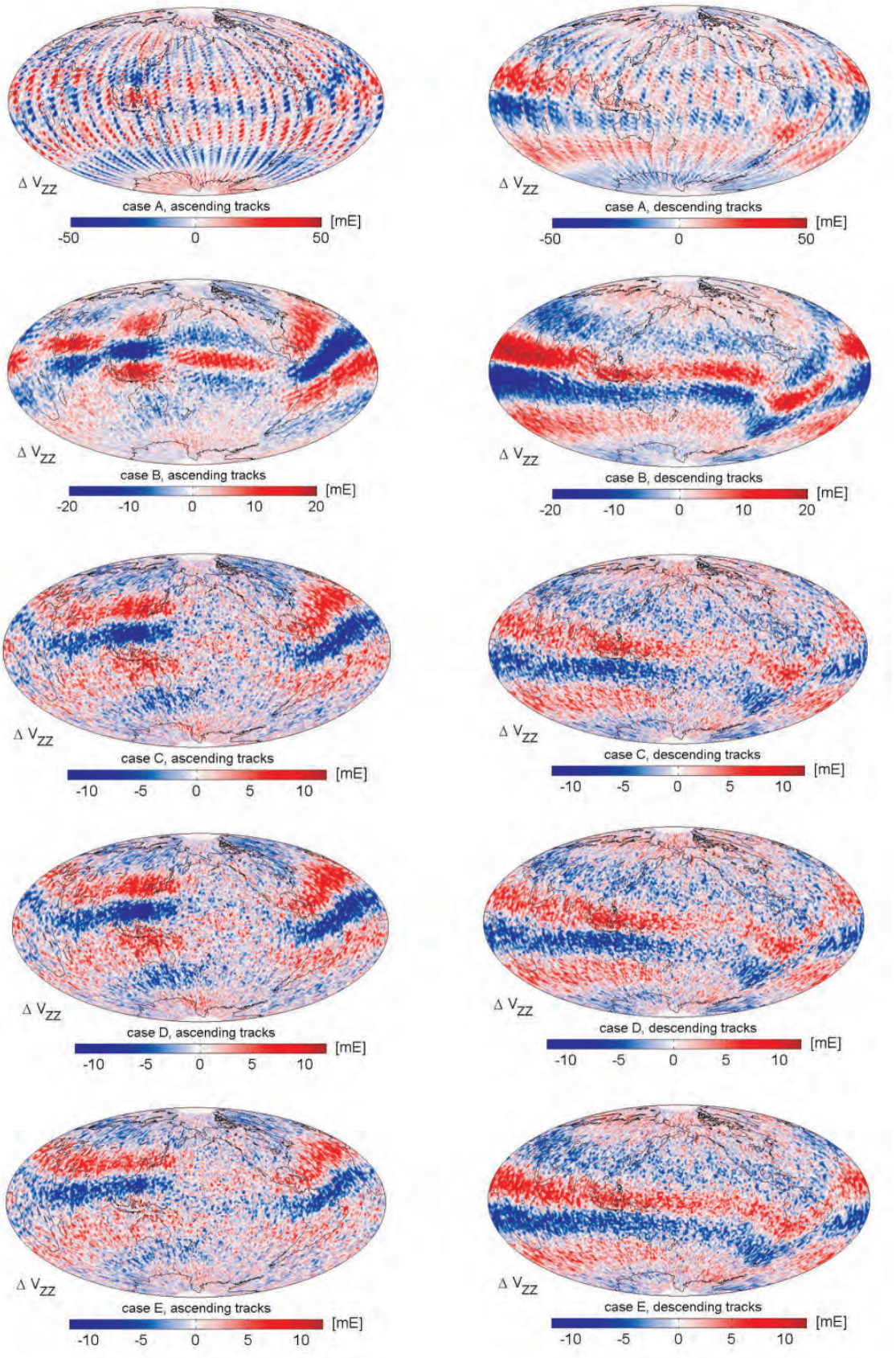

Figure 7.4.: Differences of gravity gradient V_{zz} to the ITG-Grace2010s model in GRF for case A to E, filtered to 1 to 50 mHz.

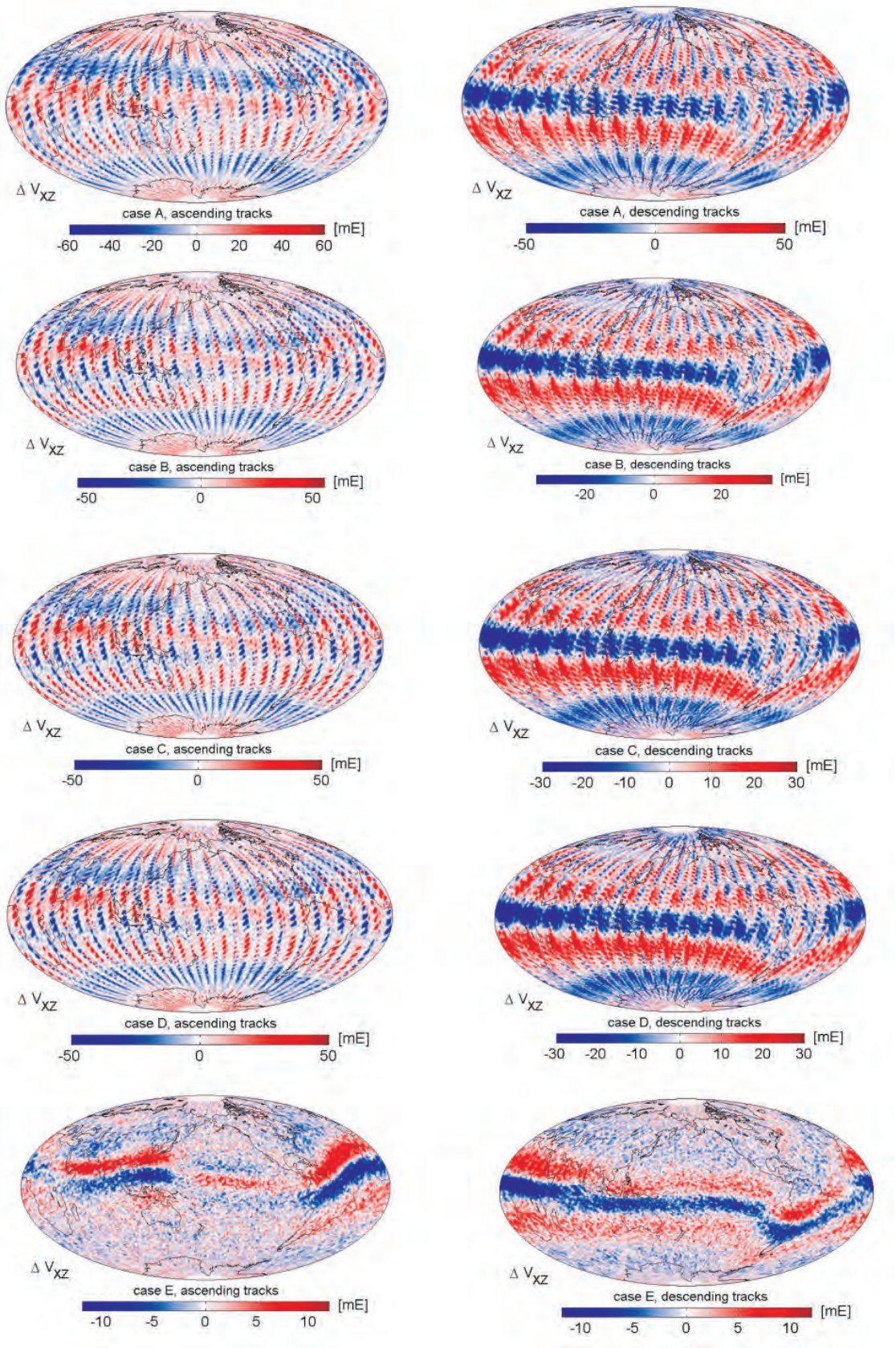

Figure 7.5.: Differences of gravity gradient V_{xz} to the ITG-Grace2010s model in GRF for case A to E, filtered to 1 to 50 mHz.

7.2. Satellite Gravity Gradiometry gravity field solutions

To evaluate the impact of the four upgraded processing steps on the level of gravity field solutions, five gravity field scenarios (GFS), according to the cases given in Table 7.1, have been computed and analyzed.

The fast gravity field processor Quick-Look Gravity Field Analysis (QL-GFA) has been applied, which has also been used in the frame of GOCE HPF in the regular processing chain during the nominal operational phase, with short latency, for the purpose of system performance analysis. A detailed description of the architecture and functionality of the QL-GFA processor can be found in Pail et al. (2007). Operational results as provided in Mayrhofer et al. (2010) demonstrate that gravity field models with a quality competitive to rigorous gravity field solutions can be achieved by QL-GFA.

The L1b updates have also been analyzed by Stummer et al. (2012) with an independent gravity field processor based on least squares adjustment of the gravity gradients, where the stochastic model for the gravity gradient noise is implemented by one auto-regressive moving-average (ARMA) filter per gravity gradient (Schuh, 1996). The results of both gravity field processors are in accordance with each other.

In order to analyze the sole effect of the L1b updates, gravity field models based only on the SGG components V_{xx}, V_{yy}, V_{zz} and V_{xz} have been computed, and the SST component has been disregarded. Since gravity field models derived from GPS orbits are also sensitive to the low to medium frequency range of the harmonic spectrum, they would partly mask the effect of the modifications discussed here. The impact of the L1b reprocessing for combined gravity field models, which include the SST component is further discussed in Sect. 7.3.2.

The scenarios A to D are in accordance with the gravity gradient sets of case A to D from Sect. 7.1, using the attitude quaternions from the original processing. For scenario E the gravity gradients from set E (new ARR method, with STR combination, with ICM interpolation) and the attitude quaternions from the new processing have been used. Scenario A reflects the status of the original processing, whereas scenario E shows the overall impact of the new processing.

In the following (cf. Figs. 7.6 and 7.7), the five gravity field scenarios are analyzed in the spatial domain in terms of geoid heights, computed between degree and order 10 to 200.

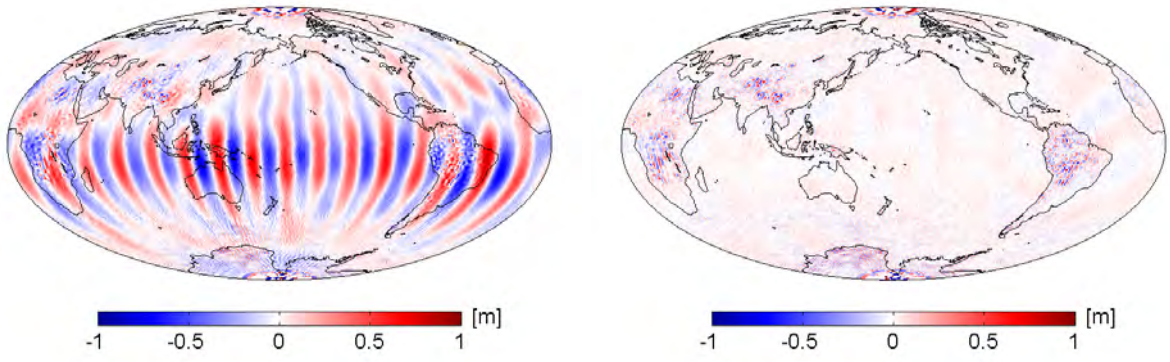

(a) Current processing (GFS A) minus EGM2008

(b) New processing (GFS E) minus EGM2008

Figure 7.6.: Difference in geoid heights (degree/order 10-200) between EGM2008 and (a) the solution based on the original L1b data, and (b) the solution based on the improved L1b data.

Figure 7.6(a) shows the differences between EGM2008 (coefficients up to degree/order 360 used) and the solution based on the original processing (GFS A). EGM2008 is a combined gravity field model containing, among others, GRACE, terrestrial gravity and satellite altimetry data. Since the performance of GRACE included in EGM2008 is superior to GOCE in the low to medium degrees (up to degree 150 for a GOCE solution based on 2 months of data), EGM2008 can serve as a very good reference for the SGG-only GFS A to E at least for the low degree coefficients. We observe a north-south striping pattern with a magnitude of ± 1 m. We attribute the north-south striping to errors in the low degree (sectorial) coefficients of GFS A. Figure 7.6(b) shows the differences between EGM2008 and the solution based on the new processing (GFS E), at the same scale as Fig. 7.6(a). With the new processing, the north-south striping is not visible anymore. We can conclude that the low degree coefficients of GOCE SGG-only gravity field solutions are improved due to the processor updates by at least one order of magnitude. In addition, we observe large differences in the Amazon region, Africa, Antarctica, and Himalaya.

The differences can be mainly attributed to terrestrial gravity data of lower quality which have been included in EGM2008 in these regions. This can be proven by the fact that solutions based on GOCE data, which show a homogenous global error structure, fit very well to EGM2008 in regions where a high quantity and quality of terrestrial data are available.

In the following, the gradual improvement due to the four upgraded processing steps is discussed. Figure 7.7(a) reflects the impact of the new ARR method. We observe a similar north-south pattern in the same order of magnitude as in Fig. 7.6(a). We can conclude that the improvement in the low degree coefficients, as seen from the comparison between Figs. 7.6(a) and 7.6(b), is mainly due to the new ARR method. Fig. 7.7(b) shows that the additional improvement due to the star sensor combination is rather small. It has a magnitude of ±10 cm and a chessboard-like pattern, which is related to the (tesseral) low degree coefficients. The impact of the new calibration approach can be seen in Fig. 7.7(c). The common mode rejection does not work properly in regions with large, highly dynamical common mode signals in the original calibration approach (Siemes et al., 2010). For the data period shown here, this is particularly the case for the region south of Australia, where we observe an improvement with a magnitude of up to ±30 cm. The new ATR method, see Fig. 7.7(d), reduces on top mainly the north-south striping in the order of ±15 cm.

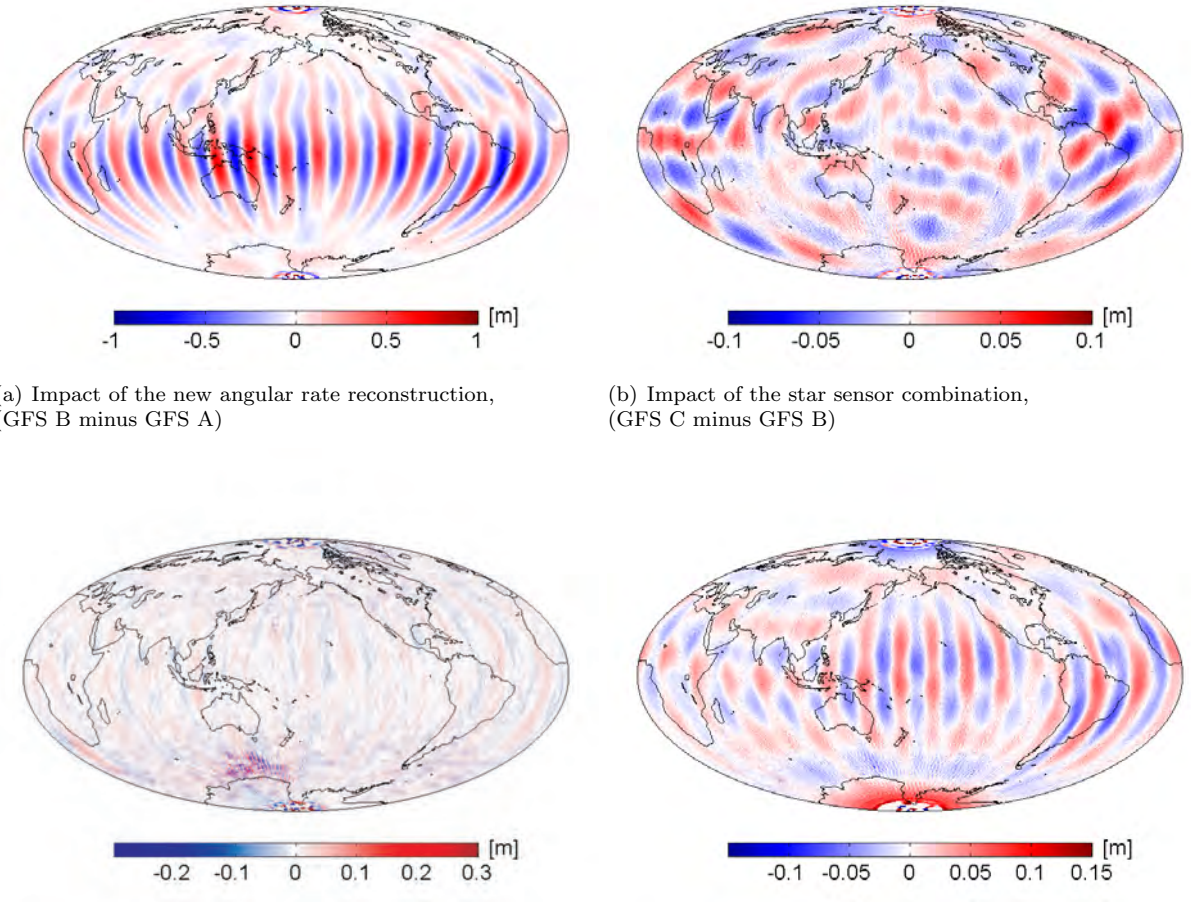

(a) Impact of the new angular rate reconstruction, (GFS B minus GFS A)

(b) Impact of the star sensor combination, (GFS C minus GFS B)

(c) Impact of interpolation of calibration parameters, (GFS D minus GFS C)

(d) Impact of the new attitude reconstruction, (GFS E minus GFS D)

Figure 7.7.: Improvement in geoid heights (degree/order 10 to 200) due to the four improved processing steps, (a) new angular rate reconstruction, (b) star sensor combination, (c) interpolation of calibration parameters and (d) new attitude reconstruction.

Next, the five gravity field scenarios are spectrally analyzed. The degree (error) median, the cumulative geoid and gravity anomaly errors as well as the error estimates of the individual coefficients are discussed.

Figure 7.8 shows the deviation of the estimated coefficients from the GRACE-only model ITG-Grace2010s (Mayer-Gürr et al., 2010) in terms of degree medians up to degree/order 180. Since degree median errors are a robust estimate of the accuracy, they have been multiplied by a factor of 1.4826 to make them comparable with corresponding standard deviations (Hettmansperger and McKean, 1998, p. 199). Also the corresponding signal (solid

black curve) and formal errors (dashed black curve) of the GRACE solution are given. For the low to medium degrees, the GRACE solution can serve as a reference to evaluate mainly the errors in the GOCE solutions. For degrees/orders higher than about 155 the formal errors of ITG-Grace2010s exceed the (error) median of the GOCE solutions. Thus, the GRACE solution can not serve as a reference for the higher degrees. Detailed studies show that the formal errors of both, the ITG-Grace2010s model and the GOCE solutions, are a very good estimate for their true error behavior, cf. e.g. Pail et al. (2010). Compared to the nominal scenario A (blue curve), we observe a substantially improved performance mainly in the lower harmonic degrees up to about degree 120 for the results of the new processing (GFS E, dashed cyan curve). When only the new ARR method (GFS B, green curve) is used, the improvement in the median is visible up to degree 70. The additional benefit of using the star sensor combination (GFS C, dashed grey curve) is too small to show up markedly in the comparison to GFS B (green curve). When also interpolating the calibration parameters (GFS D, dashed red curve), the performance can again be significantly improved. The improvement is visible up to degree 120. Above degree 120, the improvement is likely to be obscured by the errors of the ITG-Grace2010s model, which can be seen from the formal errors. The additional use of the new attitude quaternions (GFS E, dashed cyan curve) results in another visible improvement in the lower degrees up to degree 60.

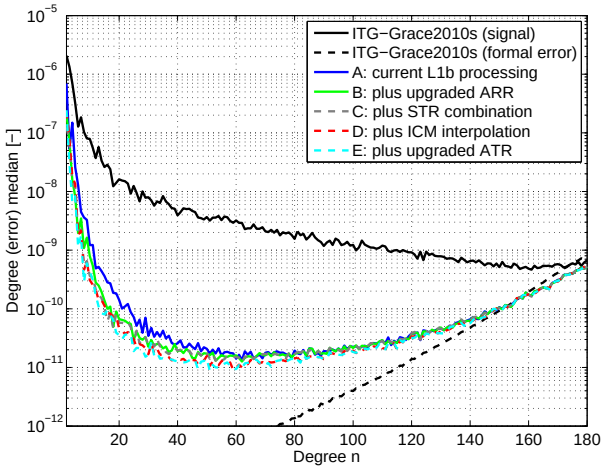

Figure 7.8.: Degree median differences between the five GFS and ITG-Grace2010s.

Figures 7.9(a) and 7.9(b) show the cumulative geoid and gravity anomaly differences, respectively, between the five gravity field models and ITG-Grace2010s. Again, the GRACE solution serves as a reference for the low to medium degrees. The computation of the cumulative errors is based on the degree median, scaled to the corresponding standard deviation by multiplication with the factor 1.4826, between degrees 20 and 150. We did not use the lower degrees for this analysis, because they can not be determined precisely with SGG-only solutions. The large error of the low degrees would therefore partly mask the analysis of the medium to high degrees, which are most important for SGG-only gravity field solutions. The cumulative geoid error can be reduced in total from 3.0 to 2.2 cm while the gravity anomaly error from 0.7 to 0.5 mGal (cf. the blue and cyan curves of Figs. 7.9(a) and 7.9(b) at degree 150). When the four upgraded processing steps are gradually included from GFS A to E, we observe that two steps contribute most to the overall improvement. These are the new ARR method (green) and the new calibration approach (red). The star sensor combination and the new ATR method cause only minor improvements.

Fig. 7.10 shows the root PSD estimates of the gravity gradient residuals after the gravity field adjustment, i.e. the difference between adjusted and original observations for V_{xx}, V_{yy} and V_{zz}. The residuals are an estimate for the total errors in the system, projected onto V_{xx}, V_{yy}, V_{zz} (and V_{xz}). The residuals of V_{xz} are discussed in the next paragraph, cf. Fig. 7.11. There are significant improvements mainly due to the new ARR method (green) with respect to the original processing (blue), which take place mainly below the MB and e.g. for V_{xx} also in the lower MB, with a strong reduction of the peaks which occur as multiples of the 1 cpr frequency. The residuals of V_{yy}, Fig. 7.10(b), can be strongly reduced for the frequencies between about 3 and 10 mHz due to the new calibration approach (red curve). Note that this strong reduction is mainly caused by the improvement in only a few areas on Earth, like e.g. in the region under Australia in Fig. 7.7(c). The star sensor combination and the new ATR method cause again only minor improvements.

The GGT component V_{xz} is very sensitive to rotations, as demonstrated e.g. in Pail (2005). Hence, it can be used for a quality assessment of and comparison between the original and new IAQ. Figure 7.11 shows in black the root PSD of V_{xz}, computed from the gravity field model EGM2008 (coefficients up to degree/order 360 used)

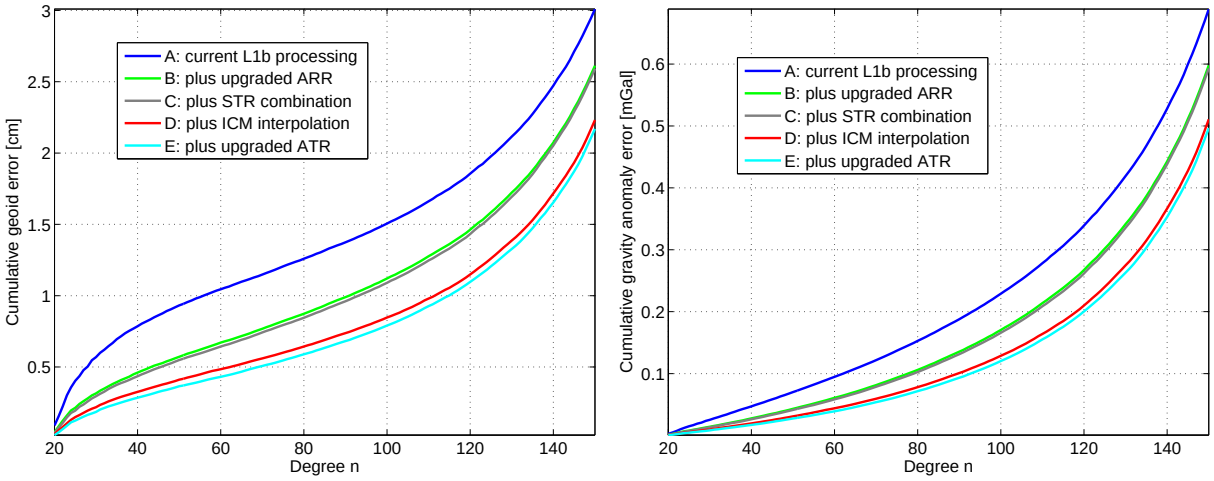

(a) (b)

Figure 7.9.: Cumulative geoid differences (a) and cumulative gravity anomaly differences (b) between the five GFS and ITG-Grace2010s. The computation is based on the respective degree median between degrees 20 and 150.

and rotated in the GRF with the IAQs from the original processing. We refer to this curve as reference gravity gradient V_{xz}. The yellow curve reflects the difference between this reference and the measured gravity gradient V_{xz}. In addition, the residuals of GFS D (red), new processing, but original ATR method (i.e. original IAQ are used here) and GFS E (cyan) with complete new processing (i.e. new IAQ are used here) are shown. For the frequencies between about 0.1 and 10 mHz the residuals of GFS D (red) are in very good agreement with the difference between the reference and measured gravity gradient V_{xz} (yellow). We conclude that the V_{xz} residuals are (for these frequencies) a very good estimate of the true errors. With the use of the new ATR method (i.e. with the new IAQ), the V_{xz} residuals can be significantly reduced for the frequencies between about 0.1 and 3 mHz. Again, especially the peaks which occur as multiples of the 1 cpr frequency are reduced. We conclude that the restricting factor for the quality of V_{xz} (for the frequencies below the MB) is the accuracy of the IAQ. Hence, the use of the improved ATR method is essential for the quality of V_{xz}.

While e.g. the degree median plot in Fig. 7.8 gives an overall picture on the improvement in the harmonic spectrum, the details of the impact of the L1b processor updates can be seen even more lucidly when analyzing individual coefficients. Figure 7.12 shows the improvement of individual coefficients in percent, computed from the error estimates (main diagonal elements of the a posteriori variance-covariance matrix) of the scenarios A and E. Note that for this visualization the scale has been confined to a maximum of 100 %. In reality, the accuracy of some very low degree coefficients is improved by more than 200 %.

Two effects are evident: first, the accuracies of the low degree coefficients could be generally improved; this conclusion is in accordance with Fig. 7.8. In particular, the (near-)sectorial coefficients could be improved, because their accurate estimation requires relatively more information from below the MB. Second, and equally important, the improvement occurs predominantly at characteristic bands at the orders $k \cdot 16$, with integer k, reflecting the mapping of the peaks of the gradiometer error spectra (cf. Fig. 7.1) onto the gravity field solution. These coefficients of order $k \cdot 16$ are particularly sensitive to those frequencies which show significantly degraded accuracies due to a lower signal to noise ratio. With the new L1b processing, these stripes at orders $k \cdot 16$ are markedly reduced, i.e. the achievable accuracy for these coefficients is significantly increased. Since the largest differences (improvements) occur for these specific coefficients, the degree medians shown in Fig. 7.8 even underestimate the impact of the new processing. As Fig. 7.12 demonstrates, for selected groups of coefficients there is an impact up to high harmonic degrees.

At this point it should be emphasized that these rather large improvements are observed for SGG-only solutions. Due to the fact that the gain due to the L1b processor updates occur to a large extent in the long wavelength range, which is largely covered by GPS-SST, the overall improvement of combined GOCE SST and SGG solutions is expected to be significantly smaller. This aspect is further analyzed in Sect. 7.3.2.

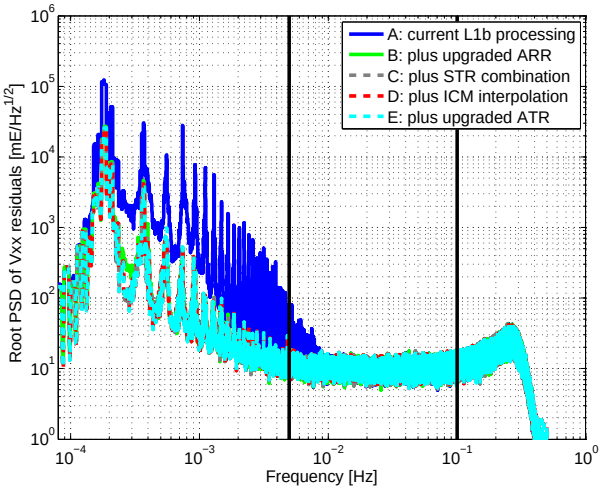

(a) Vxx.

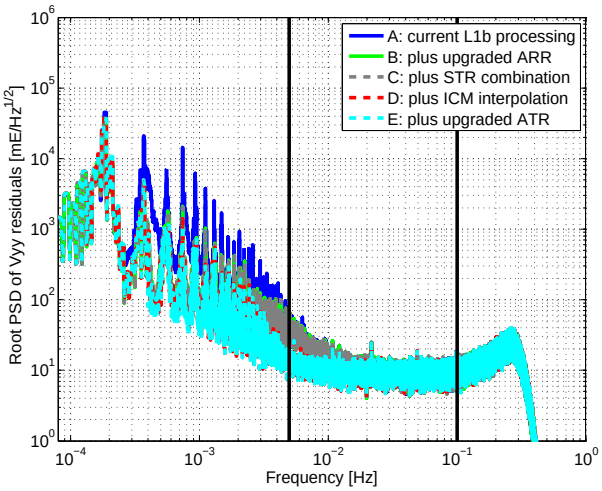

(b) Vyy.

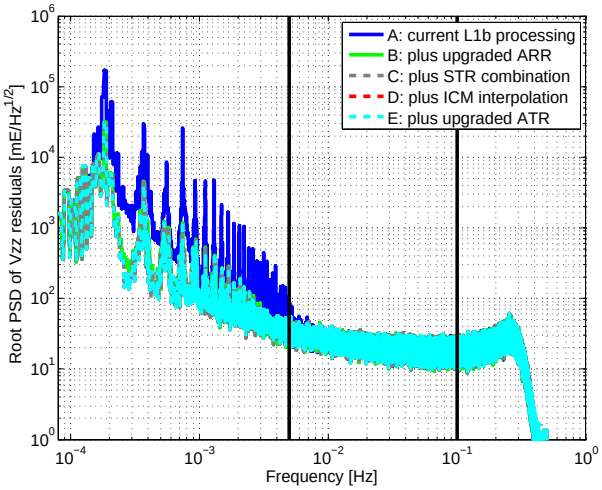

(c) Vzz.

Figure 7.10.: Root PSD of residuals of the main diagonal GGT elements.

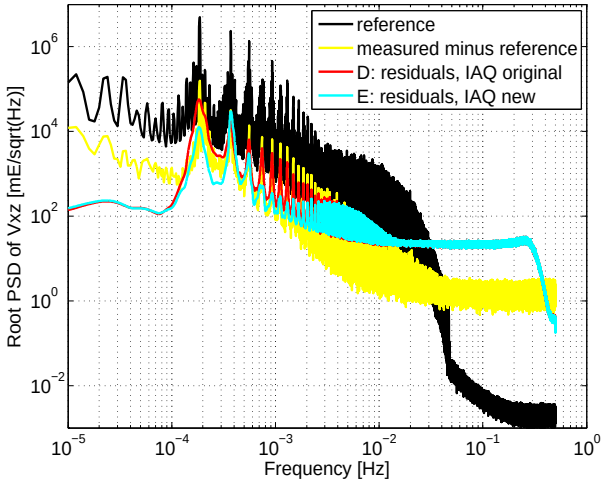

Figure 7.11.: Root PSD of gravity gradient V_{xz}, comparison with reference gradient and with Quick-Look residuals.

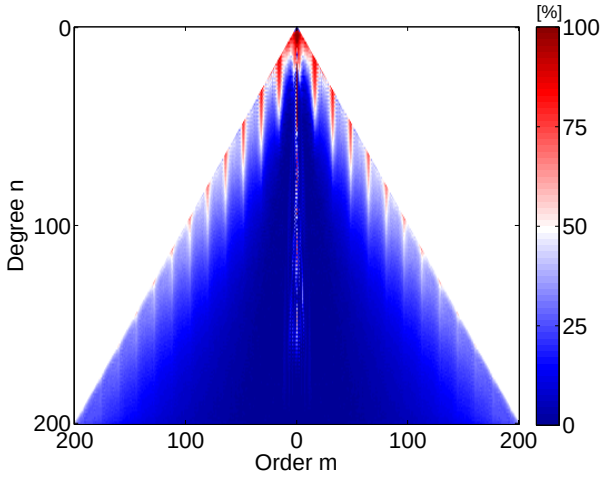

Figure 7.12.: Improvement in formal errors from GFS A to E.

7.3. Full-scale gravity field solutions

The overall impact of the EGG processor updates has been further analyzed at the level of full-scale gravity field solutions. A full-scale gravity field solver, which is implemented at IAPG (Pail et al., 2012), has been used. Note that this is, in contrast to the QL-GFA tool, which was used in Sect. 7.2, a rigorous processor which does not make use of any simplifications or approximations. In Sect. 7.2 the focus was on the analysis of the four processor updates, individually. In this section, we further intend to illuminate the overall improvement due to the new EGG processing, as implemented in PDS, for full-scale SGG-only gravity field solutions and for models which include in addition to the SGG also the SST component.

Table 7.2 gives an overview of the four gravity field models, which are analyzed in this section. We will discuss the impact of the new EGG processing for full-scale SGG-only gravity field models (O1 and N1) and for GOCE-only models (O2 and N2), based on a combination of GOCE SST and SGG data. For the models O1 and O2 the SGG data, as obtained from the original L1b EGG processing, have been used, whereas for N1 and N2 the SGG data from the improved L1b processing have been used. Further description of the four gravity field models will be given in the following in the beginning of the respective sections, (Sects. 7.3.1 and 7.3.2).

Table 7.2.: Overview of the four gravity field solutions. Models O1 and N1 are full-scale SGG solutions, either based on the original (O1) or the new (N1) EGG processor. Models O2 and N2 are combinations of the SGG components, either from O1 or N1, with GOCE GPS-SST data.

GF	Type	Maximum degree/order	Time period
O1	GOCE SGG original	224	2 months
N1	GOCE SGG new	224	2 months
O2	GOCE SST + SGG original	SST 100, SGG 224	SST 2 months, SGG 2 months
N2	GOCE SST + SGG new	SST 100, SGG 224	SST 2 months, SGG 2 months

7.3.1. Satellite Gravity Gradiometry gravity field solutions

In this section the impact of the new processing is analyzed for the two SGG gravity field models O1 and N1, cf. Table 7.2, which have been computed at IAPG, up to degree/order 224. Both models are based on V_{xx}, V_{yy}, V_{zz}, and V_{xz} from November and December 2009. The same (Kaula) regularization has been applied to zonal and near-zonal coefficients which are affected by the polar gap effect (Sneeuw and van Gelderen, 1997).

In the following (cf. Fig. 7.13), the two gravity field scenarios O1 and N1 are analyzed in the spatial domain in terms of gravity anomalies, computed between degree and order 10 to 200. Note that a similar analysis in terms of geoid heights is made in Sect. 7.2, Fig. 7.6(a) for the SGG-only GFS A and D, as derived with the QL gravity field processor.

Figure 7.13(a) shows the differences between EGM2008 (coefficients up to degree/order 360 used) and the solution based on the original processing (GFS O1). Since GRACE data is included in EGM2008, it can serve as a reference for the SGG-only GFS for the low degree coefficients. We observe a north-south striping pattern with a magnitude of about ±5 mgal. Figure 7.13(b) shows the differences between EGM2008 and the solution based on the new processing (GFS N1). With the new data, the north-south striping is not visible anymore. We can conclude that the low degree coefficients of GOCE SGG-only gravity field solutions are improved due to the processor updates by at least one order of magnitude. These findings are in very good agreement with the findings of Sect. 7.2 for the QL gravity field solutions. This also confirms additionally that the quality of QL gravity field solutions is competitive to rigorous gravity field solutions. Figure 7.13(c) shows the differences between the solutions based on the original (GFS O1) and the new processing (GFS N1). Here, again, the north-south striping clearly appears. Furthermore, large improvements in the south auroral region, here particularly in the area south of Australia and south of South America, occur. These improvements are due to the new calibration approach, which takes into account the time dependence of the calibration parameters, in particular of dSF25y. Mainly V_{yy} (cf. Fig. 7.3, ascending tracks) is affected by this aspect, as shown in Sect. 7.1.

Figure 7.14 shows the square root of degree variances of the differences of the two models O1 (SGG original) and N1 (SGG new) and ITG-Grace2010s, which shall serve again as a reference for the low to medium degrees. The solid lines represent the degree error variances estimated from the difference to the GRACE solution, the dashed lines are the degree error variances computed from the estimated coefficient standard deviations. Also the corresponding signal (solid black curve) and formal errors (dashed black curve) of the GRACE solution are

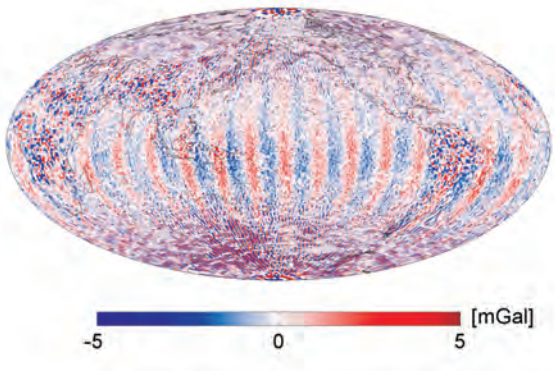

(a) Original processing (GFS O1) minus EGM2008

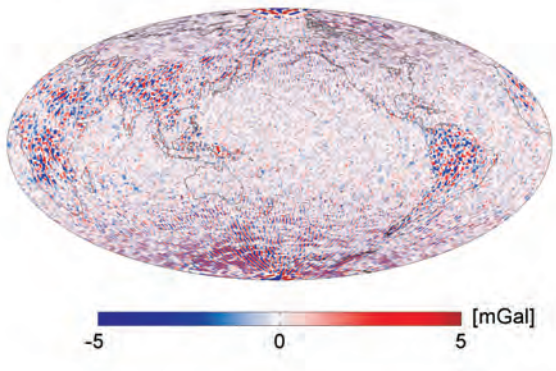

(b) New processing (GFS N1) minus EGM2008

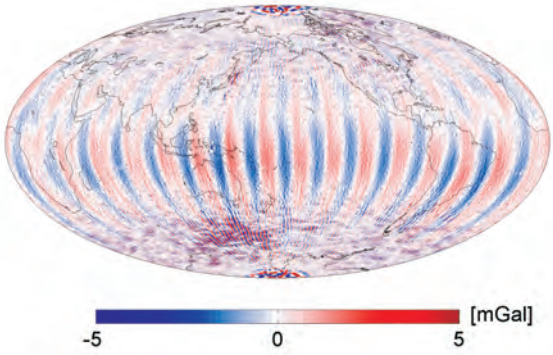

(c) New processing (GFS N1) minus original one (GFS O1)

Figure 7.13.: Difference in gravity anomalies (degree/order 10-200) between EGM2008 and (a) the full-scale SGG-only solution O1 based on the original L1b data, and (b) the full-scale SGG-only solution N1 based on the improved L1b data; (c) difference between the new processing (N1) and the original one (O1).

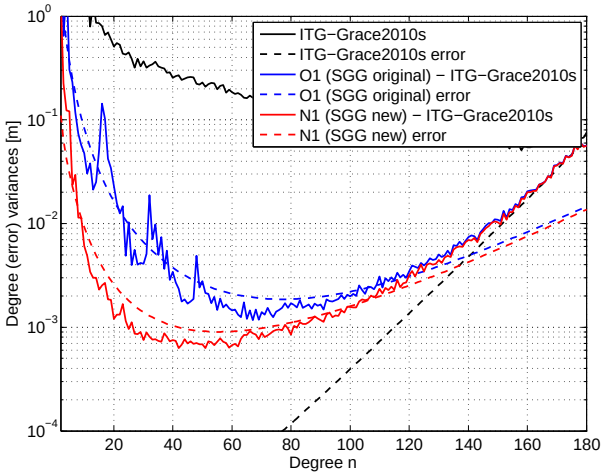

Figure 7.14.: Square root of degree (error) variances of the two models O1 (SGG original) and N1 (SGG new) with respect to ITG-Grace2010s. The near-zonal coefficients are excluded in the computations. The solid lines are degree error variances estimated from the difference to the reference solution, the dashed lines are the degree error variances computed from the estimated coefficient accuracies.

shown. We observe a strong reduction of both, the formal errors, and the differences to the GRACE solution, due to the L1b reprocessing. As expected, the improvements occur mainly at the low to medium degrees. To a small extent (about 6 %), the formal errors of the GFS N1 (red, dashed) are smaller than those of the GFS O1 (blue, dashed) even up to degree 180. In the difference of GFS O1 to the GRACE solution (blue) we observe three peaks, for which the curve exceeds the one of the formal errors (blue, dashed). These peaks occur around the degrees 16, 32, and 48, which corresponds with the orbital frequency and its first two harmonics. However, in Fig. 7.12 we have shown that the peaks in the gradiometer error spectra at the orbital frequency and its harmonics are predominantly propagated onto the gravity field solution at characteristic bands at the orders (not degrees) $k \cdot 16$, with integer k. When using the reprocessed SGG data, cf. the difference of GFS N1 to the GRACE solution (red), these peaks are eliminated completely. As shown in Sect.7.1 the low-frequency error of the gravity gradients, especially at the orbital frequency and its harmonics can be reduced significantly due to the new method for ARR.

Figures 7.15(a) and 7.15(b) show the cumulative geoid and gravity anomaly differences, respectively, between the two full-scale SGG solutions (O1 and N1) and ITG-Grace2010s, starting at degree 20. Again, the GRACE solution serves as a reference for the low to medium degrees. The computation of the cumulative errors has been performed in the same way as for Fig. 7.9, where the cumulative errors of the five QL SGG solutions are shown. This means that the computation is based on the degree median, scaled to the corresponding standard deviation by multiplication with the factor 1.4826, between degrees 20 and 150. The cumulative geoid error can be reduced in total from 3.0 to 2.1 cm, and the gravity anomaly error from 0.7 to 0.5 mGal (cf. the blue (SGG original, O2) and red (SGG new, N1) curves of Figs. 7.15(a) and 7.15(b) at degree 150). These numbers are again in very good agreement with the ones obtained from the QL SGG-only gravity field solutions of Sect. 7.2.

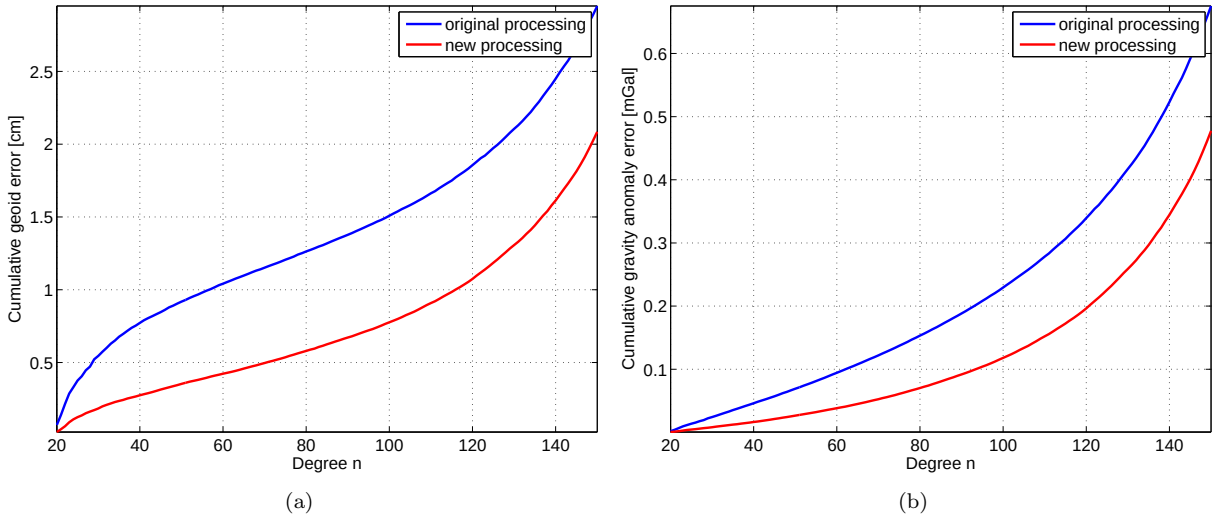

Figure 7.15.: Cumulative geoid differences (a) and cumulative gravity anomaly differences (b) between the two full-scale SGG models O1 (SGG original) and N1 (SGG new) to ITG-Grace2010s. The computation is based on the respective degree median between degrees 20 and 150 (not shown).

For the generation of the SGG-only GFS O1 and N1 stochastic models for the gravity gradient noise have been derived, cf. Pail et al. (2012). These stochastic models do not describe the peaks of the gravity gradient noise at the orbital frequency and its harmonics, as observed e.g. for the GGT trace, cf. Fig. 7.1, and for the residuals of the QL SGG-only gravity field solutions in Sect. 7.2, cf. Fig. 7.10. Note that also the stochastic modelling for the official GOCE Level 2 gravity field solutions does not include these peaks (Pail et al., 2011). According to Schuh et al. (2010) a more complex stochastic modelling, which includes the peaks, does not improve the quality of the spherical harmonic (SH) coefficients.

Figure 7.16 shows the absolute differences of the SH coefficients of GFS O1 (original SGG data) and N1 (new SGG data). We observe the same main features as visible in the improvement of the formal errors in Fig. 7.12. This means that the low degree coefficients can be improved in general, and the (near-)sectorial coefficients in particular, as expected. Moreover, the improvement occurs again predominantly at characteristic bands at the orders $k \cdot 16$. In Sect. 7.2 it was shown that these bands reflect the mapping of the peaks of the gradiometer error spectra, cf. Fig 7.10, onto the gravity field solution, cf. Fig. 7.12.

From the two full-scale SGG-only gravity field models for November and December 2009 based on the original (O1) and the new (N1) L1b processing one can analyze the effects of the reprocessing on the single gradiometer

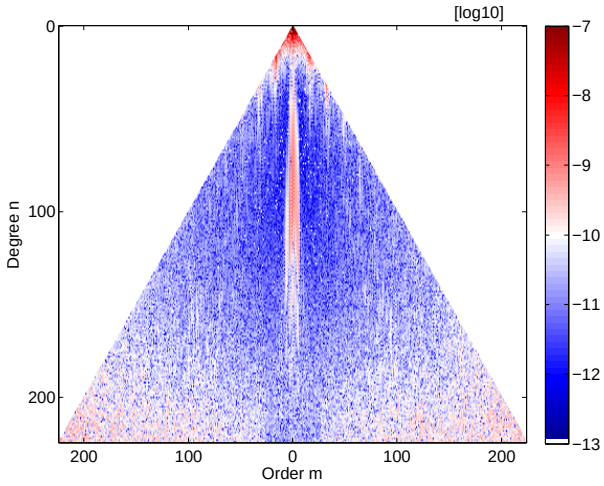

Figure 7.16.: Absolute differences of spherical harmonic coefficients of the original (GFS O1) and new (GFS N1) full-scale SGG-only models (degree/order 0-224).

components. Figure 7.17 shows the root PSD estimates of the gravity gradient residuals for V_{xx}, V_{yy}, V_{zz} and V_{xz} as obtained from the gravity field analyses for O1 (blue) and N1 (red). We observe a significant reduction of these noise representations for frequencies below about 10 mHz for all four components. Note that these noise estimates coincide very well with the ones obtained with the QL gravity field processor in Sect. 7.2 for the main diagonal GGT elements (Fig. 7.10) and for V_{xz} (Fig. 7.11). In addition to the gravity gradient residuals, also the estimated noise models for V_{xx}, V_{yy}, V_{zz} and V_{xz}, which have been used for generating the stochastic models for the GFS O1 (black) and N1 (grey, dashed) are shown. Each of these noise models is defined as a cascade of two ARMA models, which are based on the so-called first Durbin method (Durbin, 1960), as described in Stetter (2012).

With the semi-analytical approach (Sneeuw, 2000) the root PSDs of the gravity gradient residuals (Fig. 7.17) have been mapped onto the SH spectrum resulting in standard deviations for all coefficients up to degree/order 224. A comparison of the results with and without the reprocessing gives the absolute changes for each of the four components. These changes are shown in Fig. 7.18 in percent. V_{yy} shows the largest improvements for the sectorial coefficients up to 100 %. In general the peak effects around orders of multiples of 16 are reduced in all four components.

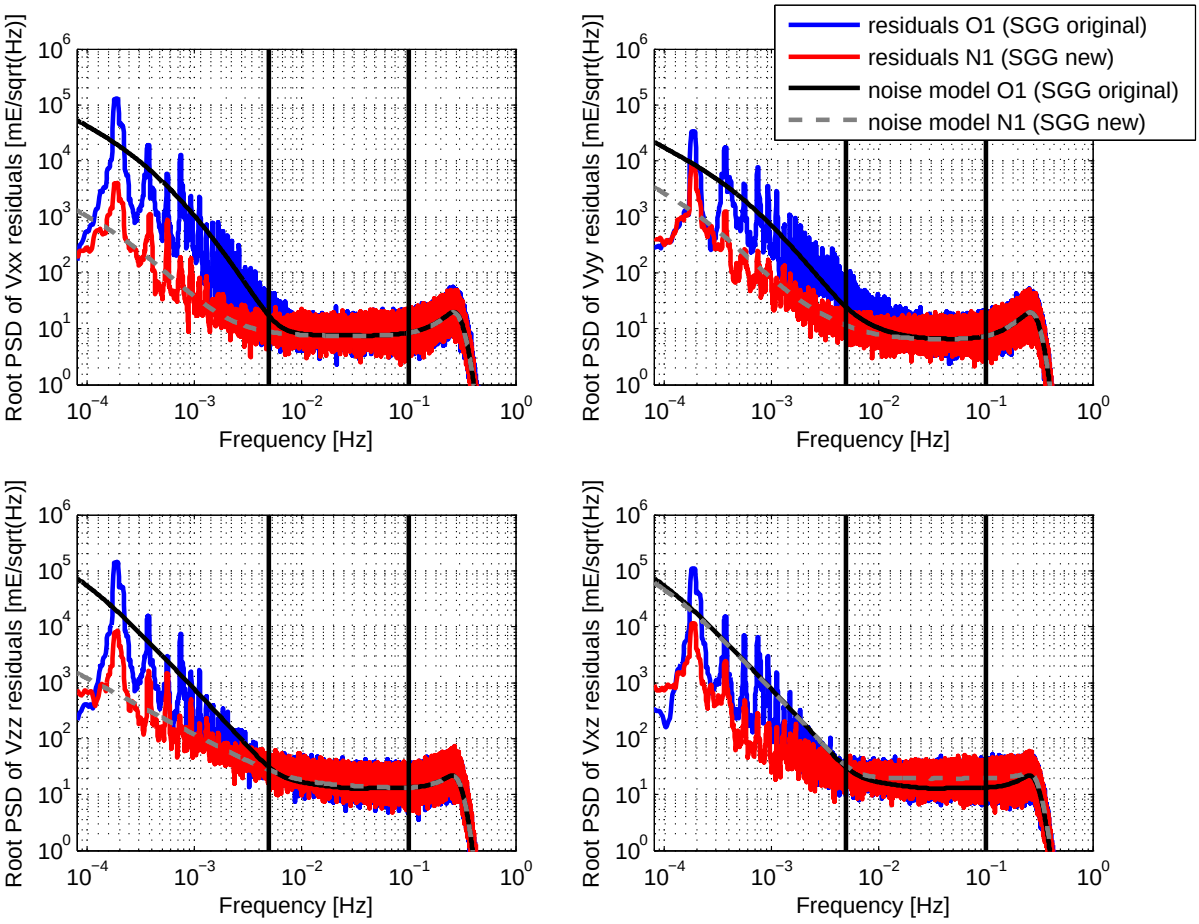

Figure 7.17.: Root PSD of V_{xx}, V_{yy}, V_{zz} and V_{xz} residuals as obtained from the GFS O1 (SGG original) and N1 (SGG new), which have been used for semi-analytical error propagation. In addition, the estimated noise models for the GGT components, which have been used for generating the stochastic models for GFS O1 and N1 are shown.

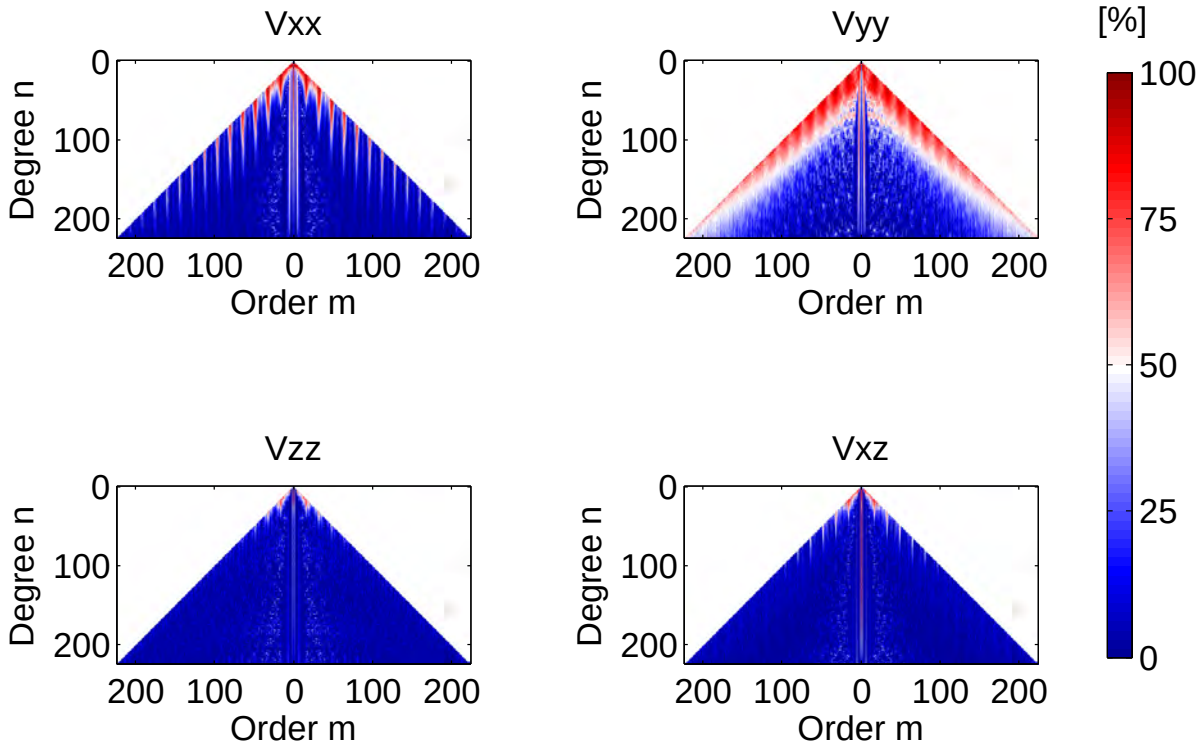

Figure 7.18.: Absolute changes [%] of standard deviations of the single GGT components V_{xx}, V_{yy}, V_{zz} and V_{xz} due to the L1b reprocessing.

7.3.2. Combination with SST

In this section we analyze the impact of the L1b reprocessing on gravity field solutions, which include besides the SGG also the SST component. The two models, O2 and N2, cf. Table 7.2, have been determined by combining the normal equations of the SGG-only solutions O1 (SGG original) and N1 (SGG new) with the normal equations of a SST solution, which is based on the approach of Mayer-Gürr (2012), using 2 months of GOCE orbit data.

In the following (cf. Fig. 7.19), the two gravity field scenarios O2 and N2 are analyzed in the spatial domain in terms of gravity anomalies, computed between degree and order 10 to 200. Figure 7.19(a) shows the differences between EGM2008 and GFS O2 (SST and SGG original). As expected, we do not observe a north-south striping pattern, as obtained for the SGG-only solution O1, which is based on the original L1b data, cf. Fig. 7.13(a). The SST component, which is very accurate for the low SH degree/order coefficients, seems to be capable of compensating the long wavelength error of the original L1b gradiometer data. Figure 7.19(b) shows the differences between EGM2008 and GFS N2 (SST and SGG new). We only observe marginal differences due to the new SGG data when comparing to Fig. 7.19(a). Figure 7.19(c) shows the differences between the combined solutions, using the original SGG component (GFS O2), and the new one (GFS N2). In the auroral regions, in particular in the area south of Australia, large improvements occur with the new SGG data. As expected, the artifacts in this area, due to non-perfect common mode rejection in the original L1b gradiometer data, are also present in the combined gravity field model O2. In this respect gravity field models, which are based on a combination of GOCE SST and SSG, benefit a lot from the L1b reprocessing.

Figure 7.20 shows the square root of degree variances of the differences of the two models O2 (SST and SGG original) and N2 (STT and SGG new) and ITG-Grace2010s. The solid lines represent the degree error variances estimated from the difference to the GRACE solution, the dashed lines are the degree error variances computed from the estimated coefficient accuracies. Also the corresponding signal (solid black curve) and formal errors (dashed black curve) of the GRACE solution are given. The formal errors of the GFS N2 (red, dashed) are smaller than the ones of the GFS O2 (blue, dashed) for the degrees 10 to 180. Only the lowest degrees (2 to 10), which are almost completely determined from the SST component, do not show a significant change. The impact of the SGG component becomes visible for degrees greater than 10. The decrease of the formal errors is confirmed by the decrease of the differences from GFS O2 (blue) and GFS N2 (red) to the GRACE reference model. This demonstrates that not only the low degree SH coefficients are improved due to the L1b preprocessing, but that there is in general a benefit for the complete SH spectrum, even of combined gravity field solutions. Note that

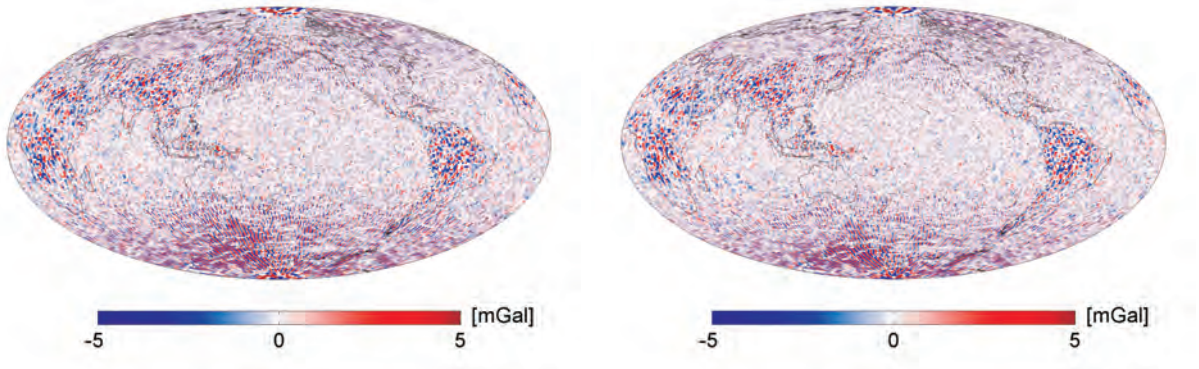

(a) Original processing (GFS O2) minus EGM2008

(b) New processing (GFS N2) minus EGM2008

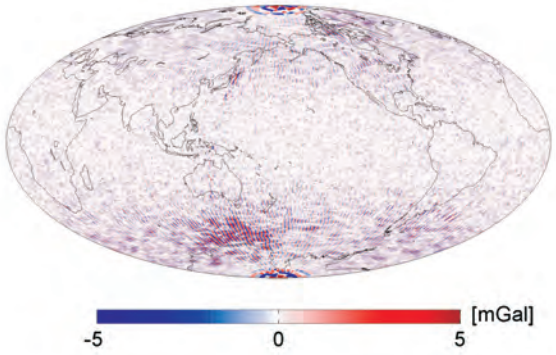

(c) New processing (GFS N2) minus original one (GFS O2)

Figure 7.19.: Difference in gravity anomalies (degree/order 10-200) between EGM2008 and (a) the GOCE-only solution O2 based on the original L1b data, and (b) the GOCE-only solution N2 based on the improved L1b data; (c) difference between the new processing (N2) and the original one (O2).

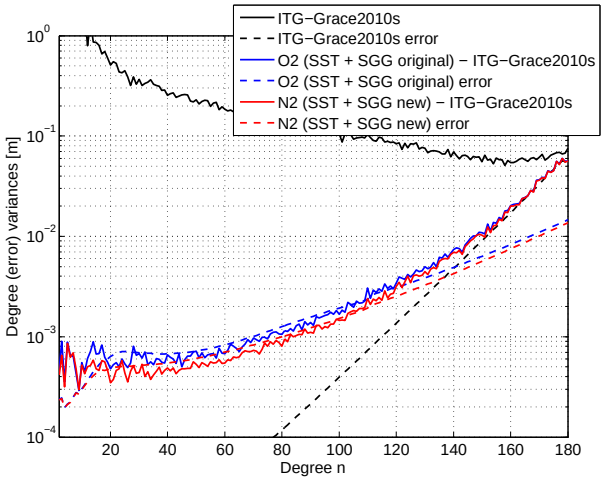

Figure 7.20.: Square root of degree (error) variances of the two models O2 (GOCE SST and SGG original) and N2 (GOCE SST and SGG new) with respect to ITG-Grace2010s. The near-zonal coefficients are excluded in the computations. The solid lines are degree error variances estimated from the difference to the reference solution, the dashed lines are the degree error variances computed from the estimated coefficient standard deviations.

these findings are also confirmed by Brockmann et al. (2012), who compare the official Level 2 gravity field TIM RL01, which is based on the first 71 days of GOCE SST and SGG data, with a new preliminary gravity field version, that makes use of the reprocessed gradiometer data.

Figures 7.21(a) and 7.21(b) show the cumulative geoid and gravity anomaly differences, respectively, between the two combined (SST and SGG) solutions (O2 and N2) and ITG-Grace2010s, starting at degree 20. The cumulative geoid error can be reduced in total from 2.1 to 1.9 cm, and the gravity anomaly error from 0.48 to 0.43 mGal (cf. the blue (SGG original, O2) and red (SGG new, N1) curves of Figs. 7.21(a) and 7.21(b) at degree 150). This means a reduction of about 10 %. For comparison, we found for the SGG-only solutions, cf. Fig. 7.15, a reduction of about 30 %. We conclude (again) that also combined models, which make use of the SST component, still benefit a lot from the L1b reprocessing.

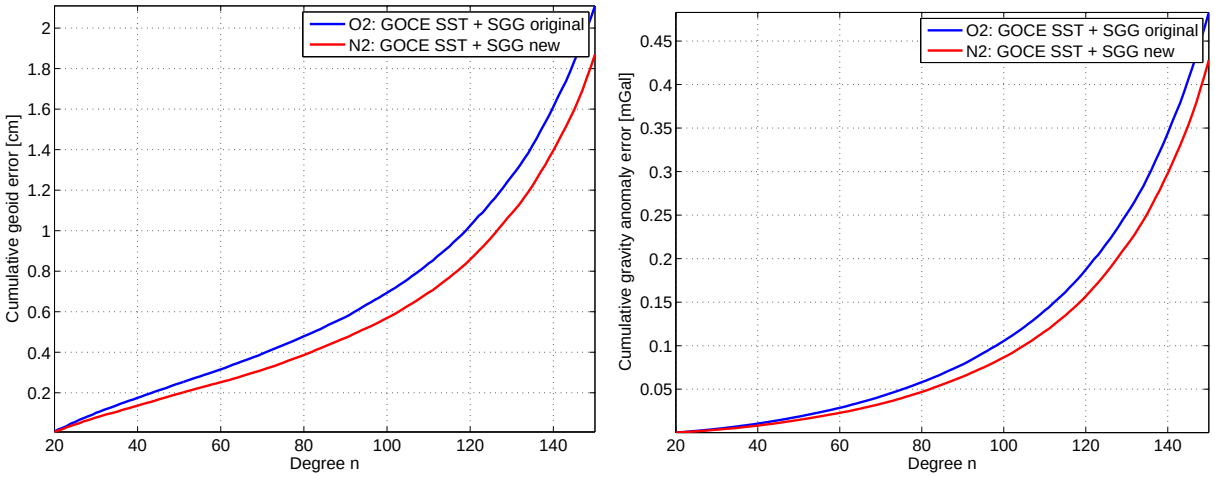

(a) (b)

Figure 7.21.: Cumulative geoid differences (a) and cumulative gravity anomaly differences (b) between the two models O2 and N2 to ITG-Grace2010s. The computation is based on the respective degree median between degrees 20 and 150 (not shown).

In order to obtain an overall picture on the improvement in the SH spectrum, Fig. 7.22 shows the improvement of the individual coefficients in percent, computed from the error estimates of the GFS O2 and N2. Note that for this visualization the scale has been confined to a maximum of 50 %. The SH coefficients up to a degree of about 15, and the (near-)sectorial coefficients up to a degree of about 60, are determined almost completely from the SST component. Hence, we do not observe a change for these coefficients. The impact of the SGG component starts to become visible for the degrees higher than about 15. The improvement due to the L1b reprocessing is largest for the coefficients with relatively low degrees between 15 and 35 (except for the near-sectorial ones) and for the higher degree (near-)sectorial coefficients, because their accurate estimation requires relatively more information from below the MB. Figure 7.22 does not show the characteristic bands at the orders $k \cdot 16$ (cf. Fig. 7.12), because the related peaks are not included in the stochastic noise models of the SGG-only solutions O1 and N1. We have shown with Fig. 7.16, however, that the related coefficients of the SGG solutions O1 and N1 are improved significantly. We conclude that also for the combined SST and SGG solutions O2 and N2 the related coefficients still benefit a lot, even if not visible in the formal errors.

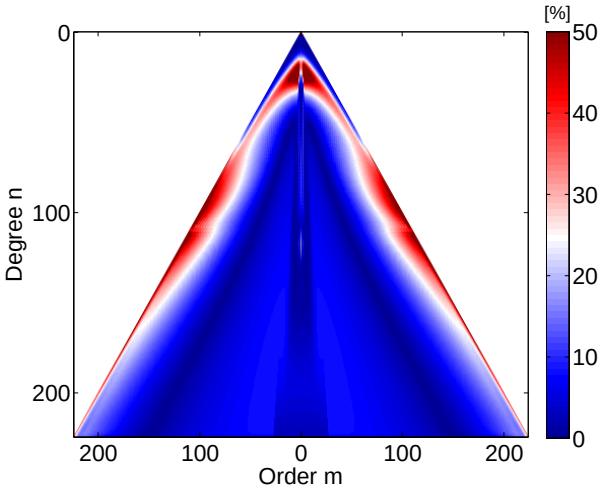

Figure 7.22.: Improvement in formal errors from GFS O2 (GOCE SST and SGG original) to N2 (GOCE SST and SGG new).

8. Summary, Conclusions, and Outlook

Since GOCE's launch in March 2009, for the first time ever a gradiometer is used is space for the recovery of the Earth's gravity field. The theory of satellite gradiometry, however, goes back several decades, cf. e.g. Carroll and Savet (1959) or Rummel (1986). In this work the basic concepts of satellite gradiometry are explained. Gravitational gradiometry is the measurement of the second derivatives of the gravitational potential. Hence, the gravitational gradients form a second-order tensor field with 3×3 components, the GGT. The GGT is symmetric, which follows from the assumption that the respective acceleration vector field is curl-free and, moreover, the GGT is trace-free, because the acceleration vector field can be regarded as source-free (Laplace equation). A geometrical interpretation of the GGT is given, and also its invariants are discussed. Moreover, the classical series expansion of the Earth's gravitational field in terms of spherical harmonics is given. Next, the basic concepts of satellite gradiometry with GOCE and its gradiometer, which is made of three orthogonally arranged one-axis gradiometers, are discussed. The gradiometer, which is rigidly mounted into the spacecraft, rotates in space. Thus, in the GRF the accelerometers pick up any rotational motion, in addition to the gravitational signal. Hence, the separation of the angular rate terms from the total measured signal plays a key role in the GOCE processing. Each accelerometer is ultra-precise along two orthogonal directions, but much less sensitive along its third axis. Hence, the arrangement of the accelerometers within the gradiometer as a whole is essential for the quality of the various GGT elements. An equally important property is related to the error behavior of the GOCE accelerometers. Their high precision of 10^{-12} m/s$^2/\sqrt{\text{Hz}}$ is only achieved in the MB between $5 \cdot 10^{-3}$ Hz and 0.1 Hz, while the noise increases with $1/f$ at lower frequencies. The basic equations for the computation of the GOCE gravity gradients, taking into account the influence of the LS accelerometer axes, are discussed, and simulated gravity gradients (and attitude quaternions) are shown as a reference for the following GOCE data analysis.

The original L1b gradiometer processing is described in detail. The main processing steps are the de-packeting of the Level 0 gradiometer data and the conversion into engineering units, the conversion of the control voltages into accelerations, e.g. in CM and DM accelerations as well as angular accelerations, the retrieval of the proof-mass accelerations, by correction of the CM and DM accelerations with the ICMs, the angular rate reconstruction, which is based on a combination of star sensor and gradiometer data, and finally the computation of the gravity gradients. Each processing step is complementarily illustrated by a flowchart. The major input and output data sets are visualized for a sample day, 11 November 2009, in time as well as in frequency domain. This allows some first quality assessment of the GOCE data. The root PSD of the gravity gradients, Fig. 3.24, follows for the frequencies below about 30 mHz the expected behavior. For frequencies higher than about 30 mHz (and lower than about 0.2 Hz) the root PSD is approximately flat, with a level of about 10 mE/$\sqrt{\text{Hz}}$ for V_{xx}, V_{yy} and V_{xz}, about 20 mE/$\sqrt{\text{Hz}}$ for V_{zz}, and about 0.6 to 0.8 E/$\sqrt{\text{Hz}}$ for the two LS GGT elements V_{xy} and V_{yz}.

For the calibration of the gradiometer, two main types of imperfections have to be considered. The first ones are non-linearities in the accelerometer transfer functions called quadratic factors, and the second ones are accelerometer scale factor errors, misalignments and non-orthogonalities, which are contained in the ICMs. The quadratic factors are measured by injection of a high-frequency signal into the accelerometer control loop. If the transfer function is not linear, an offset appears in the output voltages which is proportional to the quadratic factor, and an adequate adjustment of the proof-mass position can be made. In contrast to the quadratic factor calibration, which is performed by physical adjustment, the calibration of the second group of imperfections is performed on data level within the L1b ground processing using three sets of ICMs, which are determined from the data of dedicated satellite shaking events, which take place approximately every two months. Two methods for the determination of the ICMs are discussed in detail. The first one is the original L1b method, as defined by TAS. This method has been implemented at IAPG and is used for further GOCE data analysis. The second one is the ESA-L method, named after its inventor Daniel Lamarre. This method has proven partly more advantageous compared to the TAS method, and is hence used for calibrating the accelerations within the official L1b processing.

Based on the concept and realization of satellite gradiometry with GOCE discussed here, further data analyses have been made. The root PSD of the angular rates and DM accelerations have been compared to the one of the gravity gradients (Fig. 5.3). A possible reason for the systematic behavior of the root PSD of the gravity gradients (Fig. 5.4) could be e.g. the different low frequency systematic error behavior of each of the gradiometer

components. The measurements of individual electrode pairs and also of complete accelerometers have been omitted in the processing and replaced by either the measurements of a corresponding electrode pair or by a so-called virtual accelerometer. The impact due to replacement of control voltages on the gravity gradients has been summarized in Table 5.2. It can be excluded that there is one electrode pair with a particularly bad performance. For the virtual accelerometers, the GGT trace is degraded the most, if accelerometer 2 or 5 (on y-axis in GRF) is replaced, cf. Fig. 5.6. Combinations of CM accelerations have been built, which should ideally be identical, and which can be seen as a good indicator of the US or LS acceleration noise. The combinations of CM accelerations show best results when calibrated with the ICMs from the ESA-L method (Fig. 5.7). The development of the first 11 calibration events has been discussed (Figs. 5.9 and 5.10). The variation of the differential scale factors dSF14x and dSF25y is much larger than expected. The three star sensors and their arrangement with respect to the gradiometer, Fig. 5.11, have been analyzed. A star sensor can measure the rotation about its boresight axis only approximately 10 times worse than about the other two perpendicular axes. When rotating the STR measurements in GRF, the less accurate components leak into the very accurate ones respectively, cf. e.g. Fig. 5.14. A significant repeat pattern appears at the frequency of 1 cpr and with a 1/f-decreasing magnitude towards higher frequencies also at the corresponding harmonics (Figs. 5.12 and 5.13). The use of different star sensors in the TAS ICM calibration method is analyzed and compared to the results of the ESA-L method, which makes use of a star sensor combination (Fig. 5.16).

Four upgrades of the GOCE L1b gradiometer processing with respect to the previously applied procedures have been introduced, cf. Stummer et al. (2012). These are the methods for the determination of the angular rates and the attitude quaternions, the calibration of the accelerations, and a new approach for the combination of all available star sensor measurements. The mathematical background and the advantages of the new processing strategies have been discussed. The new ARR method has been developed in the frequency domain first, as described in Stummer et al. (2011), and has then been transformed to the time domain for the use in the official L1b processing by PDS. One big advantage of the new ARR implementation in PDS is, besides an improved performance of the resulting gravity gradients, that the new FIR filters are short compared to the Kalman filter transient of the original ARR implementation. This means that in the case of a long gap in the gradiometer measurements, the corresponding data loss in the gravity gradients can be reduced by a factor of about four. The new ATR method is separated from the ARR, but uses a very similar FIR filter approach. Additionally, the mathematical formulation of the combination of all simultaneously available star sensor measurements has been presented, which is very similar to the approach used for the GRACE data processing. For the calibration of the accelerations, the time dependence of some calibration parameters is taken into account by linear interpolation of all elements of the ICMs from the previous and the following calibration event.

The benefit of the four upgraded processing steps has been analyzed step-by-step as well as in total. At the level of gravity gradients, the noise of the diagonal GGT components, reflected by the root PSD of the GGT trace, is reduced up to a factor of 10 below the MB and to a smaller extent up to the frequency of 8 mHz. The largest improvement is due to the new ARR method. Geographical maps of filtered differences between the GOCE gravity gradients and those derived from the ITG-Grace2010s model in GRF show the strongest improvement due to the new ARR method in V_{xx}, (V_{yy}) and V_{zz}, due to the new calibration in V_{yy} and due to the new ATR method in V_{xz}. The benefit of the corresponding SGG-only gravity field solutions has been analyzed by comparing them to the EGM2008 and ITG-Grace2010s models. In the geographical plots of geoid height differences as well as in the degree error median, the cumulative geoid and gravity anomaly error and the root PSD of the Quick-Look residuals, the largest improvements have been achieved due to the new ARR method and the new calibration approach. The benefit of the star sensor combination and the new ATR method is one order of magnitude smaller, except for V_{xz}, where the Quick-Look residuals show a strong improvement due to the new ATR method. The overall improvement of the new gradiometer processing in terms of geoid heights of SGG-only solutions amounts up to 1 m, between degree and order 10 to 200. The cumulative geoid error, as well as the cumulative gravity anomaly error, between degrees 20 and 150, can be reduced by more than one quarter.

The overall impact of the L1b processor update has been further analyzed for two full-scale SGG-only gravity field solutions, calculated at IAPG. Our findings for the rigorous solutions are in very good agreement with those of the Quick-Look processor. Additionally, the root PSDs of the gravity gradient residuals have been mapped onto the SH spectrum using a semi-analytical approach. The results indicate that the largest improvements occur for the (near-)sectorial coefficients of gravity gradient V_{yy} and that in general the peak effects around orders of multiples of 16 are reduced strongly in all four components V_{xx}, V_{yy}, V_{zz}, and V_{xz}, cf. Fig. 7.18.

The full-scale SGG-only solutions, which are either based on the original or the new L1b processing, have been combined at the level of normal equations with GOCE GPS-SST data. In this case, the improvement due to the L1b reprocessing becomes much smaller. The L1b processor updates mainly occur in the long to medium wavelength range, where these complementary data contribute significantly to the combined solution. However, we have shown that also combined GOCE SST and SGG solutions still benefit from the L1b reprocessing. In

regions where large, highly dynamical common mode signals occur, as it has been shown in Fig. 7.7(c), the interpolation of the calibration parameters improves the gravity field quality in these regions over the whole spectral range. Hence, this is an improvement which is also present for combined SST and SGG solutions, as shown in Fig. 7.19(c). The cumulative geoid error, as well as the cumulative gravity anomaly error, between degrees 20 and 150, can be reduced for the combined solutions by 10 %.

In the framework of a combined (SST and SGG) GOCE gravity field solution or in combination with complementary satellite (CHAMP, GRACE) and terrestrial data, it is worthwhile to use the upgraded gravity gradients with the best possible performance also in the low to medium degree range of the harmonic spectrum. In addition to the general reduction of the error level below the measurement bandwidth, in Fig. 7.1 it could be shown that by the new L1b processing methods also the accuracy of frequencies which are multiples of the orbital frequency can be significantly improved. The noise reduction of these specific frequencies results also in an improved estimation of harmonic coefficients which are multiples of order 16 in the harmonic gravity field spectrum, cf. Fig. 7.12. For these specific orders, the performance gain shows up almost to the full resolution of GOCE models. Therefore, in the framework of the combination process they will get a higher relative weighting, resulting in a relatively larger contribution by GOCE. This is also true for the combination of GOCE with complementary gravity data on gravity gradient level, which could also be an important product for geophysical interpretation.

In general, it is highly valuable to increase the signal-to-noise ratio of the GOCE gradiometer data as much as possible, and to provide the best possible gravity gradient product to the users. This justifies also the upgrade of the L1b processor and the reprocessing effort of the complete mission by ESA. There are several applications which do not only use the gravity field models, but which rather intend to exploit the gravity gradients directly. As an example, since the new observation type of gravity gradients is particularly sensitive to high-frequency signals, individual GGT components or also combinations of them (such as invariants) are sensitive and thus best suited for the derivation of 3D sub-surface structures. Therefore, they can be used directly in geophysical applications for the modelling of structures of the lithosphere, cf. e.g. Hosse et al. (2011). For a user, the significant reduction of noise in the low frequency range will also facilitate the handling of the colored noise behavior of the gradiometer instrument when dealing with the gradients directly.

The upgrades as described in this work have been implemented into the official L1b processor in August 2011. The complete mission has been reprocessed, starting from the beginning of the mission operation phase in October 2009, and the resulting data products are successively provided to the users. In the framework of GOCE-HPF, there will also be new releases of GOCE gravity field models based on the new data, covering the nominal mission phase (October 2009 to April 2011) as well as the extended mission phase (until December 2012).

We close with some suggestions for future research. The Wiener filters for the angular rate and attitude determination methods as developed in Sect. 6.2.1 are based on simple stochastic models for the gradiometer and star sensor angular rates. These models have been derived from a comprehensive data analysis of both sensor types and an empirical refinement concerning the related cross-over frequencies. In Chapter 7 it was demonstrated that the gravity gradients and corresponding gravity fields can be significantly improved with the related filters, although they are based on rather simple error models. Moreover, simple error models can be expressed with short filters, whereas more sophisticated error models would lead to longer filters and consequently more data loss. Nevertheless, it might be worthwhile to investigate the potential benefit of more sophisticated error models for the gradiometer and star sensor data, which could possibly also include a representation of the peaks which occur at the 1 cpr frequency and its harmonics.

In Sect. 5.2.3 the impact of the used star sensor on the TAS ICM calibration results is analyzed and compared to the results of the ESA-L method. For this investigation the data of only one star sensor were used in the TAS method implemented at IAPG, whereas the results of the ESA-L method are based on a combination of star sensor data. It might be interesting to see how the TAS method behaves when also combined star sensor data is used, or similarly if the orbital harmonics are removed from the angular rate estimates, as suggested for the ESA-L method in case only one star sensor is available.

In the new L1b gradiometer processing a combination of all simultaneously available star sensor data (contained in virtual channel 2 as well as in virtual channel 3) is implemented, cf. Sect. 6.4. In the original processing chain only one star sensor, namely the one contained in virtual channel 2, had been used. Due to the combination the (LS) star sensor attitude information can be improved up to a factor of about 10. On the other hand, the combination holds the potential risk of worsening the results in the case of star sensor data of poor quality contained in virtual channel 3. This risk is reduced due to the fact that the star sensor data of virtual channel 3 is not used for periods where the respective star camera head is blinded by the Sun or Moon and its measurements are hence known to be of poor quality. Nevertheless, it might be valuable to investigate the quality of the star sensor data in the vicinity of the periods where the camera heads are blinded and in general before doing the combination. This could be done in the form of an outlier detection. One could also think about refining the

star sensor combination by taking into account stochastic modelling of the star sensor measurements, based on additional information, like e.g. the number of stars found in an image of the star camera.

Finally, one major goal of GOCE sensor analysis and progress in processing is still not reached and therefore remains a strong motivation for future investigations. It is to understand and possibly to overcome the degraded performance with respect to pre-launch expectations of the gravity gradient component V_{zz} by a factor of about 2.2 for frequencies in the upper MB. In this respect it would also be worthwhile to continue various investigations performed within this work for other time periods, like the spectral analysis of the gravity gradients, cf. Sect. 5.1.2, or the spectral error analysis using common mode accelerations, cf. Sect. 5.1.3. It might also be interesting to investigate an integrated approach, linking the L1b processing and the gravity field processing, where also a co-estimation of selected (calibration) parameters could be performed.

A. Reference frames of the GOCE gradiometer

In this section the major reference frames on instrument level of the GOCE gradiometer, as given in Cesare et al. (2008) and Gruber et al. (2010a), are specified.

A.1. AESRF - Accelerometer Electrode System Reference Frame

This is the coordinate system with respect to which the locations of the control electrodes of the accelerometer proof mass are referred. For each accelerometer it is defined as follows, cf. Figs. A.1 and 3.3:

- Origin O_{AESRF} located at the center of the accelerometer
- X_{AESRF}, Y_{AESRF} and Z_{AESRF} axes parallel to the axes of the ARF but not corresponding
- with X_{AESRF} along the less sensitive axis of the accelerometer (pointing from the ground plate to the proof mass)
- and Y_{AESRF}, Z_{AESRF} along the ultra sensitive axes of the accelerometer, so to form a right-handed coordinate system.

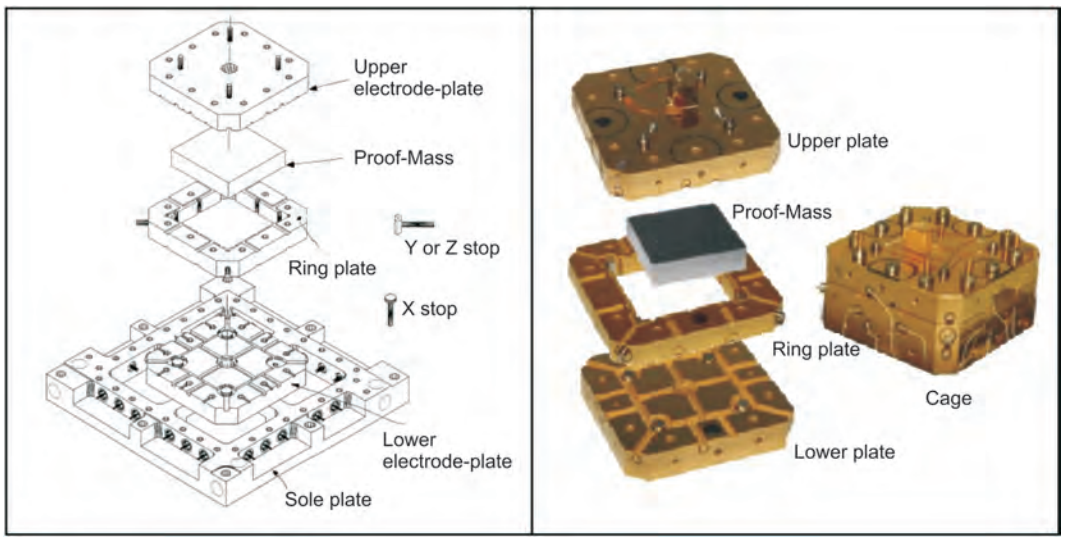

Figure A.1.: Schematic view of GOCE accelerometer (left) and realistic view (right).

A.2. ARF - Accelerometer Reference Frame

This is the reference frame in which the components of the acceleration of the proof mass relative to the cage are measured by the sensor. It is defined in a different way for the three accelerometer pairs belonging to the three one-axis gradiometers (OAGs) (see below), so that the corresponding axes of all ARFs are nominally aligned when the six accelerometers are installed in the three-axis gradiometer. All ARFs for the six accelerometers are shown in Fig. A.2 (and Fig. 2.2):

- For the accelerometers the origin of each ARF O_1 to O_6 is located in the center of the accelerometer A_1 to A_6.
- For the accelerometers A_1 and A_4 forming the OAG_1 the ARF is defined as:
  - $X_{ARF1/4}$ axis is parallel to the accelerometer ultra-sensitive axis nominally aligned with the OAG_1 baseline, positive from A_4 to A_1.
  - $Z_{ARF1/4}$ axis is defined by $\underline{X}_{ARF1/4} \times \underline{L}_{ARF1/4}$, where $\underline{X}_{ARF1/4}$ is the unit vector of the $X_{ARF1/4}$ axis and $\underline{L}_{ARF1/4}$ is the unit vector normal to the internal wall of the lower electrode plate of the cage (the lower plate is placed on the same side of the sole plate), positive in the opposite direction of the sole plate. $Z_{ARF1/4}$ is nominally parallel to the second ultra-sensitive axis of the accelerometer, cf. Fig. A.1.
  - $Y_{ARF1/4}$ axis parallel to $\underline{Z}_{ARF1/4} \times \underline{X}_{ARF1/4}$ with the same sign of $\underline{Z}_{ARF1/4} \times \underline{X}_{ARF1/4}$. $Y_{ARF1/4}$ is nominally parallel to the less sensitive axis of the accelerometer.
- For the accelerometers A_2 and A_5 forming the OAG_2 the ARF is defined as:
  - $Y_{ARF2/5}$ axis is parallel to the accelerometer ultra-sensitive axis nominally aligned with the OAG_2 baseline, positive from A_5 to A_2.
  - $X_{ARF2/5}$ axis is defined by $\underline{Y}_{ARF2/5} \times \underline{L}_{ARF2/5}$, where $\underline{Y}_{ARF2/5}$ is the unit vector of the $Y_{ARF2/5}$ axis and $\underline{L}_{ARF2/5}$ is the unit vector normal to the internal wall of the lower plate of the cage (the lower plate is placed on the same side of the sole plate), positive in the opposite direction of the sole plate. $X_{ARF2/5}$ is nominally parallel to the second ultra-sensitive axis of the accelerometer.
  - $Z_{ARF2/5}$ axis parallel to $\underline{X}_{ARF2/5} \times \underline{Y}_{ARF2/5}$ with the same sign of $\underline{X}_{ARF2/5} \times \underline{Y}_{ARF2/5}$. $Z_{ARF2/5}$ is nominally parallel to the less sensitive axis of the accelerometer.
- For the accelerometers A_3 and A_6 forming the OAG_3 the ARF is defined as:
  - $Z_{ARF3/6}$ axis is parallel to the accelerometer ultra-sensitive axis nominally aligned with the OAG_3 baseline, positive from A_6 to A_3.
  - $X_{ARF3/6}$ axis is defined by $\underline{L}_{ARF3/6} \times \underline{Z}_{ARF2/5}$, where $\underline{Z}_{ARF3/6}$ is the unit vector of the $Z_{ARF3/6}$ axis and $\underline{L}_{ARF3/6}$ is the unit vector normal to the internal wall of the lower plate of the cage (the lower plate is placed on the same side of the sole plate), positive in the opposite direction of the sole plate. $X_{ARF3/6}$ is nominally parallel to the second ultra-sensitive axis of the accelerometer.
  - $Y_{ARF3/6}$ axis parallel to $\underline{Z}_{ARF3/6} \times \underline{X}_{ARF3/6}$ with the same sign of $\underline{Z}_{ARF3/6} \times \underline{X}_{ARF3/6}$. $Y_{ARF3/6}$ is nominally parallel to the less sensitive axis of the accelerometer.

A.3. OAGRF - One-Axis Gradiometer Reference Frame

This is the reference frame in which the components of the gravity gradients are measured by the one-axis gradiometer. It is defined as follows, cf. Figs. A.1, A.2, and 4.8:

- For OAG_1, which is composed of accelerometers A_1 and A_4:
  - Origin O_{OAG1} is located at the midpoint of the straight line joining the origin of ARF_4 and ARF_1.
  - X_{OAG1} axis is parallel to the line joining O_4 to O_1, oriented from O_4 to O_1.
  - Y_{OAG1} axis is parallel to and with the same versus of the vector $\underline{\overline{Y}}_{OAG1} = \frac{\underline{Y}'_{ARF1}}{|\underline{Y}'_{ARF1}|} + \frac{\underline{Y}'_{ARF4}}{|\underline{Y}'_{ARF4}|}$ where $\underline{Y}'_{ARF1}$, $\underline{Y}'_{ARF4}$ are the projections of the vectors $\underline{Y}_{ARF1}$ and $\underline{Y}_{ARF4}$ on the plane perpendicular to the X_{OAG1} axis.
  - Z_{OAG1} axis is parallel to $\underline{X}_{OAG1} \times \underline{Y}_{OAG1}$ with the same sign of $\underline{X}_{OAG1} \times \underline{Y}_{OAG1}$
- For OAG_2, which is composed of accelerometers A_2 and A_5:
  - Origin O_{OAG2} is located at the midpoint of the straight line joining the origin of ARF_5 and ARF_2.
  - Y_{OAG2} axis is parallel to the line joining O_5 to O_2, oriented from O_5 to O_2.
  - Z_{OAG2} axis is parallel to and with the same versus of the vector $\underline{\overline{Z}}_{OAG2} = \frac{\underline{Z}'_{ARF2}}{|\underline{Z}'_{ARF2}|} + \frac{\underline{Z}'_{ARF5}}{|\underline{Z}'_{ARF5}|}$ where $\underline{Z}'_{ARF2}$, $\underline{Z}'_{ARF5}$ are the projections of the vectors $\underline{Z}_{ARF2}$ and $\underline{Z}_{ARF5}$ on the plane perpendicular to the Y_{OAG2} axis.
  - X_{OAG2} axis is parallel to $\underline{Y}_{OAG2} \times \underline{Z}_{OAG2}$ with the same sign of $\underline{Y}_{OAG2} \times \underline{Z}_{OAG2}$
- For OAG_3, which is composed of accelerometers A_3 and A_6:
  - Origin O_{OAG3} is located at the midpoint of the straight line joining the origin of ARF_6 and ARF_3.
  - Z_{OAG3} axis is parallel to the line joining O_6 to O_3, oriented from O_6 to O_3.
  - Y_{OAG3} axis is parallel to and with the same versus of the vector $\underline{\overline{Y}}_{OAG3} = \frac{\underline{Y}'_{ARF3}}{|\underline{Y}'_{ARF3}|} + \frac{\underline{Y}'_{ARF6}}{|\underline{Y}'_{ARF6}|}$ where $\underline{Y}'_{ARF3}$, $\underline{Y}'_{ARF6}$ are the projections of the vectors $\underline{Y}_{ARF3}$ and $\underline{Y}_{ARF6}$ on the plane perpendicular to the Z_{OAG3} axis.
  - X_{OAG3} axis is parallel to $\underline{Y}_{OAG3} \times \underline{Z}_{OAG3}$ with the same sign of $\underline{Y}_{OAG3} \times \underline{Z}_{OAG3}$

A.4. GRF - Gradiometer Reference Frame

This is the coordinate system in which the gravity gradients are measured by GOCE. The GRF represents the three-axis gradiometer common reference for the mutual positioning and alignment of the three one-axis gradiometers and for the positioning and orientation of the whole instrument with respect to external reference frames, cf. Fig. A.2.

- Origin O_{GRF} is located at the origin of the OAGRF_3.
- X_{GRF}, Y_{GRF}, Z_{GRF} axes are parallel to the corresponding axes of OAGRF_3 with the same sign.

Nominally the origins of all OAGRFs coincide in one intersection point. The corresponding axes of each of the three OAGRFs are parallel and point in the same directions. The corresponding six ARFs are parallel and point in the same direction.

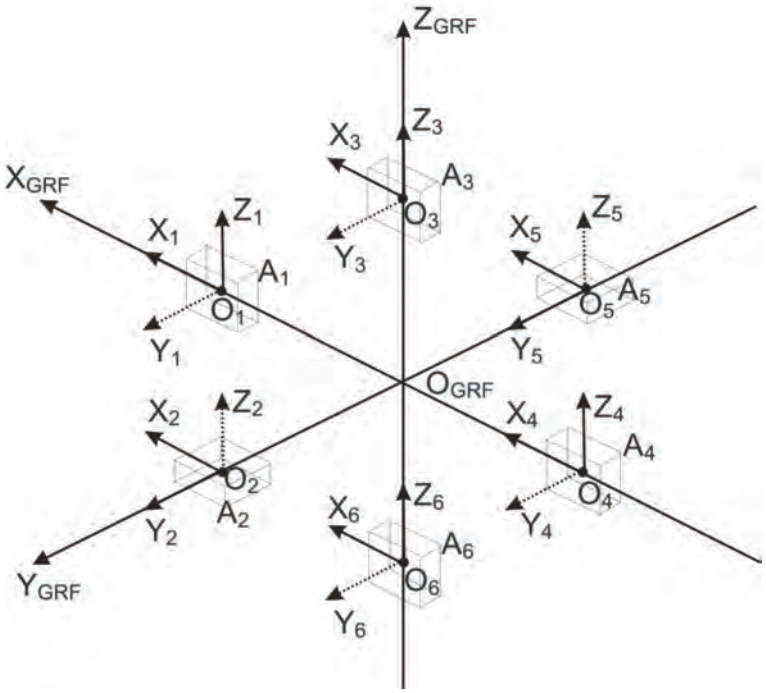

Figure A.2.: Arrangement of the six accelerometers and their respective ARF in the GOCE gradiometer and its respective GRF.

B. Orientation representations and coordinate transforms

Direction cosine matrix

An orientation representation is the description of the orientation of a coordinate system (target system) with respect to another coordinate system (source system), see Frommknecht (2008). A very common way of representation is the direction cosine matrix (DCM). It is defined as (cf. Wertz (1991)):

$$\underline{\mathrm{R}}_s^t = \begin{bmatrix} \widehat{\mathrm{X}}_t^{s'} \\ \widehat{\mathrm{Y}}_t^{s'} \\ \widehat{\mathrm{Z}}_t^{s'} \end{bmatrix} = \begin{bmatrix} X_{t,1}^s & X_{t,2}^s & X_{t,3}^s \\ Y_{t,1}^s & Y_{t,2}^s & Y_{t,3}^s \\ Z_{t,1}^s & Z_{t,2}^s & Z_{t,3}^s \end{bmatrix}, \tag{B.1}$$

where

$$\widehat{\mathrm{X}}_t^s = \begin{pmatrix} X_{t,1} \\ X_{t,2} \\ X_{t,3} \end{pmatrix}, \tag{B.2}$$

$$\widehat{\mathrm{Y}}_t^s = \begin{pmatrix} Y_{t,1} \\ Y_{t,2} \\ Y_{t,3} \end{pmatrix}, \tag{B.3}$$

$$\widehat{\mathrm{Z}}_t^s = \begin{pmatrix} Z_{t,1} \\ Z_{t,2} \\ Z_{t,3} \end{pmatrix} \tag{B.4}$$

are the unit base vectors of the target coordinate system expressed in the source coordinate system. If the vectors are arranged row wise as described above, the resulting matrix $\underline{\mathrm{R}}_s^t$ transforms a vector from the source system to the target system by a multiplication from the left:

$$\overline{\mathrm{V}}_t = \underline{\mathrm{R}}_s^t \cdot \overline{\mathrm{V}}_s. \tag{B.5}$$

The inverse transformation is given by:

$$\overline{\mathrm{V}}_s = (\underline{\mathrm{R}}_s^t)^{-1} \cdot \overline{\mathrm{V}}_t, \tag{B.6}$$

where

$$(\underline{\mathrm{R}}_s^t)^{-1} = (\underline{\mathrm{R}}_s^t)' = \begin{bmatrix} X_{t,1}^s & Y_{t,1}^s & Z_{t,1}^s \\ X_{t,2}^s & Y_{t,2}^s & Z_{t,2}^s \\ X_{t,3}^s & Y_{t,3}^s & Z_{t,3}^s \end{bmatrix}. \tag{B.7}$$

The inverse of the rotation matrix is just its transpose as it is orthonormal. Consecutive rotations can be represented as a single rotation matrix:

$$\underline{\mathrm{R}}_a^c = \underline{\mathrm{R}}_b^c \cdot \underline{\mathrm{R}}_a^b. \tag{B.8}$$

Quaternions

The quaternion representation of a rotation involves the Euler symmetric parameters. Originally they were introduced by Hamilton (1853) and Whittaker (1940); the following description is from Wertz (1991) and can also be found in Frommknecht (2008). A quaternion is a hypercomplex number, having one real part and three complex parts:

$$\begin{aligned} \overline{\mathrm{Q}}_s^t &= (q_0 + iq_1 + jq_2 + kq_3) \\ &= (\cos(\frac{\Phi}{2}) + \sin(\frac{\Phi}{2}) \cdot e_x + \sin(\frac{\Phi}{2}) \cdot e_y + \sin(\frac{\Phi}{2}) \cdot e_z), \end{aligned} \tag{B.9}$$

$$(\overline{\mathrm{Q}}_s^t)^{-1} = (-q_0 + iq_1 + jq_2 + kq_3) = (q_0 - iq_1 - jq_2 - kq_3). \tag{B.10}$$

The element $q_0 = \cos(\Phi/2)$ depends on the rotation angle Φ and q_1 to q_3 on the axis of the rotation. e_x, e_y, e_z are the components of the rotation axis. Consecutive rotations are represented by the multiplication of the quaternions representing the rotations from the right, not from the left as for the representation by the DCM:

$$\overline{\mathrm{Q}}'' = \overline{\mathrm{Q}} \star \overline{\mathrm{Q}}', \tag{B.11}$$

$$\begin{bmatrix} q_1'' \\ q_2'' \\ q_3'' \\ q_0'' \end{bmatrix} = \begin{bmatrix} q_0' & q_3' & -q_2' & q_1' \\ -q_3' & q_0' & q_1' & q_2' \\ q_2' & -q_1' & q_0' & q_3' \\ -q_1' & -q_2' & -q_3' & q_0' \end{bmatrix} \cdot \begin{bmatrix} q_1 \\ q_2 \\ q_3 \\ q_0 \end{bmatrix}. \tag{B.12}$$

The transformation of a vector can be accomplished by the following operation:

$$\overline{\mathrm{V}}_t = (\overline{\mathrm{Q}}_s^t)^{-1} \star \overline{\mathrm{V}}_s \star \overline{\mathrm{Q}}_s^t, \tag{B.13}$$

where

$$\overline{\mathrm{V}}_s = \begin{pmatrix} x_s \\ y_s \\ z_s \\ 0 \end{pmatrix}, \quad \overline{\mathrm{V}}_t = \begin{pmatrix} x_t \\ y_t \\ z_t \\ 0 \end{pmatrix}. \tag{B.14}$$

Direction cosine matrix to quaternion

From a direction cosine matrix $\underline{\mathrm{R}}_s^t$, the corresponding quaternion $\overline{\mathrm{Q}}_s^t$ can be derived in the following way, cf. Cesare et al. (2008) and Wertz (1991) (or also the GRACE document Wu et al. (2006)):

$$q_0 = \sqrt{1 + R_{1,1} + R_{2,2} + R_{3,3}}/2, \tag{B.15}$$

$$q_1 = -(R_{2,3} - R_{3,2})/4q_0, \tag{B.16}$$

$$q_2 = -(R_{3,1} - R_{1,3})/4q_0, \tag{B.17}$$

$$q_3 = -(R_{1,2} - R_{2,1})/4q_0, \tag{B.18}$$

$$\overline{\mathrm{Q}}_s^t = \begin{bmatrix} q_1 \\ q_2 \\ q_3 \\ q_0 \end{bmatrix}. \tag{B.19}$$

Quaternion to direction cosine matrix

From a given quaternion $\overline{\mathrm{Q}}_s^t$, the corresponding direction cosine matrix $\underline{\mathrm{R}}_s^t$ can be derived in the following way, cf. Cesare et al. (2008) and Wertz (1991) (or again Wu et al. (2006)):

$$\underline{\mathrm{R}}_s^t = \begin{pmatrix} q_0^2 + q_1^2 - q_2^2 - q_3^2 & 2(q_1q_2 + q_0q_3) & 2(q_1q3 - q_0q_2) \\ 2(q_1q_2 - q_0q_3) & q_0^2 - q_1^2 + q_2^2 - q_3^2 & 2(q_2q3 + q_0q_1) \\ 2(q_1q3 + q_0q_2) & 2(q_2q3 - q_0q_1) & q_0^2 - q_1^2 - q_2^2 + q_3^2 \end{pmatrix}. \tag{B.20}$$

Attitude dynamics

The dynamics of a body's attitude are reflected in the time dependency of its orientation (Frommknecht, 2008). There are two possibilities for representing a change in the orientation:

- the source system changes,
- the target system changes.

The logic of dealing with changes of orientation depends on the application: If the source system changes, one transforms first back from the changed, "new" source system to the original, "old" source system and then, using the original orientation, to the target system. If the target system changes one transforms to the "old" target system by using the original orientation and then to the changed, "new" target system.

Here, we will consider only the option of changing the target system. There are in principal two practical applications:

- The angular rates of the target system (satellite fixed body system) are known and the change in the orientation is to be derived,

- The time series of the orientation of the target system is given and the corresponding angular rates are to be derived.

Both aspects are treated by the Poisson or "kinematic" equations, cf. Wittenburg (1977), describing the connection between the orientation of a body and its angular velocity.

First, formulations for the change in orientation resulting from known angular rates are given. If the orientation is represented by quaternions, we get the following formulation, cf. Wertz (1991):

$$\begin{aligned}
\overline{\mathrm{Q}}(t+\Delta t) &= \left\{ \cos\frac{\Delta\Phi}{2}\cdot\underline{1} + \sin\frac{\Delta\Phi}{2}\cdot\begin{bmatrix} 0 & e_z & -e_y & e_x \\ -e_z & 0 & e_x & e_y \\ e_y & -e_x & 0 & e_z \\ -e_x & -e_y & -e_z & 0 \end{bmatrix} \right\} \cdot \overline{\mathrm{Q}}(t) \\
&= \left\{ \cos\frac{\Delta\Phi}{2}\cdot\underline{1} + \frac{\sin\frac{\Delta\Phi}{2}}{\omega}\cdot\begin{bmatrix} 0 & \omega_z & -\omega_y & \omega_x \\ -\omega_z & 0 & \omega_x & \omega_y \\ \omega_y & -\omega_x & 0 & \omega_z \\ -\omega_x & -\omega_y & -\omega_z & 0 \end{bmatrix} \right\} \cdot \overline{\mathrm{Q}}(t). \qquad \text{(B.21)}
\end{aligned}$$

$\Delta\Phi = \sqrt{\omega_x^2+\omega_y^2+\omega_z^2}\cdot\Delta t = \omega\cdot\Delta t$ is the rotation angle during Δt and $\underline{1}$ is a 4×4 identity matrix. The angular velocities ω_x, ω_y, ω_z refer to the respective body axes. Simplified we get:

$$\begin{aligned}
\overline{\mathrm{Q}}(t+\Delta t) &= \overline{\mathrm{Q}}(t)\star\begin{pmatrix} \sin(\frac{\Delta\Phi}{2})\cdot\frac{\omega_x}{\omega} \\ \sin(\frac{\Delta\Phi}{2})\cdot\frac{\omega_y}{\omega} \\ \sin(\frac{\Delta\Phi}{2})\cdot\frac{\omega_z}{\omega} \\ \cos(\frac{\Delta\Phi}{2}) \end{pmatrix} \\
&= \overline{\mathrm{Q}}(t)\star\overline{\Upsilon}(t). \qquad \text{(B.22)}
\end{aligned}$$

From a given time series of quaternions, the angular rates can be derived in the following way:

$$\overline{\Upsilon}(t) = \overline{\mathrm{Q}}(t)^{-1}\star\overline{\mathrm{Q}}(t+\Delta t) = \begin{pmatrix} \upsilon_1 \\ \upsilon_2 \\ \upsilon_3 \\ \upsilon_4 \end{pmatrix}, \qquad \text{(B.23)}$$

$$\Delta\Phi = 2\cdot\arccos(\upsilon_4), \qquad \text{(B.24)}$$

$$\omega = \Delta\Phi/\Delta t, \qquad \text{(B.25)}$$

$$\omega_x = \upsilon_1\cdot\frac{\omega}{\sin(\frac{\Delta\Phi}{2})}, \qquad \text{(B.26)}$$

$$\omega_y = \upsilon_2\cdot\frac{\omega}{\sin(\frac{\Delta\Phi}{2})}, \qquad \text{(B.27)}$$

$$\omega_z = \upsilon_3\cdot\frac{\omega}{\sin(\frac{\Delta\Phi}{2})}. \qquad \text{(B.28)}$$

If we assume Δt and/or ω is small, we can use the small angles approximations

$$\begin{aligned}
\cos(\frac{\Delta\Phi}{2}) &\approx 1, \\
\sin(\frac{\Delta\Phi}{2}) &\approx \frac{1}{2}\,\omega\cdot\Delta t
\end{aligned}$$

to obtain

$$\begin{aligned}
\overline{\mathrm{Q}}(t+\Delta t) &= \left\{ \underline{1} + \frac{1}{2} \cdot \Delta t \cdot \begin{bmatrix} 0 & \omega_z & -\omega_y & \omega_x \\ -\omega_z & 0 & \omega_x & \omega_y \\ \omega_y & -\omega_x & 0 & \omega_z \\ -\omega_x & -\omega_y & -\omega_z & 0 \end{bmatrix} \right\} \cdot \overline{\mathrm{Q}}(t) \\
&= \overline{\mathrm{Q}}(t) + \frac{1}{2} \cdot \Delta t \cdot \overline{\mathrm{Q}}(t) \star \begin{pmatrix} \omega_x \\ \omega_y \\ \omega_z \\ 0 \end{pmatrix} \\
&= \frac{1}{2} \cdot \Delta t \cdot \overline{\mathrm{Q}}(t) \star \begin{pmatrix} \omega_x \\ \omega_y \\ \omega_z \\ \frac{2}{\Delta t} \end{pmatrix} \\
&= \frac{1}{2} \cdot \Delta t \cdot \overline{\mathrm{Q}}(t) \star \overline{\Omega}(t). \qquad \text{(B.29)}
\end{aligned}$$

For the inverse task, the derivation of angular rates from a time series of quaternions, we obtain:

$$\overline{\Omega}(t) = 2 \cdot \overline{\mathrm{Q}}^{-1}(t) \star \frac{\overline{\mathrm{Q}}(t+\Delta t)}{\Delta t}. \qquad \text{(B.30)}$$

For the orientation representation by DCM, we get:

$$\begin{aligned}
\underline{\mathrm{R}}(t+\Delta t) &= \underline{\mathrm{R}}_{\omega} \cdot \underline{\mathrm{R}}(t) \\
&= \left[\begin{pmatrix} \frac{1}{\Delta t} & \omega_z & -\omega_y \\ -\omega_z & \frac{1}{\Delta t} & \omega_x \\ \omega_y & -\omega_x & \frac{1}{\Delta t} \end{pmatrix} \cdot \Delta t \right] \cdot \underline{\mathrm{R}}(t) \\
&= \left[\underline{\Omega}'(t) \cdot \Delta t \right] \cdot \underline{\mathrm{R}}(t). \qquad \text{(B.31)}
\end{aligned}$$

The angular rates can then be obtained from:

$$\underline{\Omega}'(t) = \frac{\underline{\mathrm{R}}(t+\Delta t)}{\Delta t} \cdot \underline{\mathrm{R}}^{-1}(t) = \frac{\underline{\mathrm{R}}(t+\Delta t)}{\Delta t} \cdot \underline{\mathrm{R}}'(t). \qquad \text{(B.32)}$$

C. Discrete Fourier Transform and comparison of window functions

C.1. Discrete Fourier Transform (DFT)

The discrete spectrum $X[k]$ of a time series $x[n]$ of N elements given at sampling intervals dt and spanning the interval $T = N \cdot dt$ is given by the Discrete Fourier Transform (DFT), cf. e.g. Meyer (1998):

$$X[k] = \sum_{n=-N_h}^{N_h} x[n] \cdot \mathrm{e}^{-i2\pi \cdot \frac{k}{T} \cdot n \cdot dt}. \tag{C.1}$$

The maximum frequency index $N_h = (N-1)/2$ for odd N and $N_h = N/2$ for even N is half the number of samples. The time series $x[n]$ corresponding to a spectrum $X[k]$ is given by the Inverse Discrete Fourier Transform (IDFT):

$$x[n] = \frac{1}{N} \sum_{k=-N_h}^{N_h} X[k] \cdot \mathrm{e}^{i2\pi \cdot \frac{k}{T} \cdot n \cdot dt}. \tag{C.2}$$

C.2. Comparison of window functions for DFT

Each measurement time series is only an extract of a true signal and is, hence, in general not periodic, cf. Meyer (1998). However, when computing the Discrete Fourier Transform (DFT) of a measured signal, periodicity is assumed, and also a non-periodic signal components are carried forward periodically. This introduces discontinuities at the junction points, leading to a degradation of the spectrum, which contains in this case amplitudes at certain frequencies which are not contained in the spectrum of the true signal. This effect is called spectral leakage. According to Meyer (1998) spectral leakage can be reduced, when the measured signal is multiplied with a window function, before building the DFT. The idea of the windowing is to weight down the first and last samples and, hence, to achieve a smooth transition when the signal is carried forward periodically.

For an illustration of different window functions in time and frequency domain it is referred to Meyer (1998). The effect of applying different window functions is illustrated with the following example. Figure C.1(a) shows the function

$$y = 4 \cdot sin(2w_0 t) + 5 \cdot sin(2000 w_0 t) \tag{C.3}$$

with main frequency $w_0 = \frac{2 \cdot \pi}{T}$, period $T = 1000$ seconds, and a sampling interval of 0.01 seconds. We use the function y for a time window of $2.75 \cdot T$, in order to have a realistic situation where the measured signal is not an integer multiple of the period T and thus discontinuities occur when the signal is carried forward periodically for the DFT. Figure C.1(b) shows the amplitude spectra of the function y, when using different window functions, before applying the DFT. Additionally, the "ideal" amplitude spectrum of the function y for a time window of $3 \cdot T$ without spectral leakage is shown (magenta).

"Boxcar" (red) refers to the case where no additional weighting is used, besides the fact that only a certain time window (here 2750 seconds) of the signal y is used, which can also be interpreted as weighting y with a Boxcar window of length 2750 seconds. The Fourier spectrum of y theoretically contains only two peaks, one at a frequency of $2 \cdot 10^{-3}$ Hz and one at a frequency of 20 Hz, cf. the magenta curve for the "ideal" case. Due to the spectral leakage (large) amplitudes appear also at other frequencies, when applying the Boxcar window. For comparison also the amplitude spectra of y, when applying a Triang, Hamming, Hanning or Kaiser window ($alpha = 20$) are shown. The Kaiser window (blue) has the advantage of rapidly decreasing side maxima in the spectrum. The parameter *alpha* is an arbitrary real number that determines the shape of the Kaiser window.

We observe the steepest decay of the (leakage) amplitudes next to the peak at the frequency of $2 \cdot 10^{-3}$ Hz, towards higher frequencies, of all shown window functions. The Kaiser window has the disadvantage of a broad

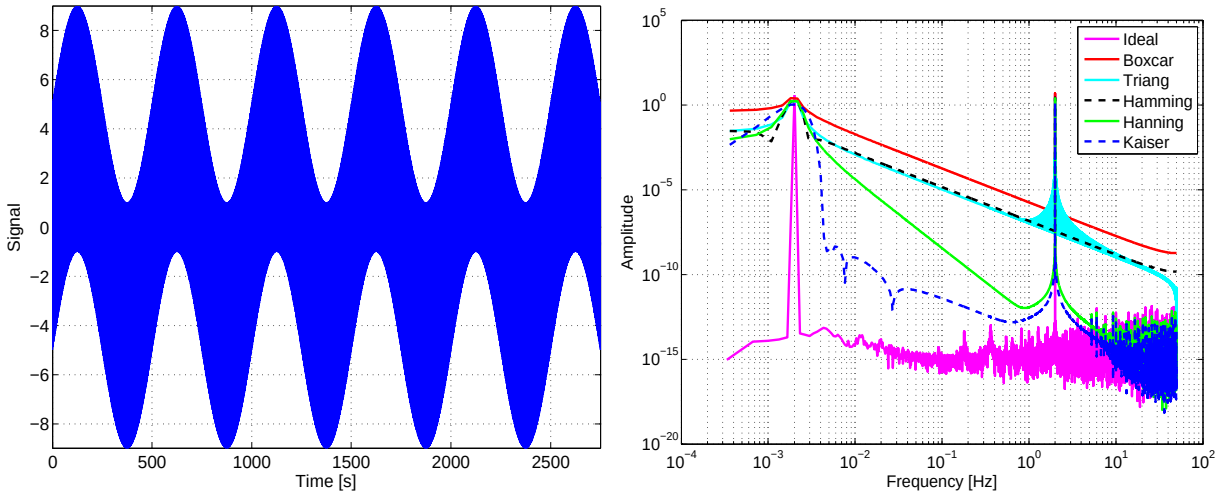

(a) (b)

Figure C.1.: Example for a measured signal (a) and its amplitude spectra (b), when applying different window functions.

main lobe in the spectrum. In Fig. C.1(b) it is the case with the slowest decay of the (leakage) amplitudes next to the peak at the frequency of $2 \cdot 10^{-3}$ Hz. This means that the peak can in this case only be solved with the poorest resolution. According to Meyer (1998), one has to find, in general, a compromise between good resolution (and bad selectivity) or good selectivity (and bad resolution), depending on the application. Further investigates on the effect of leakage for spectral analysis with DFT can also be found, e.g., in Fackler (2005).

In this work, we primarily focus on the spectral analysis of high-frequency signal content. Note that the gradiometer MB is from 5-100 mHz. The resolution of low frequency signal content is only of minor importance. Hence, we use a Kaiser window for all spectral analyses in this work.

D. Limit values for on-orbit gradiometer calibration parameters

D.1. Upper limits of the calibration matrices by construction

accelerometer pair 14

$dM_{c,14,11} < 4.05 \cdot 10^{-3}$	$dM_{c,14,12} < 1.30 \cdot 10^{-4}$	$dM_{c,14,13} < 1.30 \cdot 10^{-4}$
$dM_{c,14,21} < 1.30 \cdot 10^{-4}$	$dM_{c,14,22} < 5.18 \cdot 10^{-2}$	$dM_{c,14,23} < 1.00 \cdot 10^{-5}$
$dM_{c,14,31} < 1.30 \cdot 10^{-4}$	$dM_{c,14,32} < 1.00 \cdot 10^{-5}$	$dM_{c,14,33} < 4.05 \cdot 10^{-3}$

$dM_{d,14,11} < 4.05 \cdot 10^{-3}$	$dM_{d,14,12} < 1.30 \cdot 10^{-4}$	$dM_{d,14,13} < 1.30 \cdot 10^{-4}$
$dM_{d,14,21} < 1.30 \cdot 10^{-4}$	$dM_{d,14,22} < 5.18 \cdot 10^{-2}$	$dM_{d,14,23} < 1.30 \cdot 10^{-4}$
$dM_{d,14,31} < 1.30 \cdot 10^{-4}$	$dM_{d,14,32} < 1.30 \cdot 10^{-4}$	$dM_{d,14,33} < 4.05 \cdot 10^{-3}$

accelerometer pair 25

$dM_{c,25,11} < 4.05 \cdot 10^{-3}$	$dM_{c,25,12} < 1.30 \cdot 10^{-4}$	$dM_{c,25,13} < 1.00 \cdot 10^{-5}$
$dM_{c,25,21} < 1.30 \cdot 10^{-4}$	$dM_{c,25,22} < 4.05 \cdot 10^{-3}$	$dM_{c,25,23} < 1.30 \cdot 10^{-4}$
$dM_{c,25,31} < 1.00 \cdot 10^{-5}$	$dM_{c,25,32} < 1.30 \cdot 10^{-4}$	$dM_{c,25,33} < 5.18 \cdot 10^{-2}$

$dM_{d,25,11} < 4.05 \cdot 10^{-3}$	$dM_{d,25,12} < 1.30 \cdot 10^{-4}$	$dM_{d,25,13} < 1.30 \cdot 10^{-4}$
$dM_{d,25,21} < 1.30 \cdot 10^{-4}$	$dM_{d,25,22} < 4.05 \cdot 10^{-3}$	$dM_{d,25,23} < 1.30 \cdot 10^{-4}$
$dM_{d,25,31} < 1.30 \cdot 10^{-4}$	$dM_{d,25,32} < 1.30 \cdot 10^{-4}$	$dM_{d,25,33} < 5.18 \cdot 10^{-2}$

accelerometer pair 36

$dM_{c,36,11} < 4.05 \cdot 10^{-3}$	$dM_{c,36,12} < 1.30 \cdot 10^{-4}$	$dM_{c,36,13} < 1.30 \cdot 10^{-4}$
$dM_{c,36,21} < 1.00 \cdot 10^{-5}$	$dM_{c,36,22} < 5.18 \cdot 10^{-2}$	$dM_{c,36,23} < 1.30 \cdot 10^{-4}$
$dM_{c,36,31} < 1.30 \cdot 10^{-4}$	$dM_{c,36,32} < 1.30 \cdot 10^{-4}$	$dM_{c,36,33} < 4.05 \cdot 10^{-3}$

$dM_{d,36,11} < 4.05 \cdot 10^{-3}$	$dM_{d,36,12} < 1.30 \cdot 10^{-4}$	$dM_{d,36,13} < 1.30 \cdot 10^{-4}$
$dM_{d,36,21} < 1.00 \cdot 10^{-5}$	$dM_{d,36,22} < 5.18 \cdot 10^{-2}$	$dM_{d,36,23} < 1.30 \cdot 10^{-4}$
$dM_{d,36,31} < 1.30 \cdot 10^{-4}$	$dM_{d,36,32} < 1.30 \cdot 10^{-4}$	$dM_{d,36,33} < 4.05 \cdot 10^{-3}$

Table D.1.: Upper limits for the elements of the calibration matrices by construction. First three rows of the dM_c (above) and dM_d (below) of the three accelerometer pairs.

D.2. Upper limits of the errors due to inversion of the calibration matrices by truncated series expansion

accelerometer pair 14

$\Delta MI_{14,11} < 3.31 \cdot 10^{-5}$	$\Delta MI_{14,12} < 1.61 \cdot 10^{-5}$	$\Delta MI_{14,13} < 2.15 \cdot 10^{-6}$
$\Delta MI_{14,21} < 1.61 \cdot 10^{-5}$	$\Delta MI_{14,22} < 5.92 \cdot 10^{-3}$	$\Delta MI_{14,23} < 8.67 \cdot 10^{-6}$
$\Delta MI_{14,31} < 2.15 \cdot 10^{-6}$	$\Delta MI_{14,32} < 8.67 \cdot 10^{-6}$	$\Delta MI_{14,33} < 3.31 \cdot 10^{-5}$

$\Delta MI_{14,14} < 3.31 \cdot 10^{-5}$	$\Delta MI_{14,15} < 1.61 \cdot 10^{-5}$	$\Delta MI_{14,16} < 2.15 \cdot 10^{-6}$
$\Delta MI_{14,24} < 1.61 \cdot 10^{-5}$	$\Delta MI_{14,25} < 5.92 \cdot 10^{-3}$	$\Delta MI_{14,26} < 8.67 \cdot 10^{-6}$
$\Delta MI_{14,34} < 2.15 \cdot 10^{-6}$	$\Delta MI_{14,35} < 8.67 \cdot 10^{-6}$	$\Delta MI_{14,36} < 3.31 \cdot 10^{-5}$

accelerometer pair 25

$\Delta MI_{25,11} < 3.31 \cdot 10^{-5}$	$\Delta MI_{25,12} < 2.15 \cdot 10^{-6}$	$\Delta MI_{25,13} < 8.67 \cdot 10^{-6}$
$\Delta MI_{25,21} < 2.15 \cdot 10^{-6}$	$\Delta MI_{25,22} < 3.31 \cdot 10^{-5}$	$\Delta MI_{25,23} < 1.61 \cdot 10^{-5}$
$\Delta MI_{25,31} < 8.67 \cdot 10^{-6}$	$\Delta MI_{25,32} < 1.61 \cdot 10^{-5}$	$\Delta MI_{25,33} < 5.92 \cdot 10^{-3}$

$\Delta MI_{25,14} < 3.31 \cdot 10^{-5}$	$\Delta MI_{25,15} < 2.15 \cdot 10^{-6}$	$\Delta MI_{25,16} < 8.67 \cdot 10^{-6}$
$\Delta MI_{25,24} < 2.15 \cdot 10^{-6}$	$\Delta MI_{25,25} < 3.31 \cdot 10^{-5}$	$\Delta MI_{25,26} < 1.61 \cdot 10^{-5}$
$\Delta MI_{25,34} < 8.67 \cdot 10^{-6}$	$\Delta MI_{25,35} < 1.61 \cdot 10^{-5}$	$\Delta MI_{25,36} < 5.92 \cdot 10^{-3}$

accelerometer pair 36

$\Delta MI_{36,11} < 3.31 \cdot 10^{-5}$	$\Delta MI_{36,12} < 8.67 \cdot 10^{-6}$	$\Delta MI_{36,13} < 2.15 \cdot 10^{-6}$
$\Delta MI_{36,21} < 8.67 \cdot 10^{-6}$	$\Delta MI_{36,22} < 5.92 \cdot 10^{-3}$	$\Delta MI_{36,23} < 1.61 \cdot 10^{-5}$
$\Delta MI_{36,31} < 2.15 \cdot 10^{-6}$	$\Delta MI_{36,32} < 1.61 \cdot 10^{-5}$	$\Delta MI_{36,33} < 3.31 \cdot 10^{-5}$

$\Delta MI_{36,14} < 3.31 \cdot 10^{-5}$	$\Delta MI_{36,15} < 8.67 \cdot 10^{-6}$	$\Delta MI_{36,16} < 2.15 \cdot 10^{-6}$
$\Delta MI_{36,24} < 8.67 \cdot 10^{-6}$	$\Delta MI_{36,25} < 5.92 \cdot 10^{-3}$	$\Delta MI_{36,26} < 1.61 \cdot 10^{-5}$
$\Delta MI_{36,34} < 2.15 \cdot 10^{-6}$	$\Delta MI_{36,35} < 1.61 \cdot 10^{-5}$	$\Delta MI_{36,36} < 3.31 \cdot 10^{-5}$

Table D.2.: Upper limits of the errors due to inversion of the calibration matrices by series expansion. First three rows of the ΔMI of the three accelerometer pairs.

D.3. Upper limits of the inverse calibration matrices by construction

accelerometer pair 14

$dMI_{14,11} < 4.08 \cdot 10^{-3}$	$MI_{14,12} < 1.46 \cdot 10^{-4}$	$MI_{14,13} < 1.32 \cdot 10^{-4}$
$MI_{14,21} < 1.46 \cdot 10^{-4}$	$dMI_{14,22} < 5.77 \cdot 10^{-2}$	$MI_{14,23} < 1.87 \cdot 10^{-5}$
$MI_{14,31} < 1.32 \cdot 10^{-4}$	$MI_{14,32} < 1.87 \cdot 10^{-5}$	$dMI_{14,33} < 4.08 \cdot 10^{-3}$

$dMI_{14,14} < 4.08 \cdot 10^{-3}$	$MI_{14,15} < 1.46 \cdot 10^{-4}$	$MI_{14,16} < 1.32 \cdot 10^{-4}$
$MI_{14,24} < 1.46 \cdot 10^{-4}$	$dMI_{14,25} < 5.77 \cdot 10^{-2}$	$MI_{14,26} < 1.39 \cdot 10^{-4}$
$MI_{14,34} < 1.32 \cdot 10^{-4}$	$MI_{14,35} < 1.39 \cdot 10^{-4}$	$dMI_{14,36} < 4.08 \cdot 10^{-3}$

accelerometer pair 25

$dMI_{25,11} < 4.08 \cdot 10^{-3}$	$MI_{25,12} < 1.32 \cdot 10^{-4}$	$MI_{25,13} < 1.87 \cdot 10^{-5}$
$MI_{25,21} < 1.32 \cdot 10^{-4}$	$dMI_{25,22} < 4.08 \cdot 10^{-3}$	$MI_{25,23} < 1.46 \cdot 10^{-4}$
$MI_{25,31} < 1.87 \cdot 10^{-5}$	$MI_{25,32} < 1.46 \cdot 10^{-4}$	$dMI_{25,33} < 5.77 \cdot 10^{-2}$

$dMI_{25,14} < 4.08 \cdot 10^{-3}$	$MI_{25,15} < 1.32 \cdot 10^{-4}$	$MI_{25,16} < 1.39 \cdot 10^{-4}$
$MI_{25,24} < 1.32 \cdot 10^{-4}$	$dMI_{25,25} < 4.08 \cdot 10^{-3}$	$MI_{25,26} < 1.46 \cdot 10^{-4}$
$MI_{25,34} < 1.39 \cdot 10^{-4}$	$MI_{25,35} < 1.46 \cdot 10^{-4}$	$dMI_{25,36} < 5.77 \cdot 10^{-2}$

accelerometer pair 36

$dMI_{36,11} < 4.08 \cdot 10^{-3}$	$MI_{36,12} < 1.87 \cdot 10^{-5}$	$MI_{36,13} < 1.32 \cdot 10^{-4}$
$MI_{36,21} < 1.87 \cdot 10^{-5}$	$dMI_{36,22} < 5.77 \cdot 10^{-2}$	$MI_{36,23} < 1.46 \cdot 10^{-4}$
$MI_{36,31} < 1.32 \cdot 10^{-4}$	$MI_{36,32} < 1.46 \cdot 10^{-4}$	$dMI_{36,33} < 4.08 \cdot 10^{-3}$

$dMI_{36,14} < 4.08 \cdot 10^{-3}$	$MI_{36,15} < 1.39 \cdot 10^{-4}$	$MI_{36,16} < 1.32 \cdot 10^{-4}$
$MI_{36,24} < 1.39 \cdot 10^{-4}$	$dMI_{36,25} < 5.77 \cdot 10^{-2}$	$MI_{36,26} < 1.46 \cdot 10^{-4}$
$MI_{36,34} < 1.32 \cdot 10^{-4}$	$MI_{36,35} < 1.46 \cdot 10^{-4}$	$dMI_{36,36} < 4.08 \cdot 10^{-3}$

Table D.3.: Expected upper limits (by construction) all along the on-orbit mission lifetime for the inverse calibration matrices. First three rows of the MI (ICMs) of the three accelerometer pairs.

D.4. Upper limits due to relationship between the sub-matrices of the inverse calibration matrices

accelerometer pair 14

$\Delta MI_{c,14,11} = \Delta MI_{d,14,11} = \Delta MI_{14,11} + \Delta MI_{14,44} < 6.6 \cdot 10^{-5}$	$\Delta MI_{c,14,12} = \Delta MI_{d,14,12} = \Delta MI_{14,12} + \Delta MI_{14,45} < 3.2 \cdot 10^{-5}$	$\Delta MI_{c,14,13} = \Delta MI_{d,14,13} = \Delta MI_{14,13} + \Delta MI_{14,46} < 4.4 \cdot 10^{-6}$
$\Delta MI_{c,14,21} = \Delta MI_{d,14,21} = \Delta MI_{14,21} + \Delta MI_{14,54} < 3.2 \cdot 10^{-5}$	$\Delta MI_{c,14,22} = \Delta MI_{d,14,22} = \Delta MI_{14,22} + \Delta MI_{14,55} < 1.2 \cdot 10^{-2}$	$\Delta MI_{c,14,23} = \Delta MI_{d,14,23} = \Delta MI_{14,23} + \Delta MI_{14,56} < 1.7 \cdot 10^{-5}$
$\Delta MI_{c,14,31} = \Delta MI_{d,14,31} = \Delta MI_{14,31} + \Delta MI_{14,64} < 4.4 \cdot 10^{-6}$	$\Delta MI_{c,14,32} = \Delta MI_{d,14,32} = \Delta MI_{14,32} + \Delta MI_{14,65} < 1.7 \cdot 10^{-5}$	$\Delta MI_{c,14,33} = \Delta MI_{d,14,33} = \Delta MI_{14,33} + \Delta MI_{14,66} < 6.6 \cdot 10^{-5}$

accelerometer pair 25

$\Delta MI_{c,25,11} = \Delta MI_{d,25,11} = \Delta MI_{25,11} + \Delta MI_{25,44} < 6.6 \cdot 10^{-5}$	$\Delta MI_{c,25,12} = \Delta MI_{d,25,12} = \Delta MI_{25,12} + \Delta MI_{25,45} < 4.4 \cdot 10^{-6}$	$\Delta MI_{c,25,13} = \Delta MI_{d,25,13} = \Delta MI_{25,13} + \Delta MI_{25,46} < 1.7 \cdot 10^{-5}$
$\Delta MI_{c,25,21} = \Delta MI_{d,25,21} = \Delta MI_{25,21} + \Delta MI_{25,54} < 4.4 \cdot 10^{-6}$	$\Delta MI_{c,25,22} = \Delta MI_{d,25,22} = \Delta MI_{25,22} + \Delta MI_{25,55} < 6.6 \cdot 10^{-5}$	$\Delta MI_{c,25,23} = \Delta MI_{d,25,23} = \Delta MI_{25,23} + \Delta MI_{25,56} < 3.2 \cdot 10^{-5}$
$\Delta MI_{c,25,31} = \Delta MI_{d,25,31} = \Delta MI_{25,31} + \Delta MI_{25,64} < 1.7 \cdot 10^{-5}$	$\Delta MI_{c,25,32} = \Delta MI_{d,25,32} = \Delta MI_{25,32} + \Delta MI_{25,65} < 3.2 \cdot 10^{-5}$	$\Delta MI_{c,25,33} = \Delta MI_{d,25,33} = \Delta MI_{25,33} + \Delta MI_{25,66} < 1.2 \cdot 10^{-2}$

accelerometer pair 36

$\Delta MI_{c,36,11} = \Delta MI_{d,36,11} = \Delta MI_{36,11} + \Delta MI_{36,44} < 6.6 \cdot 10^{-5}$	$\Delta MI_{c,36,12} = \Delta MI_{d,36,12} = \Delta MI_{36,12} + \Delta MI_{36,45} < 1.7 \cdot 10^{-5}$	$\Delta MI_{c,36,13} = \Delta MI_{d,36,13} = \Delta MI_{36,13} + \Delta MI_{36,46} < 4.4 \cdot 10^{-6}$
$\Delta MI_{c,36,21} = \Delta MI_{d,36,21} = \Delta MI_{36,21} + \Delta MI_{36,54} < 1.7 \cdot 10^{-5}$	$\Delta MI_{c,36,22} = \Delta MI_{d,36,22} = \Delta MI_{36,22} + \Delta MI_{36,55} < 1.2 \cdot 10^{-2}$	$\Delta MI_{c,36,23} = \Delta MI_{d,36,23} = \Delta MI_{36,23} + \Delta MI_{36,56} < 3.2 \cdot 10^{-5}$
$\Delta MI_{c,36,31} = \Delta MI_{d,36,31} = \Delta MI_{36,31} + \Delta MI_{36,64} < 4.4 \cdot 10^{-6}$	$\Delta MI_{c,36,32} = \Delta MI_{d,36,32} = \Delta MI_{36,32} + \Delta MI_{36,65} < 3.2 \cdot 10^{-5}$	$\Delta MI_{c,36,33} = \Delta MI_{d,36,33} = \Delta MI_{36,33} + \Delta MI_{36,66} < 6.6 \cdot 10^{-5}$

Table D.4.: Upper limits of the errors for computation of the first three rows of the ICMs from the last three rows. All values of $\underline{\Delta MI}_{c,ij}$ and $\underline{\Delta MI}_{d,ij}$ for the three accelerometer pairs.

D.5. Upper limits due to orthogonality relationship

accelerometer pair 14

$$
\begin{aligned}
MI_{14,12} &= -MI_{14,21} + \Delta MI_{14,12-21}, \text{ with } \Delta MI_{14,12-21} = -2\cdot\varepsilon_{c,14} + \Delta MI_{14,12} + \Delta MI_{14,21} < 5.2\cdot10^{-5}\\
MI_{14,13} &= -MI_{14,31} + \Delta MI_{14,13-31}, \text{ with } \Delta MI_{14,13-31} = -2\cdot\eta_{c,14} + \Delta MI_{14,13} + \Delta MI_{14,31} < 2.4\cdot10^{-5}\\
MI_{14,23} &= -MI_{14,32} + \Delta MI_{14,23-32}, \text{ with } \Delta MI_{14,23-32} = -2\cdot\varsigma_{c,14} + \Delta MI_{14,23} + \Delta MI_{14,32} < 3.7\cdot10^{-5}\\
MI_{14,15} &= -MI_{14,24} + \Delta MI_{14,15-24}, \text{ with } \Delta MI_{14,15-24} = -2\cdot\varepsilon_{d,14} + \Delta MI_{14,15} + \Delta MI_{14,24} < 5.2\cdot10^{-5}\\
MI_{14,16} &= -MI_{14,34} + \Delta MI_{14,16-34}, \text{ with } \Delta MI_{14,16-34} = -2\cdot\eta_{d,14} + \Delta MI_{14,16} + \Delta MI_{14,34} < 2.4\cdot10^{-5}\\
MI_{14,26} &= -MI_{14,35} + \Delta MI_{14,26-35}, \text{ with } \Delta MI_{14,26-35} = -2\cdot\varsigma_{d,14} + \Delta MI_{14,26} + \Delta MI_{14,35} < 3.7\cdot10^{-5}\\
MI_{14,42} &= -MI_{14,51} + \Delta MI_{14,42-51}, \text{ with } \Delta MI_{14,42-51} = -2\cdot\varepsilon_{d,14} + \Delta MI_{14,42} + \Delta MI_{14,51} < 5.2\cdot10^{-5}\\
MI_{14,43} &= -MI_{14,61} + \Delta MI_{14,43-61}, \text{ with } \Delta MI_{14,43-61} = -2\cdot\eta_{d,14} + \Delta MI_{14,43} + \Delta MI_{14,61} < 2.4\cdot10^{-5}\\
MI_{14,53} &= -MI_{14,62} + \Delta MI_{14,53-62}, \text{ with } \Delta MI_{14,53-62} = -2\cdot\varsigma_{d,14} + \Delta MI_{14,53} + \Delta MI_{14,62} < 3.7\cdot10^{-5}\\
MI_{14,45} &= -MI_{14,54} + \Delta MI_{14,45-54}, \text{ with } \Delta MI_{14,45-54} = -2\cdot\varepsilon_{c,14} + \Delta MI_{14,45} + \Delta MI_{14,54} < 5.2\cdot10^{-5}\\
MI_{14,46} &= -MI_{14,64} + \Delta MI_{14,46-64}, \text{ with } \Delta MI_{14,46-64} = -2\cdot\eta_{c,14} + \Delta MI_{14,46} + \Delta MI_{14,64} < 2.4\cdot10^{-5}\\
MI_{14,56} &= -MI_{14,65} + \Delta MI_{14,56-65}, \text{ with } \Delta MI_{14,56-65} = -2\cdot\varsigma_{c,14} + \Delta MI_{14,56} + \Delta MI_{14,65} < 3.7\cdot10^{-5}
\end{aligned}
$$

accelerometer pair 25

$$
\begin{aligned}
MI_{25,12} &= -MI_{25,21} + \Delta MI_{25,12-21}, \text{ with } \Delta MI_{25,12-21} = -2\cdot\varepsilon_{c,25} + \Delta MI_{25,12} + \Delta MI_{25,21} < 2.4\cdot10^{-5}\\
MI_{25,13} &= -MI_{25,31} + \Delta MI_{25,13-31}, \text{ with } \Delta MI_{25,13-31} = -2\cdot\eta_{c,25} + \Delta MI_{25,13} + \Delta MI_{25,31} < 3.7\cdot10^{-5}\\
MI_{25,23} &= -MI_{25,32} + \Delta MI_{25,23-32}, \text{ with } \Delta MI_{25,23-32} = -2\cdot\varsigma_{c,25} + \Delta MI_{25,23} + \Delta MI_{25,32} < 5.2\cdot10^{-5}\\
MI_{25,15} &= -MI_{25,24} + \Delta MI_{25,15-24}, \text{ with } \Delta MI_{25,15-24} = -2\cdot\varepsilon_{d,ij} + \Delta MI_{25,15} + \Delta MI_{25,24} < 2.4\cdot10^{-5}\\
MI_{25,16} &= -MI_{25,34} + \Delta MI_{25,16-34}, \text{ with } \Delta MI_{25,16-34} = -2\cdot\eta_{d,25} + \Delta MI_{25,16} + \Delta MI_{25,34} < 3.7\cdot10^{-5}\\
MI_{25,26} &= -MI_{25,35} + \Delta MI_{25,26-35}, \text{ with } \Delta MI_{25,26-35} = -2\cdot\varsigma_{d,25} + \Delta MI_{25,26} + \Delta MI_{25,35} < 5.2\cdot10^{-5}\\
MI_{25,42} &= -MI_{25,51} + \Delta MI_{25,42-51}, \text{ with } \Delta MI_{25,42-51} = -2\cdot\varepsilon_{d,25} + \Delta MI_{25,42} + \Delta MI_{25,51} < 2.4\cdot10^{-5}\\
MI_{25,43} &= -MI_{25,61} + \Delta MI_{25,43-61}, \text{ with } \Delta MI_{25,43-61} = -2\cdot\eta_{d,25} + \Delta MI_{25,43} + \Delta MI_{25,61} < 3.7\cdot10^{-5}\\
MI_{25,53} &= -MI_{25,62} + \Delta MI_{25,53-62}, \text{ with } \Delta MI_{25,53-62} = -2\cdot\varsigma_{d,25} + \Delta MI_{25,53} + \Delta MI_{25,62} < 5.2\cdot10^{-5}\\
MI_{25,45} &= -MI_{25,54} + \Delta MI_{25,45-54}, \text{ with } \Delta MI_{25,45-54} = -2\cdot\varepsilon_{c,25} + \Delta MI_{25,45} + \Delta MI_{25,54} < 2.4\cdot10^{-5}\\
MI_{25,46} &= -MI_{25,64} + \Delta MI_{25,46-64}, \text{ with } \Delta MI_{25,46-64} = -2\cdot\eta_{c,25} + \Delta MI_{25,46} + \Delta MI_{25,64} < 3.7\cdot10^{-5}\\
MI_{25,56} &= -MI_{25,65} + \Delta MI_{25,56-65}, \text{ with } \Delta MI_{25,56-65} = -2\cdot\varsigma_{c,25} + \Delta MI_{25,56} + \Delta MI_{25,65} < 5.2\cdot10^{-5}
\end{aligned}
$$

accelerometer pair 36

$$
\begin{aligned}
MI_{36,12} &= -MI_{36,21} + \Delta MI_{36,12-21}, \text{ with } \Delta MI_{36,12-21} = -2\cdot\varepsilon_{c,36} + \Delta MI_{36,12} + \Delta MI_{36,21} < 3.7\cdot10^{-5}\\
MI_{36,13} &= -MI_{36,31} + \Delta MI_{36,13-31}, \text{ with } \Delta MI_{36,13-31} = -2\cdot\eta_{c,36} + \Delta MI_{36,13} + \Delta MI_{36,31} < 2.4\cdot10^{-5}\\
MI_{36,23} &= -MI_{36,32} + \Delta MI_{36,23-32}, \text{ with } \Delta MI_{36,23-32} = -2\cdot\varsigma_{c,36} + \Delta MI_{36,23} + \Delta MI_{36,32} < 5.2\cdot10^{-5}\\
MI_{36,15} &= -MI_{36,24} + \Delta MI_{36,15-24}, \text{ with } \Delta MI_{36,15-24} = -2\cdot\varepsilon_{d,ij} + \Delta MI_{36,15} + \Delta MI_{36,24} < 3.7\cdot10^{-5}\\
MI_{36,16} &= -MI_{36,34} + \Delta MI_{36,16-34}, \text{ with } \Delta MI_{36,16-34} = -2\cdot\eta_{d,36} + \Delta MI_{36,16} + \Delta MI_{36,34} < 2.4\cdot10^{-5}\\
MI_{36,26} &= -MI_{36,35} + \Delta MI_{36,26-35}, \text{ with } \Delta MI_{36,26-35} = -2\cdot\varsigma_{d,36} + \Delta MI_{36,26} + \Delta MI_{36,35} < 5.2\cdot10^{-5}\\
MI_{36,42} &= -MI_{36,51} + \Delta MI_{36,42-51}, \text{ with } \Delta MI_{36,42-51} = -2\cdot\varepsilon_{d,36} + \Delta MI_{36,42} + \Delta MI_{36,51} < 3.7\cdot10^{-5}\\
MI_{36,43} &= -MI_{36,61} + \Delta MI_{36,43-61}, \text{ with } \Delta MI_{36,43-61} = -2\cdot\eta_{d,36} + \Delta MI_{36,43} + \Delta MI_{36,61} < 2.4\cdot10^{-5}\\
MI_{36,53} &= -MI_{36,62} + \Delta MI_{36,53-62}, \text{ with } \Delta MI_{36,53-62} = -2\cdot\varsigma_{d,36} + \Delta MI_{36,53} + \Delta MI_{36,62} < 5.2\cdot10^{-5}\\
MI_{36,45} &= -MI_{36,54} + \Delta MI_{36,45-54}, \text{ with } \Delta MI_{36,45-54} = -2\cdot\varepsilon_{c,36} + \Delta MI_{36,45} + \Delta MI_{36,54} < 3.7\cdot10^{-5}\\
MI_{36,46} &= -MI_{36,64} + \Delta MI_{36,46-64}, \text{ with } \Delta MI_{36,46-64} = -2\cdot\eta_{c,36} + \Delta MI_{36,46} + \Delta MI_{36,64} < 2.4\cdot10^{-5}\\
MI_{36,56} &= -MI_{36,65} + \Delta MI_{36,56-65}, \text{ with } \Delta MI_{36,56-65} = -2\cdot\varsigma_{c,36} + \Delta MI_{36,56} + \Delta MI_{36,65} < 5.2\cdot10^{-5}
\end{aligned}
\tag{D.1}
$$

D.6. Required knowledge accuracy of the inverse calibration matrices

accelerometer pair 14

$\delta MI_{14,41} < 1.4 \cdot 10^{-5}$	$\delta MI_{14,42} < 5.0 \cdot 10^{-6}$	$\delta MI_{14,43} < 5.0 \cdot 10^{-6}$
$\delta MI_{14,51} < 1.5 \cdot 10^{-4}$	$\delta MI_{14,52} < 5.5 \cdot 10^{-4}$	$\delta MI_{14,53} < 1.5 \cdot 10^{-4}$
$\delta MI_{14,61} < 5.0 \cdot 10^{-5}$	$\delta MI_{14,62} < 5.0 \cdot 10^{-5}$	$\delta MI_{14,63} < 5.8 \cdot 10^{-5}$

$\delta MI_{14,44} < 2.02 \cdot 10^{-3}$	$\delta MI_{14,45} < 5.1 \cdot 10^{-5}$	$\delta MI_{14,46} < 5.1 \cdot 10^{-5}$
$\delta MI_{14,54} < 1.5 \cdot 10^{-4}$	$\delta MI_{14,55} < 1.01 \cdot 10^{-2}$	$\delta MI_{14,56} < 1.5 \cdot 10^{-4}$
$\delta MI_{14,64} < 1.5 \cdot 10^{-4}$	$\delta MI_{14,65} < 1.5 \cdot 10^{-4}$	$\delta MI_{14,66} < 2.02 \cdot 10^{-3}$

accelerometer pair 25

$\delta MI_{25,41} < 1.5 \cdot 10^{-4}$	$\delta MI_{25,42} < 1.5 \cdot 10^{-4}$	$\delta MI_{25,43} < 1.5 \cdot 10^{-4}$
$\delta MI_{25,51} < 5.0 \cdot 10^{-6}$	$\delta MI_{25,52} < 1.4 \cdot 10^{-5}$	$\delta MI_{25,53} < 5.0 \cdot 10^{-6}$
$\delta MI_{25,61} < 1.5 \cdot 10^{-4}$	$\delta MI_{25,62} < 5.5 \cdot 10^{-4}$	$\delta MI_{25,63} < 5.5 \cdot 10^{-4}$

$\delta MI_{25,44} < 2.1 \cdot 10^{-3}$	$\delta MI_{25,45} < 1.5 \cdot 10^{-4}$	$\delta MI_{25,46} < 1.5 \cdot 10^{-4}$
$\delta MI_{25,54} < 5.1 \cdot 10^{-5}$	$\delta MI_{25,55} < 2.02 \cdot 10^{-3}$	$\delta MI_{25,56} < 5.1 \cdot 10^{-5}$
$\delta MI_{25,64} < 1.5 \cdot 10^{-4}$	$\delta MI_{25,65} < 1.5 \cdot 10^{-4}$	$\delta MI_{25,66} < 1.01 \cdot 10^{-2}$

accelerometer pair 36

$\delta MI_{36,41} < 5.8 \cdot 10^{-5}$	$\delta MI_{36,42} < 5.0 \cdot 10^{-5}$	$\delta MI_{36,43} < 5.0 \cdot 10^{-5}$
$\delta MI_{36,51} < 1.5 \cdot 10^{-4}$	$\delta MI_{36,52} < 5.5 \cdot 10^{-4}$	$\delta MI_{36,53} < 1.5 \cdot 10^{-4}$
$\delta MI_{36,61} < 5.0 \cdot 10^{-6}$	$\delta MI_{36,62} < 5.0 \cdot 10^{-6}$	$\delta MI_{36,63} < 1.4 \cdot 10^{-5}$

$\delta MI_{36,44} < 2.02 \cdot 10^{-3}$	$\delta MI_{36,45} < 1.5 \cdot 10^{-4}$	$\delta MI_{36,46} < 1.5 \cdot 10^{-4}$
$\delta MI_{36,54} < 1.5 \cdot 10^{-4}$	$\delta MI_{36,55} < 1.01 \cdot 10^{-2}$	$\delta MI_{36,56} < 1.5 \cdot 10^{-4}$
$\delta MI_{36,64} < 5.1 \cdot 10^{-5}$	$\delta MI_{36,65} < 5.1 \cdot 10^{-5}$	$\delta MI_{36,66} < 2.02 \cdot 10^{-3}$

Table D.5.: Required knowledge accuracy of the last three rows of the MI (ICMs) during the measurement phases.

D.7. Upper limits for the ICM element variations

accelerometer pair 14

$\delta MI_{14,41} < 9.05 \cdot 10^{-6}$	$\delta MI_{14,42} < 5.0 \cdot 10^{-7}$	$\delta MI_{14,43} < 5.0 \cdot 10^{-7}$
$\delta MI_{14,51} < 5.0 \cdot 10^{-5}$	$\delta MI_{14,52} < 5.0 \cdot 10^{-5}$	$\delta MI_{14,53} < 1.5 \cdot 10^{-5}$
$\delta MI_{14,61} < 5.0 \cdot 10^{-6}$	$\delta MI_{14,62} < 5.0 \cdot 10^{-6}$	$\delta MI_{14,63} < 9.05 \cdot 10^{-6}$

$\delta MI_{14,44} < 2.0 \cdot 10^{-5}$	$\delta MI_{14,45} < 1.0 \cdot 10^{-6}$	$\delta MI_{14,46} < 1.0 \cdot 10^{-6}$
$\delta MI_{14,54} < 1.0 \cdot 10^{-4}$	$\delta MI_{14,55} < 1.0 \cdot 10^{-4}$	$\delta MI_{14,56} < 1.0 \cdot 10^{-4}$
$\delta MI_{14,64} < 1.0 \cdot 10^{-4}$	$\delta MI_{14,65} < 1.0 \cdot 10^{-4}$	$\delta MI_{14,66} < 2.0 \cdot 10^{-5}$

accelerometer pair 25

$\delta MI_{25,41} < 5.0 \cdot 10^{-5}$	$\delta MI_{25,42} < 5.0 \cdot 10^{-5}$	$\delta MI_{25,43} < 5.0 \cdot 10^{-5}$
$\delta MI_{25,51} < 5.0 \cdot 10^{-7}$	$\delta MI_{25,52} < 9.05 \cdot 10^{-6}$	$\delta MI_{25,53} < 5.0 \cdot 10^{-7}$
$\delta MI_{25,61} < 5.0 \cdot 10^{-5}$	$\delta MI_{25,62} < 5.0 \cdot 10^{-5}$	$\delta MI_{25,63} < 5.0 \cdot 10^{-5}$

$\delta MI_{25,44} < 1.0 \cdot 10^{-4}$	$\delta MI_{25,45} < 1.0 \cdot 10^{-4}$	$\delta MI_{25,46} < 1.0 \cdot 10^{-4}$
$\delta MI_{25,54} < 1.0 \cdot 10^{-6}$	$\delta MI_{25,55} < 2.0 \cdot 10^{-5}$	$\delta MI_{25,56} < 1.0 \cdot 10^{-6}$
$\delta MI_{25,64} < 1.0 \cdot 10^{-4}$	$\delta MI_{25,65} < 1.0 \cdot 10^{-4}$	$\delta MI_{25,66} < 1.0 \cdot 10^{-4}$

accelerometer pair 36

$\delta MI_{36,41} < 9.05 \cdot 10^{-6}$	$\delta MI_{36,42} < 5.0 \cdot 10^{-6}$	$\delta MI_{36,43} < 5.0 \cdot 10^{-6}$
$\delta MI_{36,51} < 5.0 \cdot 10^{-5}$	$\delta MI_{36,52} < 5.0 \cdot 10^{-5}$	$\delta MI_{36,53} < 5.0 \cdot 10^{-5}$
$\delta MI_{36,61} < 5.0 \cdot 10^{-7}$	$\delta MI_{36,62} < 5.0 \cdot 10^{-7}$	$\delta MI_{36,63} < 9.05 \cdot 10^{-6}$

$\delta MI_{36,44} < 2.0 \cdot 10^{-5}$	$\delta MI_{36,45} < 1.0 \cdot 10^{-4}$	$\delta MI_{36,46} < 1.0 \cdot 10^{-4}$
$\delta MI_{36,54} < 1.0 \cdot 10^{-4}$	$\delta MI_{36,55} < 1.0 \cdot 10^{-4}$	$\delta MI_{36,56} < 1.0 \cdot 10^{-4}$
$\delta MI_{36,64} < 1.0 \cdot 10^{-6}$	$\delta MI_{36,65} < 1.0 \cdot 10^{-6}$	$\delta MI_{36,66} < 2.0 \cdot 10^{-5}$

Table D.6.: Upper limits for the variations of the last three rows of the MI (ICMs) during one measurement cycle.

D.8. Required measurement accuracy of the inverse calibration matrices

accelerometer pair 14

$\delta MI_{14,41} < 4.7 \cdot 10^{-6}$	$\delta MI_{14,42} < 4.5 \cdot 10^{-6}$	$\delta MI_{14,43} < 4.5 \cdot 10^{-6}$
$\delta MI_{14,51} < 1.0 \cdot 10^{-4}$	$\delta MI_{14,52} < 5.0 \cdot 10^{-4}$	$\delta MI_{14,53} < 1.0 \cdot 10^{-4}$
$\delta MI_{14,61} < 4.5 \cdot 10^{-5}$	$\delta MI_{14,62} < 4.5 \cdot 10^{-5}$	$\delta MI_{14,63} < 4.87 \cdot 10^{-5}$

$\delta MI_{14,44} < 2.0 \cdot 10^{-3}$	$\delta MI_{14,45} < 5.0 \cdot 10^{-5}$	$\delta MI_{14,46} < 5.0 \cdot 10^{-5}$
$\delta MI_{14,54} < 5.0 \cdot 10^{-5}$	$\delta MI_{14,55} < 1.0 \cdot 10^{-2}$	$\delta MI_{14,56} < 5.0 \cdot 10^{-5}$
$\delta MI_{14,64} < 5.0 \cdot 10^{-5}$	$\delta MI_{14,65} < 5.0 \cdot 10^{-5}$	$\delta MI_{14,66} < 2.0 \cdot 10^{-3}$

accelerometer pair 25

$\delta MI_{25,41} < 1.0 \cdot 10^{-4}$	$\delta MI_{25,42} < 1.0 \cdot 10^{-4}$	$\delta MI_{25,43} < 1.0 \cdot 10^{-4}$
$\delta MI_{25,51} < 4.5 \cdot 10^{-6}$	$\delta MI_{25,52} < 4.7 \cdot 10^{-6}$	$\delta MI_{25,53} < 4.5 \cdot 10^{-6}$
$\delta MI_{25,61} < 1.0 \cdot 10^{-4}$	$\delta MI_{25,62} < 1.0 \cdot 10^{-4}$	$\delta MI_{25,63} < 5.0 \cdot 10^{-4}$

$\delta MI_{25,44} < 2.0 \cdot 10^{-3}$	$\delta MI_{25,45} < 5.0 \cdot 10^{-5}$	$\delta MI_{25,46} < 5.0 \cdot 10^{-5}$
$\delta MI_{25,54} < 5.0 \cdot 10^{-5}$	$\delta MI_{25,55} < 2.0 \cdot 10^{-3}$	$\delta MI_{25,56} < 5.0 \cdot 10^{-5}$
$\delta MI_{25,64} < 5.0 \cdot 10^{-5}$	$\delta MI_{25,65} < 5.0 \cdot 10^{-5}$	$\delta MI_{25,66} < 1.0 \cdot 10^{-2}$

accelerometer pair 36

$\delta MI_{36,41} < 4.87 \cdot 10^{-5}$	$\delta MI_{36,42} < 4.5 \cdot 10^{-5}$	$\delta MI_{36,43} < 4.5 \cdot 10^{-5}$
$\delta MI_{36,51} < 1.0 \cdot 10^{-4}$	$\delta MI_{36,52} < 5.0 \cdot 10^{-4}$	$\delta MI_{36,53} < 1.0 \cdot 10^{-4}$
$\delta MI_{36,61} < 4.5 \cdot 10^{-6}$	$\delta MI_{36,62} < 4.5 \cdot 10^{-6}$	$\delta MI_{36,63} < 4.7 \cdot 10^{-6}$

$\delta MI_{36,44} < 2.0 \cdot 10^{-3}$	$\delta MI_{36,45} < 5.0 \cdot 10^{-5}$	$\delta MI_{36,46} < 5.0 \cdot 10^{-5}$
$\delta MI_{36,54} < 5.0 \cdot 10^{-5}$	$\delta MI_{36,55} < 1.0 \cdot 10^{-2}$	$\delta MI_{36,56} < 5.0 \cdot 10^{-5}$
$\delta MI_{36,64} < 5.0 \cdot 10^{-5}$	$\delta MI_{36,65} < 5.0 \cdot 10^{-5}$	$\delta MI_{36,66} < 2.0 \cdot 10^{-3}$

Table D.7.: Required measurement accuracy of the last three rows of the MI (ICMs) during the measurement phases.

E. Abbreviations

AESRF	Accelerometer Electrode System Reference Frame
ARF	Accelerometer Reference Frame
ARMA	Auto-Regressive Moving-Average
ARR	Angular Rate Reconstruction
ATR	Attitude Reconstruction
CHAMP	CHAllenging MiniPayload
CM	Common Mode
DC	Direct Current
DCM	Direction Cosine Matrix
DFC	Drag-Free Control
DFT	Discrete Fourier Transform
DM	Differential Mode
EGG	Electrostatic Gravity Gradiometer
ESA	European Space Agency
FIR	Finite Impulse Response
GAR	Gradiometer Angular Accelerations
GCD	Gradiometer Calibration Device
GFA	Gravity Field Analysis
GFS	Gravity Field Scenario
GGT	Gravity Gradient Tensor
GOCE	Gravity Field and Steady-state Ocean Circulation Explorer
GRACE	Gravity Recovery And Climate Experiment
GRF	Gradiometer Reference Frame
HPF	High-Level Processing Facility
IAQ	Inertial Attitude Quaternions
ICM	Inverse Calibration Matrix
IDFT	Inverse Discrete Fourier Transform
IRF	Inertial Reference Frame
LS	Less Sensitive
L1b	Level 1b
MB	Measurement Band
MDS	Measurement Data Set
OAG	One-Axis Gradiometer
OAGRF	One-Axis Gradiometer Reference Frame

PDS	Payload Data Segment
PSD	Power Spectral Density
QL	Quick Look
SGG	Satellite Gravity Gradiometry
SH	Spherical Harmonic
SST	Satellite-to-Satellite Tracking
STR	Star Tracker / Star Sensor
TAS	Thales Alenia Space
UMB	Upper Measurement Band
US	Ultra-Sensitive

Bibliography

Aguirre-Martinez, M. and Cesare, S. (1999). GOCE mission concept, error derivation and performances. *Proceedings of the II Joint Meeting of the International Gravity Commission and the International Geoid Commission, Trieste September 1998, Bollettino di Geofisica teorica e applicata 40:295-302.*

Alenia (2002). Requirement Specification - Gradiometer Instrument Specification. Technical Note to ESA, GO-RQ-AI-0007, Issue 3, Alenia Aerospazio.

Balmino, G., Barlier, F., Bernard, A., Bouzat, C., Riviere, G., and Runavot, J. (1981). GRADIO gradiométrie par satellite. Toulouse.

Balmino, G., Letoquart, D., Barlier, F., Ducasse, F., Bernard, A., Sacleux, B., Bouzat, C., J.J, R., Le Pichon, X., and Souriau, M. (1984). Le projet GRADIO et la détermination a haute résolution du géopotentiel. *Journal of Geodesy, 58(2): 151–179.* doi: 10.1007/BF02520899.

Baur, O. (2007). Die Invariantendarstellung in der Satellitengradiometrie: theoretische Betrachtungen und numerische Realisierung anhand der Fallstudie GOCE. *DGK, Reihe C, 609, Verlag der Bayerischen Akademie der Wissenschaften, München.* ISBN: 3-7696-5048-4.

Baur, O., Sneeuw, N., and Grafarend, E. W. (2007). Methodology and use of tensor invariants for satellite gravity gradiometry. *Journal of Geodesy*, 82(4-5):279–293. doi: 10.1007/s00190-007-0178-5.

Best, R. (1991). *Digitale Meßwertverarbeitung.* R. Ouldenbourg, München,Wien.

Bigazzi, A. and Frommknecht, B. (2010). Note on GOCE instruments Positioning. XGCE-GSEG-EOPG-TN-09-0007, Frascati, Italy, http://earth.esa.int/download/goce/.

Bouman, J. (2008). Synthesis Analysis of Internal and External Calibration. Technical Report GO-TN-HPF-GS-0221, Issue 1.

Bouman, J., Fiorot, S., Fuchs, M., Gruber, T., Schrama, E., Tscherning, C. C., Veicherts, M., and Visser, P. (2011). GOCE gravitational gradients along the orbit. *Journal of Geodesy, 85(11):791-805.* doi: 10.1007/s00190-011-0464-0.

Bouman, J., Koop, R., Tscherning, C., and Visser, P. (2004). Calibration of GOCE SGG data using high-low SST, terrestrial gravity data and global gravity field models. *Journal of Geodesy, 78(1-2):124-137.* doi: 10.1007/s00190-004-0382-5.

Bouman, J., Stummer, C., Murböck, M., Fuchs, M., Rummel, R., Pail, R., Gruber, T., Bosch, W., and Schmidt, M. (2010). GOCE gravity gradients: a new satellite observable. In Münch, U.; Dransch, W., editor, *Observation of the System Earth from Space*, GEOTECHNOLOGIEN Science Report, Nr. 17, pages 52-61, Koordinierungsbüro GEOTECHNOLOGIEN, ISSN 1619-7399. doi: 10.2312/GFZ.gt.17.09.

Brockmann, J. M., Kargoll, B., Krasbutter, I., Schuh, W.-D., and Wermuth, M. (2010). Goce data analysis: From calibrated measurements to the global earth gravity field. In Flechtner, F., Gruber, T., Güntner, A., Mandea, M., Rothacher, M., Schöne, T., and Wickert, J., editors, *System Earth via Geodetic-Geophysical Space Techniques*, pages 213–229. Springer. doi: 10.1007/978-3-642-10228-8_17.

Brockmann, J. M., Schuh, W.-D., Krasbutter, I., and Gruber, T. (2012). TIM RL01 gravity field determination with reprocessed EGG_NOM_2 data, https://earth.esa.int/web/guest/missions/esa-operational-eo-missions/goce/. Technical Report GO-TN-HPF-GS-0301.

Carroll, J. J. and Savet, P. H. (1959). Gravity difference detection. *Aerospace Engineering*, pages 44–47.

Cesare, C. (2008). Performance Requirements and Budgets for the Gradiometric Mission. Technical Note to ESA, GO-TN-AI-0027, Issue 4, Alenia Aerospazio.

Cesare, C. and Catastini, G. (2008a). Gradiometer Calibration Plan. Technical Note to ESA, GO-PL-AI-0039, Issue 6, Alenia Aerospazio.

Cesare, C. and Catastini, G. (2008b). Gradiometer On-Orbit Calibration Procedure Analysis. Technical Note to ESA, GO-TN-AI-0069, Issue 4, Alenia Aerospazio.

Cesare, C., Sechi, G., and Catastini, G. (2008). Gradiometer Ground Processing Algorithms Documentation. Technical Note to ESA, GO-TN-AI-0067, Issue 7, Alenia Aerospazio.

Chan, H. A., Moody, M. V., and Paik, H. J. (1987). Superconducting gravity gradiometer for sensitive gravity measurements. II. experiment. *Physical Review D*, 35(12):3572. doi: 10.1103/PhysRevD.35.3572.

Chhun, R. and Gurard, J. (2004). Voltage to acceleration conversion algorithm. Technical Report GO-TN-ONE-GS-0001, Issue 2.

Drinkwater, M. (2005). GOCE Calibration and Validation Plan for L1b Data Products. Technical Report EOP-SM/1363/MD-md.

Drinkwater, M., Haagmans, R., Muzzi, D., Popescu, A., Floberghagen, R., Kern, M., and Fehringer, M. (2007). The GOCE gravity mission: ESA's first core explorer. In *Proceedings 3rd GOCE user workshop*, number ESA SP-627, pages 1–8, Noordwijk. European Space Agency.

Duchon, C. (1979). Lanczos Filtering in One and Two Dimensions. *J. Appl. Meteor, 18:1016-1022.* doi: 10.1175/1520-0450(1979)018<1016:LFIOAT<.0.CO;2.

Durbin, J. (1960). The fitting of time series models. *Revue Inst. Int. De Stat., 28 (3): 233–244.*

Emiliani, C. (1992). *Planet Earth: Cosmology, Geology, and the Evolution of Life and Environment.* Cambridge University Press. ISBN: 0-5214-0949-7.

Eötvös, R. V. (1906). Bestimmung der Gradienten der Schwerkraft und ihrer Niveauflächen mit Hilfe der Drehwaage. volume 1, pages 337–396. Verhandlungen der 15. allgemeinen Konferenz der Internationalen Erdmessung, Budapest.

ESA (2008). GOCE, ESA's Gravity Mission. ESA Communication Production Office, ESA SP-1314 (DVD). ISBN: 978-92-9221-407-4, ISSN: 0379-6566.

Fackler, U. (2005). GRACE - Analyse von Beschleunigungsmessungen. IAPG/FESG No. 20, ISBN: 3-934205-19-4.

Floberghagen, R., Fehringer, M., Lamarre, D., Muzi, D., and Frommknecht, B. (2011). Mission design, operation and exploitation of the Gravity field and steady-state Ocean Circulation Explorer. *Journal of Geodesy, 85(11):749-758.* doi: 10.1007/s00190-011-0498-3.

Forward, R. L. (1974). Review of artificial satellite gravity gradiometer techniques for geodesy. In Veis, G., editor, *The Use of Artificial Satellites for Geodesy and Geodynamics*, pages 157–192. publ. of the National Technical University of Athens.

Frommknecht, B. (2008). Integrated Sensor Analysis of the GRACE Mission. *DGK, Reihe C, 617, Verlag der Bayerischen Akademie der Wissenschaften, München.* ISBN: 3-7696-5056-5.

Frommknecht, B. (2009). Detailed processing model for the EGG. Technical Report GO-TN-IAPG-GS-0001.

Frommknecht, B., Lamarre, D., Bigazzi, A., Meloni, M., and Floberghagen, R. (2011). GOCE Level 1b Data Processing. *Journal of Geodesy, 85(11):759-775.* doi: 10.1007/s00190-011-0497-4.

Frommknecht, B., Stummer, C., Gilles, P., Floberghagen, R., Cesare, S., Catastini, G., Meloni, M., and Bigazzi, A. (2010). GOCE L1b Processing. *Proceedings of the ESA Living Planet Symposium, 28 June - 2 July 2010, Bergen, Norway.* ESA SP-686 (CD-ROM).

Gruber, T. (2004). GOCE High Level Processing Facility. Reference Systems and Gradiometry. Technical Report GO-TN-HPF-GS-0078.

Gruber, T., Abrikosov, O., and Hugentobler, U. (2010a). GOCE High Level Processing Facility; GOCE Standards. Technical Report GO-MA-HPF-GS-0111, Issue 3.2.

Gruber, T., Rummel, R., Abrikosov, O., and van Hees, R. (2010b). GOCE High Level Processing Facility; GOCE Level 2 Product Data Handbook. Technical Report GO-MA-HPF-GS-0110, Issue 4.2.

Hamilton, W. (1853). *Lectures on Quaternions.* Hodges and Smith, Dublin.

Hettmansperger, T. and McKean, J. (1998). *Kendall's library of statistics 5 - robust nonparametric statistical methods.* Arnold, a member of the Hodder Headline Group, London.

Höpcke, W. (1980). *Fehlerlehre und Ausgleichsrechnung.* DeGruyter, Berlin, New York.

Hosse, M., Pail, R., Horwath, M., Mahatsente, R., Götze, H., Jahr, T., Jentzsch, M., Gutknecht, B., Köther, N., Lücke, O., Sharma, R., and Zeumann, S. (2011). Integrated modeling of satellite gravity data of active plate margins - bridging the gap between geodesy and geophysics. *Abstract G43A-0752 presented at 2011 Fall Meeting, AGU, San Francisco, Calif., 8 Dec.*

Jekeli, C. (1988). The gravity gradiometer survey system (GGSS). *Eos, Transactions American Geophysical Union*, 69(8):pages 105 & 116–117.

Johannessen, J. (1999). Gravity Field and Steady-State Ocean Circulation Mission. Technical Report ESA SP-1233(1), Noordwijk.

Jørgensen, J. (2003). ASC GOCE design and performance report. Technical Note to ESA, GO-RP-DTU-2018, Issue 1.1.

Jung, K. (1961). Schwerkraftverfahren in der angewandten Geophysik. Akademische Verlags Gesellschaft, Leipzig.

Kern, M., Haagmans, R., Plank, G., Lamarre, D., Floberghagen, R., and Drinkwater, M. (2007). In-flight GOCE Gradiometer Calibration And Validation. *American Geophysical Union, Fall Meeting 2007, abstract G33A-0894.*

Lamarre, D. (2007). The very basic principles of the GOCE gradiometer in-flight calibration. In *Proceedings 3rd GOCE user workshop*, number ESA SP-627, pages 91–94, Noordwijk. European Space Agency.

Lamarre, D. (2008). Algorithm description: retrieval of gradiometer parameters. Version 2.0 draft, 23 April 2008.

Lanczos, C. (1956). *Applied Analysis.* Prentice-Hall, ISBN: 978-0486656564.

Liu, H., Lühr, H., Henize, V., and Köhler, W. (2005). Global distribution of the thermospheric total mass density derived from CHAMP. *J. Geophys. Res, Vol. 110, A04301.* doi: 10.1029/2004JA010741.

Lühr, H., Rentz, S., Ritter, P., Liu, H., and Häusler, K. (2007). Average thermospheric wind patterns over the polar regions, as observed by CHAMP. *Ann. Geophys.*, 25:1093–1101. doi: 10.5194/angeo-25-1093-2007.

Marque, J.-P., Christophe, B., and Foulon, B. (2010). Accelerometers of the GOCE mission: return of experience from one year in orbit. *Proceedings of the ESA Living Planet Symposium, 28 June - 2 July 2010, Bergen, Norway.* ESA SP-686 (CD-ROM).

Martinec, Z. (2003). Green's function solution to spherical gradiometric boundary-value problems. *Journal of Geodesy*, 77(1-2):41–49. doi: 10.1007/s00190-002-0288-z.

Marussi, A. (1985). *Intrinsic geodesy. Translated from the Italian by Reilly, WI.* Springer-Verlag, Berlin.

Mayer-Gürr (2012). Gravitationsfeldbestimmung aus der Analyse kurzer Bahnbgen am Beispiel der Satellitenmissionen CHAMP und GRACE. *DGK, Reihe C, 675, Verlag der Bayerischen Akademie der Wissenschaften, München.* ISBN 978-3-7696-5087-7.

Mayer-Gürr, T., Eicker, A., Kurtenbach, E., and Ilk, K. (2010). ITG-GRACE: Global static and temporal gravity field models from GRACE data. In Flechtner, F., Mandea, M., Gruber, T., Rothacher, M., Wickert, J., Güntner, A., and Schöne, T., editors, *System Earth via Geodetic-Geophysical Space Techniques*, Advanced Technologies in Earth Sciences, pages 159–168. doi: 10.1007/978-3-642-10228-8_13, ISBN: 978-3-642-10227-1.

Mayrhofer, R., Pail, R., and Fecher, T. (2010). Quick-look gravity field solution as part of the GOCE quality assessment. *Proceedings of the ESA Living Planet Symposium, 28 June - 2 July 2010, Bergen, Norway.* ESA SP-686 (CD-ROM).

McGuirk, J. M., Foster, G. T., Fixler, J. B., Snadden, M. J., and Kasevich, M. A. (2002). Sensitive absolute-gravity gradiometry using atom interferometry. *Physical Review A*, 65(3):033608. doi: 10.1103/PhysRevA.65.033608.

Meyer, M. (1998). *Signalverarbeitung.* Friedrich Vieweg & Sohn, Braunschweig/Wiesbaden.

Moritz, H. (1980). *Advanced physical geodesy.* Herbert Wichmann Verlag, Karlsruhe.

Müller, J. (2001). Die Satellitengradiometriemission GOCE - Theorie, technische Realisierung und wissenschaftliche Nutzung. *Habilitation, DGK, Reihe C, 541, Verlag der Bayerischen Akademie der Wissenschaften, München.* ISBN: 3-7696-9580-1.

Ohanian, H. C. and Ruffini, R. (1994). *Gravitation and spacetime.* Norton & Company, New York, 2rd edition.

Oppenheim, A. and Schafer, R. (1989). *Discrete-Time Signal Processing.* Prentice hall.

Pail, R. (2005). A parametric study on the impact of satellite attitude errors on GOCE gravity field recovery. *Journal of Geodesy, 79(4-5):231-241.* doi: 10.1007/s00190-005-0464-z.

Pail, R., Bruinsma, S., Migliaccio, F., Förste, C., Goiginger, H., Schuh, W.-D., Höck, E., Reguzzoni, M., Brockmann, J. M., Abrikosov, O., Veicherts, M., Fecher, T., Mayrhofer, R., Krasbutter, I., Sansò, F., and Tscherning, C. C. (2011). First GOCE gravity field models derived by three different approaches. *Journal of Geodesy, 85(11):819-843.* doi: 10.1007/s00190-011-0467-x.

Pail, R., Fecher, T., Murböck, M., Rexer, M., Stetter, M., and Stummer, C. (2012). Impact of GOCE Level 1b data reprocessing on GOCE-only and combined gravity field models. *paper submitted to Studia Geophysica et Geodaetica.*

Pail, R., Goiginger, H., Schuh, W.-D., Höck, E., Brockmann, J. M., Fecher, T., Gruber, T., Mayer-Gürr, T., Kusche, J., Jäggi, A., and Rieser, D. (2010). Combined satellite gravity field model GOCO01S derived from GOCE and GRACE. *Geophysical Research Letters, Vol. 37, EID L20314, American Geophysical Union.* doi: 10.1029/2010GL044906.

Pail, R., Metzler, B., Preimesberger, T., Lackner, B., and Wermuth, M. (2007). GOCE quick-look gravity field analysis in the framework of HPF. In *Proceedings 3rd GOCE user workshop*, number ESA SP-627, pages 325–332, Noordwijk. European Space Agency.

Papoulis, A. (1984). *Signal analysis.* McGraw-Hill, New York.

Pavlis, N., Holmes, S., Kenyon, S., and Factor, J. (2012). The development and evaluation of the Earth Gravitational Model 2008 (EGM2008). *JGR, 117.* doi: 10.1029/2011JB008916.

Pedersen, L. B. and Rasmussen, T. M. (1990). The gradient tensor of potential field anomalies: Some implications on data collection and data processing of maps. *Geophysics*, 55(12):1558–1566. doi: 10.1190/1.1442807.

Peterseim, N., Schlicht, A., Stummer, C., and Yi, W. (2011). Impact of cross winds in polar regions on GOCE accelerometer and gradiometer data. *Proceedings of 4th International GOCE User Workshop, 31 March – 1 April 2011, Munich, Germany.* ESA SP-696.

Rispens, S. and Bouman, J. (2009). Calibrating the GOCE accelerations with star sensor data and a global gravity field model. *Journal of Geodesy*, 83:737–749. doi: 10.1007/s00190-008-0290-1.

Romans, L. (2003). Optimal Combination of Quaternions from Multiple Star Cameras. Technical report, Jet Propulsion Laboratory.

Rummel, R. (1986). Satellite Gradiometry. *Lecture Notes in Earth Sciences, 7: 317-363.* Springer, Berlin.

Rummel, R. (1997). Spherical spectral properties of the earth's gravitational potential and its first and second derivatives. In Sansò, F. and Rummel, R., editors, *Geodetic Boundary Value Problems in View of the One Centimeter Geoid, Lecture Notes in Earth Sciences*, volume 65, pages 359–404. Springer.

Rummel, R., Gruber, T., and Koop, R. (2004). High Level Processing Facility for GOCE: Products and Processing Strategy. In Lacoste, H., editor, *Proceedings of the 2nd International GOCE User Workshop "GOCE, The Geoid and Oceanography"*, number ESA SP-569.

Rummel, R. and Rapp, R. (1976). The influence of the atmosphere on geoid and potential coefficient determinations from gravity data. *Journal of Geophysical Research*, 81(32):5639–5642.

Rummel, R. and van Gelderen, M. (1992). Spectral analysis of the full gravity tensor. *Geophysical Journal International*, 111(1):159–169. doi: 10.1111/j.1365-246X.1992.tb00562.x.

Rummel, R., Yi, W., and Stummer, C. (2011). GOCE gravitational gradiometry. *Journal of Geodesy, 85(11):777-790.* doi: 10.1007/s00190-011-0500-0.

Schreiner, M. (1994). *Tensor Spherical Harmonics and Their Application in Satellite Gradiometry.* PhD thesis, University of Kaiserslautern.

Schuh, W.-D. (1996). Tailored numerical solution strategies for the global determination of the earth's gravity field. In *Mitteilungen der Institute der Technischen Universität Graz*, number 81, Graz.

Schuh, W.-D. (2002). Improved modeling of SGG-data sets by advanced filter strategies. In *ESA-Project "From Eötvös to mGal+"*, WP 2, Final-Report, pages 113–181.

Schuh, W.-D., Brockmann, J. M., Kargoll, B., Krasbutter, I., and Pail, R. (2010). Refinement of the stochastic model of GOCE scientific data and its effect on the in-situ gravity field solution. *Proceedings of the ESA Living Planet Symposium, 28 June - 2 July 2010, Bergen, Norway.* ESA SP-686 (CD-ROM).

SERCO/DATAMAT_Consortium (2006). GOCE L1B Prodcuts User Handbook (issue 1). Technical Report GOCE-GSEG-EOPG-TN-06-0137.

Siemes, C. (2011). GOCE gradiometer calibration and Level 1b data processing. ESA Working Paper EWP-2384, Noordwijk, The Netherlands, https://earth.esa.int/web/guest/missions/esa-operational-eo-missions/goce/.

Siemes, C., Haagmans, R., Kern, M., Plank, G., Drinkwater, M., and Floberghagen, R. (2010). Monitoring and Validation of GOCE Gradiometer Calibration Parameters. *Abstract G31A-0792 presented at 2010 Fall Meeting, AGU, San Francisco, Calif., 13-17 Dec.*

Siemes, C., Haagmans, R., Kern, M., Plank, G., and Floberghagen, R. (2012). Calibration of the GOCE gradiometer - methodology and results. *Journal of Geodesy, 86(8): 629–645.* doi: 10.1007/s00190-012-0545-8.

Sneeuw, N. (2000). A semi-analytical approach to gravity field analysis from satellite observations. *DGK, Reihe C, 527, Verlag der Bayerischen Akademie der Wissenschaften, München.* ISBN: 3-7696-9566-6.

Sneeuw, N. and van Gelderen, M. (1997). The polar gap. In Sans, F.; Rummel, R., editor, *Geodetic Boundary Value Problems in View of the One Centimeter Geoid, Lecture Notes in Earth Sciences*, volume 65, pages 559–568. Springer. ISBN: 978-3-540-62636-7, doi: 10.1007/BFb0011717.

Stetter, M. (2012). Stochastische Modellierung von GOCE-Gradiometriebeobachtungen mittels digitaler Filter. *Masterarbeit.* IAPG, TU München.

Strandberg, T. (2010). GOCE STR misalignment assessment (IFTR 1 issue). Technical Report GO-TN-ASG-0217.

Stummer, C. (2006). *Analyse der Gradiometergleichungen der GOCE Satellitenmission zur Schwerefeldbestimmung.* IAPG/FESG No. 25, ISBN: 978-3-934205-24-6.

Stummer, C., Fecher, T., and Pail, R. (2011). Alternative method for angular rate determination within the GOCE gradiometer processing. *Journal of Geodesy, 85(9): 585–596.* doi: 10.1007/s00190-011-0461-3.

Stummer, C., Siemes, C., Pail, R., Frommknecht, B., and Floberghagen, R. (2012). Upgrade of the Level 1b gradiometer processor. *ASR, 49(4): 739–752.* doi: 10.1016/j.asr.2011.11.027.

Tsuboi, C. (1983). *Gravity.* George Allen & Unwin, London.

Visser, P. (2008). Exploring the possibilities for star-tracker assisted calibration of the six individual GOCE accelerometers. *Journal of Geodesy, 82(10): 591-600.* doi: 10.1007/s00190-007-0205-6.

Welch, P. D. (1967). The use of Fast Fourier Transform for the estimation of power spectra: A method based on time averaging over short modified periodograms. IEEE Trans Audio Electroacoust, AU-15:70-73.

Wells, W. (1984). Spaceborne gravity gradiometers. In *proceedings of NASA GSFC workshop.* NASA conference publication 2305.

Wertz, J. R. (1991). *Spacecraft Attitude Determination and Control.* Kluwer Academic Publishers, Dordrecht/Boston/London.

While, J., Jackson, A., Smit, D., and Biegert, E. (2006). Spectral analysis of gravity gradiometry profiles. *Geophysics, 71(1): J11–J22.* doi: 10.1190/1.2169848.

Whittaker, E. (1940). The Hamiltonian Revival. *The Mathematical Gazette, 24.*

Wittenburg, J. (1977). *Dynamics of Systems of Rigid Bodies*. B.G. Teubner, Stuttgart.

Wu, S.-C., Kruizinga, G., and Bertinger, W. (2006). Algorithm Theoretical Basis Document for GRACE Level-1B Data Processing V1.2. Technical Report JPL D-27672, Jet Propulsion Laboratory.

Yu, J. and Zhao, D. (2010). The gravitational gradient tensor's invariants and the related boundary conditions. *Science China Earth Sciences*, 53(5):781–790. doi: 10.1007/s11430-010-0014-2.

Yu, N., Kohel, J., Kellogg, J., and Maleki, L. (2006). Development of an atom-interferometer gravity gradiometer for gravity measurement from space. *Applied Physics B*, 84(4):647–652. doi: 10.1007/s00340-006-2376-x.

Acknowledgements

First of all I'd like to thank Prof. Reiner Rummel for supervising my thesis in the beginning phase and for accepting the position of third advisor. His comprehensive knowledge on satellite gradiometry and his nonetheless formidable inquisitiveness have been very motivating.

Just as much I'd like to thank Prof. Roland Pail for supervising my thesis in the final phase. I appreciate the interesting discussions, as well as the very concrete and valuable comments.

I am also indebted to Prof. Wolf-Dieter Schuh for accepting the position of second advisor and for his helpful comments.

I am also grateful to all my colleagues for the amiable working atmosphere, the scientifical support and the prompt assistance in case of technical inconveniences.

I'd like to thank especially Thomas Gruber as a key person of the GOCE HPF for introducing me to this inspiring project and its marvelous team.

Special thanks go to Björn Frommknecht for introducing me to the fascinating and challenging world of GOCE PDS and Level 1b gradiometer processing, the straightforward data and information flow from ESA and many helpful discussions.

Thanks also to Christian Siemes for a fruitful collaboration towards the final phase of my thesis, the helpfulness and exchange of knowledge.

Last but not least, I'd like to thank my parents, my sister with family and my friends, especially Lilo Zenner for all their support in my private life and research work.